Imperial College London

NUS National University of Singapore

# OPTICAL GAIN AND LOSS IN NANOPHOTONICS

by

Ngoc Bao Nguyen

Supervisors: Prof. Stefan A. Maier, Prof. Minghui Hong, Dr. Rupert F. Oulton

Submitted in part fulfilment of the requirements for the joint degree of

**Doctor of Philosophy**

Imperial College London
Department of Physics
London United Kingdom

National University of Singapore
Faculty of Engineering, ECE
Singapore

**August 2018**

IMPERIAL COLLEGE LONDON

NATIONAL UNIVERSITY OF SINGAPORE

| | |
|---|---|
| Author: | Ngoc Bao Nguyen |
| Title: | Optical gain and loss in nanophotonics |
| Department: | Department of Physics (Imperial College), Department of Electrical and Computer Engineering (NUS) |
| Degree: | Joint PhD |
| Date: | August 22, 2018 |

**Declaration of Originality**

I certify that the content presented in this thesis is, to the best of my knowledge, my own. I declare that, where appropriate, I have acknowledged and referenced the work of others.

Ngoc Bao Nguyen

**Copyright Declaration**

The copyright of this thesis rests with the author and is made available under a Creative Commons Attribution Non-Commercial No Derivatives licence. Researchers are free to copy, distribute or transmit the thesis on the condition that they attribute it, that they do not use it for commercial purposes and that they do not alter, transform or build upon it. For any reuse or redistribution, researchers must make clear to others the licence terms of this work.

*To my parents for their endless love,*

## Abstract

The topic of gain/loss and dispersion is fundamental to the construction of various nanophotonic devices. Through a unique branch of physics called Parity Time Symmetry (PTS), the interplay between gain and loss opens many opportunities to make gain/loss and dispersion necessary parts of the operation of PTS optical devices.

The spatial refractive index profile of an optical PTS system, $n(x,y,z)$ requires $\Re\{n(x,y,z)\}$ to be spatially symmetric and $\Im\{n(x,y,z)\}$ to be spatially antisymmetric. Such a system exhibits exceptional point behaviours which give rise to unusual physical phenomena including non-reciprocal propagation of light—the operational principle of optical diodes. Most solid state devices investigated in this thesis are based on GaAs to supply gain. To apply the concept of PTS to practical optical platforms where high loss/gain exists, it is essential to understand the mechanism behind the high gain in GaAs and associated gain-induced dispersion.

To assess the feasibility of generating high gain and the extent of dispersion effects in nanooptics, we demonstrate experimentally a practical GaAs plasmonic laser based on the hybrid gap plasmon waveguide. The analysis of the modal gain and losses in these nanolasers suggests that even though lasing actions can be obtained in this high loss environment, the severe effects of dispersion pose potential issues in practical PTS systems.

In PTS coupled waveguides, the detrimental influence of gain-induced dispersion is counteracted by working with non-identical waveguides and bias pumping of the optical waveguides. The coupled mode theory provides the necessary formulation for an in-depth analysis of such a highly dispersive system. The useful application of dispersion in optical PTS is investigated in a Silicon-based active PTS grating. The results of these works improve our understanding of the gain/loss and dispersion mechanism in PTS optical devices and lay the foundation for an efficient design of PTS optical diodes.

# List of Abbreviations

**CAD** Computer-aided design

**CMOS** Complementary metal-oxide semiconductor

**CMT** Coupled Mode Theory

**DBRs** Distributed Bragg reflectors

**EBL** Electron beam lithography

**EP** Exceptional Point

**FCA** Free carrier absorption

**FF** Filling factor

**FFT** Fast fourier transform

**FT** Fourier transform

**FWHM** Full width half maximum

**HF** Hydrofluoric acid

**HGPW** Hybrid gap plasmon waveguide

**HWG** Hybrid plasmon waveguide

**ICs** Integrated circuits

**iFFT** inverse Fast fourier transform

**LHS** Left hand side

**MBE** Molecular beam epitaxy

**PICs** Photonic integrated circuits

**PL** Photo-luminescence

**PTS** Parity-Time Symmetry

**QM** Quantum Mechanics

**RHS** Right hand side

**SEM** Scanning electron microscope

**SPPs** Surface plasmon polariton

**TE** Transverse electric

**TM** Transverse magnetic

**TMA** Transfer matrix method

**TPA** Two photon absorption

# Contents

**1 Introduction** **1**

1.1 Motivation . . . . . 1

1.2 Scientific goals . . . . . 4

1.3 Thesis structure . . . . . 6

**2 Parity-Time Symmetry: fundamentals and optical applications** **8**

2.1 An overview of the optical PTS applications . . . . . 9

2.2 PTS in Quantum Mechanics . . . . . 11

2.2.1 Conventional Quantum Mechanics . . . . . 11

2.2.2 Quantum mechanical formulation of PTS . . . . . 13

2.3 PTS in optics . . . . . 16

2.4 Coupled Mode Theory in optical PTS . . . . . 19

2.4.1 PTS in codirectional coupled waveguides . . . . . 19

Hermitian coupled waveguide systems . . . . . 21

Ideal PTS: perfectly balanced gain and loss in identical waveguides . . . . . 22

Evaluation of non-reciprocal propagation of light . . . 23

PTS in fixed gain/loss coupled systems . . . . . 24

2.4.2 PTS in contradirectional waveguides — Bragg gratings . . . . . 26

General CMT in the context of Bragg gratings . . . . 26

Evaluation of unidirection reflection in PTS gratings . 28

Refractive index modulation of practical PTS gratings 30

2.5 Summary . . . . . 33

**3 Technology: from photonic to plasmonic waveguides 35**

3.1 Optical Waveguides . . . 36

3.1.1 Guiding light in lossless waveguides . . . 36

3.1.2 Guiding light in lossy waveguides . . . 39

3.2 Hybrid gap plasmon waveguide . . . 39

3.2.1 An overview of plasmonic waveguides . . . 39

3.2.2 HGPW: fundamentals and practicalities . . . 41

Materials for HGPW construction . . . 41

Modal properties of HGPW . . . 43

Hybridization mechanism in HGPWs . . . 46

3.3 Summary . . . 49

**4 Loss and Gain mechanism in optical devices 50**

4.1 Gain mechanism in GaAs . . . 51

4.1.1 An overview of GaAs properties . . . 51

4.1.2 Fundamental concepts in band structure theory . . . 52

Formation of band structures in solids . . . 52

Fermi-Dirac Distribution . . . 53

4.1.3 Light in gain media . . . 54

Overview of semiconductor gain theory . . . 54

Propagation of light in polarized media . . . 55

Light – matter interactions in semiconductor gain media 57

Dynamic evolution of material properties . . . 59

Calculation of quasi chemical potentials . . . 61

4.1.4 Results and Discussion . . . 62

Results of free carrier theory . . . 62

Validity of the semiconductor gain theory . . . 64

4.2 Loss compensation in lasing mechanism . . . 67

4.2.1 Cavity Modes . . . 67

4.2.2 Einstein A and B coefficients . . . 68

4.2.3 Rate Equations . . . 70

4.2.4 Modified light-matter interactions in cavities . . . . . 72
4.3 Summary . . . . . 77

**5 GaAs based HGPW nanolasers 78**
5.1 Device design: HGPW-based cavity . . . . . 79
5.1.1 Waveguide and taper construction . . . . . 79
5.1.2 DBR design . . . . . 81
5.2 Fabrication process . . . . . 82
5.3 Experimental set-up and characterization method . . . . . 85
5.4 Results and Discussion . . . . . 88
5.4.1 Data analysis method . . . . . 88
5.4.2 Lasing action in 1-step devices . . . . . 89
5.4.3 Gain and loss analysis of lasing action . . . . . 91
5.5 Summary . . . . . 96

**6 Recovering PTS in highly dispersive coupled waveguides 98**
6.1 Components of CMT in 1D coupled systems . . . . . 99
6.2 GaAs-AlGaAs coupled waveguides . . . . . 100
6.3 Analytic and numerical calculations of supermodes in coupled systems . 100
6.4 Imperfect PTS systems . . . . . 103
6.4.1 Imbalance in gain and loss . . . . . 103
6.4.2 Imbalance in modal index . . . . . 105
6.4.3 Material dispersion effects . . . . . 107
6.5 Recovering PTS in highly dispersive systems . . . . . 107
6.6 Mode coalescence and phase rigidity . . . . . 111
6.7 Summary . . . . . 115

**7 Active PTS gratings 116**
7.1 Passive vs active PTS gratings . . . . . 118
7.2 Optical properties of Silicon . . . . . 120
7.2.1 Excited carriers in semiconductors and metals . . . . . 120
7.2.2 Pump-induced refractive index change in Silicon . . . . . 121

7.3 Waveguide integrated pump-probe spectroscopy . . . 124
7.3.1 Waveguide geometry and fabrication . . . 124
7.3.2 Experimental apparatus . . . 124
7.3.3 The physics of pump-probe spectroscopy . . . 126
7.3.4 Experimental and data extraction procedure . . . 127
$\Delta n''_{Si}$ measurement . . . 127
$\Delta n'_{Si}$ measurement . . . 129
7.3.5 Results of temporal responses of pumped silicon . . . 133
Spatial and temporal overlap of the pump and probe beams . . . 133
$\Delta n''_{Si}$ results . . . 134
$\Delta n'_{Si}$ results . . . 138
7.4 Preliminary work . . . 140
7.4.1 Construction of Si-based active PTS gratings . . . 140
7.4.2 Fabrication . . . 142
7.5 Summary . . . 143

**8 Conclusion** **145**
8.1 Summary . . . 145
8.2 Future work . . . 147
8.2.1 Plasmonic lasers . . . 147
8.2.2 PTS optical devices . . . 148

**References** **151**

**Appendices** **167**

**A Parity-time inner product** **168**

**B Detailed calculation of CMT** **169**
B.1 Calculation of CMT coefficients . . . 169
B.2 The simplified Hamiltonian of coupled codirection modes . . . 170
B.3 Finding the transfer matrix of coupled codirection modes . . . 171

B.4 Fourier analysis and CMT in contradirectional coupled modes . . . . . 172

**C FDTD simulation of PTS and conventional gratings 175**

**D Iterative steepest descent method with linear line search 177**

**E Surface Plasmon Polariton 178**

**F Optical properties of metals 182**

**G Energy and power flow in plasmonics 185**

**H Semiconductor gain formulation 188**

**I Fabrication details of hybrid gap plasmon nanolasers 191**

**List of Tables 192**

**List of Figures 192**

**Publications 197**

**Author's Contribution 198**

**Acknowledgements 199**

# Chapter 1

# Introduction

## 1.1 Motivation

Seventy years ago, the information processing landscape of our modern society changed forever with the arrival of one of the most prominent discoveries of mankind, the transistor [1, 2]. Smaller, faster and much more energy efficient than its predecessor vacuum tubes [3], the transistor has become the building blocks of modern Integrated Circuits (ICs). Nowadays, electronic devices such as computers, domestic appliances and smartphones are all built upon fingernail-sized chips. Since its invention, the IC has revolutionized our computational power. For the last 50 years, researchers have worked extremely hard to keep up with Moore's prophecy of fitting twice as many transistors on a chip every two years [4]. The record set by IBM in 2017 was a densely packed chip of 30 billion transistors of 5 nanometers in size [5]. 'Smaller-is-better' has been the motto of researchers for many years [6]. However, fundamental scaling laws will kick in when transistor sizes reach the atomic scale and the device performance ever deteriorates due to latency and detrimental thermal effects [7]. To feed our seven billion data-hungry inhabitants, unique materials, clever device designs and even novel physical concepts are required.

With the peak of the electronic age lurking on the horizon, the research community once again resumes the search for the seed of the next technological advancement. The intrinsic charge and mass of the electron are the ultimate cause of the fundamental limitations placed on the performance of electronic devices. This simple argument

might tempt us to believe that photonics is the answer to our problems. Light, as an information carrier, can overcome the problems of speed, limited bandwidth and even heating that electronics constantly faces. Indeed, low-loss optical fibers replacing traditional metal wires as long-range signal transmitters enable a gigantic volume of data to be transported around the world in less than a second [8]. Nonetheless, when moving to chip-scale applications, photons themselves are not problem-free. Photonic integrated circuits (PICs) and intrachip optical interconnects [9, 10] are restricted by the diffraction limit—the size of a typical photonic device cannot go below half of its operating wavelength, which is at least 2 orders of magnitude greater than its electronic counterpart [7]. Better performance comes at a price of larger footprint.

Though the field began more than 50 years ago, recently plasmonics has caught the attention of the research community as a promising interface to bridge the enormous gap between electronics and photonics [11–13]. Plasmonics offers a mean to circumvent the diffraction limit [14] and the ability to concentrate light into nanoscale volumes [15]. Surface plasmon polaritons (SPPs)—electromagnetic waves couple to collectively oscillating electrons in the metal plasma—are surface waves existing at the metal-dielectric interface [16]. The participation of free electrons in the propagation of light is the principal element that allows plasmonics to surpass the diffraction limit. Plasmonics, with its ability to enhance the inherently weak light-matter interactions, has powered a number of novel applications in bio-sensing [17], spectroscopy [18–20] and single molecule detection [21,22]. Although, the vital role of electrons in plasmonics is undeniable, they also bring problems. Conduction electrons in metals relentlessly interact with phonons, their nuclei and amongst themselves [11], leading to significant ohmic losses which damp the propagation of SPPs. These two aspects of electronic behaviours compose the famous trade-off in plasmonics between efficiency and field confinement [16].

The huge success of the microelectronic industry comes largely from the replacement of pure Silicon wafers with SOI (Silicon on Insulator) wafers and their built-in compatibility with CMOS (Complementary metal–oxide-semiconductor) processes [23].

While the metallic element of SPPs allows potential integration into current electronic platforms, traditional plasmonic materials, noble metals such as silver and gold, are not CMOS compatible. This complication in plasmonic device fabrication together with its high ohmic losses have hindered the industrial applications of plasmonics. However, the unparalleled capability at manipulating light in the nanoscale regime of SPPs still draws many research projects into developing innovative plasmonic platforms.

Although nanophotonics is not restricted to the world of plasmonics or the broader field of metamaterials, the high level of losses which increases significantly as the device size enters the submicron regime, remains the most prevalent issue that needs to be addressed before truly nanoscale photonic devices can make their ways into our day-to-day lives. Perhaps the most obvious solution to such a problem is to compensate the operational loss with optical gain. Optical gain is often associated with lasers which amplify light by stimulated emission, resulting in the generation of powerful and coherent optical sources. Going beyond compensating for loss is to explore novel concepts which can bring out useful functionalities of optical losses which have always been believed to be detrimental in nanophotonics.

In general, the potential solutions to the tenacious aforementioned problems, which prevent the practical applications of nanophotonics, can be classified into four main categories: synthesizing new materials with superior low-loss properties [24–28]; adapting current microelectric fabrication techniques to accommodate plasmonic materials, efficiently incorporating optical gain into pragmatic plasmonic designs [29], and most interesting of all, investigating innovative devices in which losses are desired in their operation. Although these four approaches are not mutually exclusive, the first two tackle the problem from an engineering standpoint, while the latter two, evoking many interdisciplinary notions, concern the fundamental construction of nanophotonic devices. Hence, the interplay between optical loss and gain in practical nanodevices is the focus of this thesis.

## 1.2 Scientific goals

As the interaction of optical loss and gain in nanophotonics lies at the heart of this work, our aims are firstly to investigate the mechanism of efficient loss compensation in practical nanophotonic platforms and secondly to look into new physical concepts that empower useful manipulation of loss in the context of nanodevices.

Nanophotonics brings with it a plethora of devices, ranging from modulators, waveguides to on-chip light sources. As identified above, plasmonics is the key to the miniaturization of photonic devices. Thus, plasmonic lasers provide the perfect setting for our loss-gain balance study in nanophotonics. Furthermore, these nanolasers also act as a gateway to an unfamiliar territory of physics called Parity-Time Symmetry (PTS) [30] where unusual loss-induced functionalities lead to useful optical applications. Although the physics of nanolasers and optical PTS devices has been studied for many years, the lack of practical considerations in terms of fabrication techniques, device quality and detrimental dispersion effects has stopped these devices from going beyond proof-of-principle, strongly hindering their industrial applications.

The hybrid gap plasmon laser is the chosen platform to implement the study of high gain generation in practical nanophotonics. We solve the problems of high surface recombination rate in semiconductor gain media and the poor control over device location by passivating GaAs suspended membranes [31, 32] and employing the hybrid gap plasmon waveguide (HGPW) as our laser cavity [33–35]. With its top-down construction and a close resemblance to standard SOI platforms, hybrid gap plasmon GaAs nanolasers achieve confinement and feedback solely through 2D lithographic patterning of metals on the GaAs membranes and thus eliminate the requirement to etch the semiconductor in order to define the cavity. The scope of this work extends beyond the construction of HGPWs and the demonstration of their lasing action; it also discusses in great detail the role of gain and loss and their associated dispersion effects in the high pump regime of nanolasers.

The results of this loss compensation analysis in a laser environment allow us to

assess the feasibility of applying PTS to practical devices where high gain/loss and dispersion coexist. The clever manipulation of gain and loss based on the topical PTS concept is applied to two familiar optical systems: coupled waveguides and Bragg gratings which lead to non-reciprocal propagation and unidirectional reflection of light respectively. These systems can be studied based on the conventional coupled mode theory (CMT), allowing an in-depth analysis of practical limitations to be carried out. In order to achieve close to ideal PTS, most of the demonstrated experiments limited the gain to just a few hundred $cm^{-1}$ due to strong gain-induced dispersion effects. This prevents the extension of PTS to more highly functional and practical optoelectronic or plasmonic platforms where very high loss/gain is present. Thus, our second goal is to search for strategies that manage gain-induced dispersion in the context of PTS coupled waveguides.

Any strategy that can effectively influence both gain/loss and dispersion requires an active approach where the refractive index of a material can be dynamically controlled. This leads us to our third investigation which involves turning a passive PTS system into an active one by pump-induced effects. The PTS Bragg grating work by Feng, *et al.*, proved that a unidirectional reflection device could be established [36]; however, by defining both the real and imaginary parts of the refractive index of the system at the fabrication level, the occurrence of an exceptional point (EP) cannot be tuned accurately. Here, we take the first steps in exploring a dynamic manipulation of PTS on SOI platforms, assessing the viability of using carrier-induced effects in Silicon to construct an active PTS Bragg grating.

The extensive investigation of plasmonic lasers and various optical PTS geometries in the literature show promising signs that in the coming years, we might be able to construct a new optical circuitry platform which consists of an on-chip light source based on plasmonic lasers and optical modulators or diodes built upon PTS devices [37, 38].

## 1.3 Thesis structure

The thesis is organized into eight chapters. **Chapter 2** puts in place the theoretical fundamentals of PTS and its optical applications. We begin this chapter with a brief discussion of quantum mechanics PTS followed by an introduction of PTS in optics. The mathematical platform of coupled mode theory is then presented in the context of PTS coupled waveguides and PTS Bragg gratings in order to explain the origin of non-reciprocal propagation and unidirectional reflection phenomena, which are studied in this thesis.

**Chapter 3** introduces the technological platforms upon which the works presented in this thesis are built. This chapter provides the device context in which various gain and loss mechanisms are discussed in subsequent chapters. An outline of the theory of conventional dielectric waveguides for both the lossless and lossy structures is given. Plasmonic waveguides are not only able to circumvent the diffraction limit which restricts the application of photonic waveguides at chip-scale, they are also capable of enhancing light intensity by many orders of magnitude. Amongst various plasmonic waveguide designs, we focus on investigating the properties of the hybrid gap plasmon waveguide configuration: selecting appropriate materials for their construction and understanding their modal formation.

**Chapter 4** is dedicated to the analysis of the gain mechanism in semiconductors and loss mechanism in cavities. Understanding the origin of gain generation and gain-induced dispersion in semiconductors is central to our study of hybrid gap plasmon GaAs nanolasers and PTS coupled waveguides. A review of the basic concepts in band theory is first given. This provides us with the necessary tools to study light matter interactions in GaAs using the semi-classical theory of free carriers. This is followed by a comparison between the results of our simple model and other more complex models of gain in the literature. The second part of this chapter analyzes the loss mechanism in the context of photonic cavities and nanolasers.

The next three chapters present the results on the analysis of our three devices of in-

terest. **Chapter 5** outlines the development of hybrid gap plasmon GaAs nanolasers. The first part focuses on the design, fabrication and characterization of our plasmonic lasers using passivated GaAs membranes. Results and discussions of our experiments are presented next. Here, the analysis of GaAs gain and loss mechanism detailed in Chapter 4 is used to analyze the threshold gain conditions of various nanolaser designs.

Taking a step back from experimental demonstrations, **Chapter 6** theoretically explores the feasibility of recovering PTS in highly dispersive coupled waveguide systems. The analysis requires the analytic evaluation of coupling coefficients of coupled mode theory in PTS coupled systems. We investigate the smooth transitions between PTS phases under the influence of imbalanced gain/loss and modal mismatch. This newly gained knowledge of imperfect PTS systems identifies a suitable strategy to compensate for dispersion effects.

Following this line of work, **Chapter 7** targets a different kind of PTS devices: an active PTS Bragg grating whose operation relies on the ability to dynamically control pump-induced effects. A description of conventional passive PTS gratings is first given. This is followed by a proposal of the construction of an active PTS grating. Our experimental results on the carrier-induced refractive index change in Silicon are presented in the next section. The chapter ends with a summary of our preliminary work on the device construction and fabrication.

**Chapter 8** summarizes the main findings presented in this thesis and outlines several lines of future work which can be developed based on the current results.

# Chapter 2

# Parity-Time Symmetry: fundamentals and optical applications

This chapter begins with an overview of experimental demonstrations of Parity-Time Symmetry (PTS) in optics. We outline the fundamentals of quantum and optical PTS, with an emphasis on the pertinent aspects of PTS that run parallel with conventional Hermiticity. Optical PTS allows seemingly abstract quantum mechanics (QM) phenomena to manifest into physical observations. The concept of PTS in optics is described by the well-known coupled mode theory (CMT), providing us with an intuitive description of the unusual consequences of optical PTS. The last section of this chapter lays out the mathematical platform of CMT in codirectional and contradirectional mode coupling and uses these results to explain the origin of non-reciprocal propagation and unidirectional reflection phenomena, the two most prominent optical PTS applications.

## 2.1 An overview of the optical PTS applications

In the late 1990s, several theoreticians noticed that there existed a class of non-Hermitian Hamiltonians which possessed an entirely real eigenspectrum, meaning they could describe real physical systems [39, 40]. Instead of being Hermitian, these Hamitonians need only to respect Parity-Time Symmetry (PTS). However, PTS is only a weak condition and hence can be broken. This symmetry breaking is signified by a phase transition in the eigenspectrum of the system at an exceptional point (EP) [41, 42]. The behaviour of physical systems often changes drastically around the EP. This has led to the prediction of various counter-intuitive optical phenomena—a light beam will see its dynamics greatly modified compared to conventional optics when passing through a PTS system [43, 44].

A PTS optical system requires a particular complex refractive index spatial distribution: a symmetric distribution of the real part and an antisymmetric distribution of the imaginary part which can be realized via the incorporation of gain and loss [41, 42, 45]. Here, our aim is not to present an exhaustive review of optical PTS but to highlight important findings on the experimental front that have practical relevance and demonstrate the versatility and uniqueness of PTS applications. The four most popular configurations of optical PTS are coupled waveguides [46–55], coupled lasers/absorbers [56–66], PTS Bragg gratings [37, 67–72] and PTS photonic lattices [42, 43, 73–75].

The first experimental evidence of PTS in optics dates back to 2009 when Guo *et al.,* used an 8 $\mu$m core coupled waveguide system made of a multilayer $Al_xGa_{1-x}As$ heterostructure to demonstrate PTS breaking [76]. Loss was introduced via the deposition of 100 nm Cr films on one of the waveguides with varying stripe widths, equivalent to an absorption range of 0-14 $cm^{-1}$. At the critical Cr stripe width where the system reached its EP, the total transmission power from both channels increased even though the overall metal loss of the system also got larger, a phenomenon named 'loss-induced optical transparency'. The second convincing demonstration came through in 2010 when the concept of non-reciprocal propagation of light with respect to left

and right symmetry was proved to exist in a coupled waveguide system of Fe-doped $LiNbO_3$ and Ti in-diffusion [46]. A low pump intensity of up to 1 mWcm$^{-2}$ was used to pump the gain arm of the coupled system, while leaving the lossy one untouched. Two years later, a PTS fibre loop lattice construction was used to show that the reflection and transmission of light through this optical network could either experience a reduction or an enhancement depending on the direction of propagation, effectively turning the visibility of the network on and off [43]—a demonstration of non-reciprocal behaviour.

The next experimental evidence achieved the novel PTS property called 'unidirectional reflection' by exploiting a modulation of refractive index along the propagation direction in a waveguide. Unidirectional reflection refers to the significant difference in the reflectivity of a system when the input field is either in the forward or backward directions. Feng *et al.*, employed a passive PTS structure based on 800x220 nm Si ridge waveguide with periodic Si and Ge/Cr bars on top to establish the required index profile. The authors obtained a forward reflectivity of about 7.5 dB stronger than its backward counterpart. A high contrast ratio of 0.5-0.7 was achieved over a broad wavelength range of 1520-1580 nm [36]. These unidirectional reflection and invisibility properties of PTS gratings can be exploited in unconventional designs of photonic devices such as four-port broadband chip-scale analysers.

The idea of optical PTS was further extended to the spatiotemporal domain following the first work on PTS coupled microdisk quantum cascade lasers by Brandstetter *et al.* Using transitions between quantized energy levels of semiconductor quantum wells made of GaAs/AlGaAs, a characteristic reversal of pump dependence near the vicinity of the EP was observed. The system operating in the THz regime experienced a strongly decreasing lasing intensity for increasing pump power [58]. The year 2014 saw a burgeoning interest in PTS lasers. Hodaei *et al.*, demonstrated single mode lasing in a PTS system of coupled InGaAsP microring lasers where only one of the identical microring lasers was pumped [77]. Stable single mode lasing operation was also achieved in another PTS configuration which consisted of a ring of InGaAsP/InP

with a periodic deposition of Cr/Ge on top [57]. In this work, the thresholdless PTS breaking originating from the rotational symmetry of the system was behind the selective lasing mechanism. Based on this same configuration, Miao *et al.*, experimentally demonstrated a microring laser which was able to produce a single mode orbital angular momentum vortex lasing [78]. Further PTS coupled ring resonator demonstrations include the work of Peng *et al.*, which showed how EP behaviours could effectively turn losses into gain. This mechanism gave rise to loss-induced revival and suppression of lasing, i.e., by adding loss to a resonator, the laser emission is enhanced [79]. The idea of coupled erbium-doped silica microtoroids was examined by Peng *et al.* to demonstrate a transition from reciprocity to non-reciprocity upon PTS breaking due to an enhancement of nonlinearity in the broken phase [38]. The same structure was adopted by Chang *et al.*; here the authors successfully demonstrated the operation of this PTS device as an optical isolator with a back and forth reflection ratio ranging from -8dB to +8dB [80]. Non-reciprocal propagation of light, one of the most prominent consequences of PTS, is the physical mechanism behind the operation of optical diodes—an essential component of all-optical integrated circuitry.

After 2014, breaking away from microresonator systems, a much wider range of PTS systems has been explored. Photonic lattices came into the scene with three impressive works: optically induced atomic lattices formed in a coherently prepared four level N-type atomic system by Zhang *et al.,* [81] chip-scale Bloch oscillations in a photonic PTS potential by Xu *et al.,* [75] and reconfigurable non-Hermitian photonic lattices with PTS characteristics using a novel vector field holographic interference by Hahn *et al.,* [82]. Going beyond conventional PTS, an anti-PTS optical system was realised via rapid coherence transport in a warm 87Rb vapour vell [83].

## 2.2 PTS in Quantum Mechanics

### 2.2.1 Conventional Quantum Mechanics

The most fundamental QM postulate states that for every observable $A$, there exists a corresponding linear, hermitian operator $\hat{A}$ in QM. In any measurements of ob-

servable $A$, the only values that can be observed are eigenvalues of $\hat{A}$, which follow the eigen-equation: $\hat{A}|\Psi(r,t)_i\rangle = a_i|\Psi(r,t)_i\rangle$, where $a_i$ and $|\Psi(r,t)_i\rangle$ are the eigenvalue and corresponding eigenfunction of $\hat{A}$. Measurements in practical experiments are expected to be real numbers. The hermiticity property of $\hat{A}$ ensures that $a_i$ is always real. The linearity requirement of QM operators is a consequence of another QM postulate which states that when an arbitrary system is measured with an operator $\hat{A}$, the wave function of that system will collapse into one of $\hat{A}$ 's eigenfunctions with a well-defined probability. Thus, a quantum state can only be determined in a probabilistic sense [84].

Hermiticity in fact refers to self-adjoint operators. In Dirac bra and ket notation, it takes the form:

$$\left\langle \phi|\hat{A}\psi \right\rangle = \int dx\phi^*(\hat{A}\psi) = \int dx\psi(\hat{A}^*\phi)^* = \left\langle \hat{A}^*\phi|\psi \right\rangle \tag{2.1}$$

Formally this means that the effects of the self-adjoint operator $\hat{A}$ on vectors, $\psi$ and $\phi$, in Hilbert space do not depend on which vector it acts on first. However, the matrix properties associated with self-adjoincy rely crucially on the definition of an inner product in a vector space. There are an infinite number of ways in which one can define an inner product in Hilbert space. However, the general requirements for an inner product are:

1. $(p,q) = (q,p)^*$
2. An inner product must be bilinear:
   - $(p,q+w) = (p,q) + (p,w)$ and $(p+q,w) = (p,w) + (q,w)$
   - $(p,cq) = c(p,q)$ where $c$ is a complex number
   - $(cp,q) = c^*(p,q)$

where $p$ and $q$ denote vectors in Hilbert space [84]. As an inner product is interpreted as a probability in QM, it is required that this value must be positive. If a set of basis vectors span a vector space, this set and the inner product are related by the kernel: $\kappa_{ij} = (e_i,e_j)$ with $(p,q) = (\Sigma p_i e_i, \Sigma q_j e_j) = \Sigma_i \Sigma_j p_i^* \kappa_{ij} q_j$ [84]. The chosen basis is said to be orthonormal if $\kappa_{ij} = \delta_{ij}$—the Kronecker delta function. The standard inner

product of Hermitian conjugate can then be applied where $\langle\phi|\psi\rangle = \phi^\dagger\psi$. The inner product of two vectors in Hilbert space is constant in time due to the conservation of probability, namely the unitary property. Thus, hermitian operators are self-adjoint with respect to the above definition of the inner product. In matrix representation, this corresponds to a Hermitian operator having the same form as its complex conjugate transpose.

The following properties of Hermitian operators make them suitable to be used in the description of observables in QM:

- All eigenvalues of a hermitian operator are real.
- All eigenvectors corresponding to distinct eigenvalues are orthogonal.
- Completeness: if an operator in an M-dimensional Hilbert space has M distinct eigenvalues with no degeneracy, then its eigenvectors form a complete set of unit vectors.
- Unitarity of time evolution operator ensures that the time-dependent Hamiltonian is hermitian: time evolution in QM takes the form of $|\psi(t)\rangle = \hat{U}(t)|\psi(0)\rangle$. If $\hat{H}$ is hermitian, $\hat{U}^\dagger(t)\hat{U}(t) = \hat{I}$ at all time $t$ and thus, $\hat{U}(t)$ must always be unitary. Unitary implies that the norm of the state is conserved: $\langle\Psi(t)|\Psi(t)\rangle = \langle\Psi(0)|\Psi(0)\rangle$.

### 2.2.2 Quantum mechanical formulation of PTS

The Hamiltonian $\hat{H}$, describing the energy evolution of a quantum system, must also be Hermitian in order to be observable. A class of non-hermitian Hamiltonians which respects PTS under certain conditions was found to have real eigenvalue spectra and unitary time evolution. The hermiticity requirement is replaced by the condition that the Hamiltonian has to obey PTS [41]. In other words, hermiticity is sufficient but not necessary to obtain real eigenvalue spectra [50].

The operation of $\hat{P}$ and $\hat{T}$ operators, i.e., symmetric space and time inversion, is

described below with $x$ – position, $p$ – momentum, $t$ – time, $i$ – imaginary number:

$$\begin{gathered}\hat{P}\left|x\right\rangle = \left|-x\right\rangle \quad \hat{P}\left|p\right\rangle = \left|-p\right\rangle \\ \hat{T}\left|x\right\rangle = \left|x\right\rangle \quad \hat{T}\left|t\right\rangle = \hat{T}\left|-t\right\rangle \quad \hat{T}\left|p\right\rangle = \hat{T}\left|-p\right\rangle \quad \hat{T}\left|i\right\rangle = \hat{T}\left|-i\right\rangle\end{gathered} \tag{2.2}$$

We know that if $\hat{A}$ is a linear operator and $\left[\hat{H},\hat{A}\right] = 0$, the eigenfunctions of $\hat{H}$ are also the eigenfunction of $\hat{A}$.[a] However, $\hat{P}\hat{T}$ is not a linear operator. Even though $\left[\hat{H},\hat{P}\hat{T}\right] = 0$, it does not necessarily mean that the two operators share the same eigenfunctions [46]. This distinction plays a central role in defining the different phases of a PTS system. $\hat{H}$ can always be parity-time symmetric since this only requires $\left[\hat{H},\hat{P}\hat{T}\right] = 0$; but whether the symmetry remains exact depends on the Hamiltonian's eigenvalue spectrum. PTS of a Hamiltonian is exact if $\left[\hat{H},\hat{P}\hat{T}\right] = 0$ and an eigenfunction of $\hat{H}$ is also an eigenfunction of $\hat{P}\hat{T}$, resulting in a purely real eigenvalue spectrum. PTS is said to be broken if $\hat{H}$ and $\hat{P}\hat{T}$ have different eigenfunction sets and the eigenvalue spectrum of $\hat{H}$ turns complex even though $\left[\hat{H},\hat{P}\hat{T}\right] = 0$ [46]. The point at which PTS is broken marks a PTS phase transition which results in the formation of an exceptional point (EP) [76].

We will next examine the requirements of a PTS matrix. Consider an arbitrary matrix $\boldsymbol{B} = \begin{bmatrix} a_1 & a_2 \\ a_3 & a_4 \end{bmatrix}$ where $a_{1-4}$ are complex numbers. Assume that the spatial reflection only occurs in the x-direction and represented by $S_x = \begin{bmatrix} 0 & 1 \\ 1 & 0 \end{bmatrix}$ [84]. Hence,

$$\hat{P}\hat{T}\boldsymbol{B}\psi = \begin{bmatrix} 0 & 1 \\ 1 & 0 \end{bmatrix}\hat{T}\begin{bmatrix} a_1 & a_2 \\ a_3 & a_4 \end{bmatrix}\psi = \begin{bmatrix} 0 & 1 \\ 1 & 0 \end{bmatrix}\begin{bmatrix} a_1^* & a_2^* \\ a_3^* & a_4^* \end{bmatrix}\psi^* = \begin{bmatrix} a_3^* & a_4^* \\ a_1^* & a_2^* \end{bmatrix}\psi^*$$

$$\boldsymbol{B}\hat{P}\hat{T}\psi = \begin{bmatrix} a_1 & a_2 \\ a_3 & a_4 \end{bmatrix}\begin{bmatrix} 0 & 1 \\ 1 & 0 \end{bmatrix}\psi^* = \begin{bmatrix} a_2 & a_1 \\ a_4 & a_3 \end{bmatrix}\psi^*$$

PTS requires that $\hat{P}\hat{T}\boldsymbol{B}\psi = \boldsymbol{B}\hat{P}\hat{T}\psi$. From the above example, we can deduce the following relationship of the elements of $\boldsymbol{B}$: $a_2 = a_3^*$ and $a_1 = a_4^*$. To demonstrate the differences between PTS and Hermiticity, consider the following examples of PTS

[a] An operator is linear when: $\hat{A}\left(f+g\right) = \hat{A}\left(f\right) + \hat{A}\left(g\right)$ and $\hat{A}\left(tf\right) = t\hat{A}\left(f\right)$.

and Hermitian matrices: $\boldsymbol{B}_{PT} = \begin{bmatrix} i\alpha & \beta \\ \beta & -i\alpha \end{bmatrix}$ and $\boldsymbol{B}_{H} = \begin{bmatrix} \alpha & \beta \\ \beta & -\alpha \end{bmatrix}$ where $\alpha$ and $\beta$ are real numbers.

**Table 2.1** – Comparison of basic properties of Hermitian and PTS matrices.

| Property | | Hermitian | PTS |
|---|---|---|---|
| Eigenvalues | Definition | $\sigma_{\pm} = \pm\sqrt{\beta^2 + \alpha^2}$ | $\sigma_{\pm} = \pm\sqrt{\beta^2 - \alpha^2}$ |
| | $\beta > \alpha$ | $\sigma_{\pm} \in \Re$ | $\sigma_{\pm} \in \Re$ |
| | $\beta = \alpha$ | $\sigma_{\pm} \in \Re$ | $\sigma_{\pm} = 0$ |
| | $\beta < \alpha$ | $\sigma_{\pm} \in \Re$ | $\sigma_{\pm} \in \Im$ |
| Eigenfunction | Definition | $\psi_{-} = \begin{bmatrix} cos(\theta/2) \\ sin(\theta/2) \end{bmatrix}$; $\psi_{+} = \begin{bmatrix} -sin(\theta/2) \\ cos(\theta/2) \end{bmatrix}$ where $tan(\theta) = \frac{\beta}{\alpha}$ | $\psi = \begin{bmatrix} 1 \\ \pm e^{\mp i\phi} \end{bmatrix}$ where $sin(\phi) = \frac{\alpha}{\beta}$ |
| | $\beta > \alpha$ | $\theta \in \Re$ $\langle\psi_{+}\|\psi_{-}\rangle = \psi_{+}^{\dagger}\psi_{-} = 0$ Orthogonal | $\phi \in \Re$ $\langle\psi_{+}\|\psi_{-}\rangle = 1 - e^{2i\phi}$ Non-orthogonal |
| | $\beta = \alpha$ | $\theta = \pi/4$ $\langle\psi_{+}\|\psi_{-}\rangle = 0$ Orthogonal | $\phi = \pi/2$ $\psi_{\pm} = \begin{bmatrix} 1 \\ i \end{bmatrix}$ Coalescence |
| | $\beta < \alpha$ | $\theta \in \Re$ $\langle\psi_{+}\|\psi_{-}\rangle = 0$ Orthogonal | $\phi \in \Im$ $\langle\psi_{+}\|\psi_{-}\rangle = 1 - e^{2i\phi}$ Non-orthogonal |
| $\upsilon$: phase difference between the elements of $\psi_{\pm}$. | Definition | $\upsilon$ and $\theta$ have different meanings. $cos(\theta)$ and $sin(\theta) \in \Re$ regardless of the value of $\theta$. | According to the above definition of PTS eigenfunctions, $\upsilon = \phi$. |
| | $\beta > \alpha$ | $\upsilon_{\pm} = 0$ and $\pi$. | $\upsilon$ can take any value between 0 and $\pi$ |
| | $\beta = \alpha$ | | $\upsilon = \pi/2$. Degenerate supermodes. |
| | $\beta < \alpha$ | | $\upsilon \in \Im$ |

Table 2.1 summarizes the basic properties of the eigenfunctions and eigenvalues of $\boldsymbol{B}_{H}$ and $\boldsymbol{B}_{PT}$. We focus on investigating aspects of PTS eigenspectra and eigenfunctions that are relevant to our subsequent discussion of PTS in optics. A detailed proof of unitary evolution in PTS is beyond the scope of this thesis as it requires a new definition of the inner product. A brief introduction to PTS inner product is given in

Appendix A; for further details, the readers are referred to [84].

For a PTS matrix, as we scan through the parameter space, there exists a region where its eigenvalues, $\sigma_{\pm}$ defined in Table 2.1, take purely real values. The EP is defined at $\sigma_{\pm} = 0$ with $\beta = \alpha$. Beyond this point, PTS is said to be broken. The non-orthogonal eigenfunctions of a PTS system mean that the basic vector space of such a system is intrinsically skewed. The degree of skewness depends on the value of the relative phase difference, $\upsilon$, defined as the phase difference between the elements of $\psi_{\pm}$ [46].[b]

## 2.3 PTS in optics

The remarkable resemblance between the Schrödinger equation and the wave equation has led to the extension of PTS into classical optics regime [85]. Consider the familiar form of the Schrödinger equation:

$$\begin{aligned} &\text{Time-dependent:} \quad i\hbar\frac{d}{dt}\Psi(\boldsymbol{r},t) &&= \hat{H}\Psi(\boldsymbol{r},t) \\ &\text{Time-independent:} \quad \hat{H}\Psi(\boldsymbol{r},t) &&= E\Psi(\boldsymbol{r},t) \end{aligned} \tag{2.3}$$

where the Hamiltonian takes the form of $\hat{H} = \frac{-\hbar^2}{2m}\nabla^2 + \hat{V}(\boldsymbol{r},t)$, $E$ is its eigenvalue and $\hbar$ is the usual Planck's constant and $\hat{V}(\boldsymbol{r},t)$ is the potential energy.

In optics, the propagation of a time-varying electromagnetic wave in a medium where there are no free currents, $\boldsymbol{\mathcal{J}} = 0$ and no free charges $\rho = 0$, is governed by the macroscopic Maxwell equations [86, 87]:

$$\nabla \cdot \boldsymbol{\mathcal{B}} = 0 \tag{2.4}$$

$$\nabla \cdot \boldsymbol{\mathcal{D}} = 0 \tag{2.5}$$

$$\nabla \times \boldsymbol{\mathcal{E}} = -\frac{\partial \boldsymbol{\mathcal{B}}}{\partial t} \tag{2.6}$$

[b] For example: the eigenmode $\psi_+$with the elements $-\sin(\theta/2)$ and $\cos(\theta/2)$ has $\upsilon = \pi$ as the minus sign can be written as $e^{i\pi}$.

$$\nabla \times \boldsymbol{\mathcal{H}} = \frac{\partial \boldsymbol{\mathcal{D}}}{\partial t} \tag{2.7}$$

where $\boldsymbol{\mathcal{B}}(\boldsymbol{r},t)$ is the magnetic induction, $\boldsymbol{\mathcal{H}}(\boldsymbol{r},t)$ is the magnetic field, $\boldsymbol{\mathcal{D}}(\boldsymbol{r},t)$ is the electric displacement and $\boldsymbol{\mathcal{E}}(\boldsymbol{r},t)$ is the electric field. A medium responds to an incident electromagnetic field by generating polarization, $\boldsymbol{\mathcal{P}}(\boldsymbol{r},t)$ and magnetization, $\boldsymbol{\mathcal{M}}(\boldsymbol{r},t)$. The following relations connect these field quantities: $\boldsymbol{\mathcal{B}} = \mu_0\boldsymbol{\mathcal{H}} + \mu_0\boldsymbol{\mathcal{M}}$ and $\boldsymbol{\mathcal{D}} = \epsilon_0\boldsymbol{\mathcal{E}} + \boldsymbol{\mathcal{P}} = \epsilon\boldsymbol{\mathcal{E}}$. The constants $\epsilon_0$ and $\mu_0$ are the usual electric permittivity and magnetic permeability of free space and $\epsilon$ denotes the medium's electric permittivity. For non-magnetic materials and at optical frequencies and beyond, $\boldsymbol{\mathcal{M}} = 0$ [88]. The most general form of the wave equation in Cartesian coordinate is then found by taking the curl of Eqn. 2.6 and applying the identity $\nabla \times \nabla \times \boldsymbol{G} = \nabla(\nabla \cdot \boldsymbol{G}) - \nabla^2\boldsymbol{G}$:

$$\left(\nabla^2 - \frac{1}{c^2}\frac{\partial^2}{\partial t^2}\right)\boldsymbol{\mathcal{E}}(x,y,z) = \left(\nabla^2 - \frac{\omega^2}{c^2}\epsilon(x,y,z)\right)\boldsymbol{\mathcal{E}}(x,y,z) = 0 \tag{2.8}$$

where $c$ is the light speed in vacuum. Table 2.2 elucidates the isomorphic resemblance between the two equations which govern the quantum and optical worlds [89].

**Table 2.2** – Comparison of QM's Schrödinger equation and classical optics's wave equation.

| | QM - Schrödinger Eqn. | Optics - Wave Eqn. |
|---|---|---|
| Field function | $\psi(r,t) = \psi(r)e^{iEt/\hbar}$ | $\boldsymbol{\mathcal{E}}(\boldsymbol{r},t) = \boldsymbol{A}(x,y,z)e^{i(\omega t - \beta z)}$ |
| $\hat{H}$ | $\frac{-\hbar^2}{2m}\nabla^2 + \widehat{V}(\boldsymbol{r},t)$ | $\nabla^2 - \frac{\omega^2}{c^2}\epsilon(x,y,z)$ |

Assume that the system is homogeneous in $y$-direction and light is propagating in a 1D slab waveguide. The paraxial approximation assumes that the variation of the electric field amplitude $\boldsymbol{A}(x,z)$ in $z$ is small compared to transverse variations and an optical wavelength [90]; i.e., $\left|\frac{\partial^2 \boldsymbol{A}}{\partial z^2}\right| \ll \left|2\beta\frac{\partial \boldsymbol{A}}{\partial z}\right|, \left|\frac{\partial^2 \boldsymbol{A}}{\partial x^2}\right|$. Thus, the propagation of an optical beam in a system of refractive index distribution $n(x,z) = n'(x,z) + in''(x,z)$ and $\epsilon = n^2$ follows the paraxial equation of diffraction [44, 46]:

$$i\frac{\partial \boldsymbol{A}}{\partial z} = \frac{1}{2\beta}\frac{\partial^2 \boldsymbol{A}}{\partial x^2} + K_0[n'(x,z) + in''(x,z)]\boldsymbol{A} \tag{2.9}$$

where $K_0 = 2\pi/\lambda$ and $\lambda$ is the wavelength of light in free space. Solving the Schrödinger Eqn., we get the energy eigenvalues of a quantum system, whereas the paraxial equation gives us the propagation constants, $\beta$, of an electromagnetic wave.

While energy eigenvalues have to be real in conventional QM, in optics, dissipative systems are characterized by complex propagation constants. Based on Eqn. 2.9, we can identify an effective optical Hamiltonian of the form $H_{op} = \frac{1}{2\beta}\frac{\partial^2 \boldsymbol{A}}{\partial x^2} + V_{op}(x,z)$. $V_{op}(x,z)$ is directly related to the refractive index distribution of the system, $n(x,z) = \Re\{n(x,z)\} + i\Im\{n(x,z)\} = n'(x,z) + in''(x,z)$.

For $\left[H_{op},\hat{P}\hat{T}\right] = 0$, it requires that $[V_{op}(x,z),\hat{P}\hat{T}] = 0$. By writing the optical potential as $V_{op}(x,z) = V'_{op}(x,z) + iV''_{op}(x,z)$, under $\hat{P}$ and $\hat{T}$ operation, we have, $\hat{P}\hat{T}V_{op}(x,z) = V'_{op}(-x,-z) - iV''_{op}(-x,-z)$. Thus, for $H_{op}$ to be parity-time symmetric, we require $V_{op}(x,z) = V^*_{op}(-x,-z)$, meaning a spatially symmetric $\Re\{n\}$ distribution and a spatially antisymmetric $\Im\{n\}$ profile. In optics, the imaginary part of a refractive index is associated with either gain or loss. An antisymmetric $\Im\{n\}$ profile is hence satisfied by alternatively arranging regions of gain and loss. It must be emphasized that $V_{op}(x,z) = V^*_{op}(-x,-z)$ is a necessary but not sufficient condition to have a real eigenvalue spectrum [44].

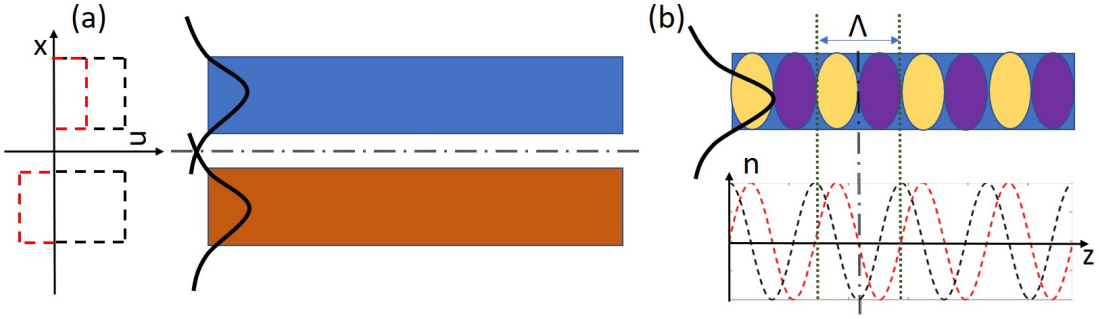



**Figure 2.1** – Schematics of optical PTS systems: (a) Coupled waveguides (b) Bragg grating with period Λ. The corresponding PTS index profile of each configuration is also indicated. The black dash lines represent modulation in $\Re\{n\}$ and the red dash lines show variation in $\Im\{n\}$. The black solid lines represent the propagating modes in each system. The black dash-dot lines indicate the axis of symmetry.

Figure 2.1 identifies two methods to define PTS index profiles. A PTS coupled waveguide system shown in Fig. 2.1(a) has its refractive index modulation along the $x$ axis, perpendicular to the propagation direction of light. On the other hand, the operation of a PTS Bragg grating depicted in Fig. 2.1(b) relies on a delicate index profile in the propagation direction, along the $z$ axis. It is clear from Fig. 2.1 that whether the index distribution is in the form of a step function (Fig. 2.1(a)) or a sinusoidal

function (Fig. 2.1(b)), the required symmetric and antisymmetric conditions of $\Re\{n\}$ and $\Im\{n\}$ are satisfied with respect to the symmetry axis of each system.

## 2.4 Coupled Mode Theory in optical PTS

Coupled mode theory (CMT)—a perturbative treatment of mode propagation relies on the fact that the spatial distribution of one mode is altered by the presence of the other [86,91,92]—provides a convenient mathematical platform on which our understanding of the abstract PTS applications in optics can be built. In the case of the coupled waveguides shown in Fig. 2.1(a), the two propagating modes are codirectional. The overlap of their evanescent tails leads to the mutual perturbation of their fields. On the other hand, in an optical grating system (Fig. 2.1(b)), the modes of interest are contradirectional. In the single mode regime, every time a forward propagating mode meets a change in the index profile along the grating, part of it gets reflected and it is this reflected wave that can potentially couple to the initial incident wave. The periodic arrangement of units in an optical grating results in the interference of multiple counter-propagating waves [93].

An overview of CMT in coupled optical systems and the calculation of its coefficients are detailed in Appendix B.1. In the next section, we focus on finding the form of the Hamiltonian, $\boldsymbol{H}$, that governs the evolution of the physical system of interest and on making use of CMT results to explain the peculiar effects of PTS on the transmission and reflection properties of coupled waveguides and Bragg gratings.

### 2.4.1 PTS in codirectional coupled waveguides

Considering the coupled system depicted in Fig. 2.1(a), the propagation of two codirectional first order TE modes denoted by the subscript $\mu = 1,2$ with field magnitude $\mathcal{E}_\mu(x,z) = \mathcal{E}_\mu(z)\mathcal{E}_\mu(x) = A_\mu(z)\mathcal{E}_\mu(x)e^{i\beta_\mu z}$ follows the partial differential equations:

$$\begin{aligned} \frac{dA_1(z)}{dz} &= i\kappa_{11}A_1 + i\kappa_{12}A_2 e^{i(\beta_2-\beta_1)z} \\ \frac{dA_2(z)}{dz} &= i\kappa_{22}A_2 + i\kappa_{21}A_1 e^{i(\beta_1-\beta_2)z} \end{aligned} \tag{2.10}$$

where $\kappa_{\nu\mu}$ are the coupling coefficients. Here, the propagation constants, $\beta_{1,2}$ can take complex values in order to accommodate the gain/loss requirement of optical PTS: $\beta_{1,2} = \beta'_{1,2} + i\beta''_{1,2} = (n'_{1,2} + in''_{1,2})\omega/c$ where $\beta'_{1,2}$, $\beta''_{1,2}$ are real numbers and $n'_{1,2} + in''_{1,2}$ are the effective refractive indices of the propagating modes. Note here that the full $z$ component of the electric field is $\mathcal{E}_\mu(z) = A_\mu(z)e^{i\beta_\mu z}$. Eqn. 2.10 can be recast into the matrix form of the Hamiltonian with $i\frac{\partial}{\partial z}\begin{bmatrix} A'_1(z) \\ A'_2(z) \end{bmatrix} = \boldsymbol{H}\begin{bmatrix} A'_1(z) \\ A'_2(z) \end{bmatrix}$ via the phasor $\beta_0 = \frac{(\beta_1+\kappa_{11}+\beta_2+\kappa_{22})}{2}$ where $\begin{bmatrix} \mathcal{E}_1(z) \\ \mathcal{E}_2(z) \end{bmatrix} = \begin{bmatrix} A_1(z)e^{i\beta_1 z} \\ A_2(z)e^{i\beta_2 z} \end{bmatrix} = e^{i\beta_0 z}\begin{bmatrix} A'_1(z) \\ A'_2(z) \end{bmatrix}$:[c]

$$\boldsymbol{H} = \begin{bmatrix} \delta_{mode} & \kappa_{eff} \\ \kappa_{eff} & -\delta_{mode} \end{bmatrix} \tag{2.11}$$

Here $\kappa_{eff} = \sqrt{\kappa_{12}\kappa_{21}}$ and $\delta_{mode} = (\beta_2 + \kappa_{22} - \beta_1 - \kappa_{11})/2$. $\delta_{mode}$ is often called the detuning factor, accounting for any modal index difference between the two waveguide modes. The transmission properties of the system are governed by the transfer matrix, $\boldsymbol{M(z)}$, according to:

$$\begin{bmatrix} \mathcal{E}_1(z) \\ \mathcal{E}_2(z) \end{bmatrix} = \boldsymbol{M(z)}\begin{bmatrix} \mathcal{E}_1(0) \\ \mathcal{E}_2(0) \end{bmatrix} \tag{2.12}$$

The elements of $\boldsymbol{M(z)}$ can be found using the standard method outlined in Appendix B.3 and take the form of:

$$\boldsymbol{M(z)} = \begin{bmatrix} cos(\sigma_0 z) - \frac{i\delta_{mode}}{\sigma_0}sin(\sigma_0 z) & \frac{\kappa_{eff}}{\sigma_0}sin(\sigma_0 z) \\ \frac{\kappa_{eff}}{\sigma_0}sin(\sigma_0 z) & cos(\sigma_0 z) + \frac{i\delta_{mode}}{\sigma_0}sin(\sigma_0 z) \end{bmatrix} e^{-i\beta_0 z} \tag{2.13}$$

where $\sigma_0 = \sqrt{\delta^2_{mode} + \kappa^2_{eff}}$. The eigenvalues of $\boldsymbol{H}$, $\sigma_\pm$ corresponding to the formation of two supermodes, is related to $\sigma_0$ via:

$$\sigma_\pm = \beta_0 \pm \sqrt{\delta^2_{mode} + \kappa^2_{eff}} = \beta_0 \pm \sigma_0 \tag{2.14}$$

[c]Details of this basis transformation is given in Appendix B.2.

The intensity evolution of the fields along the propagation direction is related to $\boldsymbol{M(z)}$ via $I(z)_{ij} = |M_{ij}(z)|^2$. We consider two situations where the initial excitation state is in either one of the waveguides, as depicted in Fig. 2.2. With these initial states, the output intensity of both channels at $z = z_L$ can be explicitly evaluated:

$$\begin{aligned} I_{11}(z_L) &= |cos(\sigma_0 z_L) - \frac{i\delta_{mode}}{\sigma_0} sin(\sigma_0 z_L)|^2 |e^{-i\beta_0 z_L}|^2 \\ I_{21}(z_L) = I_{12}(z_L) &= |\frac{\kappa_{eff}}{\sigma_0} sin(\sigma_0 z_L)|^2 |e^{-i\beta_0 z_L}|^2 \\ I_{22}(z_L) &= |cos(\sigma_0 z_L) + \frac{i\delta_{mode}}{\sigma_0} sin(\sigma_0 z_L)|^2 |e^{-i\beta_0 z_L}|^2 \end{aligned} \tag{2.15}$$

The formulation outlined above can be used to describe both Hermitian and PTS coupled systems.

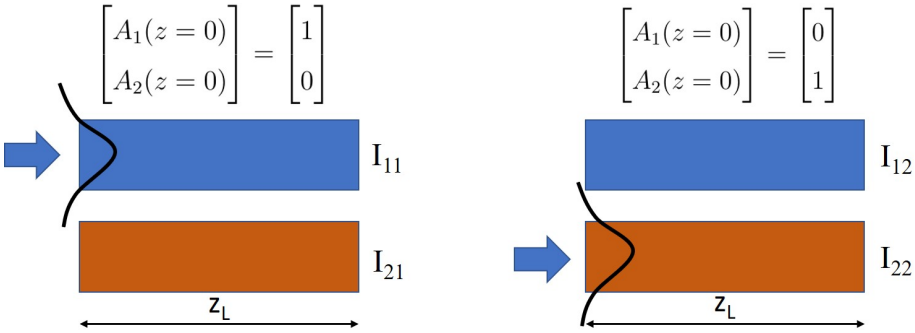



**Figure 2.2** – Different initial conditions correspond to different input channels. The label $I_{ij}$ indicates the respective magnitude of the field intensity at each output. The corresponding excitation states in matrix form are also shown.

One of the most peculiar consequences of optical PTS is to generate non-reciprocal propagation of light without breaking the Lorentz reciprocity [46, 94]. By considering the phase transition of a PTS eigenspectrum and its effects on the transmission properties, $I_{ij}(z)$, CMT can provide us with an intuitive yet rigorous explanation of the origin of this unusual propagation phenomenon.

### Hermitian coupled waveguide systems

For a Hermitian coupled system, the two coupled waveguides are identical without any gain and loss incorporated; this implies that $\beta_1' = \beta_2'$, $\beta_1'' = \beta_2'' = 0$; hence $\delta_{mode} = 0$. According to Eqn. 2.14, $\sigma_0 = \kappa_{eff}$. Since $\kappa_{12} = \kappa_{21}^*$ for a Hermitian system, $\kappa_{eff}$ is purely real (Appendix B.1).

Similar properties to Hermitian QM are found: $\boldsymbol{H}$ possesses a purely real eigenvalue spectrum and orthogonal eigenfunctions (symmetric and antisymmetric supermodes). Eqn. 2.15 gives $I_{11}(z) = I_{22}(z) = |cos(\sigma_0 z)|^2$ and $I_{12}(z) = I_{21}(z) = |sin(\sigma_0 z)|^2$. This means that when the input state is switched from the left to right waveguide, the output fields at the other ends of the waveguides are also switched to reflect this left-right symmetry. We call this behaviour reciprocal transmission. The field sloshes back and forth between the two waveguides with a period $L_c = \pi/2\kappa_{eff}$, equivalent to a complete crossover of fields from one waveguide to the other, $I_{ii}(L_c) = 0$ and $I_{ij}(L_c) = 1$. This lossless system conserves energy at all points along the propagation direction.

**Ideal PTS: perfectly balanced gain and loss in identical waveguides**

An ideal PTS coupled waveguide system requires $\beta_1' = \beta_2'$, $-\beta_1'' = \beta_2'' = \beta''$, i.e., waveguide 1 has gain while waveguide 2 contains loss and the gain/loss magnitudes are equal. Thus, $\Im\{\delta_{mode}\} = i\beta''$ and $\Re\{\delta_{mode}\} = 0$.[d] The eigenvalues become: $\sigma_0 = \pm\sqrt{(\kappa_{eff}^2 - \beta''^2)}$. Based on Eqn. 2.15, $I_{11} \neq I_{22}$ while $I_{12} = I_{21}$. The reality of $\sigma_0$ now depends on the difference between $\kappa_{eff}$ and $\beta''$ which defines the three regimes of PTS:

1. Exact PTS: $\beta''/\kappa_{eff} < 1$. The eigenvalue spectrum of $\boldsymbol{H}$ remains purely real with two supermode eigenfrequencies: $\Re(\beta_0 \pm \sigma_0)$. The corresponding eigenvectors, $\begin{bmatrix} 1 \\ \mp e^{\pm i\eta} \end{bmatrix}$ with eigenvalues $\pm\kappa_{eff} cos(\eta)$ where $sin(\eta) = \beta''/\kappa_{eff}$, are no longer orthogonal [46]. This skewed basis is key to the non-reciprocal propagation behaviour of this system. As the ratio $\beta''/\kappa_{eff}$ increases, the relative phase difference, $\upsilon$ defined in Table 2.1, falls in the range $0 \rightarrow \pi$ [46].

2. Phase transition – EP: $\beta''/\kappa_{eff} = 1$ and $\upsilon = \pi/2$. The two supermodes coalesce with the eigenfunction $\begin{bmatrix} 1 \\ i \end{bmatrix}$ and the system becomes degenerate.

3. Broken PTS: $\beta''/\kappa_{eff} > 1$, the eigenvalue spectrum becomes purely imagi-

[d] The effect of $\kappa_{11,22}$ is negligible (Appendix B.1).

nary, specified by $\mp i\kappa_{eff} sinh(\zeta)$ with eigenfunctions $\begin{bmatrix} 1 \\ -ie^{\pm\zeta} \end{bmatrix}$ where $cosh(\zeta) = \beta''/\kappa_{eff}$. Above the threshold $\beta''/\kappa_{eff} = 1$, the eigenvalues of the two supermodes are either exponentially decaying or exponentially increasing. Consequently, only one supermode survives.

The behaviour of the eigenvalue spectrum of a perfect PTS coupled optical system is illustrated in Fig. 2.3. The vertical difference between $\sigma_0$ and $\sigma_\pm$ spectra comes from a constant value of $\Re\{\beta_0\}$. Since $\Im\{\beta_0\} = 0$, the spectra of $\Im\{\sigma_0\}$ and $\Im\{\sigma\}$ are identical.

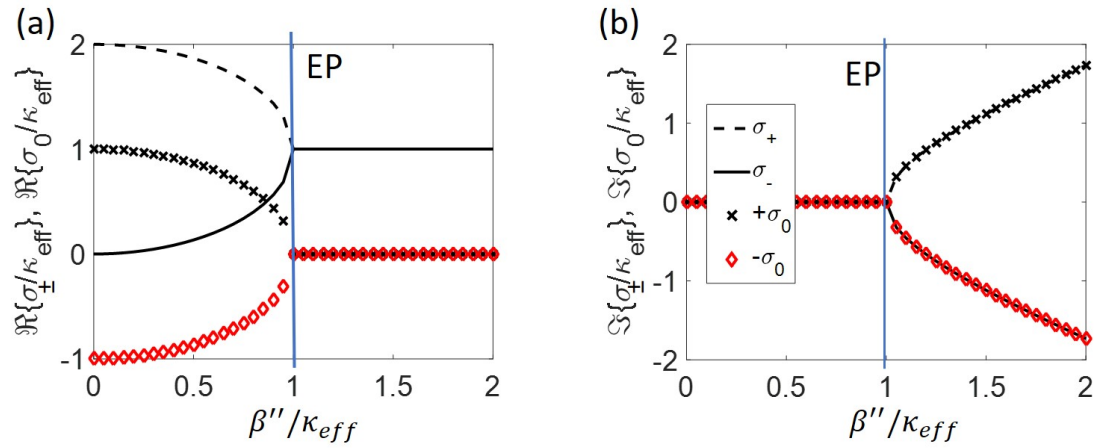



**Figure 2.3** – Eigenspectra of an ideal PTS coupled waveguide system where gain and loss are controlled dynamically to maintain equal magnitudes; i.e., scanning value of $\beta''$ while $\kappa_{eff}$ is constant. (a) The real part of the eigenvalues (b) The imaginary part of the eigenvalues as a function of $\beta''/\kappa_{eff}$.

### Evaluation of non-reciprocal propagation of light

Now we are fully equipped to understand the non-reciprocal propagation of light in this PTS coupled system. We can monitor the output fields at the ends of the waveguides as a function of $\beta''$ for a fixed waveguide length $z_L = 2L_c$, $I_{ij}(z_L)$, using Eqn. 2.15 for the two excitation states of interest. This result is plotted in Fig. 2.4, demonstrating the non-reciprocal behaviour with respect to the left and right symmetry of the PTS system. Beyond the EP, regardless of the input channels, most of the field comes out at the end of the gain channel (channel 1).

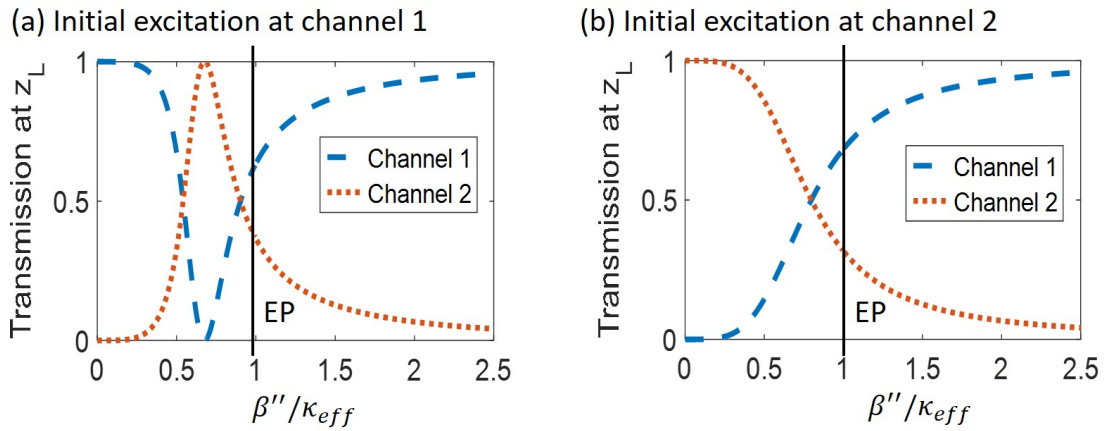



**Figure 2.4** – Normalized output fields at $z_L$ of channel 1 (gain channel - blue dash) and channel 2 (loss channel - orange dot) as a function of $\beta''$ for two excitation state described in Fig. 2.2 (a) Excitation at channel 1: $I_{11,21}(z_L)/(I_{11}(z_L)+I_{21}(z_L))$ (b) Excitation at channel 2: $\mathrm{I}_{12,22}(z_L)/(I_{12}(z_L)+I_{22}(z_L))$.

Furthermore, the normalized field magnitudes along the propagation direction are plotted in Fig. 2.5 for fixed values of $\beta''$. Recall the Hermitian behaviour discussed earlier, if the input channel is swapped, we observe the corresponding swapping of the output fields, as illustrated in Fig. 2.5(a). This swapping behaviour is not observed in an equivalent PTS coupled system. When $\beta'' < \kappa_{eff}$ (see Fig. 2.5(b)), though the field sloshes back and forth between the 2 coupled waveguides, the field amplitude is not exchanged in accordance with the swapping of the excitation channel. The Hermitian reciprocal behaviour with respect to the left and right symmetry ceases to exist. Interestingly, in the broken PTS phase when $\beta'' > \kappa_{eff}$, the field always prefers to propagate in the gain channel (channel 1) regardless of the initial excitation states, as seen in Fig. 2.5(c). This non-reciprocal propagation can also be thought of as the decoupling of two original single waveguide modes in broken PTS regime.

### PTS in fixed gain/loss coupled systems

Coupled optical systems where gain and loss cannot be controlled simultaneously can still exhibit PTS breaking [36,55,68,95,96]. We consider the case where the loss in one waveguide is fixed and the gain in the other waveguide can be dynamically controlled for instance via optical pumping. Here, we assume that $\beta_1' = \beta_2'$, $\beta_2'' = \beta_0''$ is fixed while $\beta_1'' = -\beta''$ can be dynamically varied.

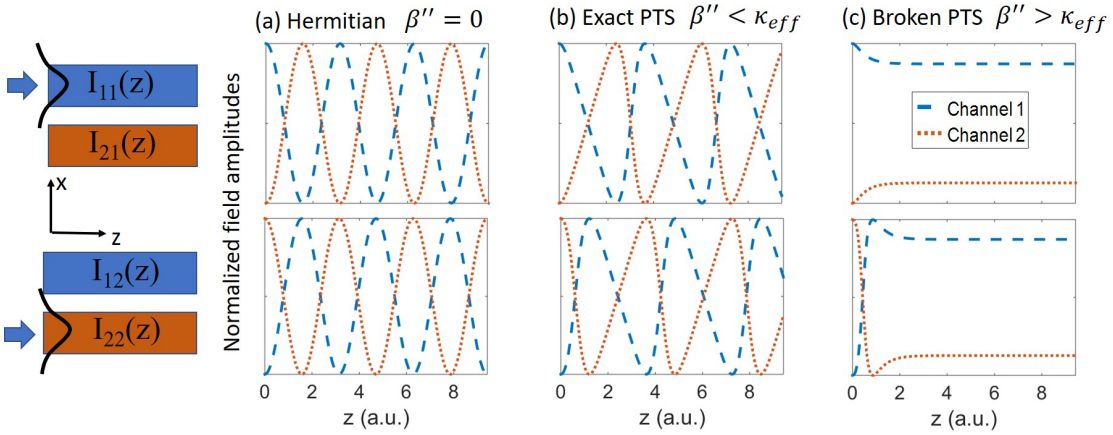



**Figure 2.5** – Normalized field amplitudes along the propagation direction of two excitation states of interest: upper panel – input in channel 1 with field amplitudes $I_{11,21}(z)/(I_{11}(z)+I_{21}(z))$ and lower panel – input in channel 2 with field amplitudes $I_{12,22}(z)/(I_{12}(z)+I_{22}(z))$ for the three values of fixed $\beta''$ corresponding to (a) Hermitian coupled waveguides – lossless waveguides with $\beta''=0$ (b) Exact PTS – $\beta''/\kappa_{eff}<1$ and (c) Broken PTS – $\beta''/\kappa_{eff}>1$.

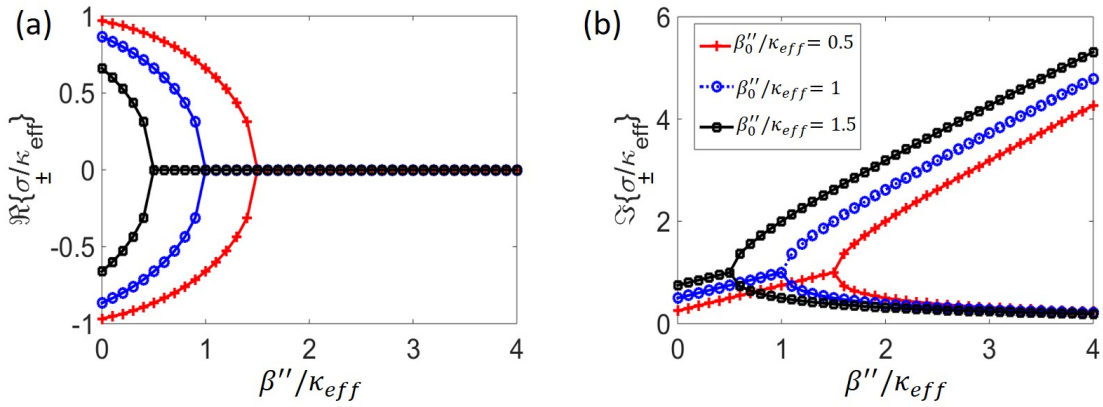



**Figure 2.6** – Real and imaginary parts of eigenvalues of the supermodes for the case of various fixed losses as a function of gain.

The eigenvalues of $\boldsymbol{H}$ become: $\sigma_0 = \pm\sqrt{\kappa_{eff}^2 - (\frac{\beta_1''+\beta_0''}{2})^2}$. In the ideal PTS case, $\beta_0$ is purely real and is not affected by the ratio $\beta''/\kappa_{eff}$; hence, there is no difference in the shape of the spectra of $\Im\{\sigma_\pm\}$ and $\Im\{\sigma_0\}$ (as seen in Fig. 2.3). However, in the case of PTS with fixed loss, $\beta_0$ becomes complex. While $\Re\{\beta_0\}$ remains constant, $\Im\{\beta_0\} = \beta_1'' - \beta_0''$ varies with $\beta_1''$ due to the presence of fixed losses. This is the cause of the tilting of basis in the $\Im\{\sigma_\pm\}$ spectrum in Fig. 2.6(b). The degree of tilting depends on the relative difference between the coupling coefficient and the fixed loss magnitude. Although, the phase transition point is still preserved, its position is shifted according

to $\beta_0''/\kappa_{eff}$.[e] The establishment of an EP allows interesting phenomena such as non-reciprocal propagation to survive the influence of a deviation from an ideal PTS system. In arriving at these results, the coupling coefficients were implicitly assumed to remain real even when an imbalance in loss and gain was present. However, based on the CMT formulation of mutual coupling coefficients outlined in Eqn. B.3, Appendix B.1, this assumption is not strictly true: the effective coupling constant, $\kappa_{eff}$, turns complex when gain is not equal to loss. The consequences of complex coupling in non-ideal PTS systems with unequal gain/loss, non-zero modal mismatch and detrimental dispersion effects will be further explored in Chapter 6.

### 2.4.2 PTS in contradirectional waveguides — Bragg gratings

#### General CMT in the context of Bragg gratings

For counter-propagating modes—the incident and reflected waves propagating in a grating (Fig. 2.1(b))—the coupled mode equations take the form of:

$$\begin{aligned} \frac{dA_1(z)}{dz} &= i\kappa_{11}(z)A_1 + i\kappa_{12}(z)A_2 e^{i(\beta_2-\beta_1)z} \\ -\frac{dA_2(z)}{dz} &= i\kappa_{22}(z)A_2 + i\kappa_{21}(z)A_1 e^{i(\beta_1-\beta_2)z} \end{aligned} \tag{2.16}$$

Here $\beta_1 = -\beta_2 = \beta$. As the spatial modulation of the permittivity is periodic in the propagation direction, the dependence of the coupling coefficients $\kappa_{\mu\mu}(z)$ and $\kappa_{\mu\nu}(z)$ on the permittivity variation means that they are also periodic in $z$ with a grating period $\Lambda$. This periodicity allows an analysis of the coupling coefficients based on Fourier theory to be carried out. The Fourier analysis and CMT dictate that [86, 93]:

$$\begin{aligned} \kappa_{\mu\mu}(z) &= \omega \int \mathcal{E}_\mu^*(x)\Delta\epsilon(x,z)\mathcal{E}_\mu(x)dx = \sum_{\xi=\pm}^{\infty} \kappa_{\mu\mu}(\xi)e^{\frac{-i2\pi\xi z}{\Lambda}} \\ \kappa_{\mu\nu}(z) &= \omega \int \mathcal{E}_\mu^*(x)\Delta\epsilon(x,z)\mathcal{E}_\nu(x)dx = \sum_{\xi=\pm}^{\infty} \kappa_{\mu\nu}(\xi)e^{\frac{-i2\pi\xi z}{\Lambda}} \end{aligned} \tag{2.17}$$

[e]Note that this tilting does not occur in the spectrum of $\Im\{\sigma_0\}$ while the shifting of EP is still observed.

where the summation is over all positive and negative integers, $\xi$, and the values of the Fourier coefficients are computed as:

$$\begin{aligned}\kappa_{\mu\mu}(\xi) &= \frac{1}{\Lambda}\int_0^{\Lambda} \kappa_{\mu\mu}(z) e^{\frac{i2\pi\xi z}{\Lambda}} dz \\ \kappa_{\mu\nu}(\xi) &= \frac{1}{\Lambda}\int_0^{\Lambda} \kappa_{\mu\nu}(z) e^{\frac{i2\pi\xi z}{\Lambda}} dz\end{aligned} \tag{2.18}$$

Due to the spatial harmonics of the system, the coupling between the backward and forward propagating modes of a grating only occurs at the Bragg condition: $\Lambda = \frac{\pi\xi}{\beta}$. In other words, the spatial index discontinuity allows the energy of the forward propagating mode to be transferred to the backward one, leading to the decay of waves in the forward direction, equivalent to the formation of complex propagation constants within the stop band of the grating [97]. Therefore, only the Fourier terms that satisfy the Bragg condition $\beta_\nu - \beta_\mu - \frac{2\pi\xi}{\Lambda} = 0$ survive; thus, $\sum_{\xi=\pm}^{\infty} \kappa_{\mu\nu}(\xi) e^{i\left(\beta_\nu - \beta_\mu - \frac{2\pi\xi}{\Lambda}\right)z}$ $\longrightarrow \kappa_{\mu\nu}(\xi = \frac{(\beta_\nu - \beta_\mu)\Lambda}{2\pi})$. A detailed calculation of the coupling coefficients in the context of standard Bragg gratings following CMT and Fourier analysis [86, 93] is given in Appendix B.4. For a Bragg grating, the coefficients, $\kappa(\xi)$, can be simplified as:

$$\begin{aligned}\kappa_{\mu\mu}(\xi = 0) &= \frac{1}{\Lambda}\int_0^{\Lambda} \Delta\epsilon(z) e^{\frac{i2\pi\xi z}{\Lambda}} dz \times \omega \int \mathcal{E}_\mu^*(x)\Delta\epsilon(x)\mathcal{E}_\mu(x)dx &&= C_0\alpha_0 \\ \kappa_{\mu\nu}(\xi = \frac{\beta\Lambda}{\pi}) &= \frac{1}{\Lambda}\int_0^{\Lambda} \Delta\epsilon(z) e^{\frac{i2\pi\xi z}{\Lambda}} dz \times \omega \int \mathcal{E}_\mu^*(x)\Delta\epsilon(x)\mathcal{E}_\nu(x)dx &&= C_\xi\kappa_0\end{aligned} \tag{2.19}$$

where $C_\xi = \frac{1}{\Lambda}\int_0^{\Lambda} \Delta\epsilon(z) e^{\frac{i2\pi\xi z}{\Lambda}} dz$, $\xi = 0$ for $C_0$, $\kappa_0 = \int \mathcal{E}_\mu^*(x)\Delta\epsilon(x)\mathcal{E}_\nu(x)dx$ and $\alpha_0 = \int \mathcal{E}_\mu^*(x)\Delta\epsilon(x)\mathcal{E}_\mu(x)dx$ [36]. While $\Delta\epsilon(x)$ determines the transverse modal field pattern of the system, the periodic variations of both real and imaginary parts of the index profile along the propagation direction are factored into $\Delta\epsilon(z)$ where $\Delta\epsilon(z) = \epsilon(z) - \epsilon_{WG} = n(z)^2 - n_{WG}^2$. Here we assume that the slab waveguide without any index/loss modulation on top is lossless, hence, $n''_{WG} = 0$. Thus, $n(z) = n'_{WG} + \Delta n'(z) + i\Delta n''(z)$. Assuming $\Delta n'(z)$ and $\Delta n''(z) \ll n'_{WG}$, we arrive at $\Delta\epsilon(z) \approx 2n_{WG}(\Delta n'(z) + i\Delta n''(z)) = 2n_{WG}\Delta n(z)$.

The coupling mechanism of contradirectional modes at the Bragg frequency can be represented by an effective Hamiltonian:

$$\boldsymbol{H} = \begin{bmatrix} iC_0\alpha_0 & iC_\xi\kappa_0 \\ -iC_{-\xi}\kappa_0 & -iC_0\alpha_0 \end{bmatrix} = \begin{bmatrix} ia & ib_1 \\ -ib_2 & -ia \end{bmatrix} \tag{2.20}$$

Considering two initial excitation states in Fig. 2.7, the black arrows, $I_f$ and $I_b$, denote the incident beams and the red arrows, $R_f$ and $R_b$, represent the reflected beams. The calculation of $R_f$ and $R_b$ requires a similar analysis of the transfer matrix $\boldsymbol{M(z)}$ to that of codirectional modes where $\boldsymbol{M(z)}$ and $\boldsymbol{H}$ are linked by Eqn. 2.11, 2.12:[f]

$$\boldsymbol{M(z)} = \begin{bmatrix} \cosh(\phi z) + \frac{a}{\sigma}\sinh(\phi z) & \frac{ib_1}{\sigma}\sinh(\phi z) \\ \frac{ib_2}{\sigma}\sinh(\phi z) & cosh(\phi z) - \frac{a}{\sigma}\sinh(\phi z) \end{bmatrix} \tag{2.21}$$

where $\phi = \pm\sqrt{a^2 - b_1 b_2}$ and $\sigma = i\phi$, the eigenvalues of $\boldsymbol{H}$. $R_f$ and $R_b$ are related to $\boldsymbol{M(z)}$ via:

$$R_f = \left|\frac{M_{21}}{M_{22}}\right|^2 \quad \text{and} \quad R_b = \left|\frac{M_{12}}{M_{22}}\right|^2 \tag{2.22}$$

Explicit forms of $R_{b,f}$ rely on the index distribution of the gratings of interest, $\Delta n(z)$.

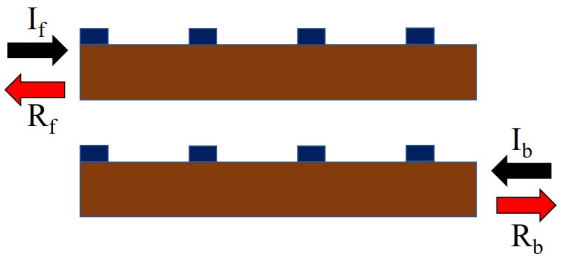



**Figure 2.7** – Hypothetical 1D system with periodic arrangement of identical blocks on top of a slab waveguide. The directions of forward and backward reflections are also defined here.

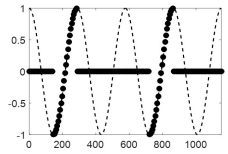
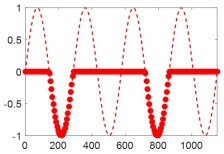
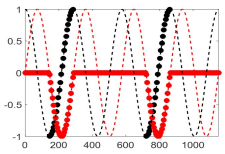
### Evaluation of unidirectional reflection in PTS gratings

The difference in the magnitudes of $R_f$ and $R_b$ in PTS Bragg grating systems gives rise to the unidirectional reflection phenomenon [36]. In practice, a Bragg grating can

[f] Details calculation is given in Appendix B.4.

have either a periodic index modulation or a periodic structural corrugation [86]. In the context of PTS, the first design is relevant. Here we consider a hypothetical 1D system where the modulation of indices is performed by periodically arranged identical blocks on top of a slab waveguide.

**Table 2.3** – Different types of periodic distribution of indices on top of a waveguide.

| Properties | Conventional Bragg grating | Periodic loss only (L) | PTS grating (PT) |
|---|---|---|---|
| Index profile | $\Delta n' \cos(\xi 2\pi z/\Lambda)$ | $i\Delta n'' \sin(\xi 2\pi z/\Lambda)$ | $\Delta n' \cos(\xi 2\pi z/\Lambda) + i\Delta n'' \sin(\xi 2\pi z/\Lambda)$ |
| Visual |  |  |  |
| $\boldsymbol{H}$ | $\begin{bmatrix} 0 & i\frac{\Delta n'}{8}\kappa_0 \\ -i\frac{\Delta n'}{8}\kappa_0 & 0 \end{bmatrix}$ | $\begin{bmatrix} -\frac{\Delta n''}{2\pi}\alpha_0 & -i\frac{\Delta n''}{8}\kappa_0 \\ -i\frac{\Delta n''}{8}\kappa_0 & \frac{\Delta n''}{2\pi}\alpha_0 \end{bmatrix}$ | $\begin{bmatrix} \frac{-\Delta n''}{2\pi}\alpha_0 & i\frac{\Delta n'-\Delta n''}{8}\kappa_0 \\ -i\frac{\Delta n''+\Delta n'}{8}\kappa_0 & \frac{\Delta n''}{2\pi}\alpha_0 \end{bmatrix}$ |

To compare a PTS grating with a conventional Bragg grating, we assume that this hypothetical system is able to support any of the three index distributions shown in Table 2.3. An index period corresponding to the first Bragg order is often very small, making it difficult for practical implementation. Here, we choose the second Bragg order with $\Lambda = \frac{4\pi}{q}$ where $q = 2|\beta|$, the grating vector. For the calculation of $\kappa_{\mu\nu}$, $\xi = 2$ and the index distribution is defined within the range of $\frac{4l\pi}{q} + \frac{\pi}{q} < z < \frac{4l\pi}{q} + \frac{2\pi}{q}$, where $l \in Z$. The visualization of these index distributions shows both the theoretical function of $\cos(qz)$ and $\sin(qz)$ (dash lines) and the actual spatial index distribution (filled circles: black denotes $\Re\{n(z)\}$ and red denotes $\Im\{n(z)\}$ distribution).

A PTS grating configuration requires the combination of an even spatial distribution of $\Re\{n(z)\}$ (cosine profile) and an odd spatial distribution of $\Im\{n(z)\}$ (sine profile). The distinction between PTS and conventional Bragg gratings is already reflected in the form of $\boldsymbol{H}$. However, it is more useful to look at the explicit expression of $\boldsymbol{M(z)}$ for each of the index distributions above which directly relate to the reflection

spectrum of the grating:

$$\boldsymbol{M_{Bragg}(z)} = \begin{bmatrix} \cosh(\frac{\Delta n'\kappa_0}{8}z) & \sinh(\frac{\Delta n'\kappa_0}{8}z) \\ \sinh(\frac{\Delta n'\kappa_0}{8}z) & \cosh(\frac{\Delta n'\kappa_0}{8}z) \end{bmatrix}$$

$$\boldsymbol{M_L(z)} = \begin{bmatrix} \cosh(\phi_L z) + \frac{\alpha_0\Delta n''}{2\pi\phi_L}\sinh(\phi_L z) & \frac{8\phi_L\kappa_0\pi^2}{\Delta n''}\sinh(\phi_L z) \\ -\frac{8\phi_L\kappa_0\pi^2}{\Delta n''}\sinh(\phi_L z) & \cosh(\phi_L z) - \frac{\alpha_0\Delta n''}{2\pi\phi_L}\sinh(\phi_L z) \end{bmatrix}$$

$$\boldsymbol{M_{PT}(z)} = \begin{bmatrix} \cosh(\phi_{PT} z) + \frac{i\Delta n''\alpha_0}{2\pi\phi_{PT}}\sinh(\phi_{PT} z) & \frac{i(\Delta n'-\Delta n'')\kappa_0}{8\phi_{PT}}\sinh(\phi_{PT} z) \\ \frac{i(\Delta n'+\Delta n'')\kappa_0}{8\phi_{PT}}\sinh(\phi_{PT} z) & \cosh(\phi_{PT} z) - \frac{i\Delta n''\alpha_0}{2\pi\phi_{PT}}\sinh(\phi_{PT} z) \end{bmatrix} \tag{2.23}$$

where $\phi_L = \frac{\Delta n''}{8\pi}\sqrt{\kappa_0^2\pi^2 + 16\alpha_0^2}$ and $\phi_{PT} = \sqrt{\frac{\Delta n''^2 - \Delta n'^2}{64}\kappa_0 - (\frac{\Delta n''\alpha_0}{2\pi})^2}$. For a conventional Bragg grating, there is no distinction between $R_f$ and $R_b$ since $|M_{Bragg,12}| = |M_{Bragg,21}|$ and $|M_{Bragg,11}| = |M_{Bragg,22}|$. Similar behaviour is observed for the case of a periodic loss configuration, the system on average acts as a lossy waveguide as no index modulation is present to facilitate the generation of a backward propagating mode. Thus, whether the field is incident from the left or the right of the grating, we achieve the same transmission/absorption results. However, the picture drastically changes when both of the above periodic modulations are combined to form a PTS grating. $R_f$ and $R_b$ now have distinct functional forms. This is because $|M_{PT,12}|$ is no longer identical to $|M_{PT,21}|$. The reflection coefficients strongly depend on the relative magnitudes of $\Delta n'$ and $\Delta n''$. In particular, when $|\Delta n''| = |\Delta n'|$, either $R_b$ or $R_f$ becomes zero while the other one obtains non-zero value, achieving the optimal contrast between $R_b$ and $R_f$.

### Refractive index modulation of practical PTS gratings

Constructing the PTS index distribution depicted in Table 2.3 requires a mechanism which allows both the distribution of $\Re\{n(z)\}$ and $\Im\{n(z)\}$ to be controlled simultaneously as desired; this in practice is extremely difficult as $\Re\{n(z)\}$ and $\Im\{n(z)\}$ are always intrinsically interlinked by the Kramers-Kronig relations. It is important to realize that the even and odd symmetries of the cosine and sine distributions are the crucial requirement of optical PTS. Thus, translational shifts of these functions are allowed as long as these symmetries of the refractive index distribution are retained.

By performing an in-phase shift of $\Re\{n(z)\}$, we can spatially separate the real and imaginary components of the refractive index distribution of interest [36]. Figure 2.8 describes how such an in-phase shift can be visualized. The in-phase shifted Hamiltonian has the form:

$$\boldsymbol{H}_{shifted} = \begin{bmatrix} \frac{-\Delta n'' - i\Delta n'}{2\pi}\alpha_0 & i\frac{\Delta n' - \Delta n''}{8}\kappa_0 \\ -i\frac{\Delta n'' + \Delta n'}{8}\kappa_0 & \frac{\Delta n'' - i\Delta n'}{2\pi}\alpha_0 \end{bmatrix}.$$

The off-diagonal terms of $\boldsymbol{H}_{shifted}$, which are responsible for the unidirectional reflection property of a PTS grating, are identical to those of the original $\boldsymbol{H}_{PT}$ in Table 2.3. The only difference lies in the expression of $C_0$, which only causes a shift in the spectral response of the grating but does not have any effects on the unidirectionality property [36].

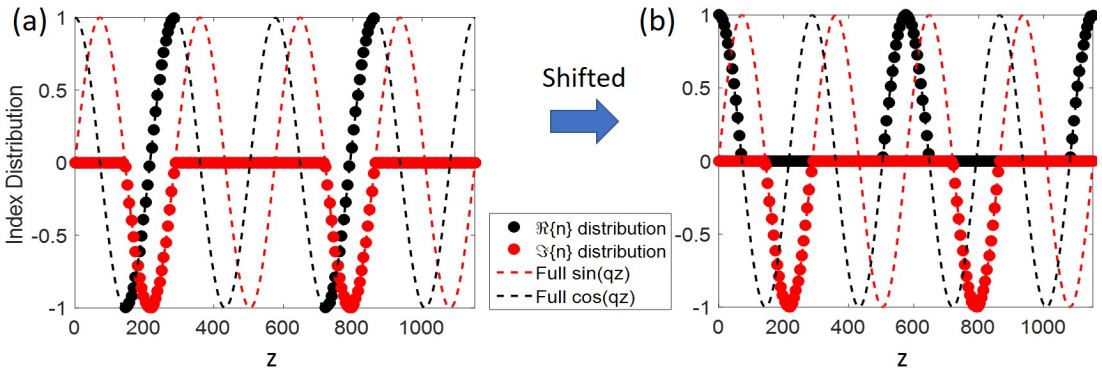



**Figure 2.8** – (a) The original index distribution of a simple PTS grating. (b) In-phase shifting of the index distribution.

We can extend our model to include the broadband response of this passive PTS system, which requires small modifications of $\boldsymbol{H}$ and $\boldsymbol{M(z)}$ to accommodate the phase mismatch, $\Delta K = \beta_{Bragg} - K$. The derivation of a broadband PTS grating is essentially identical to the analysis outlined in this section; the readers are referred to [36] for further details. We proceed to numerically simulate the three systems of interest: a conventional lossless Bragg grating, a waveguide with a periodic loss and a PTS grating with an appropriate laterally shifted index distribution. All three systems were modeled based on 1D slab Si waveguides with periodic lossless (Si) and lossy (Ge/Cr) bars on top. Details of this simulation can be found in Appendix C.

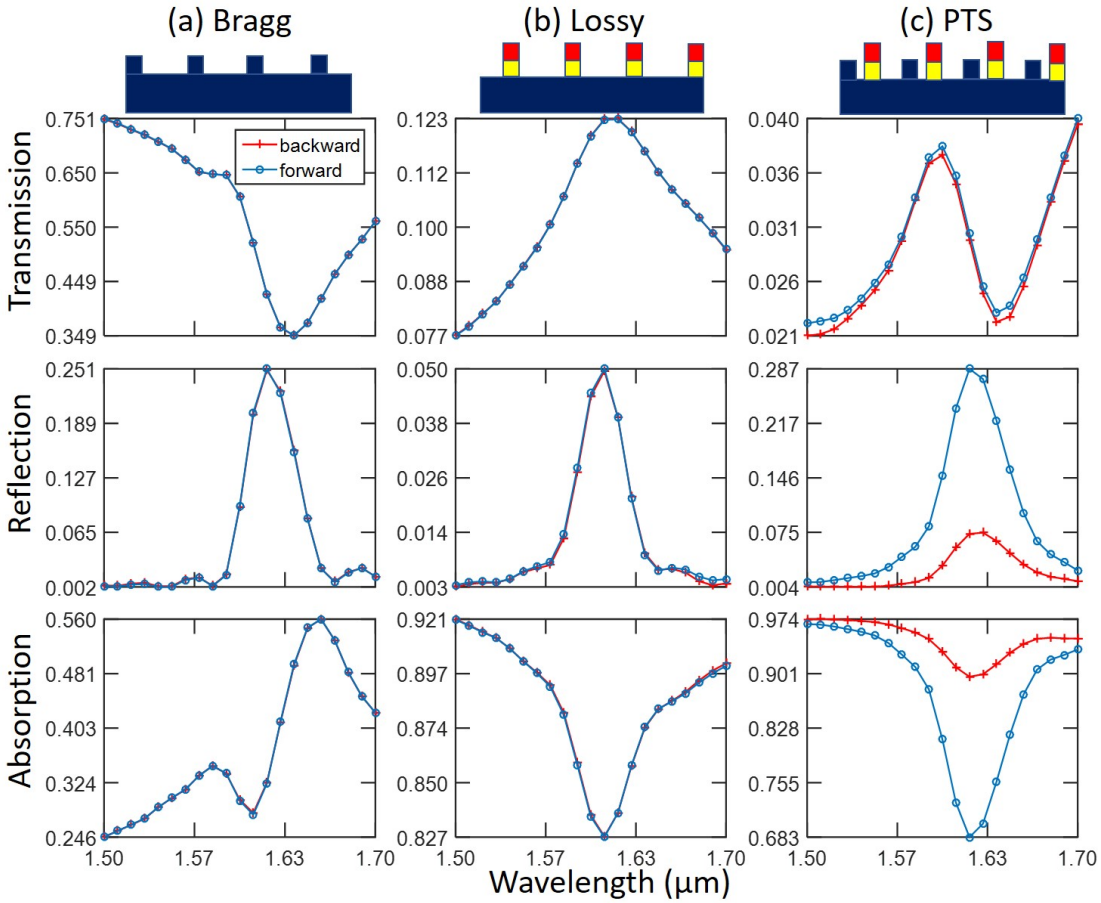



**Figure 2.9** – Numerical simulation results of the transmission, reflection and absorption of (a) conventional Bragg grating (b) Periodic loss only and (c) PTS grating under broadband excitation. Backward and forward refer to the input propagation directions shown in Fig. 2.7. The top panel of the figure depicts the corresponding structural configuration of each index modulation. Incident waves were input left to right (forward propagating) and right to left (backward propagting) in the simulation.

The results of our 2D FDTD broadband simulations for both excitation directions defined in Fig. 2.7 are presented in Fig. 2.9. Clearly, the excitation direction does not play a role in manipulating the transmission, reflection and absorption spectra of the conventional Bragg grating or the periodic loss waveguide: the forward and backward spectra overlap precisely with each other in Fig. 2.9(a) and (b). When these two index distributions are combined to form a PTS grating, the symmetry between backward and forward reflection of light is broken. The dimensions of the system

were chosen such that it operated in the vicinity of the EP where the unidirectional reflection effect is most prominent ($|\Delta n''| = |\Delta n'|$). As seen in Fig. 2.9(c), while the peak value of $R_f$ reaches 0.3, $R_b$ is greatly suppressed with a maximum value of just 0.07.

Without the addition of lossy materials, the field distribution along the propagation direction of a Bragg grating is reversed when the excitation direction is swapped from forward to backward directions, leading to the symmetrical behaviour of $R_f$ and $R_b$ (Fig. 2.9(a)). When loss is added, the fixed locations of lossy bars mean that the total amount of absorption in the system depends on how the energy profile of the propagating waves spatially overlap with this distribution of loss. The antisymmetric nature of the $\Im\{n(z)\}$ distribution breaks the symmetry of the absorption following backward and forward excitations. Consequently, when the input field is incident in the forward direction, it experiences much less loss than when the incident direction is reversed (Fig. 2.9(c)).

## 2.5 Summary

This chapter reviewed the fundamental concepts of PTS in the context of QM and classical coupled mode optics. The conventional requirement of an observable being Hermitian is replaced by the weaker condition of PTS whose symmetry can be broken at the exceptional point. This broken symmetry, signified by a phase transition, is the physical mechanism behind many counter-intuitive PTS optical phenonmena that can potentially be used to construct practical optical devices. The mathematical platform of CMT provided a rigorous yet intuitive explanation for the origin of two useful PTS phenomena: non-reciprocal propagation of light with respect to left-right symmetry in coupled waveguide systems and broadband unidirectional reflection in PTS Bragg gratings.

Optical PTS is realized by introducing a symmetric spatial distribution of $\Re\{n\}$ and an antisymmetric distribution of $\Im\{n\}$. In the case of coupled codirectional waveguides with balanced gain and loss, the decoupling of the two single waveguide modes

occurred when the gain/loss magnitude surpassed the coupling strength, resulting in dominant transmission of light in the gain waveguide regardless of the input channels. Non-reciprocity took a different form in PTS Bragg gratings. CMT dictated that the coupling of forward and backward propagating modes in a conventional Bragg grating resulted in the decay of the incident waves and the growth of reflected waves, irrespective of the propagation direction of the input mode. However, the inclusion of an antisymmetric sinusoidal distribution of lossy materials into a conventional Bragg grating created a passive PTS grating which allowed the reflection of light from such a system to be suppressed only in one direction. This unidirectional reflection property of PTS grating came from a selective spatial overlap between lossy regions and the field distribution of the propagating mode, leading to a high level of absorption of light only when the incident wave traveled in a particular direction.

Although the unusual consequences of optical PTS could be explained in the context of CMT, two implicit assumptions were made in arriving at these results. Firstly, the coupling coefficients were assumed to remain real even when loss and gain were present. Secondly, dispersion effects were ignored, meaning only systems of low gain/loss may be considered. In practice, simultaneously controlling both gain/loss and dispersion is extremely challenging. To extend PTS applications to more practical platforms where strong dispersion and high gain/loss exist, an understanding of the complex coupling mechanism and an approach to circumvent detrimental dispersion effects need to be developed. These topics will be the focus of Chapter 6.

# Chapter 3

# Technology: from photonic to plasmonic waveguides

This chapter lays out the foundation of the technological platforms on which our investigation of gain and loss and their interplay is conducted. All devices studied in this thesis, hybrid gap plasmon lasers, parity-time symmetry coupled waveguides and Bragg gratings, are built upon optical guiding structures. Thus, we begin the chapter with an analysis of the modal properties of transverse electric (TE) modes of a conventional lossless dielectric waveguide, which includes the calculation of the effective index of the propagating TE mode and the explicit form of its field distribution. This study is extended to include an overview of the calculation of modal properties in lossy photonic waveguides. The discussion of losses in guiding structures brings us to the final topic of this chapter which focuses on a particular type of plasmonic waveguide: the hybrid gap plasmon waveguide (HGPW). After reviewing the prominent properties of popular plasmonic waveguides in the literature, the detailed physics of HGPW is given where both fundamental and practical aspects are considered.

## 3.1 Optical Waveguides

### 3.1.1 Guiding light in lossless waveguides

In a waveguide, propagating waves must travel in only one direction with a well-defined field distribution in the other two directions. The traveling wave can take the form $\boldsymbol{\mathcal{E}(x,y,z)} = \boldsymbol{u}(x,y)e^{i(\omega t-\beta z)}$, where $\boldsymbol{u}(x,y)$ describes the electric field distribution in the structure and $\beta$ signifies the propagation constant of the guided wave [86, 97]. In its simplest form, a 1D optical waveguide is composed of three lossless dielectric layers (Fig. 3.1).

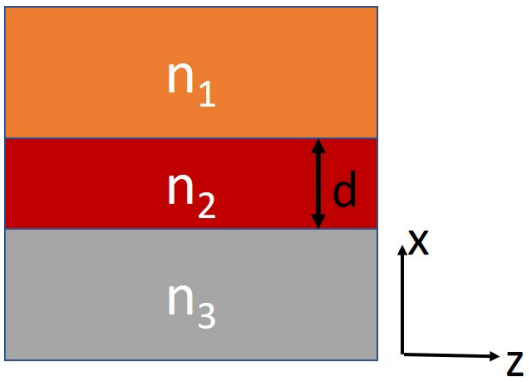



**Figure 3.1** – Material composition of a typical dielectric slab waveguide with the corresponding refractive indices of each layer.

As there is no loss or gain in the system, the field amplitude does not vary along $z$ and energy is conserved in the system. Assuming that the structure is homogeneous in the $y$-direction, we have $\frac{\partial \boldsymbol{\mathcal{E}}}{\partial y} = 0$. For an input wavelength, $\lambda = \frac{2\pi}{K_0}$, the wave equation is hence simplified:

$$\frac{\partial^2 \boldsymbol{u}(x)}{\partial x^2} = (K_0^2 n_i^2 - \beta^2)\boldsymbol{u}(x) \tag{3.1}$$

where the subscript $i$ denotes the different layers of the dielectric waveguide. This partial differential equation has solutions corresponding to transverse electric (TE) modes with $\mathcal{E}_x = \mathcal{E}_z = \mathcal{H}_y = 0$. The wave equation also gives rise to a set of transverse magnetic (TM) solutions with $\mathcal{H}_x = \mathcal{H}_z = \mathcal{E}_y = 0$. Pure TE and TM modes only exist in 1D waveguides; in 2D waveguides, in general, optical modes contain both TE and TM components, forming hybrid modes whose components $\mathcal{E}_z$ and $\mathcal{H}_z$ are

both non-zero [86]. In this analysis, we focus on the derivation of an analytic solution of TE modes as most structures subsequently investigated in this thesis have their fundamental modes being predominantly TE. For a pure TE mode, the solution of the wave equation yields a particular form of the $y$-component of the field amplitude, $u_y(x)$:

$$u_y(x) = \begin{cases} De^{-qx} & (x \geq d/2) \\ B\cos(hx) + C\sin(hx) & (-d/2 \leq x \leq d/2) \\ De^{qx} & (x \leq -d/2) \end{cases}$$

where $h$ and $q$ are the transverse wavevectors in the core and cladding regions respectively. For simplicity, we only consider a symmetric dielectric waveguide with $n_1 = n_3$. Substituting these field functions into the wave equation for each layer of the waveguide, we arrive at:

$$\begin{aligned} h &= \sqrt{\left(\frac{\omega n_2}{c}\right)^2 - \beta^2} \\ q &= \sqrt{\beta^2 - \left(\frac{\omega n_1}{c}\right)^2} \end{aligned} \tag{3.2}$$

The field distribution of a guided mode requires an evanescent field decay outside of the core layer. Thus, the form of $u_y(x)$ defined above and Eqn. 3.2 dictate that to sustain a TE mode, $\beta > \frac{\omega n_1}{c}$ and $\beta < \frac{\omega n_2}{c}$; in other words, a guiding structure must have $n_2 > n_1$. The continuity conditions at the boundaries $x = \pm d/2$ requires that $\mathcal{E}_y$ and $\partial\mathcal{E}_y/\partial x$ are continuous. Imposing these conditions, we arrive at two possible relationships linking $h$ and $q$, corresponding to even and odd TE modes:

$$h\tan(hd/2) = q \qquad \textit{and} \qquad h\cot(hd/2) = q \tag{3.3}$$

Let $\bar{u} = 1/2hd$ and $\bar{v} = 1/2qd$, thus, we have a system of 2 simultaneous equations for each mode which can be solved graphically. For an even TE mode:

$$\bar{u}\tan\bar{u} = \bar{v} \qquad \textit{and} \qquad \bar{u}^2 + \bar{v}^2 = (n_1^2 - n_2^2)\left(\frac{\omega d}{2c}\right)^2 \tag{3.4}$$

As $d$ increases for the same input wavelength, the graphical solution based on Eqn. 3.4 gives results corresponding to higher order modes. The first solution is often called the fundamental mode. Implementing the above analysis on a waveguide of $n_{core} = 3.64$ and $n_{clad} = 1$, the electric field of the fundamental TE mode is presented in Fig. 3.2(a). We can see that most of the field energy is confined in the core region and as $d$ increases, the amount of field inside the core also increases. For a particular input wavelength, there exists a cut-off core thickness at which higher order modes can no longer propagate in the structure. On the other hand, the fundamental mode of a symmetric slab waveguide always exists regardless of the core thickness.

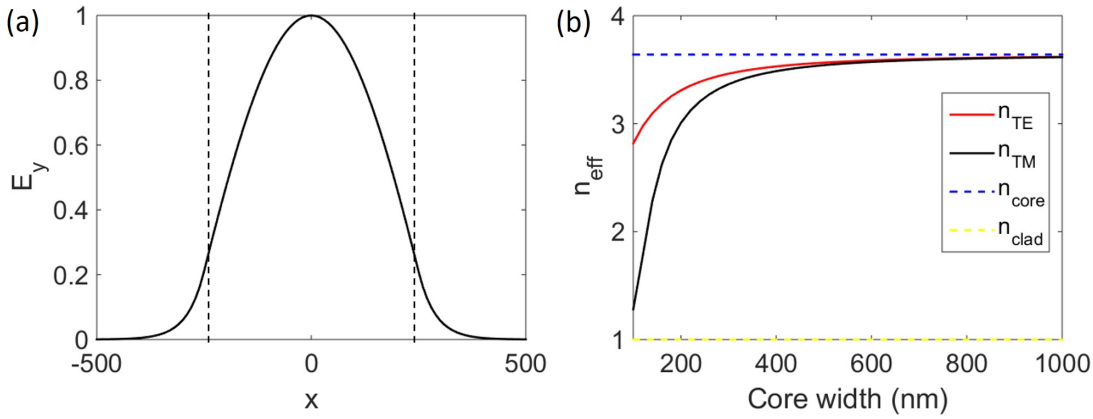



**Figure 3.2** – (a) Spatial field distribution of a TE symmetric mode for $n_{core} = 3.64$ and $n_{clad} = 1$. The dash line indicates the thickness of the core region $d = 500$ nm. (b) Effective refractive index of the TE and TM fundamental modes of a symmetric waveguide with $n_{core} = 3.64$ and $n_{clad} = 1$ as a function of the core width.

Although not presented here, a similar set of solutions for TM modes can also be obtained [97]. Figure 3.2(b) shows the variation of $n_{eff}$ for the fundamental TE and TM modes as a function of the core width. The effective refractive index of a guided mode is defined as $n_{eff} = \frac{\beta}{K_0}$. The first order TE mode always has a higher effective index than that of the corresponding TM mode. The refractive indices of the cladding and the core regions, $n_1 = n_{clad}$ and $n_2 = n_{core}$, define the lower and upper limits of $n_{eff}$. As $n_1 < n_{eff} < n_2$, the more field residing in the cladding region, the faster the mode. Thus, when $d$ becomes larger, both TE and TM solutions have their speeds approaching the speed of light in the core region, leading to a smaller difference between $n_{TE}$ and $n_{TM}$ in the very large core thickness regime.

### 3.1.2 Guiding light in lossy waveguides

When the core layer of the waveguide is made up of a lossy material, the propagation constant, $\beta$, must be expressed as a complex number whose imaginary part signifies the decay of field in the propagation direction. The procedure to find the exact solution of the first order guided TE wave changes as many other parameters such as $q$, $h$ and the field magnitudes $C, B, D$ can also take complex values. In this lossy environment, the field normalization is modified as $E_{TE} = \sqrt{\frac{\omega\mu_0}{d_{TE}\Re\{\beta\}}}$ where $d_{TE} = d + 2/\Re\{q\}$ [86,98]. To solve this transcendental eigen-equation, we employed an iterative steepest descent method with linear line search [98,99], which is detailed in Appendix D.

## 3.2 Hybrid gap plasmon waveguide

### 3.2.1 An overview of plasmonic waveguides

Plasmonic waveguides have many advanced functionalities compared to their photonic counterparts described above, such as greater modal confinement, higher field enhancement, and various modulation capabilities. In particular, it is the confinement characteristic of plasmonics that allows nanoscale devices to be engineered. Different plasmonic geometries can offer confinement in 1D (metal-dielectric slab) [100,101], 2D (nanowires, rectangular) [102,103] or 3D (nanospheres) [104]. A summary of various plasmonic waveguide geometries and their field distributions is given in Fig. 3.3.

While all of these plasmonic waveguides are able to confine light to subwavelength scales, they possess relative advantages in terms of device fabrication, the amount of loss versus confinement and focusing capabilities [15,33,105–107]. These waveguides can also operate at different wavelengths. The two wavelength regimes of practical interests are the telecommunication (∼1,300-1,550nm) and the visible (∼ 400-700 nm). Amongst popular plasmonic waveguide designs, hybrid photonic-plasmonic waveguides (HWG) show outstanding properties that outperform other designs [100,108–113]. These hybrid structures consist of a high index semiconductor layer and a metal slab separated by a low index dielectric spacer, possessing modal confinement of up to $\lambda^2/400$ and a relatively large propagation length reaching 150

$\mu$m [33, 114]. A few examples of HWGs are shown in Fig. 3.4. Going beyond guiding applications, a passive plasmonic design can be turned into a laser cavity by replacing the passive core with an active medium. Amongst these three HWG designs, the hybrid gap plasmon waveguide (HGPW) shown in Fig. 3.4(b) is the only geometry that supports both easy access to the gain region via optical pumping and simple top-down lithographic patterning. Thus, it is the appropriate platform to explore the feasibility of compensating for losses and lasing applications using practical plasmonic designs, a topic which will be explored further in Chapter 5.

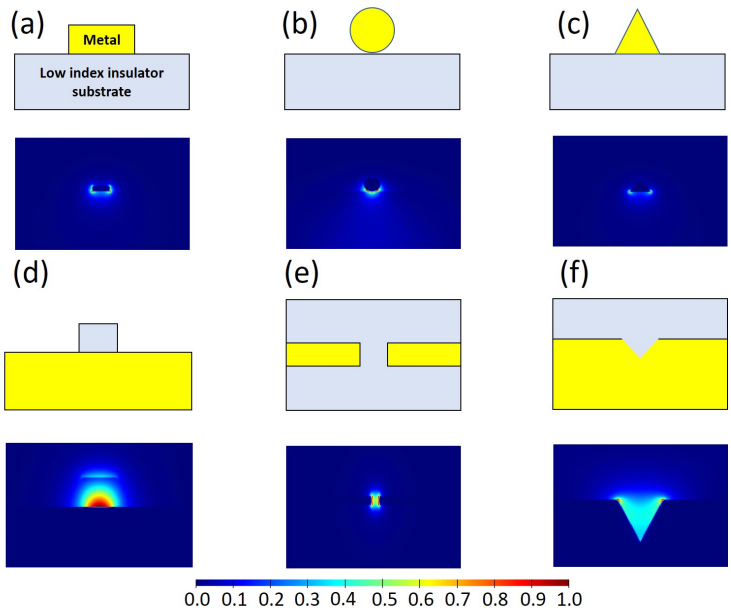



**Figure 3.3** – Various plasmonic waveguide geometries. The metal layer is gold (yellow) and the low index insulator is $SiO_2$ (grey). The numerical simulations of the fundamental modes, implemented in COMSOL 4.3a – radio frequency module, eigenmode-solver at $\lambda = 1500$ nm, are presented in the lower blue panels. (a) Strip plasmonic waveguide: $n_{eff,TM} = 1.458 + i0.013$, Au bar dimensions $200 \times 50$ nm. (b) Mettalic nanowire: $n_{eff,TM} = 1.367 + i0.005$, nanowire radius 100 nm. (c) Wedge plasmonic waveguide: $n_{eff,TM} = 1.45 + i0.008$, Au wedge dimensions: base 300 nm, height 400 nm. (d) Dielectric loaded surface plasmon polariton waveguides: $n_{eff,TM} = 1.169 + i0.0035$, $SiO_2$ bar dimensions $500 \times 500$ nm. (e) Metal-Insulator-Metal plasmonic waveguide: $n_{eff,TE} = 1.738 + i0.0256$, gap dimension 100 nm. (f) Channel plasmon polariton waveguide: $n_{eff,TE} = 1.228 + i0.017$, groove angle 37°.

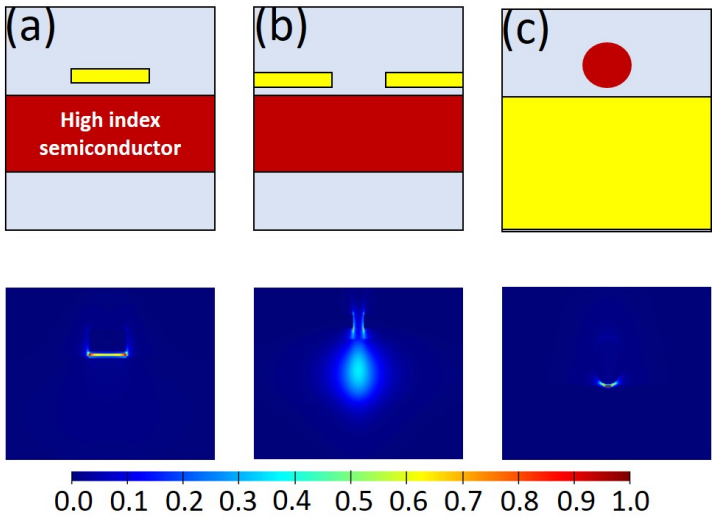


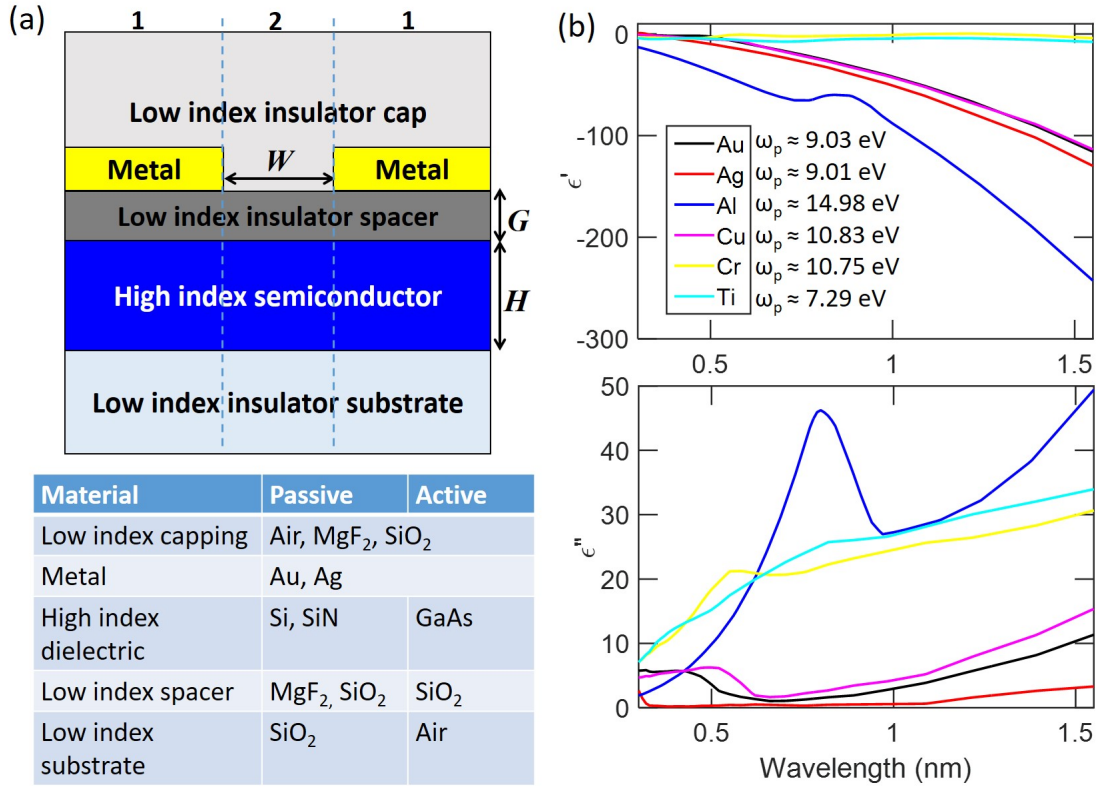

**Figure 3.4** – Various HWG designs. The metal layer is gold (yellow), the low index insulator is $SiO_2$ (grey) and the high index semiconductor is Silicon (red). The numerical simulations of the fundamental modes, implemented in COMSOL 4.3a – RF module at $\lambda = 1500$ nm, are presented in the lower blue panels. (a) Strip HWG: $n_{eff,TM} = 2.86 + i0.021$, Au bar dimension 200 nm and spacer thickness 10 nm. (b) Gap HWGs: $n_{eff,TE} = 2.76 + i0.0034$, Au bar dimension 220 nm and spacer thickness 40 nm. (c) Nanowire HWGs: $n_{eff,TM} = 1.543 + i0.016$, wire radius 100 nm and spacer thickness 10 nm.

## 3.2.2 HGPW: fundamentals and practicalities

### Materials for HGPW construction

The cross-section of the material composition of a typical HGPW is shown in Fig. 3.5(a).

Without the metallic bars, the structure looks identical to a conventional slab waveguide with two low index cladding layers surrounding a high index core, which confines the field only in 1D. The incorporation of the metallic layers adds another confinement dimension to the field. The bottom panel of Fig. 3.5(a) gives a summary of typical material selections for passive and active HGPWs. Both kinds of HGPWs are governed by the same fundamental physics as they satisfy the requirement of the index distribution in Fig. 3.5(a). The difference between an active and passive HGPW only lies in their fabrication techniques and potential applications. Thus, for simplicity's sake, we will use a passive HGPW made up of a Si core, a $SiO_2$ cladding and a $SiO_2$ spacer to demonstrate the modal properties of the fundamental hybrid




| Material | Passive | Active |
|---|---|---|
| Low index capping | Air, $MgF_2$, $SiO_2$ | |
| Metal | Au, Ag | |
| High index dielectric | Si, SiN | GaAs |
| Low index spacer | $MgF_2$, $SiO_2$ | $SiO_2$ |
| Low index substrate | $SiO_2$ | Air |

**Figure 3.5** – (a) Cross-section and material composition/positioning of a typical HGPW. The blue dash line divides the structure into 2 identical regions (labeled 1) and one central region (labeled 2). Each region can be thought of as a separate structure with an effective refractive index of its own. The table gives examples of possible selections of materials that make up passive/active HGPWs. (b) Dispersion property of common plasmonic metals: Real and imaginary part of the electric permittivity as a function of wavelength. Also shown here is the calculated values of the plasma frequency, $\omega_p$ for the corresponding metals based on Lorentz-Drude model [115].

mode of HGPWs [34].

The selection criteria for the metal layer of a HGPW include low loss, low surface roughness and room condition operation. Figure 3.5(b) plots the real and imaginary parts of the permittivity function of common materials considered for plasmonic applications. The existence of a surface plasmon requires a material with a negative permittivity in the wavelength range of interest (See Appendix E for details on the modal calculation of surface plasmon polaritons). When $\omega$ is smaller than $\omega_p$, the plasma frequency of metals, according to the Drude model, $\epsilon'$ becomes negative. An overview of optical properties of metals is given in Appendix F. Figure 3.5(b) shows

that Au, Ag, Al, Cu, Ti can exhibit plasmon resonances at visible and lower frequencies [115]. While Al with a relatively large $\omega_p$ has been used in UV-plasmonics [116], Au and Ag are restricted to visible and infra-red plasmonic applications because their interband transitions kick in at $\lambda \approx 500$ nm and 310 nm respectively. $\epsilon''$ tells us about the lossiness of a material. Au and Ag have their plasmon resonance in the visible spectrum and conveniently have the lowest loss in this spectral range, making them the most popular plasmonic materials.

However, Au and Ag are not CMOS (Complementary metal-oxide-semiconductor) compatible. This is because Au and Ag have high diffusion constants in Silicon.[a] There has been recent developments in non-CMOS compatible fabrication which pave the way for more commercial applications of these two noble metals. Au is often favoured over Ag as it is more chemically stable, i.e., less susceptible to oxidation, making it the ideal material for room condition operation. Furthermore, the problem with surface roughness in Ag deposition can lower the device quality and add imperfections to the structures while with Au we can generally achieve higher material quality deposition [117].

### Modal properties of HGPW

Next we investigate how the geometric parameters of HGPWs affect their modal properties. Figure 3.6(a) shows an example of the field distribution of the fundamental HGPW mode for two extreme values of the waveguide gap, W = 20 nm and W = 2000 nm. At W = 20 nm, most of the field stays in the dielectric gap region between the metal bars whereas the field resides mainly in the semiconductor region when W = 2000 nm. In both cases, the field is confined in the central region of the waveguide. To understand the influence of the core thickness, H, on this lateral confinement characteristic, the cross-section of the device is divided into 3 regions, as drawn in Fig. 3.5(a). Each region is considered a separate structure[b] and their effective indices are found for the fundamental TE modes using COMSOL 4.3a – radio frequency module, eigen-solver. It was found that for TE waves, $n_{TE2}$ is always greater than

[a] To be CMOS compatible, the metal also needs to have a high melting point.
[b] See the photonic mode composition in Fig. 3.8(a).

$n_{TE1}$, leading to the confinement of the modal field in region 2. The larger the effective index contrast value $n_{TE2} - n_{TE1}$, the greater the lateral field confinement.

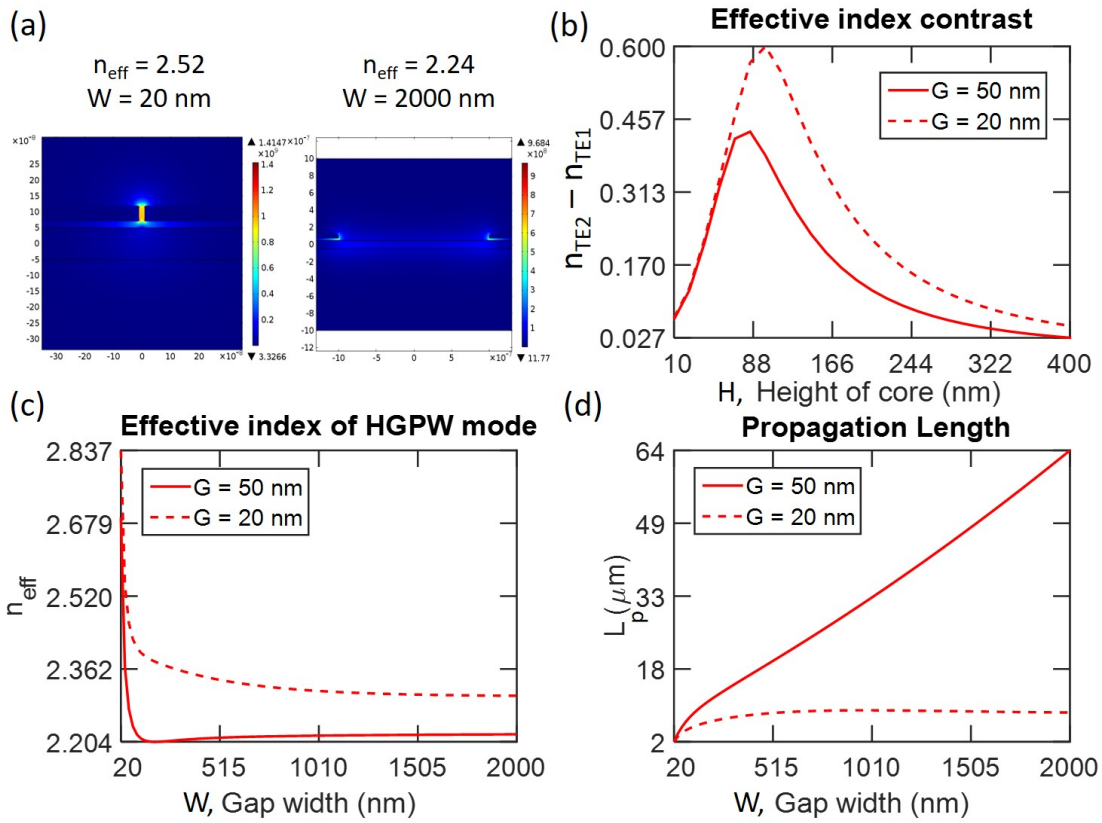



**Figure 3.6** – (a) Field distribution and effective refractive indices of a passive HGPW's fundamental mode for two gap width values. The substrate, spacer, capping layers are $SiO_2$, the semiconductor core is Si and the metal is Au. Here H = 100 nm and G = 20 nm and $\lambda$ = 1550 nm. (b-d) Modal properties of the HGPW described in (a) for two spacer thicknesses G = 20 nm and 50 nm and two different metals Au and Al. (b) Effective index contrast between regions 1 and 2 for the TE fundamental mode as a function of the height of semiconductor core. (c) Effective index of the HGPW's fundamental mode as a function of gap width (W). (d) Propagation length of the HGPW's fundamental mode as a function of gap width.

Figure 3.6(b) shows the dependence of the effective index contrast on the values of H. There exists an optimum value of H for which the maximum lateral confinement is achieved. The thickness of the spacer, G, also influences $n_{TE2} - n_{TE1}$: the smaller the value of G, the greater the magnitude of this index contrast. In this case, an optimum $n_{TE2} - n_{TE1}$ is obtained at H = 88 nm for G = 50 nm and at H = 103 nm for G = 20 nm. The dependence of the hybrid mode effective index on the gap width is shown in Fig. 3.6(c). Clearly, there is a change in the behaviour of the hybrid mode as the

gap width shrinks below 50 nm. This is represented by a rapid increase in $n_{eff}$ with decreasing W values. This characteristic of the hybrid mode will be studied using the hybridization theory in the final section of this chapter. Another pertinent property, often used to characterize the quality of a lossy waveguide design, is the propagation length, $L_p = [2K_0\Im\{n_{eff}\}]^{-1}$, where $K_0 = 2\pi/\lambda$. Figure 3.6(d) shows the variation of $L_p$ as a function of W. For G = 50 nm, $L_p$ increases with increasing W whereas for a smaller value of G, G = 20 nm, $L_p$ reaches a plateau once W gets larger than approximately 200 nm.

The well-known tradeoff between confinement and loss in this plasmonic system is illustrated in Fig. 3.7(a). This figure shows a parametric plot of the propagation length of the HGPW as a function of its modal area parameterised by the gap width. We consider here two definitions of the modal area. The following definition is typically used in assessing the local light-matter interaction strength with the greatest interaction occurring where the light intensity is highest:

$$A_1 = \frac{\int U dS}{Max\{2U_E\}} \tag{3.5}$$

$U = U_E + U_M$ is the total electromagnetic energy density, $U_E$ and $U_M$ are the electric and magnetic energy densities respectively, and $A_0 = \lambda^2/4$.[c] While this method is more applicable to situations where nonlinearities are involved, it does not reflect the true extent of the mode. To do this, we employ:

$$A_2 = \frac{(\int U dS)^2}{\int U^2 dS} \tag{3.6}$$

Clearly, an increase in the propagation length comes at a price of rising modal area. Regardless of the modal area definitions, the curves in Fig. 3.7(a) feature a kink which signifies the point at which a significant increase in the propagation length is accompanied by a relatively smaller increase in modal areas. This makes the HGPW structure very appealing for on-chip guiding applications. When G increases, the separation between the Si core and the metallic bar increases; hence, the overall

[c]Further details on the energy flow in plasmonics is given in Appendix G.

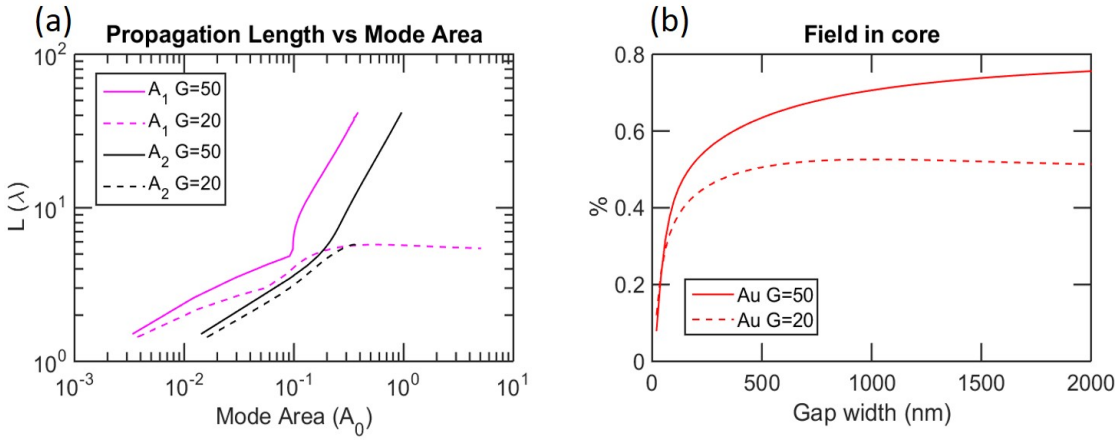



**Figure 3.7** – (a) Propagation length as a function of modal area of the fundamental hybrid mode for W = 20-2000 nm and two spacer thicknesses G = 20 nm and 50 nm. Plotted here are the corresponding modal areas calculated based on the two definitions described above. (b) The amount of electric field in the core region as a function of gap width for G = 20 nm and 50 nm.

structure experiences less loss. This is why at G = 50 nm, a much longer propagation length can be achieved at a given W compared to when G = 20 nm. For G = 20 nm, the stronger influence of metallic losses puts a limit to the maximum achievable propagation length. It is also interesting to look at how the amount of field residing in the core region changes with increasing W. Figure 3.7(b) shows that when W < 100 nm, the percentage of fields in the core experiences a steep decrease with decreasing W. Above 100 nm, the amount of fields residing in the Si core increases slowly then reaches a plateau. For G = 50 nm, the maximum achievable amount of energy in the Si core is higher than when G = 20 nm, due to a weaker interaction of the fundamental mode with the metal bars.

### Hybridization mechanism in HGPWs

To further explore the dependence of the modal properties of HGPW on its geometric dimensions, the fundamental hybrid mode can be broken down into its hypothetical constituent modes, a photonic-like mode and a plasmonic-like mode. The construction of these constituent modes is shown in Fig. 3.8(a). As explained above, the existence of a lateral confinement in a HGPW can be attributed to the formation of an effective photonic mode with $n_{TE2} > n_{TE1}$ for the fundamental TE modes.

Figure 3.8(b) shows that as W increases, $n_{eff}$ of the hybrid mode approaches that of region 2 as more and more field sits in the central region. However, when W $<$ 100 nm, the mode obtains an increasingly plasmonic-like character with an exponential increase in $n_{eff}$ with decreasing W. The difference between $n_{TE2}$ and the largest $n_{TM1}$—the light blue shaded region in Fig. 3.8(b)—denotes the limits of the lateral confinement, signifying the existence of a bound photonic mode. The grey shade in Fig. 3.8(b) indicates the region where 2D confinement is no longer achieved in the system. The cutoff of the hybrid mode marks the point at which $n_{eff}$ of the HGPW is equal to the effective index of the TM mode in region 1. At this point, the hybrid mode can couple to unbounded modes in region 1. The spacer thickness controls the effective index contrast between regions 1 and 2, and thus the degree of lateral confinement. However, too thin a spacer can lead to a loss of lateral confinement through coupling to TM waves in region 1, $G > G_{critical} \approx 16$ nm [34].

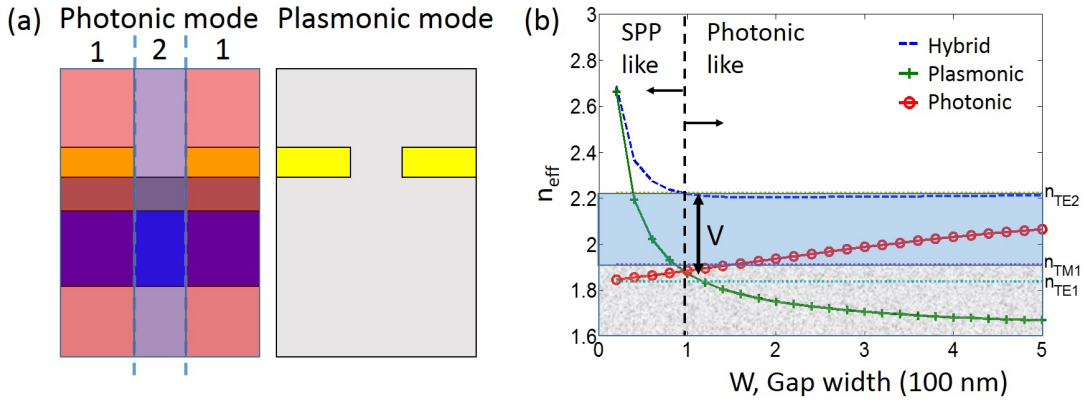



**Figure 3.8** – (a) Constituent modes of the fundamental hybrid mode. The TE photonic mode is built based on the construction of a conventional photonic waveguide mode using effective index approach where G = 50 nm. For TE waves, a guided mode exists if $n_{TE1} < n_{TE2}$. The plasmonic mode is a conventional MIM (metal-insulator-metal) TE mode. (b) $n_{eff}$ of the fundamental hybrid mode and its constituent modes as a function of the gap width. $V$ denotes the coupling strength. Also shown is the separation of the plasmonic and photonic like regimes.

The hybridized nature of the HGPW fundamental mode is evidenced by the splitting between the two constituent modes—this splitting refers to the distance from the crossing point of effective indices of the constituent modes to $n_{eff}$ of the hybrid mode. The theory of mode hybridization can be constructed similarly to the mathematical formulation of coupled mode theory. Assuming that $\Psi_{photonic}$ and $\Psi_{plasmonic}$ form the

orthogonal basis of the system, the amplitude of the field of the hybrid mode can be expressed as a linear superposition of its constituent modes, ignoring higher order terms [33]:

$$\Psi_{\pm} = a_{\pm}\Psi_{photonic} + b_{\pm}\Psi_{plasmonic} \tag{3.7}$$

where $a_{\pm}$ and $b_{\pm}$ are the amplitude of the photonic and plasmonic modes respectively. Normalization of the total field gives: $b_{\pm} = \sqrt{1 - |a_{\pm}|^2}$. The $\pm$ denotes the two possible hybridized mechanisms in this system: symmetric and anti-symmetric hybrid modes. The mode can be characterized with an effective index, $n_{ph}$ and $n_{pl}$. This subsequently leads to:

$$\begin{bmatrix} n_{ph} & V \\ V & n_{pl} \end{bmatrix} \begin{bmatrix} a_{\pm} \\ b_{\pm} \end{bmatrix} = n_{\pm} \begin{bmatrix} a_{\pm} \\ b_{\pm} \end{bmatrix}$$

where $V$ specifies the strength of the hybridization mechanism. The theoretical effective index of the hybrid mode, $n_{\pm}$, is the eigenvalue of the hybridization matrix:

$$n_{\pm} = \frac{n_{ph} + n_{pl}}{2} \pm \sqrt{\frac{(n_{ph} - n_{pl})^2}{4} + V^2} \tag{3.8}$$

Together with the normalization condition of $\Psi$, we can find an expression for $|a_+|^2$:

$$|a_+|^2 = \frac{n_+ - n_{pl}}{(n_+ - n_{ph}) + (n_+ - n_{pl})} \tag{3.9}$$

This value of $|a_+|^2$ characterizes the degree of hybridization of the two constituent modes. We consider three regimes of hybridization:

1. $|a_+|^2 < 0.5$ : The hybrid mode is more plasmonic-like.

2. $|a_+|^2 = 0.5$ : Equal contribution of the plasmonic and photonic modes to the hybrid mode. This is the point of splitting in order to prevent crossing of energy levels in the hybrid system.

3. $|a_+|^2 > 0.5$ : The hybrid mode obtains a more photonic-like character.

Unlike in usual hybrid systems, here only one possible mode of the hybrid system exists, $n_+ > n_{ph}, n_{pl}$. The other branch of the hybrid system is cutoff because $n_- < n_{ph}$ representing an unbound solution [33]. For this HGPW, the gap width determines the

relative contribution of the photonic-like and the plasmonic-like constituent modes to the fundamental mode of a HGPW, which in turn determines its modal behaviour in the small (W< 50 nm) and the large gap width regimes.

## 3.3 Summary

The physics of photonic dielectric slab waveguides and hybrid gap plasmon waveguides was outlined. For a lossless slab waveguide, a bound mode required the field to decay evanescently outside the core layer. The fundamental TE mode was found to always have an effective refractive index larger than that of the corresponding TM mode. As the core width increased, more field resided in the core layer, and the speed of the guided modes approached light's speed in this layer. When loss was introduced into the core region, the propagation constant turned complex in order to accommodate the decay of fields in the propagation direction. The numerical method, iterative steepest descent with linear line search, was used to solve for the equation of bound TE modes in this lossy environment. The modal distribution of TE dielectric slab waveguides outlined here is used in the study of Parity-Time symmetry coupled waveguides in Chapter 6.

In order to achieve a modal size below the diffraction limit, a particular type of plasmonic waveguides called the hybrid gap plasmon waveguide was investigated. It was found that the degree of plasmonic and photonic characteristics of the fundamental hybrid mode of this structure depended on the distance between the metal bars. At small gap widths, the field resided in the dielectric region between the metals while at larger widths, most of the field stayed in the high index semiconductor core. The transition from a dominantly plasmonic character to a dominantly photonic character was also signified by an increase in the propagation length of the hybrid mode. With these properties, together with an easy access to the semiconductor layer, HGPWs can be used as plasmonic cavities by replacing the passive core with a gain medium and adding appropriate feedback. An experimental demonstration of plasmonic lasers based on HGPWs is detailed in Chapter 5.

# Chapter 4

# Loss and Gain mechanism in optical devices

Most of solid state devices described in this thesis are based on GaAs to supply gain for the experimental demonstration of plasmonic lasers and for dispersion corrected parity-time symmetric coupled waveguides. It is essential to understand the mechanism behind the high gain achieved in GaAs and the inevitable dispersion that occurs by operating in such an extreme regime. We begin this chapter with an overview of GaAs band structure properties. This is followed by a detailed summary of the semiclassical free carrier theory upon which our gain model is built. The results of our gain model are then compared with other more complicated models often used in the literature. This study of the gain mechanism in bulk GaAs leads us to the second part of this chapter which focuses on analyzing the role of gain in compensating for loss in the context of nanophotonic devices and in particular the lasing mechanism. The fundamental physics of optical cavities and the rate equations of lasers are outlined. The modification of lasing properties when the laser dimensions shrink down to the nanoscale regime is also considered.

# 4.1 Gain mechanism in GaAs

## 4.1.1 An overview of GaAs properties

GaAs is a typical III-V semiconductor with a direct bandgap of $E_g \approx 1.424$ eV, equivalent to a wavelength of $\lambda_g \approx 870$ nm. The history of GaAs dates back to the year 1929 when the compound was first created [118,119]. However, it took another 20 years for the first research on the exceptional electronic properties of III-V semiconductors to be reported [120], stirring up a huge research interest in novel semiconductor devices. It was not until 1962 when the first semiconductor lasers, whose light emission came from GaAs [121–123] and $GaAs_{1-x}P_x$ [124], were demonstrated. GaAs is superior to Silicon in terms of carrier transport as it has higher mobility and saturated drift velocity—a result of lower lattice and impurity scattering.

While most III-V (GaAs, InGaP, GaN, etc) and II-VI (ZnO, ZnS, ZnSe, etc) semiconductors are direct bandgap materials, GaAs is of great importance as its bandgap falls into the near infra-red range. Commercial semiconductor lasers are commonly grown on either GaAs substrates or InP substrates. InP-based devices dominate applications in the range of 1100-2000 nm while GaAs-based lasers emit in the range of 630 - 1100 nm [125] with applications in optical storage, displays, solar cells and printing [126]. Since the minima of the conduction band and the maxima of the valence band of a direct bandgap semiconductor occur at the same crystal momentum, $k$, conservation of momentum of optical transitions at this point is automatically satisfied without the involvement of phonons, making direct bandgap semiconductors more efficient as light emitters, hence suitable candidates for the role of laser gain media.

The band structure of GaAs is in reality quite complicated. However, at visible and near infra-red frequencies, it is reasonable to describe GaAs as a direct bandgap material around $k = 0$ with a parabolic band structure. GaAs has a single conduction band made up of 4s-states: l = 0, j = 1/2 gives $|j,m_j\rangle = |1/2, \pm 1/2\rangle$ and three valence bands made up of 4p-states: l = 1, j = 3/2 and 1/2, leading to $|j,m_j\rangle = |1/2, \pm 1/2\rangle$,

$|3/2, \pm 1/2\rangle$ and $|3/2, \pm 3/2\rangle$ [127]. The lowest valence band often called the split-off band corresponding to $|j,m_j\rangle = |1/2, \pm 1/2\rangle$. The two higher bands come from j = 3/2, are degenerate at $k = 0$, with the highest band having $|j,m_j\rangle = |3/2, \pm 3/2\rangle$, usually called heavy holes, and the middle band $|j,m_j\rangle = |3/2, \pm 1/2\rangle$, named light holes. Figure 4.1(a) gives a schematic sketch of the simplified band structure of GaAs at $k = 0$.

### 4.1.2 Fundamental concepts in band structure theory

#### Formation of band structures in solids

Electrons in an atom occupy discrete energy levels. The orbital of an electron in an atom can be characterized by its size, shape and orientation using the three familiar quantum numbers n, l, m. These quantum numbers tell us about the spatial probability of finding an electron in an atom. Electrons are organized in shells. Each shell consists of different orbital shapes. A particular orbital shape can be orientated in several ways. In this picture, there are two kinds of electrons in an atom: valence electrons which have the lowest binding energy and largest orbitals, and core electrons which occupy the inner shells and stay under a stronger influence of the nucleus.

In general, the behaviour of an electron whose mass and energy are $m$ and $E$ respectively in a potential, $V(r)$, is described by the Schrödinger equation:

$$\left[-\frac{\hbar^2}{2m}\nabla^2 + V(r)\right]\psi(r) = E\psi(r) \tag{4.1}$$

where $\psi(r)$ is the state function. As fermions, electrons follow the Pauli exclusion principle which prevents two electrons of parallel spins to occupy the same electronic state or orbital. Quantization and the exclusion principle make up the basis of the fundamental rule of filling electronic states in a Fermionic system under the potential $V(r)$.

When N atoms are put next to each other, typically $\approx 10^{23}$ cm$^{-3}$ atoms in a solid, their valence electron orbitals overlap (orbitals of core electrons are too small to overlap) and form N combinations of different shapes and energies which can ac-

commodate 2N electrons [128]. A given valence orbit combining with those from neighbouring atoms form an energy band with distinct sublevels of infinitesimal difference in energy. The splitting due to perturbation effects does not only result in the formation of energy bands but also gives rise to regions separating these bands where no states exist, called bandgaps. In other words, the familiar discrete electronic levels in an atom broaden into a band. In particular, the wavefunctions describing electronic states in the bands extend throughout the solid, rather than being localized to an atom. In general, the higher the band the greater its width due to a greater influence of the field perturbation.[a]

### Fermi-Dirac Distribution

When the concentration of fermions in the system is so high such that the average interparticle separation is smaller than the de broglie wavelength of the particle, we enter the regime of quantum statistical mechanics.[b] This is the case for most solids. In solid state physics, the Fermi-Dirac distribution—a quantum statistical mechanics concept—is used to describe the distribution of electrons among energy levels at thermal equilibrium, regardless of the electronic state distribution of a system:

$$f_{FD}(E) = \frac{1}{e^{E-\mu/k_BT}+1} \tag{4.2}$$

where $\mu$ is the chemical potential denoting a particular energy state at which the occupation probability is 1/2: $f_{FD}(\mu) = 1/2$, $k_B$ is the Boltzmann constant and $T$ is temperature. At T = 0, the Fermi-Dirac distribution becomes a step function. The occupation probability of states below the chemical potential is 1: all states with $E < \mu$ are occupied, and the probability of states above the chemical potential is zero: all states with $E > \mu$ are empty. At absolute zero temperature, $\mu = E_f$ where $E_f$ is the Fermi energy defined as the uppermost energy level filled by carriers. This behaviour nonetheless changes drastically when temperature increases and carriers start to fill higher energy levels. However, the Fermi-Dirac distribution retains its

[a] For example, 1s orbital is smaller and closer to its own nucleus hence is not affected much by the perturbation of the other atom.

[b] Electron concentration in solids typically reaches the level of $10^{15}$ cm$^{-3}$ while the de Broglie wavelength of an electron is approximately 1.23 nm.

symmetry property about $f(E) = 0.5$ (Fig. 4.1(b)).

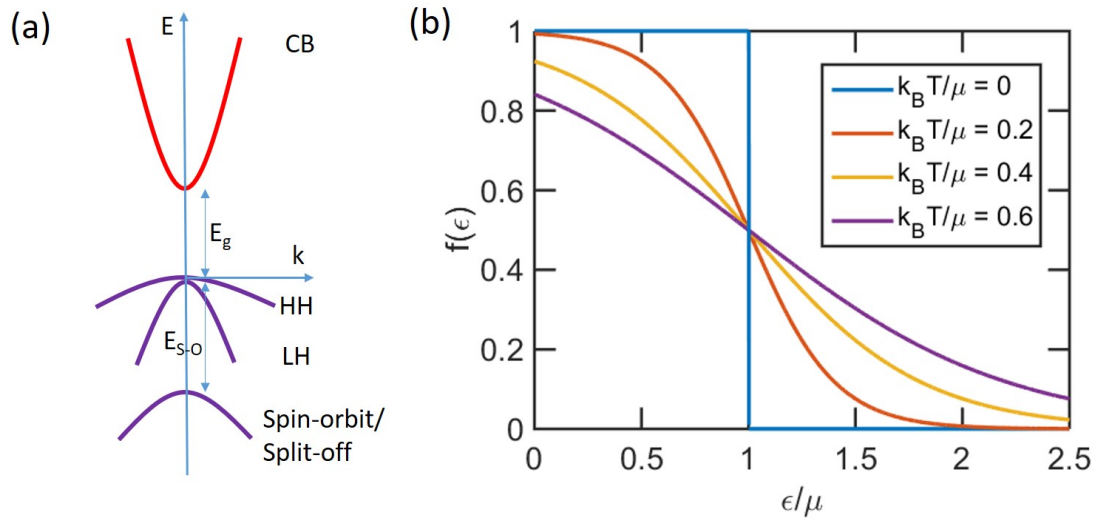



**Figure 4.1** – (a) Simplified band structure of GaAs: 1 Conduction band (CB) and three valence bands (Heavy Hole (HH), Light Hole (LH) and Spin-orbit (S-O)). (b) Fermi-Dirac distribution at different temperature — $k_BT$ is normalized to $\mu$.

At $E \gg E_f$, the system can be described by classical statistical mechanics: the Fermi-Dirac distribution tends to the Maxwell-Boltzmann distribution in this regime: $(E - E_F)/k_BT \gg 1$, $f_{FD}(E) \to e^{E_F/k_BT}e^{-E/k_BT} \propto e^{-E/k_BT}$. The actual filling process however depends on the number of electrons available in the solid and the existing distribution of electronic states in the crystal: two electrons of opposite spins are used at a time to fill the states from lowest to highest energy levels until all valence electrons have been accounted for.

### 4.1.3 Light in gain media

#### Overview of semiconductor gain theory

Free-Carrier theory pivots on the assumption that the polarization in the medium induced by the electric field in turn drives this field self-consistently. This theory was originally derived in the context of a laser field interacting with a gain medium. However, the essence of the theory lies in the description of the mutual interaction between light and free carriers: how light creates electric dipoles in a semiconductor and how these electric dipoles then affect the propagating field, giving us the phenomena of

gain and gain-induced refractive index change. This is a semi classical approach where the description of the electric field $\boldsymbol{\mathcal{E}}(\mathbf{r},t)$ follows the classical Maxwell equations while the interaction between the field and atoms is examined quantum mechanically. The derivation of free-carrier theory in this chapter follows [127]. Figure 4.2 summarizes the logical sequence behind the free-carrier theory.

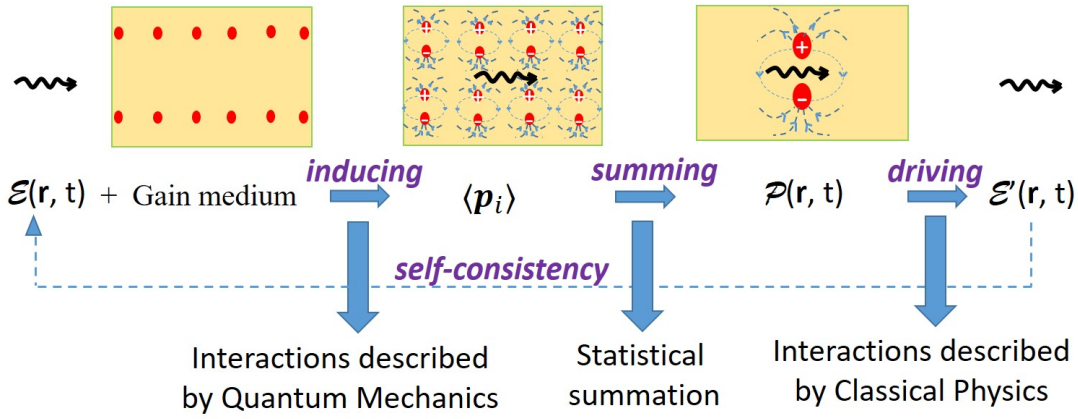



**Figure 4.2** – Sequential steps in the calculation of semiconductor gain in Free-Carrier theory following reference [127].

### Propagation of light in polarized media

The propagation of light inside a polarized medium follows the classical Maxwell equations, Eqn. 2.4–2.7. $\boldsymbol{\mathcal{D}} = \epsilon\boldsymbol{\mathcal{E}} = \epsilon_b\boldsymbol{\mathcal{E}} + \boldsymbol{\mathcal{P}}$ with $\epsilon_b = n^2\epsilon_0$ being the permittivity of the host medium. The calculation of $\boldsymbol{\mathcal{P}}$—the polarization of the medium—is central in this gain analysis. $\boldsymbol{\mathcal{P}}$ is induced by the interaction of the light field with electrons in the valence and conduction bands. This polarization then influences the propagating fields, inducing a complex susceptibility which results in the interrelated generation of gain and a carrier-induced index change. In a polarized medium, the wave equation has the form:

$$-\nabla^2\mathcal{E} + \left(\frac{n}{c}\right)^2 \frac{\partial^2\boldsymbol{\mathcal{E}}}{\partial^2 t} = -\mu_0 \frac{\partial^2\boldsymbol{\mathcal{P}}}{\partial^2 t} \tag{4.3}$$

The electric field can be expressed as a plane wave with a monochromatic field—a reasonable approximation only when a small volume compared to the transverse variations of the light field is considered.[c] This allows us to calculate the local properties

[c]Note here that by only looking at a monochromatic field, we cannot assess the coherent response of a gain medium to multimode fields, which is beyond the scope of this thesis.

of the gain medium hence how these local effects change the propagation of the beam. The light field and its induced polarization take the form of:

$$\boldsymbol{\mathcal{E}}(z,t) = \frac{1}{2}\hat{x}\mathcal{E}(z)e^{i[Kz-\omega t-\phi(z)]} + c.c \tag{4.4}$$

$$\boldsymbol{\mathcal{P}}(z,t) = \frac{1}{2}\hat{x}\mathcal{P}(z)e^{i[Kz-\omega t-\phi(z)]} + c.c \tag{4.5}$$

The complex polarization amplitude is related to the electric field amplitude via $\mathcal{P}(z) = \epsilon_b\chi(z)\mathcal{E}(z)$ where $\chi(z)$, the susceptibility of the gain material, is modified when a light field travels through the medium. $K = n\omega/c = nK_0$ and $K_0 = 2\pi/\lambda$. $\mathcal{P}(z)$, $\mathcal{E}(z)$ and the phase shift $\phi(z)$ are assumed to have small variations within the optical wavelength.[d] Thus, the terms $\frac{d^2\mathcal{E}(z)}{dz^2}$, $\frac{d^2\phi(z)}{dz^2}$ and $\frac{d\mathcal{E}(z)}{dz}\frac{d\phi(z)}{dz}$ are neglected in the explicit form of Eqn. 4.3:

$$\frac{d\mathcal{E}(z)}{dz} - i\mathcal{E}(z)\frac{d\phi}{dz} = \frac{i\mu_0\omega^2}{2K}\mathcal{P}(z) = \frac{iK}{2}\chi(z)\mathcal{E}(z) \tag{4.6}$$

Equating the real and imaginary parts of Eqn. 4.6, we arrive at a set of self-consistency equations with the light field appearing on both sides of the equations:

$$\frac{d\mathcal{E}(z)}{dz} = -\frac{K}{2}\chi''(z)\mathcal{E}(z) = g\mathcal{E}(z) \tag{4.7}$$

$$\frac{d\phi(z)}{dz} = -\frac{K}{2}\chi'(z) = -K_0\delta n_{ind} \tag{4.8}$$

where $\chi(z) = \chi'(z) + i\chi''(z)$. The second equality signs in Eqn. 4.7 and 4.8 incorporate the notion of gain and carrier-induced refractive change into our analysis for the first time. The intensity gain coefficient is defined as twice the value of $g$. A change in the magnitude of the field in the propagation direction is often described as either gain or loss in an optical system and is governed by Eqn. 4.7. The spatial variation of the field is accounted for by the phase term: $Kz - \phi(z)$. A change in the phase of the field signifies a change in the index of the medium in which the field is propagating through. A change in $\phi(z)$ along the propagation direction can be incorporated into the overall wave number of the propagating field via:

[d] Often known as the slow varying envelope approximation.

$Kz - \phi(z) = (K - \frac{d\phi}{dz})z = (n + \delta n_{ind})K_0 z = n_{ind}K_0 z$. Overall, we can see that the induced polarization influences both the magnitudes of the propagating field and its phase. These changes are characterized by the gain coefficient, $g$ and the carrier-induced refractive index change, $\delta n_{ind}$.

### Light – matter interactions in semiconductor gain media

In order to quantify $g$ and $\delta n_{ind}$, we need to first quantify the polarization that has been induced by the interaction between the propagating field and the electrons in the valence and conduction bands of the semiconductor. This semiclassical theory of semiconductor gain follows a quantum mechanical treatment of the gain medium, giving rise to a quantum description of the induced polarization.

When electrons are excited from the valence to the conduction band, leaving behind a positively charged hole in the valence band, a single global Fermi-Dirac distribution is not sufficient to describe the dynamics of the polarized material. The procedure implemented to determine the distribution of both positively and negatively charged carriers in a polarized medium hinges on the assumption that Coulomb interactions which lead to carrier scattering events are much faster than the field transients. In other words, an equilibrium is established before the field arrives. Coulomb interactions can be treated as reservoir interactions which force carriers into their respective intraband thermodynamic quasi equilibrium Fermi-Dirac distributions, characterized by two quasi-chemical potentials for electrons and holes: $\mu_e$ and $\mu_h$.

As carriers fill up the energy states available in a band, the total carrier density, $N = \frac{1}{V}\Sigma_{states} f_{FD,\alpha,\boldsymbol{k}}$, increases where the subscript $\alpha$ denotes the carrier species. Since the chemical potential defines the point where $f_{FD}(E) = 1/2$, a change in $N$ corresponds to a different value of $\mu$. The next step in this analysis is to find the link between the gain coefficient, $g$ and the total carrier density, $N$ via the chemical potential $\mu$.

To solve for the dynamics of electrons and holes in a polarized medium, we need to find quantum mechanical expressions for the polarization of the gain medium and

the Hamiltonian of the system. In quantum mechanics (QM), the description of the polarization follows: $\mathcal{P} = \frac{1}{V_l}\Sigma_k(\bar{\mu}_k a^\dagger_{ck} a_{vk} + \bar{\mu}^*_k a^\dagger_{vk} a_{ck})$ where $\bar{\mu}_k$ represents the dipole matrix element[e] between the conduction and valence bands, the operators $a^\dagger_{ck,vk}$ and $a_{ck,vk}$ are the electron creation and annihilation operators respectively; the subscripts $c$ and $v$ denote the conduction and valence bands, $k$ is again the corresponding crystal momentum of a state and $V_l$ is the volume of the gain medium. This expression of $\mathcal{P}$ involves creating a new electron in the conduction band and at the same time annihilating one in the valence band—equivalently to creating a hole having the opposite momentum and $z$-component of the particle spin to those of the annihilated electron.

The full Hamiltonian governing the dynamics of carriers includes terms that describe the free-carrier effects, the interactions amongst carriers, pumping conditions and various relaxation processes. In this analysis, we neglect the Coulomb many-body interactions amongst carriers. This many-body effect leads to the renormalization of the bandgap and of the electric dipole interaction energy. By neglecting Coulombic interactions, charge carriers are essentially treated as free carriers in an ideal Fermi gas. The interaction between a light field and a medium is modeled in QM as $H_d = -V_l \boldsymbol{\mathcal{P}}.\boldsymbol{\mathcal{E}}$. Thus, the Hamiltonian for free carriers is constructed as follows:

$$\begin{aligned} H &= \Sigma_k(E_{ck} a^\dagger_{ck} a_{ck} + E_{ck} a^\dagger_{ck} a_{ck}) - \Sigma_k(\bar{\mu}_k a^\dagger_{ck} a_{vk} + \bar{\mu}^*_k a^\dagger_{vk} a_{ck})\mathcal{E}(z,t) \\ &= H_{KE} + H_d \end{aligned} \tag{4.9}$$

where $H_{KE}$ and $H_d$ account for the kinetic energies and the carrier-field dipole interactions respectively. In the electron-hole picture, the missing valence electrons are referred to as holes and the conduction electrons are simply referred to as electrons with $a^\dagger_{ck} = a^\dagger_k$ and $a_{ck} = a_k$. The hole annihilation and creation operators are defined as: $b_{-k} = a^\dagger_{vk}$ and $b^\dagger_{-k} = a_{vk}$. The evolution of the system can be monitored using: $n_{ek} = \left\langle a^\dagger_k a_k \right\rangle$, the electron occupation number, $n_{hk} = \left\langle b^\dagger_{-k} b_{-k} \right\rangle$, the hole occupation number and $p_k = \langle b_{-k} a_k \rangle$, the polarization of the medium which is equivalent to the creation of an electron-hole pair. While the additional factors, such as pumping conditions, radiative and non-radiative emissions, are only present in the equation governing

[e]Not to be confused with $\mu$ denoting the chemical potential.

the dynamics of the carrier concentration number, collisional processes also influence the dynamics of $p_k$. Collisions in semiconductors occur between carriers and carriers, carriers and phonons, carriers and impurities, leading to various relaxation processes. To investigate the gain mechanism in GaAs, we focus on analyzing the dynamics of $p_k$.

The dynamic evolution of $p_k$ obeys the Schrödinger equation. However, the Heisenberg picture of QM offers a more physical description of a quantum mechanical system by assuming that operators which represent observables evolve in time while the wavefunctions remain stationary (Appendix H). Following a Heisenberg picture of QM and adding the collision-dependent term, we achieve the following dynamic evolution of $p_k$:

$$\frac{dp_k}{dt} = -i\omega_k p_k - \frac{i}{\hbar}\bar{\mu}_k \mathcal{E}(z,t)(n_{ek} + n_{hk} - 1) + \frac{\partial p_k}{\partial t}|_{collision} \tag{4.10}$$

Collisions result in the polarization decay, thus, $\frac{\partial p_k}{\partial t}|_{collision} \approx -\gamma p_k$ where $\gamma = 1/T_d$ is the decay rate and $T_d$ is the dipole lifetime.

### Dynamic evolution of material properties

Due to the effects of various collision mechanisms, the Fermi-Dirac distribution is retained in the system, allowing us to track the variation in $N$ via $\mu(N)$. We further make the assumption that the carrier density and the field envelope do not change significantly in time $T_d$. This means that $\mathcal{E}(z,t) \simeq \mathcal{E}(z)$ in Eqn. 4.10. Integrating this equation using the integrating factor $e^{(i\omega_k+\gamma)t}$ and making the rotating wave approximation we achieve:[f]

$$p_k(t) = -\frac{i}{2\hbar}\bar{\mu}_k \mathcal{E}(z) e^{i(Kz-\omega t-\phi(z))} \times [n_{ek}(t) + n_{hk}(t) - 1]\frac{1}{i(\omega_k - \omega) + \gamma} \tag{4.11}$$

Combining the classical and quantum description of $\mathcal{P}(z,t)$:[g]

$$\begin{aligned}\mathcal{P}(z) &= 2e^{-i[Kz-\omega t-\phi(z)]}\frac{1}{V_l}\Sigma_k \bar{\mu}_k^* p_k \\ &= -\frac{i\mathcal{E}(z)}{2\hbar\gamma V_l}\Sigma_k |\bar{\mu}_k|^2 [n_{ek}(t) + n_{hk}(t) - 1] \times \left(1 - i\frac{\omega_k - \omega}{\gamma}\right) f_{Lor}(\omega_k - \omega)\end{aligned} \tag{4.12}$$

[f] The full expression of $p_k(t)$ includes terms with $\frac{1}{i(\omega_k+\omega)+\gamma}$ and $\frac{1}{i(\omega_k-\omega)+\gamma}$. The rotating-wave assumption ignores the term with $\frac{1}{i(\omega_k+\omega)+\gamma}$ as this term is negligible in the optical frequecies.

[g] A summary of the mathematical language used in this formulation is given in Appendix H.

where $f_{Lor}(\omega_k - \omega) = \frac{\gamma^2}{\gamma^2+(\omega_k-\omega)^2}$. Since $\mathcal{P}(z) = \epsilon_b \chi(z)\mathcal{E}(z)$, the modified $\chi(z)$ follows:

$$\chi(z) = -\frac{i}{2\hbar\gamma\epsilon_b V_l}\Sigma_k|\bar{\mu}_k|^2[n_{ek}(t) + n_{hk}(t) - 1] \times \left(1 - i\frac{\omega_k - \omega}{\gamma}\right) f_{Lor}(\omega_k - \omega) \quad (4.13)$$

The function $f_{Lor}(\omega_k - \omega)$ has a Lorentzian shape. This function describes the homogeneous broadening process in semiconductor gain. Homogeneous broadening refers to the process where transitions of electrons from an upper level to a lower level occur at equal probabilities, leading to an increase in optical linewidths. The force behind homogeneous broadening is the various collision processes in semiconductors since they affect all carriers equally. However, in a semiconductor gain medium, homogeneous broadening is better described by a hyperbolic secant lineshape which avoids the effect of absorption below the bandgap: $\frac{\gamma^2}{\gamma^2+(\omega_k-\omega)^2} \rightarrow sech\left(\frac{\omega_k-\omega}{\gamma}\right)$ (See Fig. 4.3) [127].

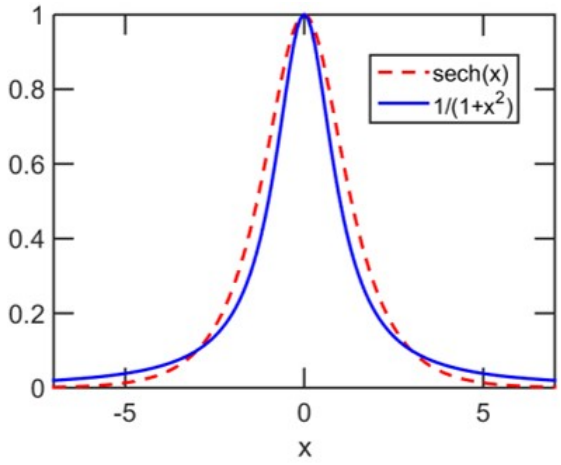



**Figure 4.3** – Lorentzian and Sech lineshapes.

Here, the quasi-equilibrium assumption dictates that $n_{ek} = f_{ek}$ and $n_{hk} = f_{hk}$. Equation 4.7 links the susceptibility, $\chi(z)$, to the gain coefficient:

$$g = \frac{\omega}{2\epsilon_0 n_s' c\hbar\gamma V_l}\Sigma_k|\bar{\mu}_k|^2[f_{ek}(t) + f_{hk}(t) - 1]sech\left(\frac{\omega_k - \omega}{\gamma}\right) \quad (4.14)$$

where $n_s'$ is the real part of refractive index of the semiconductor gain material. To do this sum over all $k$ states, assuming that our system is made up of a continuous distribution of energy levels. The summation over $k$ can be rewritten as $\frac{1}{V_l}\Sigma_k \rightarrow \int_0^\infty dED(E)$. To find the joint density of states $D(E)$ in 3D, we follow:

1. Volume of a $k$-state: $(2\pi/L)^3$ where $L$ is the typical length scale of the system.
2. The number of $k$-states in $k$-space: $\frac{4\pi k^2 dk}{(2\pi/L)^3} = \frac{V_l k^2 dk}{2\pi^2}$
3. The number of $k$-states per unit volume is: $D(E) = \frac{1}{2\pi^2}\left(\frac{2m_r}{\hbar^2}\right)^{3/2}\sqrt{E}$. Here, $m_r$ denotes the reduced electron-hole mass, defined as $\frac{1}{m_r} = \frac{1}{m_e} + \frac{1}{m_h}$.

Note that $[f_e(E) + f_h(E) - 1] = f_e(E) - (1 - f_h(E)) = f_e(E) - f_v(E)$. Here, the last equality sign implies that in the valence band, we only have filled states which are valence electrons and empty states which are holes.

In the case of GaAs, we have 3 valance bands and 1 conduction band, summing over all possible spin state transitions[h] [129–132] and averaging over polarization states, the gain coefficient can be calculated as [133]:

$$g = \frac{2\omega|\bar{\mu}|^2}{3n_s'\pi^2\epsilon_0 c\hbar\gamma}\left(\frac{2m_r}{\hbar^2}\right)^{3/2}\int_0^\infty dE'\sqrt{E'}\left[f_e(E') - f_v(E')\right] sech\left(\frac{E' + E_g - E}{\hbar\gamma}\right) \tag{4.15}$$

The dipole matrix has been assumed to be $k$-independent, $\bar{\mu}_k = \bar{\mu}$. Similarly, the carrier-induced refractive index change, $\delta n_{ind}$ can be found based on Eqn. 4.8 and 4.13. However, this calculation of $\delta n_{ind}$ is no longer accurate when the Lorentzian lineshape is replaced by a hyperbolic secant function. Nonetheless, we can make use of the inherent Kramers-Kronig relationship between the real and imaginary parts of a refractive index to compute $\delta n_{ind}$ [127]:

$$\Delta(\delta n_{ind}) = \frac{c}{\pi}P_v\int_0^\infty \frac{\Delta g(\omega')}{\omega'^2 - \omega^2}d\omega' \tag{4.16}$$

where $P_v$ signifies the principal-value integral.

### Calculation of quasi chemical potentials

The calculation of $g$ and $\delta n_{ind}$ relies on the estimation of the combined chemical potential of electrons and holes $\mu = \mu_e + \mu_h$. Both $g$ and $\delta n_{ind}$ are functions of $E$ and $N$. To see how a change in the carrier density affects $g$ and $\delta n_{ind}$, we need to calculate $\mu_e$ and $\mu_h$ corresponding to each value of $N$. The total carrier density, $N$ is

[h] This summation over all spin states requires the consideration of allowed optical transitions for each hole band (HH, LH and SO).

computed as $N = \frac{1}{V_l}\Sigma_k f_{ek}$. Using the joint density of states $D(E)$ described above, the summation over all $k$-states leads to:

$$\begin{aligned} N &= \int_0^\infty dE_\alpha D(E_\alpha) f_\alpha(E_\alpha) \\ &= \frac{1}{2\pi^2}\left(\frac{2m_r}{\hbar^2}\right)^{3/2} \int_0^\infty dE_\alpha \frac{\sqrt{E_\alpha}}{e^{\frac{\frac{m_r}{m_\alpha}E_\alpha - \mu_\alpha}{k_B T}} + 1} \end{aligned} \tag{4.17}$$

Here, the functional form of the Fermi-Dirac distribution has been modified to take into account the reduced electron-hole mass, $m_r$. The subscript $\alpha$ again denotes the carrier species. To achieve gain, the quasi chemical potentials must fall within the band of the respective carriers. Furthermore, the energy of a $k$-state above the bandgap can be rewritten as $E' = E + E_g$, where the extrema of the bands are used as reference points. Equation 4.17 then facilitates the conversion of a carrier density into a set of quasi Fermi levels.

### 4.1.4 Results and Discussion

#### Results of free carrier theory

Figure 4.4 summarizes the results on the gain available in GaAs based on Eqn. 4.15. The difference in the calculation of GaAs gain using hyperbolic secant function instead of a conventional Lorentzian lineshape is visible in Fig. 4.4(a,b). A Lorentzian lineshape tends to overestimate the effects of homogeneous broadening, giving a gain value lower than that of a sech function, especially in the region below the bandgap leading to a negative value of gain. As the carrier concentration number increases, the gain spectrum is significantly blue-shifted (see Fig. 4.4(c)). On the other hand, the dephasing rate, $\gamma$ does not seem to significantly modify the gain spectrum, as shown in Fig. 4.4(d).

Similarly, the results of our carrier-induced refractive index change using Eqn. 4.16 are presented in Fig. 4.5. The effects of both the hyperbolic secant lineshape and the higher dephasing rate are barely noticeable in our $\delta n_{ind}$ results shown in Fig. 4.5 (a,b). An increase in the carrier concentration leads to a downward translational shift and a blue-shift of the peak of the $\delta n_{ind}$ spectrum.

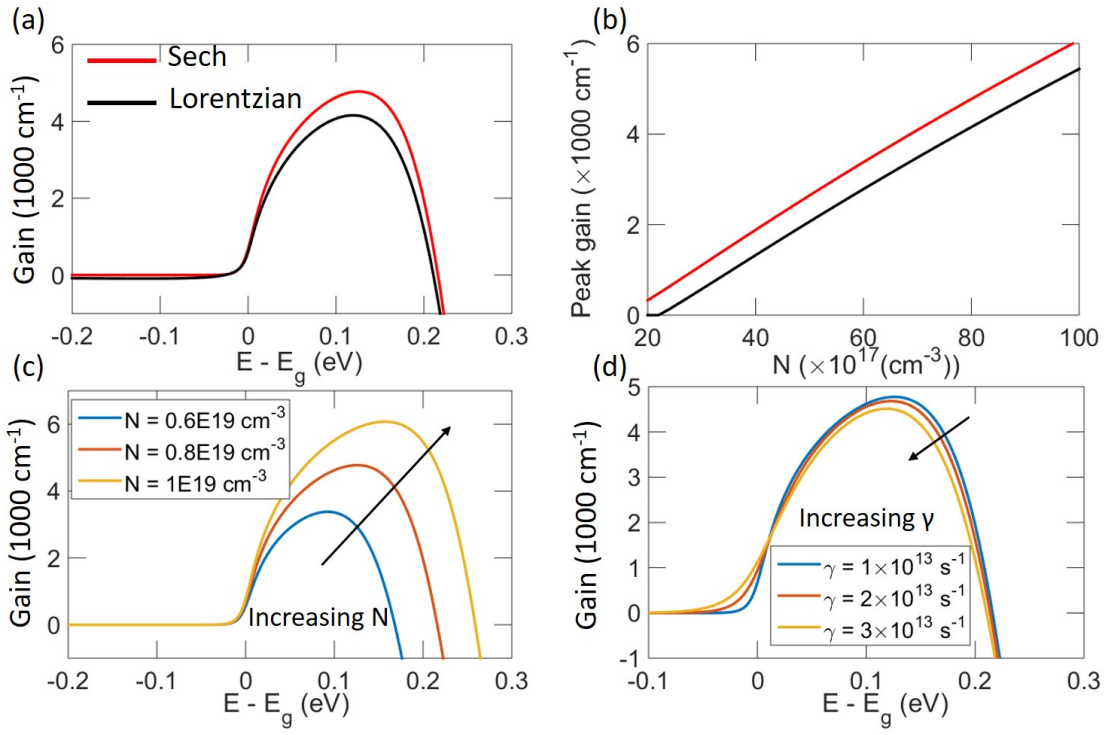



**Figure 4.4** – (a) Gain as a function of energy for the 2 lineshapes: hyperbolic secant function and Lorentzian function. $N = 8 \times 10^{18}$ cm$^{-3}$. (b) Peak gain as a function of carrier concentration N for the 2 aforementioned lineshapes. (c) Effect of increasing carrier concentration on the gain spectrum. (d) Effect of increasing dephasing rate on the gain spectrum. Here a sech lineshape was used and $N = 8 \times 10^{18}$ cm$^{-3}$. The material parameters are $m_e = 0.067\ m_0$, $m_h = 0.520\ m_0$, $E_g = 1.424$ eV and $\bar{\mu} = 0.473$ nm. $m_0 = 9.1 \times 10^{-31}$ kg: mass of a free electron.

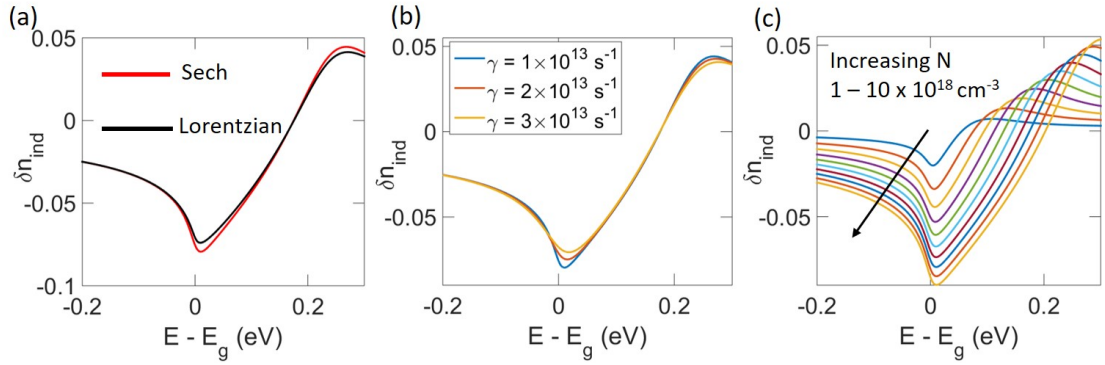



**Figure 4.5** – (a) Carrier-induced refractive change as a function of energy for the 2 lineshapes: hyperbolic secant function and Lorentzian function. $N = 8 \times 10^{18}$ cm$^{-3}$. (b) Effect of increasing dephasing rate on $\delta n_{ind}$ spectrum. $N = 8 \times 10^{18}$ cm$^{-3}$. (c) Effect of increasing carrier concentration on $\delta n_{ind}$ spectrum.

### Validity of the semiconductor gain theory

Next, we assess the accuracy of our simplified gain model by comparing our assumptions and results with a more sophisticated method detailed in [134]. This model assumes that the optical gain mechanism of GaAs involves the following three processes: band-filling effect, bandgap shrinkage and intraband absorption. For more information on the origin and effects of each process, the reader is referred to [134]. Here, only a concise summary of this model is given, outlining the relevant equations and assumptions.

When carriers are injected into a semiconductor medium, the lowest energy states in the conduction band are filled first. For semiconductors with low density of states, a significant depth of the band can be filled by a relatively small number of electrons. Thus, valence electrons require a much greater energy than $E_g$ to continue being promoted to the conduction band. Consequently, the absorption of photons with energies slightly larger than $E_g$ is reduced when free carriers are present, leading to a shift in the absorption edge. This effect is more significant in semiconductors with small bandgaps and effective masses [134].[i] The band filling effect, which can be described by the free carrier theory, assumes that there is no absorption below the bandedge. In reality, this phenomenon does occur due to the assistance of phonons, excitons and impurities. This absorption edge is called the Urbach tail. Therefore, these two methods tend to give an overestimated value of $\delta n_{ind}$ at high carrier concentrations $\approx 10^{19}$ cm$^{-3}$.

The second process stems from the many-body effect in an interacting Fermi sea. Bandgap shrinkage, also known as the renormalization effect, becomes noticeable when the wavefunctions of individual carriers start to overlap. In this regime, electrons repel each other due to Coulombic forces and the Pauli exclusion principle. These two phenomena combined give rise to the screening of electrons, together with a reduction in the energies of the conduction band edge. Figure 4.6 shows the magnitude of the bandgap shrinkage effect according to an analytic expression given in [134, 135] and

[i] An equivalent argument can be drawn for holes whose effective masses and density of states are larger than that of electrons.

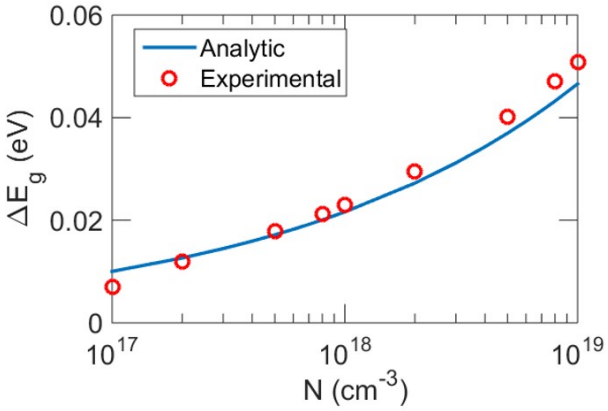



**Figure 4.6** – The analytic and experimental results of bandgap shrinkage effect in many-body interaction analysis.

a fitted experimental model [134]:

$$\begin{aligned} \text{Analytic:} \quad & \Delta E_g(N) = -\frac{e}{2\pi\epsilon_0\epsilon_s}\left(\frac{3}{\pi}\right)^{1/3} N^{1/3} \\ \text{Experimental:} \quad & \Delta E_g(N) = \frac{p_0}{\epsilon_s}\left(1-\frac{N}{N_{cr}}\right)^{1/3} \qquad \text{for} \quad N > N_{cr} \\ & \Delta E_g(N) = 0 \qquad\qquad\qquad\qquad\quad \text{for} \quad N < N_{cr} \end{aligned} \tag{4.18}$$

where $\epsilon_s$ is the permittivity of the semiconductor, $p_0 = 0.14$ is the fitting parameter and $N_{cr} \simeq 7 \times 10^{16}$ cm$^{-3}$ for GaAs and $e$ is the electron charge [134]. The cube-root dependence on $N$ of $\Delta E_g(N)$ does not hold for low carrier concentrations as in this regime, carriers are too far apart to generate significant correlation effects [134]. The analytic and experimental results of $\Delta E_g$ agree well with each other in the high $N$ regime.

The final physical process considered in this model is the intraband absorption. As its name suggests, this process takes into account optical transitions of carriers within their respective bands. This effect is enhanced at energies smaller than the bandgap. The influence of intraband absorption on the magnitude of $\delta n_{ind}$ is quantifies as: $\delta n_{ind} = -\frac{e^2\lambda^2}{8\pi^2c^2\epsilon_0 n_s'}\left(\frac{N_e}{m_e}+\frac{N_h}{m_h}\right)$.

All of the mechanisms described above are combined and this result is demonstrated in Fig. 4.7 for a range of carrier concentrations. The intraband absorption always

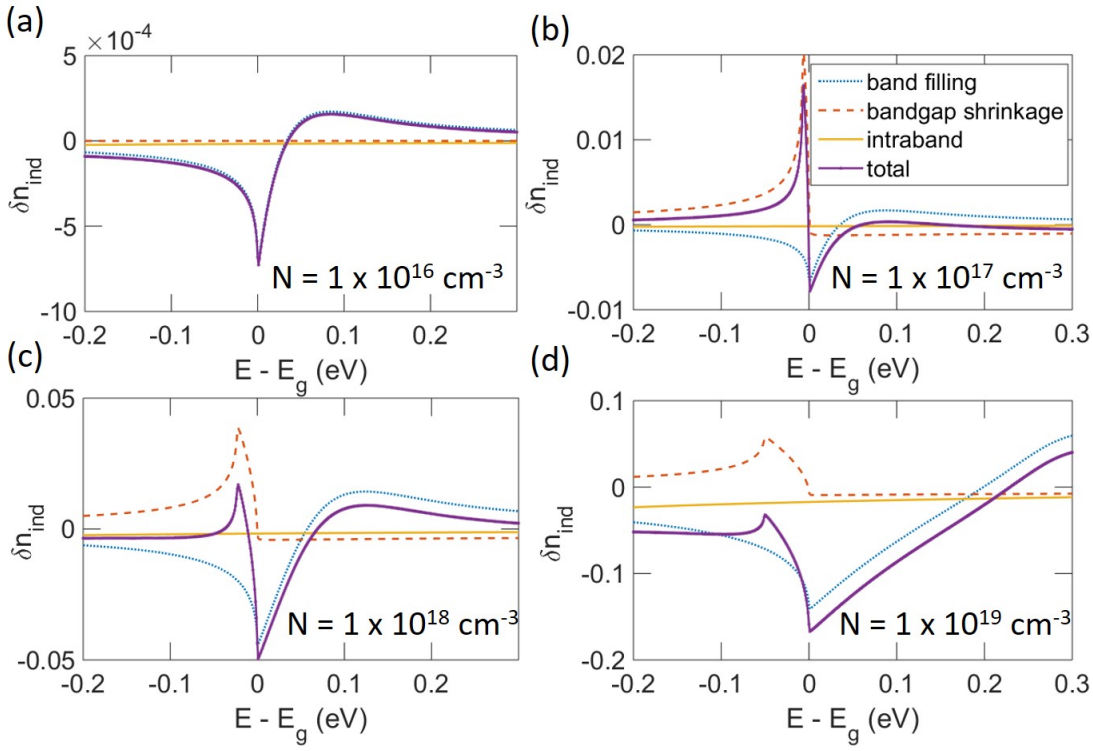



**Figure 4.7** – The independent effects on $\delta n_{ind}$ of band filling, bandgap shrinkage, intraband absorption and the sum of them all at (a) $N = 10^{16}$ cm$^{-3}$, (b) $N = 10^{17}$ cm$^{-3}$, (c) $N = 10^{18}$ cm$^{-3}$ and (d) $N = 10^{19}$ cm$^{-3}$.

takes negative values and stays fairly constant across the energy range of interest. On the other hand, the band filling and the bandgap shrinkage effects have dominant features around the bandgap region. At $N < N_{cr}$, the bandgap shrinkage effect is negligible (see Fig. 4.7(a)). At energies above the bandgap, we can clearly see that the most influential effect comes from the band filling process; the combination of all processes have most of the signature features of the band filling effect, especially in the high concentration regime, $N > 10^{18}$ cm$^{-3}$. Moreover, the spectrum of $\delta n_{ind}$ shown in Fig. 4.5(c) resembles closely those in Fig. 4.7(c,d) for energies above the bandgap. The calculated magnitude of $\delta n_{ind}$ also agrees with those experimentally measured in the literature [136, 137]. In conclusion, the description of the gain mechanism and the carrier-induced refractive index change in GaAs based on free carrier theory gives us results that do not only agree with more complicated modeling of gain materials but also align with experimental evidences in the energy range greater than the bandgap.

## 4.2 Loss compensation in lasing mechanism

The theory of the gain mechanism derived in the previous section allows us to calculate the amount of gain and its associated carrier-induced refractive index change obtained in bulk GaAs when carriers are injected into the semiconductor. However, to incorporate this analysis into the photonic device context, we need to understand the origin of device losses and furthermore how the number of carriers and photons dynamically evolves in the system. Lasers provide the appropriate platform for a discussion of loss compensation in photonic devices.

### 4.2.1 Cavity Modes

A typical example of a photonic cavity of length $L$ is a Fabry-Perot resonator consisting of a pair of parallel mirrors with a reflectivity, $R$, as shown in Fig. 4.8. The cavity is made up of a medium with a refractive index $n$. There are two relevant physical aspects of a Fabry-Perot cavity we need to consider: the longitudinal mode generation and the cavity loss [90].

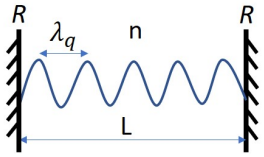



**Figure 4.8** – A typical laser cavity with length $L$ and mirror reflection $R$. An example of longitudinal modes is also shown with a period $\lambda_q$.

Every time a wave reaches either end of the cavity, part of it gets reflected, leading to the superposition of two counter-propagating waves. This phenomenon gives rise to the establishment of a set of standing waves. However, only those standing waves whose wavelengths are multiples of $2L$ are allowed to exist: $\lambda_q = \frac{2nL}{q}$, where $q$ is an integer. These standing waves in turn become the basis of a set of longitudinal modes with discrete frequencies. The spacing between 2 consecutive longitudinal modes of an optical cavity follows:

$$\Delta\nu = \frac{c}{2nL} \tag{4.19}$$

As the reflectivity of the mirrors is not 100%, this represents a form of loss in the

system. The point at which the gain provided by the active medium fully compensates the cavity loss defines the gain threshold for lasing:

$$\alpha_{th} = -\frac{1}{L} ln(R) \tag{4.20}$$

Thus, $\alpha_{th}$ is inversely proportional to the length of the cavity. While longitudinal modes of a laser system have been defined as a set of standing waves, the transverse mode refers to the particular distribution of the field in the direction perpendicular to the propagation direction, also known as the waveguide mode. The transverse mode propagating between the mirrors can also be lossy with a modal loss $\alpha_{mode}$; this modifies the threshold gain condition of the cavity:

$$\alpha_{th} = \alpha_{mode} - \frac{1}{L} ln(R) \tag{4.21}$$

A guiding structure and an active medium together with an appropriate feedback mechanism make up the essential components of a laser system.

### 4.2.2 Einstein A and B coefficients

A detailed description of the gain mechanism in semiconductor materials was outlined in Section 4.1. Here, we consider a phenomenological treatment of the basic interactions between light and matter to understand the fundamental macroscopic observations of a typical laser [138].

The interaction between an optical field and electrons takes the form of optical absorption and emission. Regardless of the nature of the electrons, an optical absorption and transmission of a photon involves a resonant transition of an electron between a lower energy $E_1$ and an upper energy, $E_2$. Considering the simplest case of a two-level energy system, this transition has a frequency defined as: $\omega = \frac{E_2 - E_1}{\hbar}$.

According to Einstein, there are three possible optical processes occurring between two energy levels that can influence the electron number: absorption, spontaneous emission and stimulated emission. Each process is associated with a transition rate.

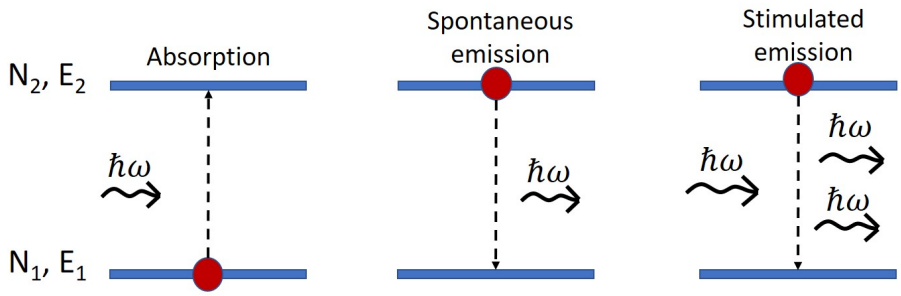



**Figure 4.9** – Two-level energy system: lower energy level $E_1$ with a carrier density $N_1$ and higher energy level $E_2$ with a carrier density $N_2$. Three optical transition processes: absorption, spontaneous emission and stimulated emission. The red circles represent electrons while the curled arrows indicate photons.

The key assumption here is that these rates are proportional to the carrier density of the initial state of a particular optical transition. The schematic sketches of these three processes are given in Fig. 4.9. We can see that stimulated emission and absorption require the presence of an optical field with a field density $U(\omega)$. The physics behind spontaneous emission can be understood in a similar way by treating this optical field as vacuum fluctuations. While spontaneous emission is allowed by energy conservation, the opposite process, spontaneous absorption, is forbidden. Note here that the photon emitted via stimulated process has identical phase, frequency, polarization and propagation direction with those of the incident photon, leading to the generation of coherent light in a laser. The following equation shows the dependence of each of the transition rates on the carrier and field densities:

$$\begin{aligned} \text{Absorption} \quad & R_{12} = B_{12}U(\omega)N_1 \\ \text{Spontaneous emission} \quad & R_{21,sp} = A_{21}N_2 \\ \text{Stimulated emission} \quad & R_{21,st} = B_{21}U(\omega)N_2 \end{aligned} \tag{4.22}$$

where $A_{12}$, $B_{21,12}$ are the well-known Einstein coefficients. A full quantum mechanical treatment is required to derive these coefficients from first principle. The focus of the next section is only to find an interdependent relationship between these coefficients.

Assume that there are two and only two energy levels in this system. Thus, the total number of available electrons is simply: $N = N_1 + N_2$ and an electron can only

reside in either one of the two levels. All the above optical processes affect the number of electrons in the system temporally. At any time $t$, an increase in the number of electrons in one level must equal to a decrease in the number of electrons in the other level, leading to the rate equation:

$$\frac{dN_1}{dt} = -\frac{dN_2}{dt} = A_{21}N_2 + B_{21}U(\omega)N_2 - B_{12}U(\omega)N_1 \tag{4.23}$$

The carrier concentration becomes time-independent in steady state, hence, Eqn. 4.23 is equal to zero. Furthermore, the occupation of a two-level system obeys the Boltzmann distribution—an approximation of the Fermi-Dirac distribution in the classical regime:

$$\frac{N_1}{N_2} = \frac{g_1 e^{-E_1/k_B T}}{g_2 e^{-E_2/k_B T}} = \frac{g_1}{g_2} e^{\hbar\omega/k_B T} \tag{4.24}$$

where $g_1$ and $g_2$ denote the degeneracy of the two energy levels. Rearranging Eqn. 4.23 and substituting for $N_1$ and $N_2$, we obtain the following expression of $U(\omega)$:

$$U(\omega) = \frac{A_{21}}{(\frac{g_1}{g_2} e^{\hbar\omega/k_B T})B_{12} - B_{21}} = \frac{\hbar\omega^3}{\pi^2 c^3} \frac{1}{e^{\hbar\omega/k_B T} - 1} \tag{4.25}$$

The second equality sign corresponds to the expression of the spectral density of the electromagnetic radiation of a black body at a given temperature according to Planck's law. Equating the components of Eqn. 4.25, we achieve the following relationship: $g_1 B_{12} = g_2 B_{21}$ and:

$$A_{21} = \frac{\hbar\omega^3}{\pi^2 c^3} B_{21} \tag{4.26}$$

### 4.2.3 Rate Equations

Stimulated emission is required for lasing action as this process generates coherent photons. Furthermore, to reach the lasing threshold, the stimulated process must dominate the spontaneous emission which emits photons at random intervals and the optical absorption which represents a loss channel for photons. The dominance of stimulated emission in turn demands the occurrence of a population inversion—referring to the state of a system which has more electrons in the upper energy level than in the lower one.

In a simple two-level system, a population inversion cannot be achieved. This is because the probabilities of promoting an electron from the ground state to the excited state and the decay of an electron from the excited state to the ground state via the absorption/emission of a photon are exactly identical. In other words, at best we can only achieve the situation where the occupation number of the two levels are equal.

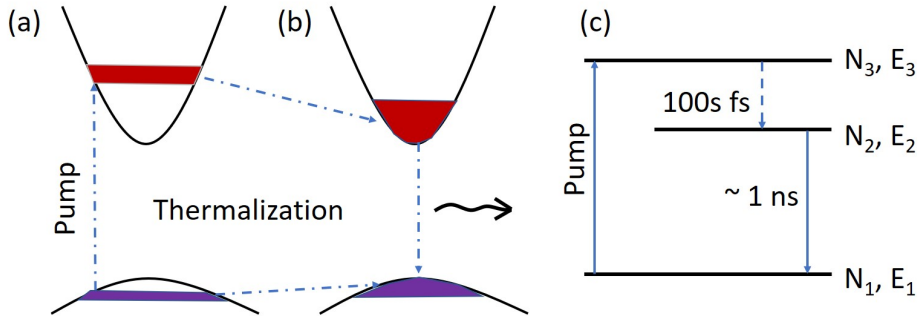



**Figure 4.10** – (a) Excitation of electrons from the valence to the conduction band via the absorption of photons. (b) Thermalization of hot electrons to the band edge in hundreds of femtoseconds. Interband transitions occur in nanosecond time scale. (c) 3-level energy system. $E_3$ states have much shorter lifetime than that of $E_2$ states.

To obtain the demanded population inversion, we require a system of three energy levels or more. Electrons in a semiconductor gain medium of a simple conduction-valence band structure can be excited to higher energy levels either electrically or optically. These excited electrons then relax to the bottom of the conduction band via thermalization. Finally, thermalized electrons decay to the valence band via photon emissions. The finite spectral width of the pump and the effect of homogeneous broadening lead to the emission of photons with a group of frequencies rather than a single frequency defined by $E_2 - E_1$ (See Fig. 4.10(a,b)). Thermalization occurs in 100s femtosecond time scale while interband transition occurs in nanoseconds, 10,000 times slower than the intraband processes. This difference in transition rates implies that such a semiconductor gain medium can be effectively described as a 3-level system depicted in Fig. 4.10(c). In a 3-level system, electrons are pumped from the ground state with an energy $E_1$ to an excited state with an energy $E_3$. However $E_3$ states are short-lived and quickly decay to $E_2$ where the electrons are accumulated.

The exchange of electrons amongst the three levels of energy is governed by a set

of coupled rate equations:

$$\begin{aligned}
\frac{dN_3}{dt} &= P_p N_1 - A_{32}N_3 - A_{31}N_3 \\
\frac{dN_2}{dt} &= A_{32}N_3 + BU(\omega)N_1 - A_{21}N_2 - BU(\omega)N_2 \\
\frac{dN_1}{dt} &= A_{31}N_3 + A_{21}N_2 + BU(\omega)N_2 - P_p N_1 - BU(\omega)N_1
\end{aligned} \tag{4.27}$$

where $P_p$ signifies the pump rate and $B$ again denotes the stimulated emission rate. The occupation number of any level is a result of the difference between electrons injected into that level and those decaying from it through various processes. For electrons to accumulate in level 2, we require $A_{32} > A_{21}, A_{31}$. When the fraction of population in level 2 reaches 50% or more of the total electrons in the system, $N = N_1 + N_2 + N_3$, we achieve the state of population inversion. To further relate the exchange of electrons amongst energy levels with the gain in bulk semiconductors described in Section 4.1.4, we simplify our gain model result to a simple linear model:

$$g(N) = G_0(N - N_0) \tag{4.28}$$

where $G_0$ is the gain coefficient and $N_0$ is the carrier concentration at transparency. The approximately linear relationship between the peak gain and the carrier concentration, shown in Fig. 4.4(b), justifies the application of such a simple phenomenological gain model.

### 4.2.4 Modified light-matter interactions in cavities

Fermi's Golden Rule is often used to calculate the transition rate from an initial state $|i\rangle$ to a final state $|f\rangle$ in the continuum by employing time-dependent perturbation theory. The detailed derivation of Fermi's Golden rule can be found in many standard textbooks [139, 140]; here we only quote the final result of this well-known rule:

$$R_{Fermi} = \frac{\pi}{2\hbar^2} e^2 |\bar{\mu}_{if}|^2 |\mathcal{E}_0|^2 \rho(\omega_{if}) \tag{4.29}$$

The perturbation of the original Hamiltonian originates from the dipole interaction between the atomic polarization and the incident electric field. The magnitude of this

dipolar perturbation is proportional to $\bar{\mu}_{if}$, the dipole matrix element of this particular transition and $\mathcal{E}_0$, the magnitude of the electric field. Here, $\omega_{if} = (E_f - E_i)/\hbar$. The continuum includes all possible directions and polarizations that a photon can be emitted into. Thus, the calculation of the transition rate, $R_{Fermi}$, must take into account the number of optical states that exist at $\omega_{if}$, denoted by $\rho(\omega_{if})$.

The transition rate of stimulated emission can be calculated according to Fermi's Golden rule using the assumption that there is only a single final state $\rho(\omega) = 1$:

$$BU(\omega) = \frac{1}{3}\frac{\pi}{2\hbar^2}e^2|\bar{\mu}_{if}|^2|\mathcal{E}_0|^2 \tag{4.30}$$

where $U(\omega) = \frac{1}{2}\epsilon_0\epsilon|\mathcal{E}_0|^2$ is the time averaged optical energy density in the stimulating mode in a medium with permittivity $\epsilon$. The factor $1/3$ is included to average out the three possible orientations of the dipole. Equating both sides of Eqn. 4.30, we have:

$$B = \frac{\pi e^2}{3n^2\epsilon_0\hbar^2}|\bar{\mu}_{if}|^2 \tag{4.31}$$

where $n = \sqrt{\epsilon}$ is the refractive index. We can now derive an expression for the spontaneous emission rate between these two energy levels using Eqn. 4.26:

$$A = \frac{\hbar\omega^3}{\pi^2c^3}B = \frac{ne^2\omega^3}{3\pi\epsilon_0^3}|\bar{\mu}_{if}|^2 \tag{4.32}$$

In a closed cavity, we have well-defined cavity walls. These walls put certain constraints on how the density of optical states is calculated. First of all we take a look at how the optical density of states is calculated in free space. The volume of a K-state is $V_K = (2\pi/L)^3$. In a spherical shell in K-space of volume $V_0 = 4\pi K^2 dK$, the number of K-states that exist in a unit volume is $(2V_0/V_K)/V = \frac{K^2dK}{\pi^2}$ where the factor of 2 accounts for the two polarizations. The effect of a cavity on the transition rate is two-fold. Firstly, the reduced volume affects the way the electric energy density is defined in a cavity. Assuming that a single photon occupies the cavity, we arrive at:

$$UV_l = 2U_EV_l = \frac{\epsilon_0\epsilon|\mathcal{E}_0|^2}{2}V_l = \hbar\omega \tag{4.33}$$

where $V_l$ is now the cavity volume. Rearranging Eqn. 4.33, the expression of the magnitude of the electric field in a cavity is modified as: $|\mathcal{E}_0|^2 = \frac{2\hbar\omega}{\epsilon_0 \epsilon V_l}$. Secondly, a reduced volume also affects the density of an optical state but in a more abstract way, requiring the consideration of the spectral width of a cavity mode in our calculation. Assuming that the cavity only supports a single mode, the spectral distribution of a cavity mode has a Lorentzian shape:

$$\rho(\omega) = \frac{\gamma/2\pi}{(\omega - \omega_0)^2 + \gamma^2/4} \tag{4.34}$$

where $\gamma^{-1}$ is the cavity lifetime. At $\omega = \omega_0$, the expression of $\rho(\omega_0)$ on resonance becomes: $\rho_{\omega=\omega_0} = \frac{2Q}{\pi/\omega_0}$ where $Q = \omega_0/\gamma$ the quality factor (or Q-factor) of the cavity. The modifications of the electric field and the density of states are factored into the original expression of the transition rate. Substituting these corrected terms into Eqn. 4.29, we achieve the well-known Purcell factor, $F_p$ which describes how the spontaneous emission rate, $A$ is enhanced in a cavity, $A_{cavity}$ [141]:

$$\frac{A_{cavity}}{A} = F_p = \frac{3\lambda^3 Q}{4\pi^2 n^3 V_l} \tag{4.35}$$

Now the question is how this enhanced spontaneous emission rate changes when we consider an emitter in a waveguide. One of the key differences between a cavity and a guiding structure is that in a waveguide, the field is not distributed uniformly across its geometric extent but concentrates mainly in the core. Thus, the energy density can be redefined as:

$$U = \frac{1}{2}\epsilon(z_0)\epsilon_0|\mathcal{E}_0|^2 = \frac{\hbar\omega}{A_m L} \tag{4.36}$$

where $z_0$ indicates the position of the emitter within the waveguide. Note here that the volume of the field has been modified to include the modal area $A_m$. Next we take a look at the correction to the density of states in the context of a waveguide. We need to find the optical density states for the case where the system is confined in 2D and thus the region of interest becomes a thin length in K-space. The dependence of $K$ on $\omega$ takes the form of $K(\omega) = n_m(\omega)\omega/c$ where $n_m$ is the effective refractive

index of the waveguide mode. Thus, the modified density of states is expressed as:

$$\rho(\omega) = 2\frac{dK(\omega)}{d\omega}\frac{L}{2\pi} = \frac{n_g L}{\pi c} \tag{4.37}$$

where $n_g = \frac{d[\omega n_m(\omega)]}{d\omega}$ is the group index and the factor of 2 accounts for two possible directions along a line. Similarly, we can substitute these modified terms into Eqn. 4.29, giving rise in another expression of the Purcell factor:

$$\frac{A_{emitter+WG}}{A} = F_p = \frac{n_g}{\pi n \epsilon(z_0)}\frac{(\lambda/2)^2}{A_m} \tag{4.38}$$

Equations 4.35 and 4.38 clearly indicate the inverse relationship between the enhancement of spontaneous emission and the relevant geometrical extent of the structure, i.e., the area of the waveguide mode or the volume of the cavity. Thus, small cavities and well confined modes will give rise to a large spontaneous emission enhancement. We also see that this enhancement is proportional to the Q-factor of a cavity: the higher quality a cavity is engineered, the larger the spontaneous emission enhancement it can generate. As the coefficient $A$ is always linked to $B$, the Purcell effect consequently leads to an enhancement of the stimulated emission.

Another factor that can modify the spontaneous emission rate between two energy levels is the spontaneous emission factor, $\beta$-factor, denoted as $\beta_f$. $\beta_f$ defines the ratio between the spontaneous emission into the desired mode and the emission into all other modes [142–144]. A value of $\beta_f = 1$ corresponds to the situation where all the emitted light goes into the desired mode. The effect of $\beta_f$ can be analyzed using a simple 2-level system which is placed inside a cavity with a cavity loss $\gamma_c$, equivalent to a cavity lifetime of $1/\gamma_c$. We further make the assumption that carriers only stay in the lower level briefly, hence $N_1 = 0$ and $N = N_2$. Making use of the linear gain model described in Eqn. 4.28 together with a constant pump rate, we achieve the following coupled rate equations:

$$\begin{aligned} \frac{dN}{dt} &= P_p - \beta_f A_{21} S(N - N_0) - A_{21} N \\ \frac{dS}{dt} &= \beta_f A_{21} S(N - N_0) + \beta_f A_{21} N - \gamma_c S \end{aligned} \tag{4.39}$$

where $S$ is the number of photons in the cavity. Assuming steady-state conditions, we can find the explicit relationship between $S$ and $N$. Figure 4.11 plots the dependence of the photon number and the upper state occupation number on the pump rate for four different values of $\beta_f$.

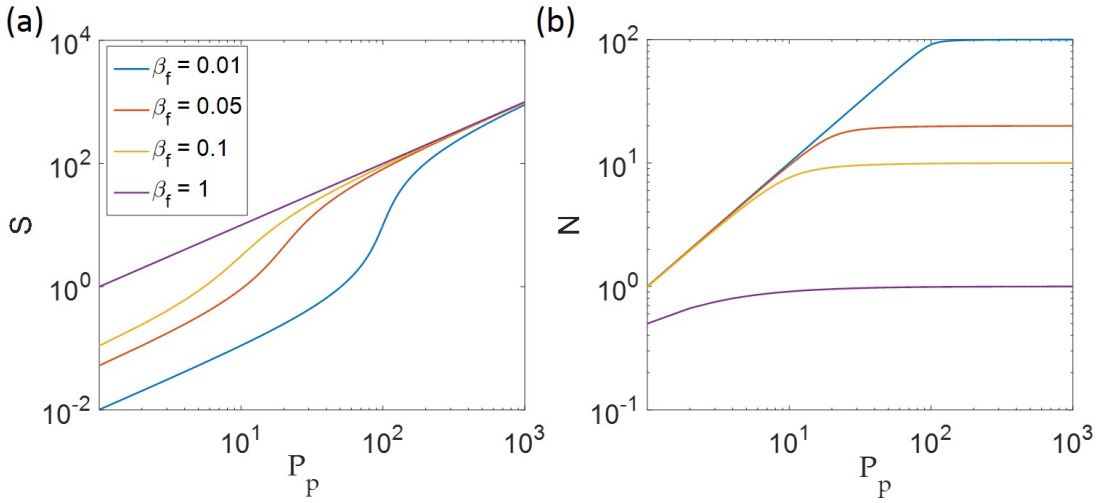



**Figure 4.11** – (a) The dependence of the photon number on the pump rate for various values of $\beta_f$. (b) The dependence of the upper state occupation on the pump rate for various values of $\beta_f$. Note here that all constants in Eqn. 4.39 take a value of 1 and $N_0 = 0$.

Laser cavities built upon photonic waveguides often have very low $\beta_f \lesssim 10^{-2}$ [145, 146] while plasmonic ones tend to have higher emission into the desired mode, hence higher $\beta_f > 10^{-2}$. This is because plasmonic modes are in general more confined than their photonic counterpart. The log-log plot shown in Fig. 4.11(a) clearly demonstrate the kink signature in most lasers where the laser output shoots up at threshold. This superlinear behaviour is an indication of the dominance of stimulated emission over spontaneous emission when lasing action starts occurring. However, as $\beta_f$ increases, the transition becomes less visible and when $\beta_f = 1$, any threshold-related behaviour totally disappears. This high $\beta_f$ regime is often referred to as thresholdless lasing [147, 148]. Figure 4.11(b) shows the corresponding behaviour of the upper state occupation. At threshold, we observe a phenomenon called gain clamping where $N$ reaches a plateau even though the material is continuously being pumped. The $N - P_p$ plot can also be used to identify the lasing threshold. As $\beta_f$ increases, the appearance of a threshold-kink becomes smoother in the $N - P_p$ plot. Thus, even when the kink signature disappears in $S - P_p$ plot for $\beta_f = 1$, a threshold

can still be defined based on gain clamping.

## 4.3 Summary

We introduced in this chapter a gain model based on the free carrier theory and used Kramers-Kronig relations to estimate the carrier-induced refractive index change as a function of carrier concentration in bulk GaAs semiconductor. Our gain model approximated the lineshape function as a hyperbolic secant distribution in order to remove absorption below the bandgap. Taking into account the spin-orbit interaction, the result of our modified free carrier theory agreed with those of other complicated models and also experimental measurements for energies above the bandgap. This is because in this energy regime the band filling is the dominating effect. The mathematical formulation of the gain coefficient and the carrier-induced refractive index change at different values of carrier concentration allows us to apply this knowledge to the analysis of high loss plasmonic lasers (Chapter 5) and to the correction mechanism of dispersion effects in parity-time symmetric coupled waveguides (Chapter 6).

The loss compensation mechanism in the context of lasers was also discussed. A waveguide can be turned into a laser when a gain medium is supplied and sufficient feedback is provided. The analysis of lasing action in this chapter focused on deriving the coupled rate equations which governed the dynamics of photons and carriers in a cavity. The modification of the spontaneous emission of light in a cavity was shown to depend on the cavity feedback and the area of the transverse mode. The interrelated relationship between the spontaneous and stimulated emissions meant that the stimulated process, which gave rise to a population inversion, also experienced this enhancement. The superlinear increase in the upper level occupation number with increasing pump power signified a lasing threshold. This signature kink in the laser behaviour became less prominent as the $\beta$-factor—the fraction of emission into the laser mode—approached unity.

# Chapter 5

# GaAs based HGPW nanolasers

This chapter explores the viability of hybrid plasmonic-photonic nanolasers constructed on a suspended GaAs core layer. We begin the chapter with an overview of the construction of these GaAs nanolasers based on the hybrid gap plasmon waveguide (HGPW). This hybrid plasmonic design has superior modal properties for laser applications compared to other plasmonic waveguide designs, including the flexibility in designing channels to access the gain material, the ease in modifying modal profile for different applications and the compatibility with standard photonic substrates. Next, the fabrication process of this novel laser design is detailed, showcasing the advantages of a well controlled top-down fabrication approach. This top-down fabrication technique does not only overcome common problems associated with bottom-up fabrication, such as a lack of control over device quality and positioning [31,32,102,149,150], but also avoids issues of in-situ etching of the semiconductor gain element and of using metallic substrates [151].

The next section of the chapter describes the characterization and the analysis of the nanolasers. Finally, results and discussions are presented where the simple III-V gain model described in Chapter 4 is employed to examine the threshold gain conditions and their associated dispersion effects for the various nanolaser designs considered [152].

# 5.1 Device design: HGPW-based cavity

## 5.1.1 Waveguide and taper construction

GaAs was chosen as the gain medium due to its high gain property and direct bandgap in the near infrared spectrum. However, the epitaxy growth technique for III-V semiconductors requires that semiconductors have to be lattice matched with their substrates, limiting the choice of materials for the substrate. Furthermore, a HGPW design requires this substrate to have a low refractive index, as described in Chapter 3. To satisfy both the lattice and the index criteria, suspended GaAs membranes were used as the core layer for this HGPW-based cavity. Au was chosen over Ag as the plasmonic material due to its higher stability when operating at room conditions (Section 3.2).

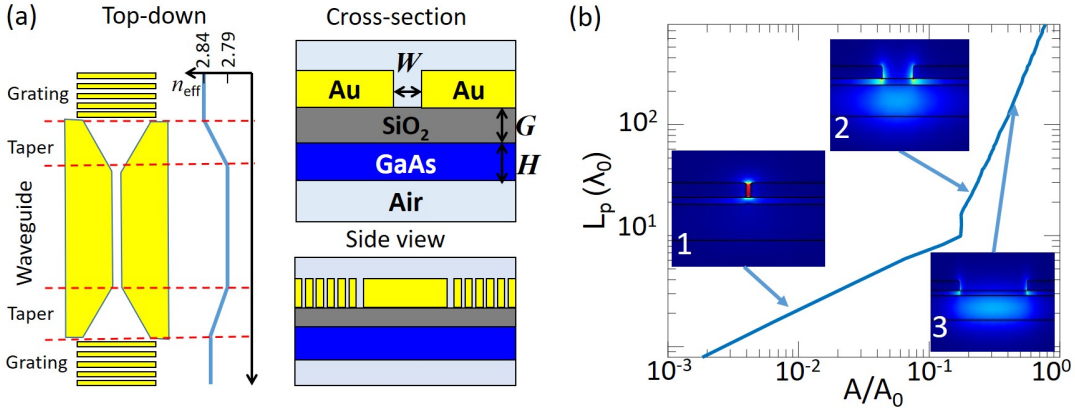



**Figure 5.1** – (a) Top-down view of a HGPW laser with 3 main sections: waveguide, taper and grating. Correspondingly shown is the effective refractive index of the TE fundamental hybrid mode along the structure axis. Also shown in (a) are the side view and cross-section of the fabricated design. (b) Propagation length as a function of modal area for a range of gap width W = 5-3000 nm with H = 100 nm and G = 20 nm. Insets 1, 2, 3 show the electric field distribution of HGPW mode of W = 10 nm, 195 nm and 800 nm respectively. $\lambda_0 = 850$ nm [152].

Figure 5.1(a) depicts three viewing angles of the device. The taper sections aim to mitigate the modal mismatch arising from the abrupt termination of the waveguide. This adiabatic guiding of the hybrid mode reduces the back scattering and diffraction of fields while maintaining a close enough effective index to that of the waveguide mode [35, 107] ($n_{eff,HGPW} = 2.79$ and $n_{eff,grating} = 2.84$). Feedback is provided by

two sets of metallic DBRs (Distributed Bragg reflectors) placed at both ends of the waveguide. Metallic gratings were chosen to simplify the fabrication process.

Figure 5.1(b) shows the vacuum wavelength normalized propagation length, $L_p(\lambda_0)$ versus the normalized modal area, $A/A_0$, for a gap width range of W $= 5 - 3000$ nm. The modal area was defined according to Eqn. 3.5 and $A_0 = \lambda_0^2/4$. With reference to the field distributions in the insets of Fig. 5.1(b), it is clear that similar to Fig. 3.6(a) the increase in propagation length at larger gap widths can be attributed to a larger contribution of the photonic-like component to the hybrid mode.

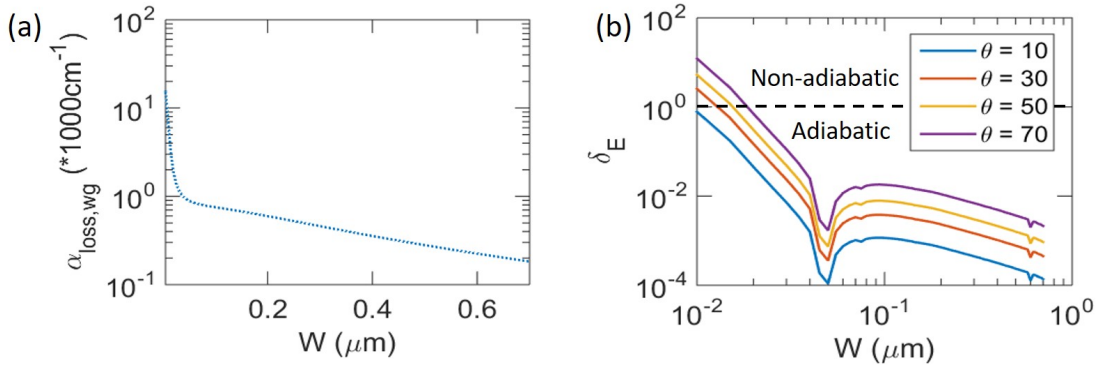



**Figure 5.2** – (a) Modal loss of the fundamental HGPW mode as a function of gap width. (b) Eikonal value as a function of gap width for different taper angles (shown in degrees).

The relationship between the modal loss, $\alpha_{loss,wg}$ and W is plotted in Fig. 5.2(a). Here $\alpha_{loss,wg} = 2|\Im\{n_{eff}\}|K_0$ where $n_{eff}$ is the effective index of the hybrid mode and $K_0 = 2\pi/\lambda_0$. The analytic expression of $\alpha_{loss,wg}$ can be found in Appendix G. The distinction between the plasmonic-like and the photonic-like regimes is manifested by a change in slope gradient at W $\approx$ 50 nm. Beyond this width, the modal loss decreases gradually with increasing gap width. The design of the taper angle must meet the requirement of the adiabatic guiding condition. Figure 5.2(b) describes the dependence of the Eikonal parameter, $\delta_E$, on W for various angles [34, 153]. The Eikonal is defined as:

$$\delta_E = \frac{1}{K_0}\left|\frac{d\Re(\beta(z))^{-1}}{dz}\right| \tag{5.1}$$

where $\beta = n_{eff}K_0$. Adiabatic guiding is ensured when $\delta_E < 1$. For this particular HGPW configuration, unless the gap width goes down to sub 20 nm, the adiabatic condition is always met for a wide range of tapering angles.

A waveguide width in the region of 195 nm was chosen. In this regime, the modal property is dominated by the photonic characteristics while the crossover to dominantly plasmonic mode only occurs at W $\approx$ 25 nm [35], leading to a large overlap between the fundamental mode and the gain medium. The relatively larger gap width also allows an efficient optical pumping mechanism (Section 5.3) to be incorporated into the measurement system.

### 5.1.2 DBR design

The two most important variables when it comes to designing a DBR is the pitch of the grating and the filling factor (FF).[a] There are many excellent descriptions of DBRs used in lasing applications in the literature [86, 93, 154]. Also, the physics of DBR operation based on coupled mode theory can be found in Section 2.4.1 and Appendix B.4.

The central wavelength of a DBR's reflection spectrum follows the relationship: $\Lambda = \lambda_0/2n_{eff}$ where $\Lambda$ is the period of the DBR. Thus, for a GaAs gain spectrum covering the wavelength range 800 - 900 nm, the range of $\Lambda$ of interest is: 140 - 160 nm when $n_{eff} = 2.79$ for the HGPW of $W = 195$ nm. In this particular configuration, the reflectivity of metallic DBRs also depends on how far they are positioned away from the GaAs core. While the HGPW mode is constrained by $G_{critical}$,[b] the DBRs could be brought closer to the GaAs core to increase the reflectivity. This separation between the DBRs and the GaAs core is denoted as S to distinguish from the separation between the waveguide and the GaAs core, G.

Figure 5.3 summarizes the dependence of DBR spectra on $\Lambda$, FF and the number of metallic bars, $N_b$. Regardless of the values of $\Lambda$ or FF, higher $N_b$ values always lead to a higher peak reflectivity of the DBRs and a narrower bandwidth of the reflectivity spectrum. Even though an increase in FF does give rise to a slight blue shift of the reflection spectra and a reduction in the peak reflectivity, the major factor that determines the spectral position of a DBR is its period. It is clear that, the reflectivity spectrum blue-shifts with smaller periods. Accompanying this blue-shifting behaviour

[a] FF is expressed as a ratio of the grating period. For example: for $\Lambda = 150$ nm and FF = 0.5, the width of the metallic bar is 75 nm.

[b] $G_{critical}$ is the cutoff spacer thickness of a HGPW mode introduced in Section 3.2.2.

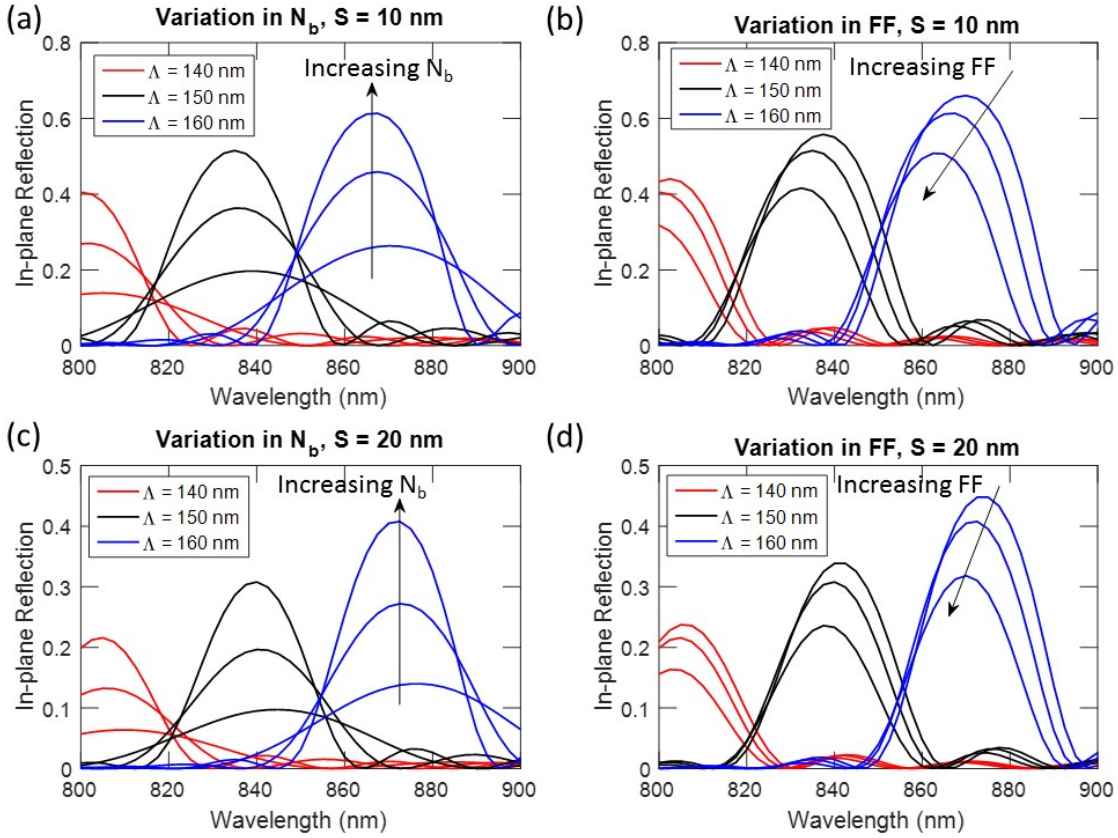



**Figure 5.3** – Spectral shift in reflectivity of metallic DBRs for various combinations of spacer thicknesses (G = 10 nm for 2-step devices and G = 20 nm for 1-step devices), number of metal bars, filling factor (FF) and different grating periods. (a) S = 10 nm, FF = 0.5, $\Lambda = 140 - 160$ nm, $N_b = 15, 20, 25$ bars (b) S = 10 nm, $N_b = 20$ bars, $\Lambda = 140, 150, 160$ nm, FF = 0.4, 0.5, 0.6. (c) S = 20 nm, FF = 0.5, $\Lambda = 140, 150, 160$ nm, $N_b = 15, 20, 25$ bars (d) G = 20 nm, $N_b = 20$ bars, $\Lambda = 140, 150, 160$ nm, FF = 0.4, 0.5, 0.6.

is a reduction in the peak magnitude of the DBR reflectivity. Figure 5.3(a,b) show the results of S = 10 nm and Fig. 5.3(c,d) display those of S = 20 nm. Clearly, the closer the DBRs are to the GaAs layer, the higher the index contrast between the filled (metallic bars) and un-filled parts within one period, resulting in a higher peak reflectivity for a given period, FF and $N_b$.

## 5.2 Fabrication process

For a good overlap with the gain medium, we chose W ≈ 195 nm, giving a mode overlap with the GaAs core region of ≈ 80%,[c] a modal area of $\approx 0.048\lambda_0^2$ and a modal

[c]The analytic expression of the modal overlap is given in Appendix G.

loss of $\approx 620$ cm$^{-1}$ at $\lambda_0 = 850$ nm.

The fabrication process of the GaAs HGPWs is summarized in Fig. 5.4(a). Etch windows were created using reactive ion etching with a $SiCl_4$/Ar plasma, following by 40% HF etching of a sacrificial 2 $\mu m$ thick $Al_{0.65}Ga_{0.35}As$ layer to create 100 nm thick suspended GaAs membranes. The size of the undercut regions was kept to about 25 x 20 $\mu m$ to ensure membrane integrity. However, these dimensions put a limit on the size of the grating and the cavity that could be fabricated on the membranes.

The problem of surface recombination in the exposed thin suspended GaAs membrane was overcome by growing two 5 nm thick InGaP layers either side of the GaAs membrane during MBE (Molecular Beam Epitaxy) [31,32].[d] In Fig. 5.4(b), photoluminescence (PL) intensities as a function of pump power were plotted for the bulk and membrane regions of passivated and unpassivated samples. PL yields were observed to improve by more than 2 orders of magnitude for the passivated GaAs membranes. In particular, the emission from passivated bulk and passivated membrane regions attained similar PL compared to an order of magnitude difference when both were left unpassivated.

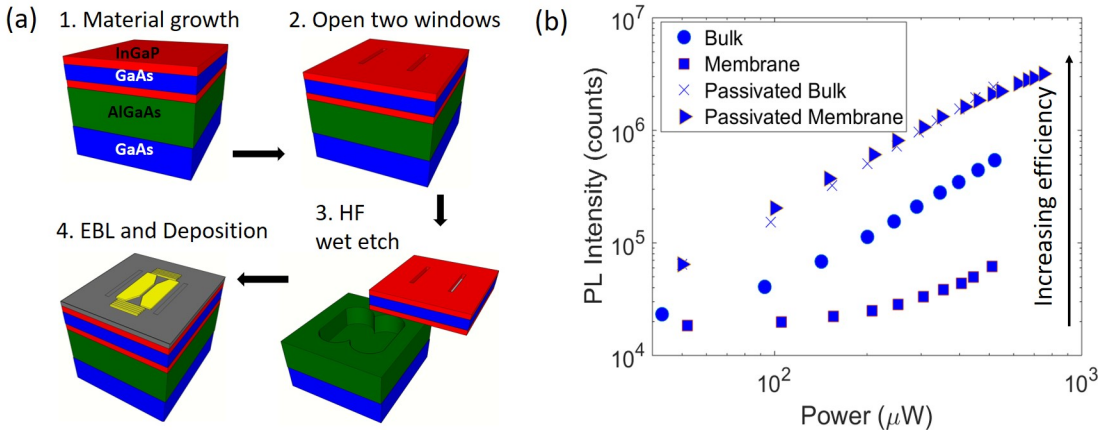



**Figure 5.4** – (a) Summary of fabrication steps. (b) Photoluminescence (PL) intensity from samples with and without passivation layers as a function of pump power at $\lambda = 650$ nm demonstrating the effect of surface passivation. These measurements were taken by Dr. Lucas Lafone [152].

[d]The semiconductor growth and etching process were done at the University of Sheffield by our collaborators Dr. Edmund Clarke and Dr. Paul Fry.

Figure 5.5 shows microscopic images of the undercut membranes grown by two methods MOCVD (Metal-Organic Chemical Vapour Deposition) and MBE. Circular and rectangular windows were made to test the integrity of the membranes under HF etching. Preliminary experiments showed that the use of rectangular windows and MBE results in better material quality and higher resistance to membrane collapse. The flow chart shown in Fig. 5.6 summarizes the steps taken to make a finished device after the suspended membranes were made.

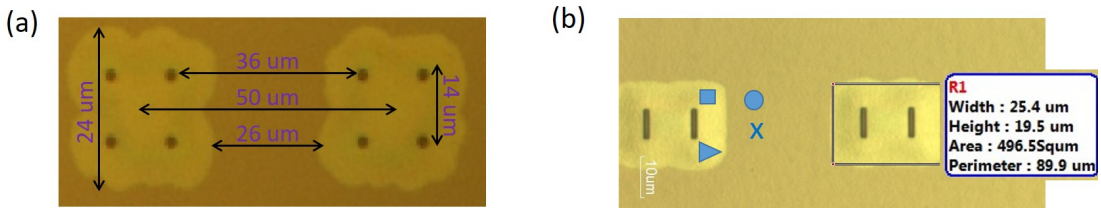



**Figure 5.5** – (a) Microscopic images of membranes grown by MOCVD (circular windows) and (b) MBE (rectangular windows). The blue symbols shown in (b) indicate the spatial locations of data points shown in Fig. 5.4(b).

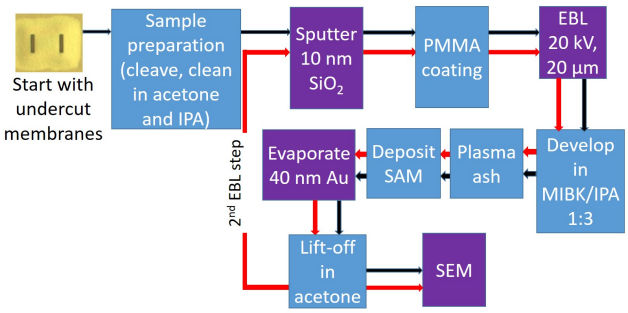



**Figure 5.6** – Flow chart of fabrication process detailing the patterning of waveguide and grating and $SiO_2$, Au deposition op top of a suspended GaAs membrane. SAM stands for self-assembled monolayer. The detail of this fabrication is given in Appendix I. The fabrication of the devices was done by Dr. Michael P. Nielsen at Imperial College London. I was in charged of designing the device using a CAD (Computer-aided design) machine and imaging the devices using SEM.

The use of metallic gold DBRs to define the cavity enables both the waveguide and the feedback sections to be fabricated in a single lithography step using EBL (Electron beam lithography). These 1-step devices have S = G = 20 nm: the waveguide and DBRs are at the same distance from the GaAs core. To improve the DBR reflectivity, a second device design was considered where the gratings and the waveguide were

fabricated in two separate lithography steps (referred to as 2-step devices). Here S = 10 nm while G remains at 20 nm. Additionally, following the first lithography step, DBR-only devices consisting of two sets of metallic gratings spaced 10 nm away from the GaAs core and without the waveguide section in between, were fabricated. These DBR-only devices could be used to assess the cavity loss, excluding modal losses. Figure 5.7(a) illustrates the side view and SEM (Scanning Electron Microscope) images of all three device designs considered. Two zoom-in SEM images of the metallic cavity and the metallic bars are shown in Fig. 5.7(b,c).

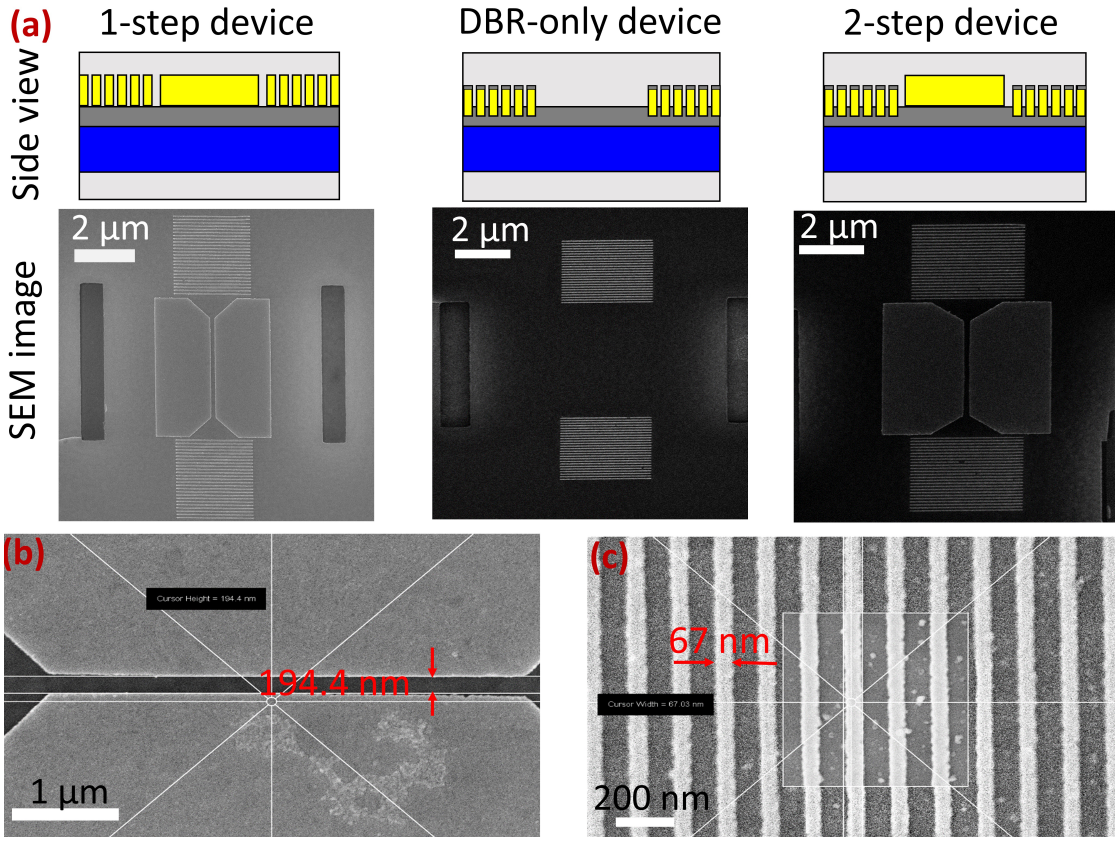



**Figure 5.7** – (a) Sketch of side view and SEM images of fabricated structures: 1-step device with S = G = 20 nm, DBR-only device with S = 10nm and 2-step device with S = 10 nm, G = 20 nm. (b) Waveguide width. (c) Metallic Grating.

## 5.3 Experimental set-up and characterization method

The devices were optically pumped near an absorption peak of the geometry at 725 nm with 150 fs laser pulses at a repetition rate of 100 kHz. A Chameleon Ultra

Ti-Sapphire mode locked laser of frequency f = 80 MHz was used to pump the devices. At this repetition rate, heating effects could lead to irreversible damages to the membranes and the metal. Thus, we used a pulse selector to reduce the repetition rate by 1/800. We pumped the laser using an elliptical beam, which was shaped by a cylindrical lens and was centered along the long axis of the device, as illustrated in Fig. 5.8(a). The whole region of the device, including the gratings, was illuminated. These pump photons made their ways to the core GaAs, promoting valence electrons to the conduction band. The relaxation of these excited electrons leading to photons being preferentially emitted into the fundamental transverse mode of the system—the HGPW mode—together with the feedback provided by the DBRs at both ends of the device (denoted by the red returning arrows in Fig. 5.8(b)) gave rise to a population inversion and consequently lasing action.

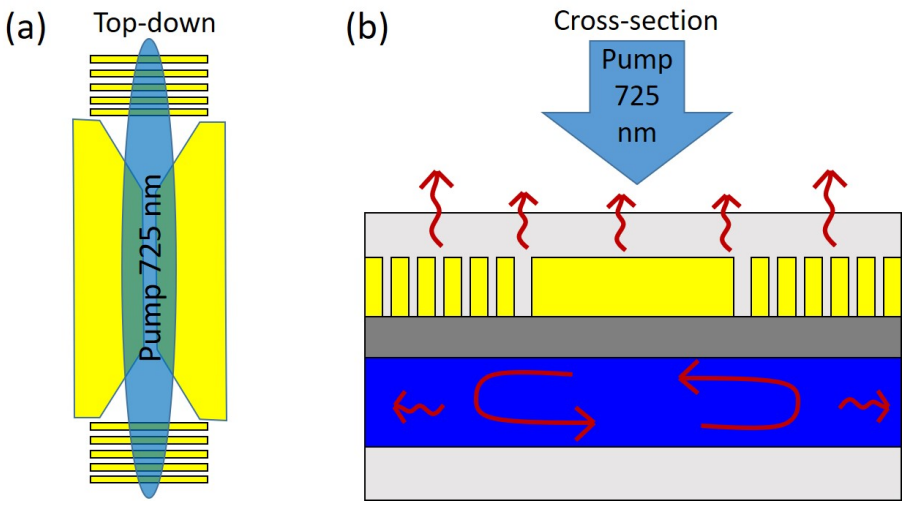



**Figure 5.8** – (a) Top-down and (b) cross-section of the pumping and collection method of hybrid gap plasmon GaAs nanolaser experiment. The elliptical pump beam was centred along the long axis of the device. The returning red arrows indicate the feedback mechanism provided by the DBRs. As the reflectivity of the DBRs is not unity, part of the stimulated emission got lost outside of the cavity or scattered upward by the gratings and imperfections along the waveguide, indicated by the curled red arrows.

Due to fabrication imperfections and impurities on the sample surface, the in-plane lasing signals could be scattered upward along the waveguide gap (Fig. 5.8(b)). By design, the DBRs only gave a high reflectivity to the TE HGPW mode traveling in the plane of the membranes, while acting as poor out-couplers to the far-field. FDTD

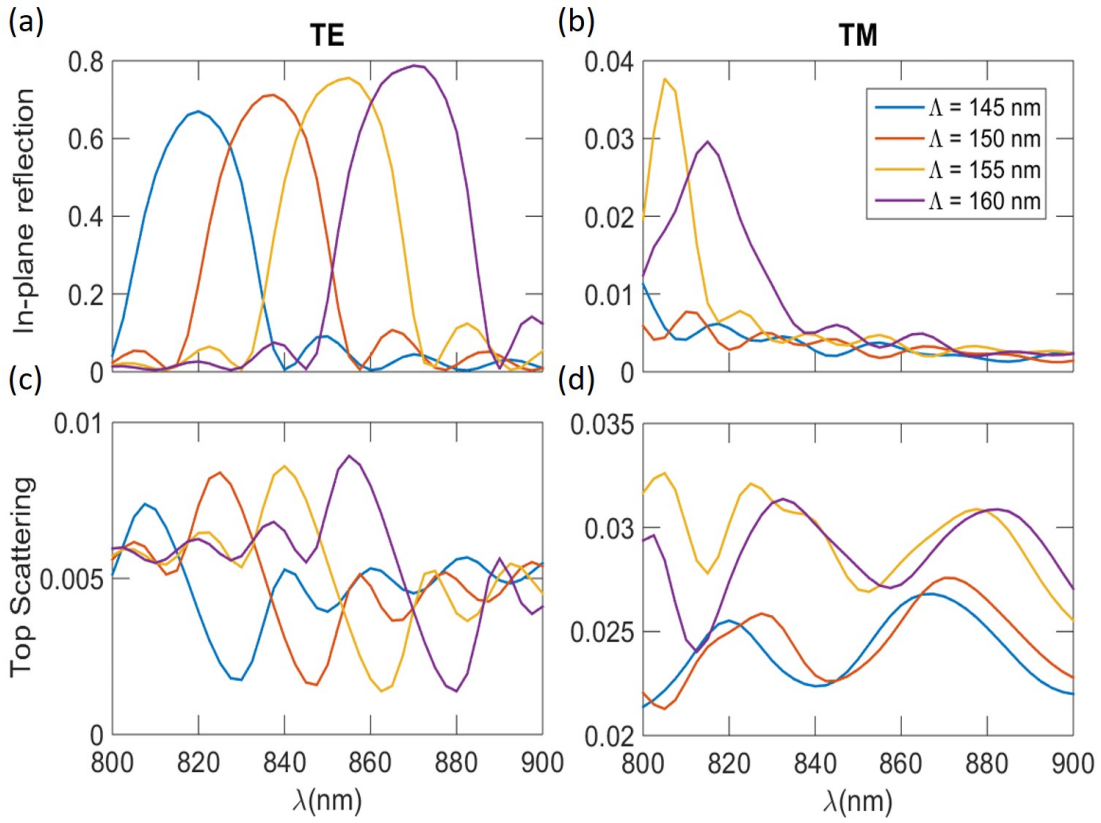



**Figure 5.9** – In-plane reflection and percentage of field scattered from the top of the devices of various grating periods with $N_b = 25$ and FF $= 0.4$ for the existing TE and TM modes. Simulations were done in Lumerical FDTD Solutions using a mode source of the slab waveguide and two field monitors above the grating for scattering calculation and behind the mode source for reflectivity calculation.

simulation results shown in Fig. 5.9 confirm that the DBRs scatter weakly to the far-field for both TE and TM waves—scattering from the top of the grating has an efficiency of $< 4\%$. With the chosen dimensions of the grating, the TM mode is suppressed with negligible feedback or scattering. This scattering property of the TE wave means that by collecting emission from the top of the device with a limited collection angle, we effectively only access a small fraction of the laser emission.

These upwardly scattered signals were then collected using a low noise liquid nitrogen cooled Spec-10 Si detector and Princeton Instruments SP-2300i spectrometer. By modelling the pump spot as a 2D Gaussian beam and taking into account the geometry of the pumped region, the absorption in the GaAs gain region was estimated to be 10%, with most of the energy absorbed in the taper regions ($\approx 70\%$). A sketch of

the experimental set-up is shown in Fig. 5.10. The pump wavelength was chosen to maximize absorption in the GaAs core based on transfer matrix approach (TMA) (see inset A in Fig. 5.10) [97]. The TMA treats the structure as a 1D stack of materials. The absorption of the core layer was found by representing the propagation of plane waves across interfaces and within materials as a scattering matrix.

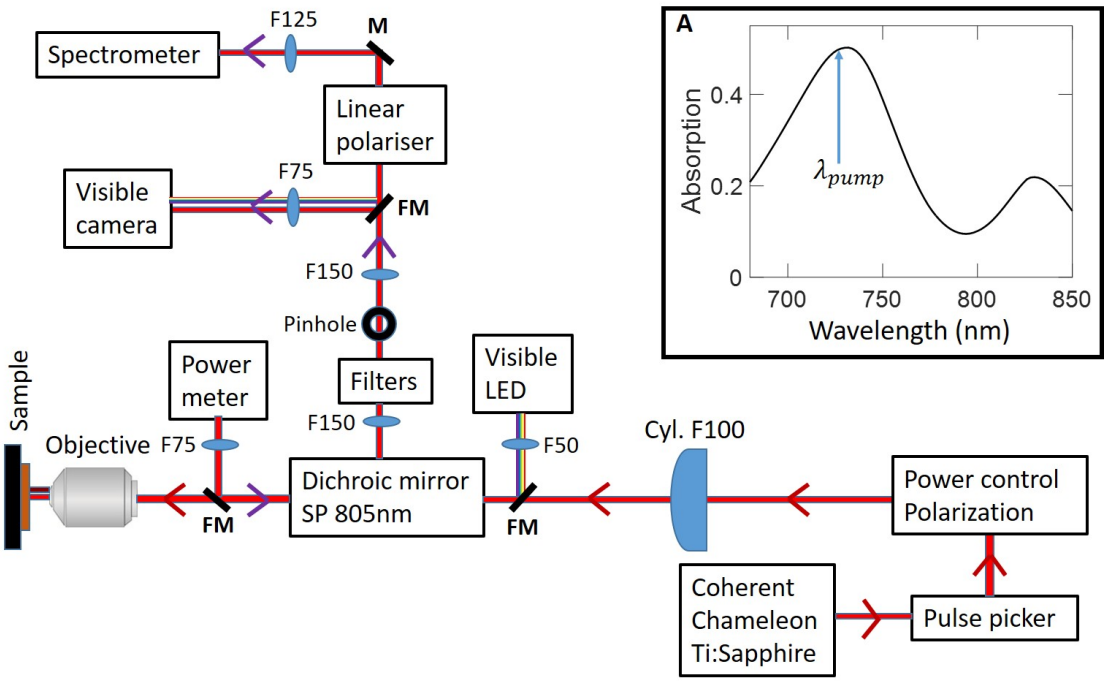



**Figure 5.10** – Set-up of the experiment. Inset A shows the amount of absorption inside the 100 nm GaAs layer based on TMA as a function of wavelength and $\lambda_{pump} = 725$ nm. This calculation assumes that we have a suspended GaAs membrane with an air gap of roughly 2000 nm underneath.

## 5.4 Results and Discussion

### 5.4.1 Data analysis method

The 2D CCD (Charge-coupled device) detector allows a 1D spatial vs spectral map of a device's response to be created. Figure 5.11 shows an example of the spectral map of the signal. A typical spectrometer consists of several gratings mounted on a rotating stage. The resolution power and the spectral range of the spectrometer depend on the groove spacing of the grating, the grating width and the diffracted angle. At $0^{th}$ diffraction order, the grating acts like a mirror reflecting the incoming

signal onto the 2D CCD. In this case, the obtained image shows a spatial distribution of the collected light in real space (Fig. 5.11). In our case, the collected signal along the long axis of the lasers was resolved spatially. The real space image shows that the collected light came mostly from the DBR areas and beyond the cavity. By changing the angle of the spectrometer's grating with respect to the incoming signals, we were able to resolve the signal both spatially and spectrally. The spectrally resolved image in Fig. 5.11 shows the corresponding spectrum of the real space image on the left. While the vertical axis maintains the initial spatial resolution, the horizontal axis now shows the wavelength dependent property of the signal.

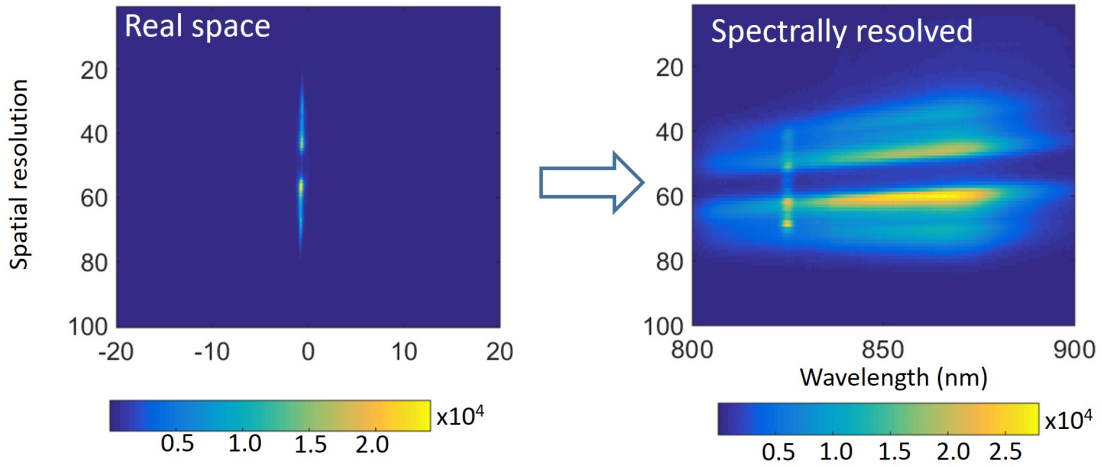



**Figure 5.11** – 2D CCD images of spatial and spectral resolution of the signal from a 1-step device with $\Lambda = 150$ nm. In the $0^{th}$ order operation, the grating acts as a mirror and has no spectral resolution power (Real space). Spectral and spatial resolution of the signal at the central wavelength of 850 nm is shown in the spectrally resolved image.

### 5.4.2 Lasing action in 1-step devices

The characteristics of a typical 1 step-device with a grating period of $\Lambda = 150$ nm and W $\approx$ 195 nm are summarized in Fig. 5.12. The data was taken from a single horizontal pixel line across the middle of the device. Figure 5.12(a) shows a clear spectral change in the response of the device when the pump energy is increased. A peak appears in the broad spectral response of the spontaneous emission as stimulated emission begins to dominate. The insets show two camera images of the PL response of the device below threshold (1) and above threshold (2). When the device enters the

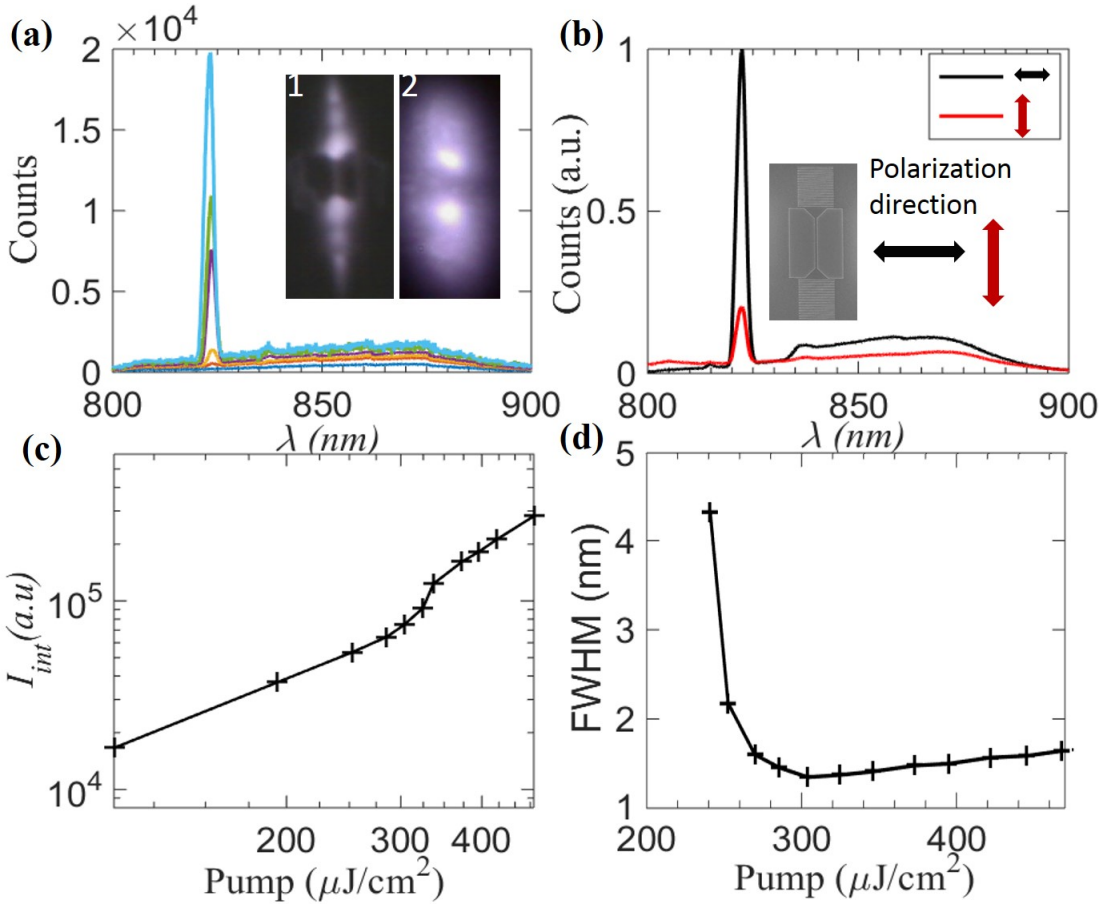



**Figure 5.12** – (a) Spectral response of photoluminescence of the device in different pump regimes. Insets show spatial locations where the signals come from below (inset 1) and above (inset 2) the lasing threshold (images shown here are subject to comparable intensity scale). (b) Polarization characteristics of the lasing signal. The data plotted here was taken from the whole device above threshold. The polarization direction is defined with respect to the cavity orientation. (c) Integrated intensity of the signal as a function of pump energy density. (d) FWHM of the lasing signal as a function of pump intensity [152].

stimulated emission regime (2), most of the signal predominantly originates from the ends of the device rather than being distributed evenly across its whole area (1). The scattered light is shown to polarize mostly in the direction perpendicular to the long axis of the waveguide (black double arrow in Fig. 5.12(b)). This is a clear indication that the lasing response originates from a TE-like hybrid gap mode.

Figure 5.12(c) presents the integrated intensity of the PL spectra, $I_{int}$, as a function of pump energy density, normalized by the simulated pump absorptivity of the device. The kink signature of the onset of lasing is observed here, with amplified spontaneous

emission followed by stimulated emission. The lasing characteristic is further emphasized by a reduction in the FWHM (full width at half maximum) followed by a broadening of the lasing peak as the pump continues to increase (see Fig. 5.12(d)). This phenomenon was also observed in other laser devices [155].

The extent and behavior of the spontaneous emission background in our data is also influenced by the emission material extending well beyond the lithographically defined cavity. Although the extension of signals beyond the gratings can be seen in Fig. 5.11, it is worth noting that our imaging system was not able to spatially resolve signals in the horizontal direction, transverse to the long axis of the device. While a laser response will only be achieved in the cavity region, spontaneous emission can emanate from other areas exposed to the pump beam as well as areas pumped by emission from the cavity region due to the continuous extent of the gain medium. We thus observe regions where the carrier concentration does not clamp at the laser cavity threshold, which has also been observed in other nanoscale laser designs [156, 157].

### 5.4.3 Gain and loss analysis of lasing action

The total cavity losses in these lasers consist of the modal loss $\alpha_{mode}(\lambda)$, which is a function of the HGPW mode field distribution, and the mirrors loss, $\alpha_{mir}(\lambda)$, which defines the feedback efficiency. To separate these two loss mechanisms and estimate their individual contributions to the total loss, we further analyze the response of 2-step and DBR-only devices. Owing to the higher DBR reflectivity, 2-step devices had lower lasing thresholds: in this case, a 25% increase in DBR reflectivity resulted in a decrease of lasing threshold by nearly half. This suggests that cavity feedback was the dominant loss mechanism for the 1-step devices.

Our analysis of the material gain and carrier concentration of the lasing condition was built upon the semiconductor gain model of bulk GaAs and free carrier theory developed in Chapter 4. Figure 5.13(a) plots the material gain and its associated induced refractive index, $n_{ind}$, as a function of wavelength. The band-filling effect leads to a blue-shift in the gain spectra of GaAs as the carrier density gets larger. An increase in carrier concentration, $N$, results in a substantial reduction of the re-

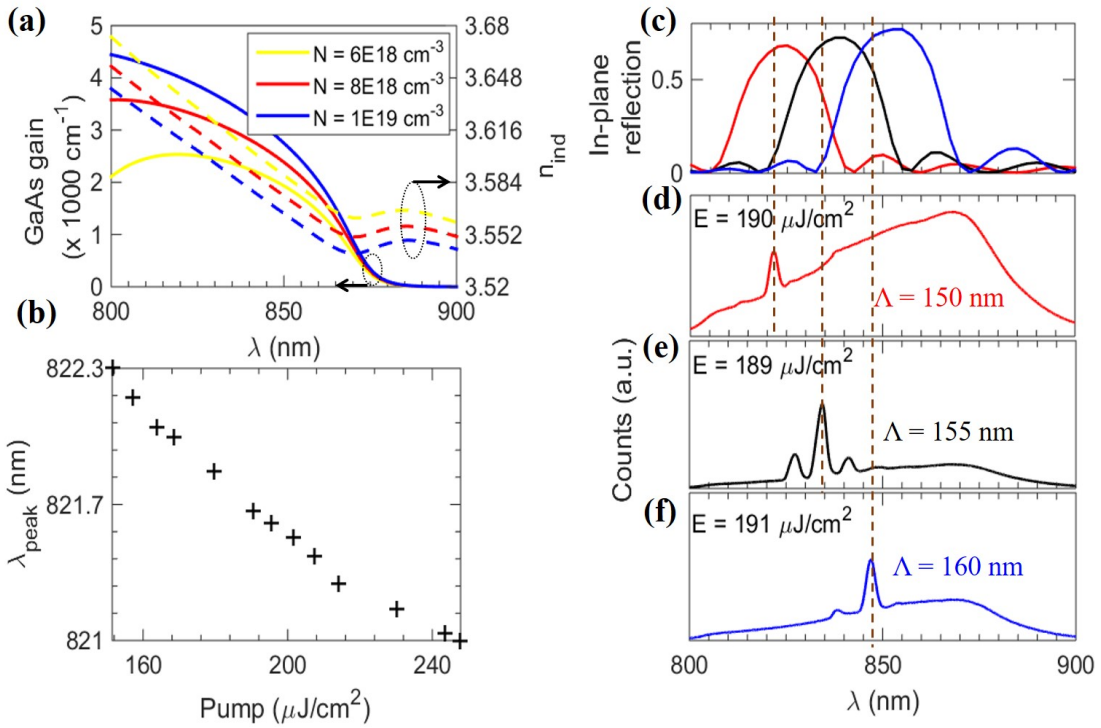



**Figure 5.13** – (a) GaAs material gain and carrier induced refractive index change as a function of wavelength for different values of carrier concentration, N. Line colors indicate different values of carrier concentrations. (b) Peak wavelength of the observed lasing signals as a function of pump intensity for a typical 2-step device of W ≈ 195 nm and Λ = 150 nm. (c) Numerical simulation of the in-plane reflection of the gratings for three different periods: Λ = 150 nm, 155 nm and 160 nm of 2-step devices, S = 10 nm, FF = 0.4 and $N_b$ = 25. Correspondingly shown here are the spectral responses of these devices at a pump density of ≈ 190 $\mu J/cm^2$. Line colors show different values of grating period [152].

fractive index of GaAs across the wavelength range of interest. Figure 5.13(b) shows the experimentally observed shift of the lasing peak wavelength as the pump intensity increases for a 2-step device of $W \approx 195$ nm and $\Lambda = 150$ nm. Here, the maximum wavelength value monotonically reduces following the onset of lasing. Meanwhile, a group index, $n_g \approx 6.9$ was determined near threshold via $\Delta\lambda = \frac{\lambda^2}{2n_g L}$, using the three visible laser modes. This exceeds $n_g = n - \lambda\frac{dn}{d\lambda} = 4.4$—obtained from numerical simulations where a passive GaAs layer was used. This discrepancy arises from the increased dispersion in the high gain regime, further emphasizing the role of carrier induced refractive index change in the operation of these plasmonic lasers.

Using values of $n_{ind}$ calculated from our gain model, the in-plane reflection of the

DBRs simulation was carried out for $N \approx 10^{19}$ cm$^{-3}$. The simulated reflection of the gratings and the experimental data of their corresponding HGPW devices are shown in Fig. 5.13(c-f) for the case of 2-step devices. Without accounting for carrier induced refractive index change, simulated DBR reflection bands would be red-shifted by roughly 20 nm with respect to those shown in Fig. 5.13(c). It is worth noting that the gain bandwidth is roughly twice that of the DBR stop band. The lasing wavelength therefore should fall into the region where the overlap of these two distinct spectral responses gives sufficient gain to overcome the total loss of the device.

In the case of DBR-only devices, the cavity mode was the TE mode of the slab waveguide. This low loss photonic mode does not contribute significantly to the total loss of the device. Here we have assumed that both the HGPW mode and the TE slab mode have similar reflectivities for a given DBR, hence similar mirror losses. This assumption is based on the fact that at $W \approx 195$ nm, the effective indices of the TE slab mode and the HGPW mode are approximately equal. In this large gap regime, the photonic component of the hybrid mode starts to dominate over its plasmonic counterpart as explained in Section 3.2.2.

For 2-step devices, the total loss can be separated into, $\alpha_{tot}(\lambda) = \alpha_{mode}(\lambda) + \alpha_{mir}(\lambda)$ where $\alpha_{DBR-only} \approx \alpha_{mir}$ based on the above argument. Figure 5.13(d-f) suggest DBR reflectivities of $\approx 65 - 70\%$ at peak reflection for the three periods considered. This similarity in reflectivities for the different grating periods means that we can approximate all gratings under consideration to have the same mirror loss. By maintaining identical metal gap widths (W $\approx$ 195 nm) to ensure similar modal losses, we can assume that regardless of grating periodicity, all 2-step devices have comparable total device loss albeit their different lasing wavelengths.

Figure 5.14(a) shows emission spectra for DBR-only and 2-step HGPW devices near their respective threshold pump conditions. A clear blue-shift of the emerging lasing peaks (arrows in Fig. 5.14(a)) occurs for each 2-step device relative to the DBR-only device of the same grating period due to the addition of modal losses. These distinct lasing wavelengths reflect the different threshold gain and corresponding carrier con-

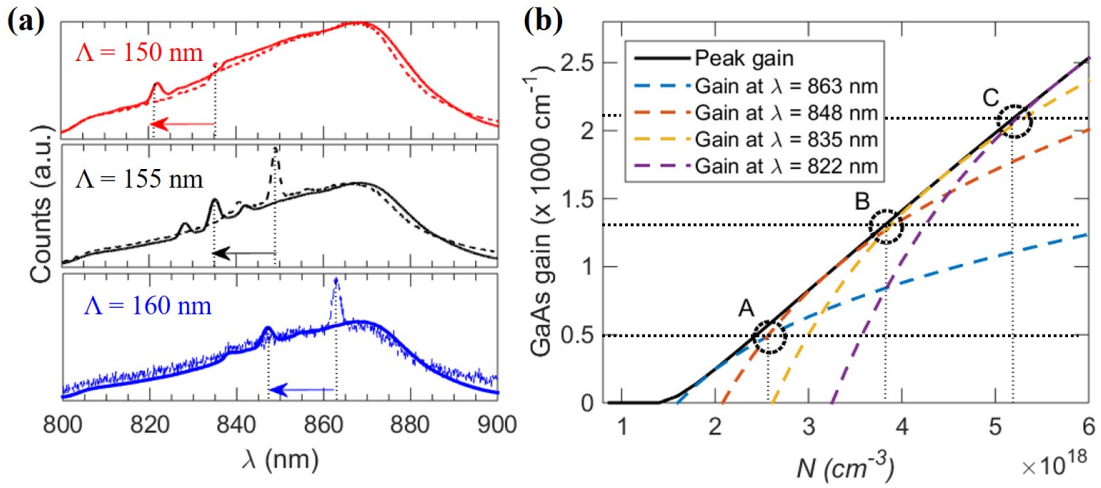



**Figure 5.14** – (a) Photoluminescence spectra of DBR-only devices (dash lines) and corresponding 2-step devices (solid lines) of the same grating period for $\Lambda$ = 150 nm, 155 nm and 160 nm at power values near thresholds (for the 2-step lasers, W $\approx$ 195 nm). (b) Peak gain and gain at particular wavelengths plotted as a function of carrier concentration [152]. Lines of equal gain are represented as horizontal dotted lines.

centrations required. The dependence of gain on carrier concentration for the four laser wavelengths identified in Fig. 5.14(a) are plotted in Fig. 5.14(b). To estimate the threshold gain, we need to know the relationship between threshold pump intensity, $P_{th}$ ($\lambda$) at a given wavelength and threshold carrier concentration $N_{th}$. However, calculating $N_{th}$ directly from $P_{th}(\lambda)$ would involve speculation of the various hidden efficiency factors such as pumping conditions, design geometry and intrinsic gain properties. Nonetheless, by assuming that $N_{th}$ is a monotonic function of $P_{th}(\lambda)$, we can determine bounds for the required threshold gain in our devices.

It should be emphasized here that the gain of bulk GaAs material is a function of both $\lambda$ and carrier concentration, $N$. Thus, two different sets of $\lambda$ and N can give the same value of GaAs gain, shown as black dotted lines in Fig. 5.14(b). Assuming that all 3 gratings ($\Lambda$ = 150 nm, 155 nm and 160 nm) lead to the same cavity loss in 2-step devices, we expect threshold gain to be the same while any differences in threshold power can be attributed to the different operation wavelengths and threshold carrier concentrations of these devices. The same argument can be applied to DBR-only devices, implying that these devices can also be assumed to have approximately identical threshold gain. This is the key assumption in estimating the threshold gain and

the threshold carrier concentration in this work.

In the case of the DBR-only devices, we observed that the device with $\Lambda = 160$ nm had the lowest lasing threshold. This implies that the threshold power density of the three devices follows the relationship: $P_{th}(863\text{ nm}) < P_{th}(835\text{ nm})$ and $P_{th}(848$ nm), where the lasing wavelengths of DBR-only devices of $\Lambda = 150$ nm, 155 nm, 160 nm are $\lambda \approx 835$ nm, 848 nm, 863 nm respectively. We can directly deduce $N_{th}(863$ nm ) $< N_{th}(835\text{ nm})$ and $N_{th}(848\text{ nm})$. This deduction together with the condition that the threshold material gain, $\alpha_{th}$, of these three devices must be equal imply that point A in Fig. 5.14(b), which corresponds to $N \approx 2.55 \times 10^{18}$ cm$^{-3}$, sets an upper bound for the mirror loss, $\alpha_{mir} < 430$ cm$^{-1}$.[e] With a cavity length of 6.5 $\mu m$, the estimated DBR reflectivity was 75.6%, in reasonable agreement with the simulated peak reflectivities of the three DBRs shown in Fig. 5.13(d-f).

A similar observation reveals that for the case of 2-step devices, the device with $\Lambda = 155$ nm obtained the lowest threshold. Here, the lasing wavelengths of the 2-step devices for $\Lambda = 150$ nm, 155 nm, 160 nm are $\lambda \approx 822$ nm, 835 nm, 848 nm, respectively. Given that $N_{th}(835\text{ nm}) < N_{th}(822\text{ nm})$ and $N_{th}(848\text{ nm})$, the only region, where the conditions of having similar gain thresholds and obtaining the above $N_{th}$ relationship are both satisfied, lies between points B and C—defining upper and lower bounds, respectively. Therefore, the threshold material gain for a typical 2-step device must be in the range of 1300 - 2000 cm$^{-1}$, which is equivalent to $N_{th} = 3.8 - 5.2 \times 10^{18}$ cm$^{-3}$. Accounting for the mirror loss, $\alpha_{mir} < 430$ cm$^{-1}$, and with the GaAs/mode overlap factor of 80%, this suggests a modal loss in the range of $650 < \alpha_{mode} < 1130$ cm$^{-1}$, where the calculated value is 620 cm$^{-1}$.

The question remains is how we can be sure that the mode that lased was the HGPW mode. A study by Nielsen, *et al.,* illustrated the existence of this mode along the gap for a width of 24 nm in SOI-based HGPW [35] using selective spatial deposition of CdSe/ZnS quantum dots. Though not directly, our study of gain/loss

[e]This calculation takes into account the overlap factor of the TE slab mode of a DBR-only device, which is above 90%.

compensation in these nanolasers confirmed the hybrid mode existence by comparing the level of losses in photonic and hybrid devices (DBR-only vs 2-step devices). While a photonic mode has a negligible modal loss, a hybrid mode (HGPW mode) has a fairly high modal loss. Both our numerical simulation and experimental demonstration show that the modal loss of lasing modes in 2-step devices is well above 600 $cm^{-1}$.

To assess the feasibility of electrical pumping of such a laser, the bounds on $N_{th}$ can be linked to the lasing threshold current density, $J_{th}$, via: $J_{th} = eN_{th}H/\tau$. Here, $\tau = 1$ ns, representing the carrier lifetime. With $N_{th} \approx 3.8 - 5.2 \times 10^{18}$ $cm^{-3}$, this estimation results in a value of $J_{th} \sim 6 - 8$ $kAcm^{-2}$.

## 5.5 Summary

We experimentally demonstrated a hybrid gap plasmon GaAs nanolaser operating at room temperature, emitting in the near infrared and exhibiting relatively low lasing threshold carrier densities. The problem of surface recombination in GaAs was solved by growing two InGaP passivation layers either side of the planar GaAs slab. This is possible here as our design did not require etching of the semiconductor near the laser cavity for optical confinement. Laser resonators were defined only by patterning gold on top of these GaAs membranes, which would introduce additional surface recombination. Our gain analysis suggests that a material gain in the region of 1300-2000 $cm^{-1}$ is required to achieve lasing—potentially achievable with a current density of 6 - 8 $kAcm^{-2}$. It was found that although the intrinsic high loss of the plasmonic device could be compensated, dispersion in this high gain regime was severe, requiring careful consideration in future device design.

Since the scalability of any nanolaser demands a fabrication method that ensures reproducibility and a device design that can both efficiently confine light and allow potential incorporation of electrical injection [101, 150, 158–160], hybrid gap plasmon lasers built on suspended GaAs membranes, with their simple yet well controlled lithographical fabrication, represent a move toward practical plasmonic lasers and enable potentially greater integration into the current electronic infrastructure.

The importance of these lasing and dispersion results in the context of applying Parity-Time Symmetry (PTS) to practical optoelectronic systems is two-fold. Firstly, although our results confirm the feasibility of achieving sufficient gain in highly functional optoelectronic devices, they also suggest that the strong effect of dispersion can potentially damage the establishment of an exceptional point in a PTS system. The detrimental consequences of high loss/gain and dispersion in PTS coupled waveguides is the topic of the next chapter.

Secondly, this demonstration of a functioning plasmonic laser paves the way for potential applications of spatiotemporal PTS systems based on coupled nanolasers. As outlined in Section 2.1, coupled lasers obeying PTS can exhibit unusual physical phenomena such as loss-induced lasing, single mode lasing and perfect laser-absorbers. Plasmonic lasers with their intrinsic high loss can not only easily satisfy the PTS refractive index distribution requirements but also provide sub-wavelength confinement, facilitating chip-scale applications of PTS coupled laser systems.

# Chapter 6

# Recovering PTS in highly dispersive coupled waveguides

In this chapter, we make use of the coupled mode theory (CMT) formalism to understand the origin of various imperfect Parity-Time Symmetry (PTS) effects and hence propose a mechanism which facilitates the recovery of PTS in highly dispersive optical systems. Even though various coupled PTS systems have been demonstrated in the literature, the establishment of the ideal index profile $n(x) = n(-x)^*$ in practice is difficult due to the challenge of controlling gain, loss and material dispersion simultaneously, as shown in the plasmonic nanolaser study in Chapter 5, leading to various observations of imperfect PTS. Consequently, most research has focused on dilute or low gain optical systems of just a few hundreds $cm^{-1}$ where material dispersion is minimal.

We will first look at how the coupling coefficients of CMT can be analytically evaluated. To do this, we study a theoretical 1D model of a PTS system made up of a GaAs core with potentially high gain (>1,500 $cm^{-1}$). We then investigate the smooth transitions between PTS phases under the influence of imbalanced gain/loss, modal mismatch and dispersion. This analysis is followed by the introduction of a recovery mechanism where working with non-identical waveguides and bias pumping, the key features of PTS optical systems are recovered.

## 6.1 Components of CMT in 1D coupled systems

To understand the origin of imperfect PTS, we need to look closer at the behaviours of CMT's coefficients and see how a deviation from perfect PTS influences them. By modeling a coupled optical system as simple 1D waveguides, it is possible to evaluate the parameters of CMT analytically, and then use them to understand the different degrees of imperfection in practical PTS devices. Consider the most general case of coupling between two first order TE modes of semiconductor slab waveguides with $\mathcal{E}_\mu(x,z) = A_\mu(z)\mathcal{E}_\mu(x)e^{i\beta_\mu z}$ (Fig. 6.1). For simplicity, the whole structure is clad with the same material of refractive index $n_c$, leading to a perturbed permittivity $\Delta\epsilon_\mu(x) = \epsilon_0(\epsilon_\nu - n_c^2)\theta_\nu(x)$ where $\theta_\nu(x)$ is the top-hat function defining the spatial distribution of the refractive indices and $\epsilon_\nu = n_\nu^2$. The subscripts $\mu, \nu = 1, 2$ are the mode label. Based on the mathematical expression of $\kappa_{\mu\nu}$ outlined in Appendix B.1, Eqn. B.3, the coupling coefficients can be computed as [86]:

$$\hat{\kappa}_{\mu\nu} = \omega\epsilon_0(\epsilon_\mu - \epsilon_c)\int_{-\infty}^{\infty} \boldsymbol{\mathcal{E}}_\mu^* \cdot \theta_\mu\left(\frac{x - x_\mu}{d_\mu}\right) \cdot \boldsymbol{\mathcal{E}}_\nu dx = \omega\epsilon_0(\epsilon_\mu - \epsilon_c)f_\mu(x) \tag{6.1}$$

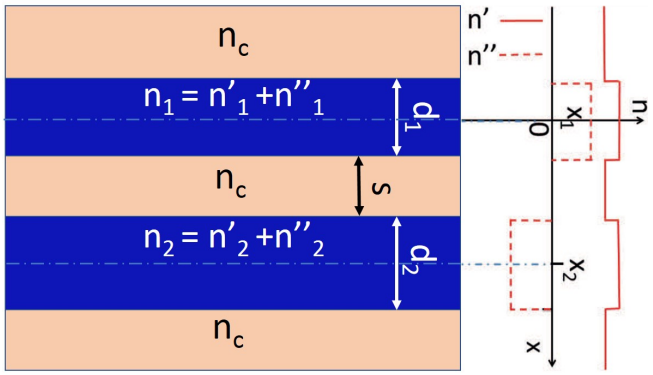



**Figure 6.1** – Spatial dimensions of the coupled system. Each individual waveguide is symmetric with lossless cladding layers of index $n_c$ and lossy/gainy cores of indices, $n_\mu = n'_\mu \pm in''_\mu$ [161].

In the conventional case of lossless CMT with identical waveguides, Eqn. 6.1 implies that $\kappa_{12} = \kappa_{21}^*$; in PTS systems with zero net gain/loss, recall that $\kappa_{eff} = \sqrt{\kappa_{12}\kappa_{21}}$, hence $\kappa_{eff}$ is always real. This condition holds subject to the approximation of weak coupling of CMT and that no gain-induced dispersion is present. According to the

form of the Hamiltonian in Eqn 2.11, PTS behaviours also depend on $\delta_{mode}$. In an ideal PTS situation, $\kappa_{eff}$ must be purely real and $\delta_{mode}$ purely imaginary. Any departure from these upsets the abrupt transition at the exceptional point (EP) [51], as discussed in Section 2.4.1. Our analysis of non-ideal PTS in this chapter goes beyond the simple case of unbalanced gain and loss to include a modal mismatch and dispersion effects.

## 6.2 GaAs-AlGaAs coupled waveguides

To facilitate the analysis of practical PTS systems, we use GaAs as our core material. GaAs exhibits both gain/loss characteristics, making it a suitable material for the construction of an active PTS coupled waveguide system. Without pumping, GaAs is a highly lossy material. This loss can become gain by externally pumping the GaAs layer. Thus, by having a pumping mechanism where the pump power is controlled separately in each waveguide, we can simultaneously vary the gain/loss level in this coupled system.

The cladding material is assumed to be $Al_{0.8}Ga_{0.2}As$ of $n_c = 3.1$ at $\lambda = 850$ nm. $Al_{0.8}Ga_{0.2}As$ has a bandgap of 2.07 eV, corresponding to a wavelength of 600 nm [162]. The results of the GaAs gain and carrier-induced dispersion model were presented in Chapter 4. A summary of relevant characteristics of bulk GaAs in the high gain regime for emission at 850 nm is given in Fig. 6.2. The focus here is on the gain-induced dispersion, $\delta n_{ind}$. Figure 6.2 (b-d) clearly illustrate the drawback of having high gain in a PTS device. With more and more carriers made available, the increase in gain slows down, reaching a saturating region while $\delta n_{ind}$ continues to change rapidly.

## 6.3 Analytic and numerical calculations of supermodes in coupled systems

Explicit calculation of coupling coefficients discussed in the previous section requires the modal field distribution of each waveguide and the permittivity perturbation, $\Delta\epsilon(x)$. The calculation of complex propagation constants and field distributions for lossy waveguides are outlined in Section 3.1.2 and Appendix D.

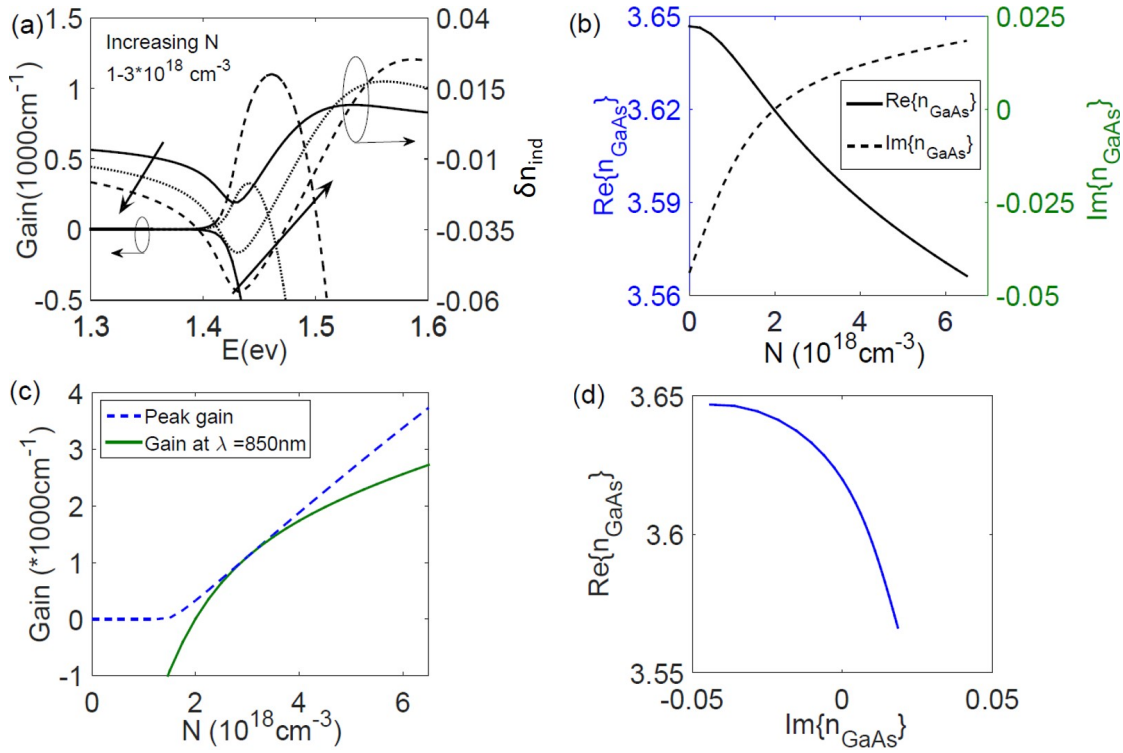



**Figure 6.2** – (a) Gain and carrier induced refractive index as a function of photon energy. Arrows point in the direction of increasing carrier concentration. (b) Real and imaginary part of $n_{GaAs}$ at $\lambda = 850$ nm as a function of carrier density. (c) Available gain versus carrier concentration at $\lambda = 850$ nm and at peak gain values. (d) $\Re\{n_{GaAs}\}$ as a function of $\Im\{n_{GaAs}\}$ at 850 nm [161].

Figure 6.3 shows the COMSOL numerical and analytic calculations of the eigenvalues for the ideal PTS scenario ($n_1 = n_2^*$ and $f_1(x) = f_2^*(x)$) and various waveguide separations. The mode solver under the RF module in COMSOL v4.3a was used to solve for the effective refractive indices of the supermodes. A maximum element mesh size of 0.1 $\mu m$ and a minimum element mesh size of 0.2 nm were implemented to achieve reasonable convergence. Gain and loss were modeled as negative and positive values of the imaginary parts of GaAs.

The numerical and analytic results agree well with each other for separations above s=100 nm. Below this separation, a discrepancy between the two results arises; however, there is no dramatic breakdown of CMT as the coupling strength increases. CMT is also robust against loss and gain added to the system. CMT predicts a smaller cou-

pling compared to numerical solutions for cases of separation smaller than 100 nm.[a] This is because at these small separations, the spatial overlap of the two codirectional TE modes becomes significantly larger and the simple perturbation theory no longer accurately describes the coupling process. Higher order terms must now be employed to explain the strength of the coupling mechanism in this regime. Descriptions of the modified perturbation theory and the strong coupling mechanism are beyond the scope of this thesis. In this work, the chosen dimensions of our system fall into the coupling regime in which the physical description of CMT is sufficiently accurate.

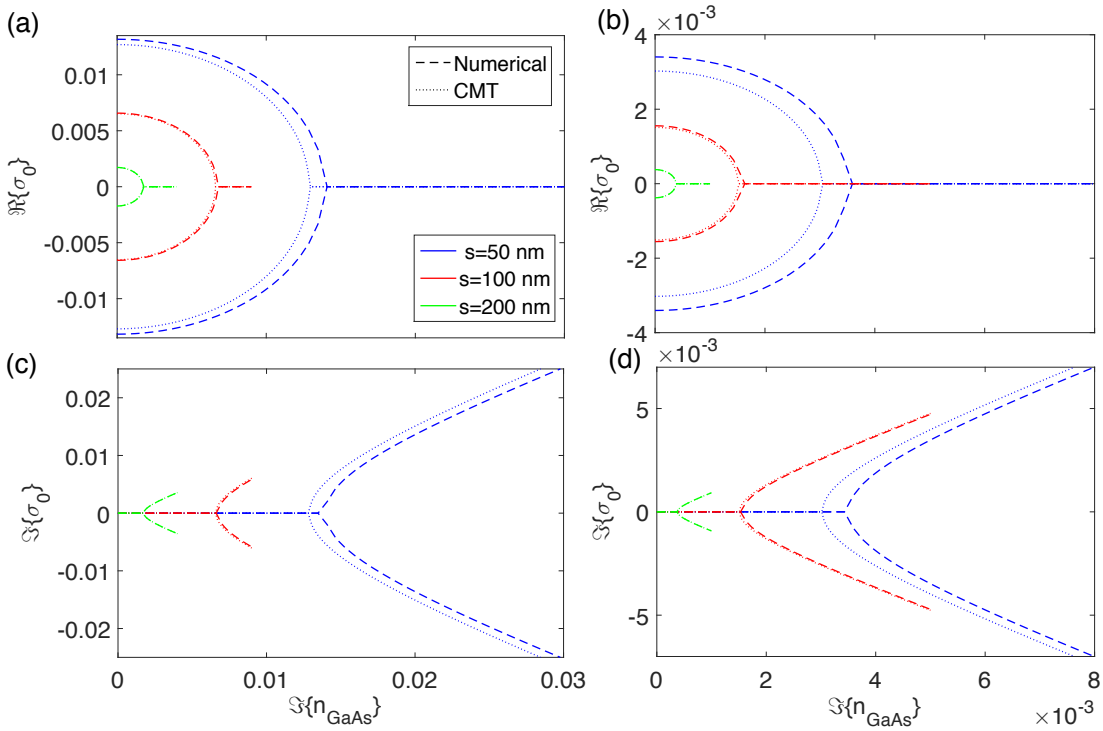



**Figure 6.3** – Simulation and analytic results of $\pm\sigma_0$ as a function of $\Im\{n_{GaAs}\}$. The results are plotted for $d_1 = d_2 = d = 500$ nm (a, c) and $d_1 = d_2 = d = 900$ nm (b, d) under ideal PTS configuration for $n_1 = n_2^*$ at $\lambda = 850$ nm and $n_{1,2} = 3.6468 \pm i\Im\{n_{GaAs}\}$. Different colours correspond to the results of three separation distances, s = 50-200 nm . Here, $\sigma_0$, $\sigma_\pm = n_{eff\pm}$, $\kappa_{eff}$ and $\delta_{mode}$ have been normalized to $K_0 = 2\pi/\lambda$ [161].

Having obtained the analytic expressions of CMT's components and the numerical simulation of the supermodes, we are now able not only to assess the practical in-

[a]When plotting $\sigma_\pm$ as a function of $n''_\mu = \Im\{n_{GaAs}\}$ for $s < 100$ nm, besides a horizontal discrepancy in the position of the EP there is also a vertical difference between CMT and numerical solutions. This observation further confirms the breakdown of CMT in the close proximity limit of the two waveguides.

fluences of various deviations from ideal PTS, but also to evaluate the robustness of CMT against modifications from its conventional usage in lossless coupled systems.

## 6.4 Imperfect PTS systems

### 6.4.1 Imbalance in gain and loss

In practice, it is very difficult to achieve exactly equal gain and loss in a coupled system as gain and loss are often controlled by two separate physical mechanisms. Loss is often introduced via the addition of metals while gain is incorporated via either electrical or optical pumping of a gain material. Using Eqn. 6.1, it was found that [161]:

$$\kappa_{12} = \kappa_{21}^{*} \frac{\Delta\epsilon_1}{\Delta\epsilon_2^{*}} \frac{f_2(x)}{f_1^{*}(x)} \tag{6.2}$$

In the case of identical waveguides where $\epsilon'' \ll \epsilon'$ and $\delta\epsilon = \epsilon_1' - n_c^2 = \epsilon_2' - n_c^2$, we arrived at [161]:

$$\kappa_{12} \approx \kappa_{21}^{*}(1 + i\frac{\epsilon_1'' + \epsilon_2''}{\delta\epsilon}) \tag{6.3}$$

The modal asymmetry, $f_2(x)/f_1^{*}(x)$, is assumed to vary weakly in this situation such that $\Im\{\kappa_{eff}\}/\Re\{\kappa_{eff}\} \approx (\epsilon_1'' + \epsilon_2'')/\delta\epsilon$. A number of theoretical reports have predicted that optical PTS systems with net gain/loss are mappable onto the ideal PTS formalism [42, 48, 76]. However, it should be strongly emphasized that this mapping is only strictly feasible if $\kappa_{eff}$ is assumed to be real. The reality of $\kappa_{eff}$ in turn relies on the assumption that the net gain/loss does not affect the symmetry of the mutual coupling coefficients, i.e. the condition $\kappa_{12} = \kappa_{21}^{*}$ is still met. Following Eqn. 6.2 and 6.3, if this assumption is relaxed, the modified complex coupling coefficient, $\kappa_{eff}$, can be used to quantify the effects of imbalanced gain and loss in this non-ideal PTS system. Here, $\kappa_{eff}$ can take complex value—a departure from the ideal PTS coupled system.

For an imbalance of gain and loss ($n_1' = n_2'$ and $|n_1''| \neq |n_2''|$), the difference in $|n_\mu''|$ between the two GaAs core layers is conveniently expressed as: $n_{1,2}'' = g_{0,GaAs} \pm \Delta_{GaAs}$ where $g_{0,GaAs}$ can be either negative or positive depending on whether the overall system exhibits net loss or net gain. $g_{0,GaAs} = 0$ corresponds to an ideal PTS system.

Figure 6.4(a,b) show the eigenspectra of the coupled system for various values of $g_{0,GaAs}$ and the location of the phase transition point is denoted as $\alpha_{EP}$ on the gain spectrum. For $g_{0,GaAs} \neq 0$, a residual splitting of the modes near the position of $\alpha_{EP}$ exists. This residue increases with the magnitude of $|g_{0,GaAs}|$. The two phases of the PTS system are no longer well-defined as $\sigma_0$ is always complex along the gain spectrum. A close look at the extracted parameters from CMT (Fig. 6.4(c,d)) reveals that the splitting is caused by the emergence of the imaginary part of $\kappa_{eff}$. Here, $\sigma_0$ can be approximated as [161]:

$$\sigma_0 \approx \sqrt{|\kappa_{21}|^2 + \delta_{mode}^2 + i|\kappa_{21}|^2 \frac{(\epsilon_1'' + \epsilon_2'')}{\delta\epsilon}} \tag{6.4}$$

With the use of a complex $\kappa_{eff}$, CMT agrees qualitatively with COMSOL numerical

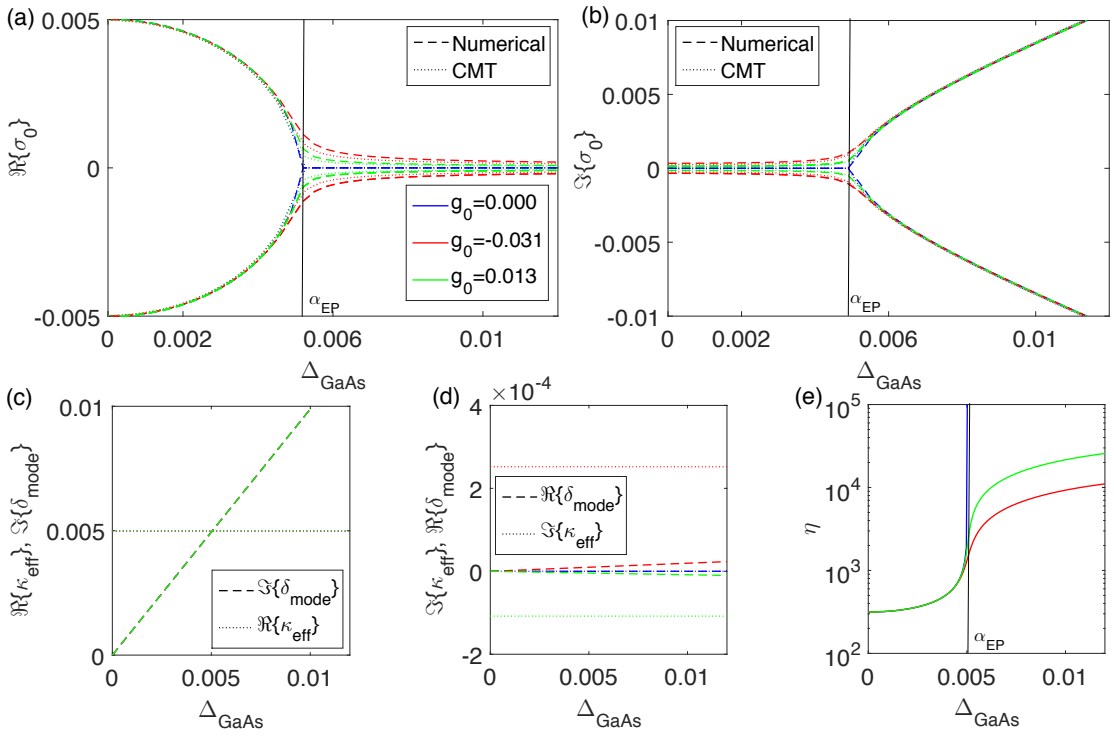



**Figure 6.4** – (a,b) Real and imaginary parts of $\pm\sigma_0$ as a function of $\Delta_{GaAs}$ for three values of $g_{0,GaAs} = g_0$ (results from each $g_0$ case are shown as a different colour). Here, $d_1 = d_2 = d = 500$ nm, s = 120 nm at $\lambda = 850$ nm and $n_{1,2} = 3.6468 + i(g_{0,GaAs} \pm \Delta_{GaAs})$, $\delta_{GaAs} = (n_1'' - n_2'')/2 = \Delta_{GaAs}$. (c-d) Extracted parameters from CMT. Comparison of the corresponding real and imaginary parts of the components of $\sigma_0$. In (c), $\Re\{\kappa_{eff}\}$ and $\Im\{\delta_{mode}\}$ are insensitive to different values of $g_0$, leading to almost overlapping of the three coloured lines. (e) Assessing the quality of switching close to the EP of coupled system, $\eta$ vs $\Delta_{GaAs}$. Black vertical line indicates the position of $\alpha_{EP}$ [161].

solutions. We found that the larger the value of $g_{0,GaAs}$, the larger the discrepancy between CMT results and COMSOL rigorous solutions. This discrepancy arises as CMT requires an estimation of the average index of the whole system, which in this case has been taken to be the lossless cladding index ($n_c$).

Non-zero values of $\Im\{\kappa_{eff}\}$ inhibit the occurrence of an ideal EP. The abrupt transition of an ideal PTS system is replaced by a smooth bifurcation of the supermode eigenvalues. Any practical application relying on the sharp transitions between the two PTS phases hence sees its effectiveness greatly reduced [79]. We further define $\eta = \pi/(2\Re\{\sigma_0\})$ to characterize the quality of PTS phase transition. $\eta$ corresponds to the familiar coupling length of coupled waveguide systems in a perfect PTS coupled system: $\eta$ evolves with gain/loss and reaches infinity at the EP where the two waveguides decouple while having exactly the same modal index. In contrast, in an imperfect PTS system, the correspondence between the coupling length and $\eta$ is less well-defined as $\sigma_0$ is always complex. Only when the condition $\Re\{\sigma_0\} \gg \Im\{\sigma_0\}$ is satisfied, can $\eta$ be used as an approximation for the true coupling length. According to Eqn. 6.4, close to $\alpha_{EP}$ where $|\kappa_{21}|^2 + \delta_{mode}^2 \approx 0$, the value of real and imaginary parts of $\sigma_0$ are equal. Note here that this residual $\sigma_0$ exists in all practical optical systems and quantifies the quality of PTS in those systems. Deviations of such imperfect PTS systems from ideal behaviour can be characterized by evaluating the term $|\kappa_{21}|^2(\epsilon_1'' + \epsilon_2'')/\delta\epsilon$. Beyond this point, $\eta$ can be thought of as an intrinsic residual modal mismatch between the two resultant decoupled modes. $\eta$ of an imperfect PTS system changes smoothly in the region around $\alpha_{EP}$ and slowly increases after. The value of $\eta$ increases by one order of magnitude close to $\alpha_{EP}$ (Fig. 6.4(e)).

### 6.4.2 Imbalance in modal index

An imbalance in the phase evolution of the modes of this coupled system can be represented as a geometric asymmetry of unequal corewidths. While the material parameters are kept the same as in the ideal PTS case where $n_1 = n_2^*$, with unequal corewidths, the modal indices of each waveguide are no longer complex conjugates of each other; a phase mismatch thus arises in the coupled system, $\Re\{\delta_{mode}\} = n_1' -$

$n_2' \neq 0$. Figure 6.5(a,b) show the sensitivity of the coupled system to geometric mismatch. Again a departure from ideal PTS setting leads to a residual splitting in the real eigenspectrum. The magnitude of the splitting approaches the value of $|\Re\{\delta_{mode}\}|$ beyond $\alpha_{EP}$. Correspondingly, $\Im\{\sigma_0\}$ has non-zero values throughout the gain spectrum. Figure 6.5 (c,d) reveal that $|\Re\{\delta_{mode}\}|$ reaches 10% and 20% of the coupling strength for $\Delta d = 10$ nm and $-5$ nm respectively.

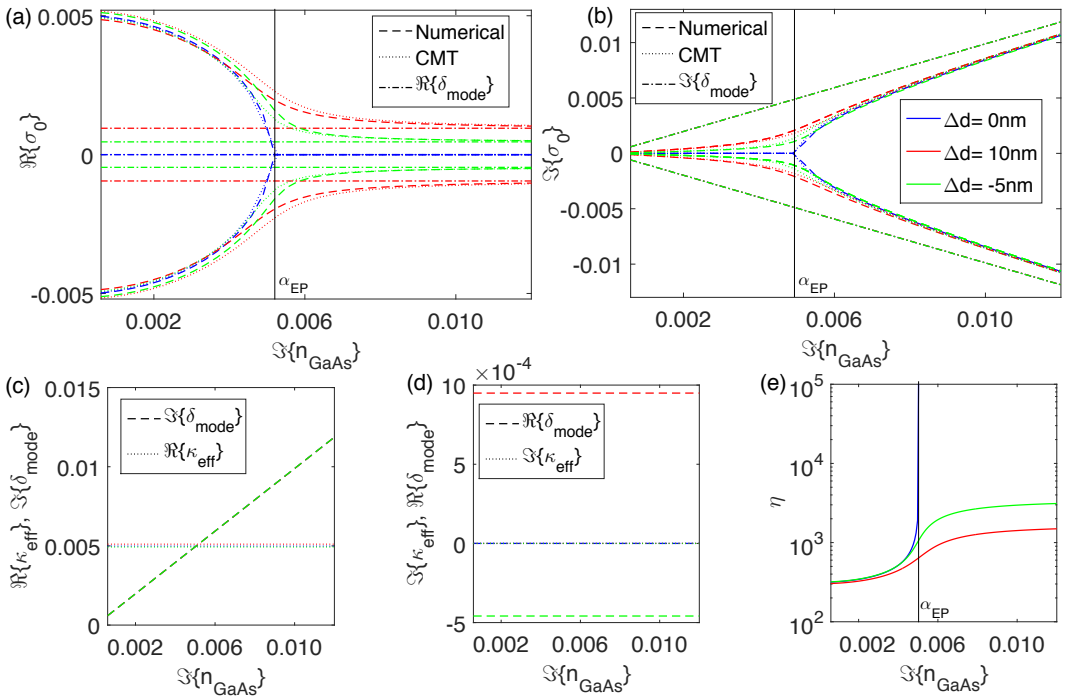



**Figure 6.5** – (a,b) Real and imaginary parts of $\pm\sigma_0$ as a function of $\Im\{n_{GaAs}\}$ for various values of $\Delta d = d_1 - d_2$ (different colours correspond to the results of three $\Delta d$ cases considered) where $d_1 = 500$ nm and s=120 nm at $\lambda = 850$ nm. Here, $n_{1,2} = 3.6468 \pm i\Im\{n_{GaAs}\}$. (c-d) Extracted parameters from CMT. Comparison of the corresponding real and imaginary parts of the components of $\sigma_0$. In (c), $\Re\{\kappa_{eff}\}$ and $\Im\{\delta_{mode}\}$ are insensitive to different values of $\Delta d$, leading to almost overlapping of the three coloured lines. (e) Assessing the quality of switching close to the EP of coupled system, $\eta$ vs $\Delta_{GaAs}$. Black vertical line indicates the position of $\alpha_{EP}$ [161].

It was found that for each coupling strength level, there is a maximum geometric mismatch that the system can tolerate before the detuning effect due to unequal modal indices of the two waveguides takes over. For instance, when $d_1 = 700$ nm and $s = 200$ nm, an equivalence of only 10% of the coupling strength mentioned above, the mismatch tolerance goes down to 2 nm, making this device impractical

due to fabrication limitations. The stronger the coupling, the greater the mismatch tolerance the system can take. Similar to an imbalance in gain and loss, geometric asymmetry also causes a smooth variation of $\eta$ near the position of $\alpha_{EP}$ (Fig. 6.5(e)). While CMT still produces results closely resembling the numerical solutions, the slight disagreement can again be attributed to the estimation of the average index of the system.

### 6.4.3 Material dispersion effects

The third deviation from the ideal PTS considered here is an important one as it is not a practical limitation but rather an inherent constraint of material physics, the gain-induced dispersion effect.

Figure 6.6 shows $\sigma_0$ for the PTS coupled system where both semiconductor waveguides have the same corewidth of d = 500 nm and a separation of s = 150 nm between them. When the gain induced dispersion is included in the material property, we no longer observe the formation of an exceptional point in this system. Once the dynamic change of $\Re\{n_{GaAs}\}$ with $\Im\{n_{GaAs}\}$ is incorporated, the coupling mechanism is totally destroyed by dispersion effects. Compared to the effects described in Section 6.4.1 and 6.4.2, the effect of carrier-induced refractive index change is definitely the most detrimental. Furthermore, its inherent nature means that the consequences of $\delta n_{ind}$ are inevitable regardless of how perfect our fabrication and experiment techniques can be. In the next section, we investigate a mechanism which recovers the EP behaviour of PTS even in this highly dispersive regime.

## 6.5 Recovering PTS in highly dispersive systems

In this section, we consider the use of asymmetries in gain/loss and waveguide geometry to compensate the gain-induced dispersion and recover the abrupt dynamics of PTS near $\alpha_{EP}$. This is the compensation that would have to be used to realize PTS in semiconductor based nanophotonic systems where severe gain-induced dispersion exists. Firstly, we investigate the dispersion of waveguides with different core thicknesses. The dispersion curves for waveguides of d = 450 - 550 nm are shown

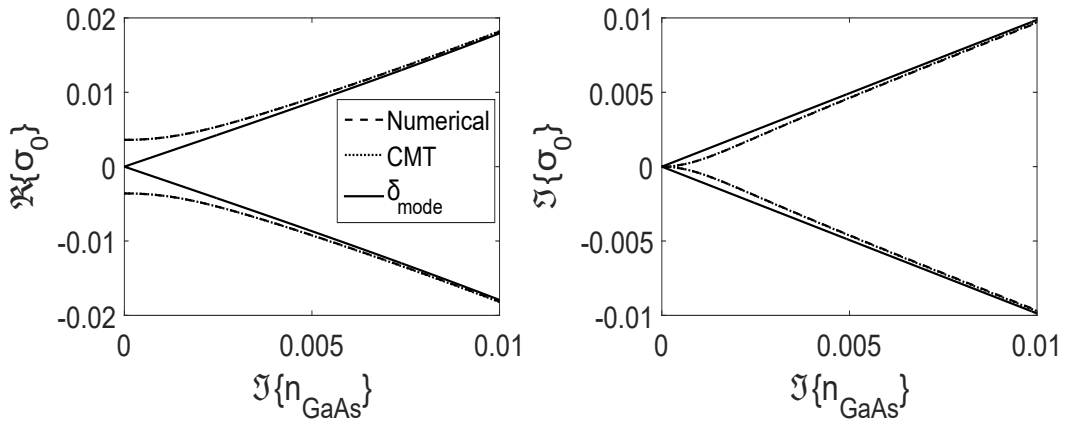



**Figure 6.6** – Real and imaginary part of $\sigma_0$ in the case where two identical waveguides with balanced gain and loss are considered. Material dispersion effects are taken into account. Modal index manipulation is destroyed by the huge carrier induced refractive index change [161].

in Fig. 6.7(a). Waveguides of different core thicknesses follow different dispersion curves which are vertically shifted from each other on this plot. The monotonically decreasing nature of these curve implies that there exist no two values of $\Im\{n_{GaAs}\}$ which give equal modal indices.

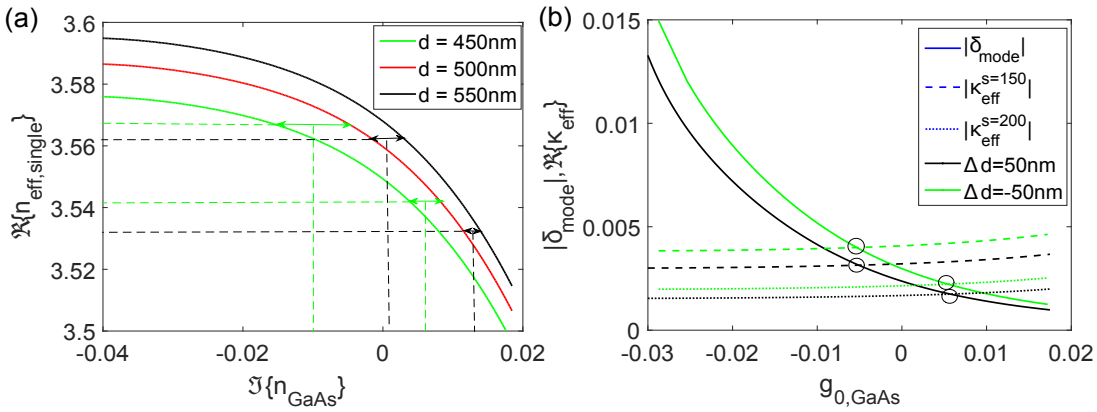



**Figure 6.7** – (a) $n_{eff}$ of single waveguide as a function of $\Im\{n_{GaAs}\}$ for different values of corewidth. Vertical and horizontal dash lines correspond to the values of $g_{0,GaAs}$ and $\Re\{n_{eff}\}$ respectively. The length of the double-headed arrows indicates the magnitude of $2\Delta_{GaAs}$. $\Re\{\delta_{mode}\} = 0$ along the horizontal dash lines. (b) Coupling of two waveguides with $d_1 = 500$ nm and $d_2 = d_1 + \Delta d$ for $\Delta d = 50$ nm (black lines), $\Delta d = -50$ nm (green lines). Shown here are the corresponding values of $|\delta_{mode}|$ (solid lines) as we sweep through the gain spectrum. Also plotted are two values of $\kappa_{eff}$ corresponding to s = 200 nm (dotted lines) and s = 150 nm (dash lines) for each $\Delta d$ case. The circles specify the coordinates ($g_{0,GaAs}$,$\delta_{mode}$) at which $\Re\{\kappa_{eff}\} = |\delta_{mode}|$ [161].

Nonetheless, we can see that by working with waveguides of dissimilar core widths,

it is possible to find two equal modal indices at two distinct points on the gain spectrum. The values of $\Im\{n_{GaAs}\}$ at these points are denoted as: $g_{1,2} = g_{0,GaAs} \pm \Delta_{GaAs}$. The two sets of green and black double-headed arrows indicate the magnitude of $\Delta_{GaAs}$ when sweeping through the values of $\Im\{n_{GaAs}\}$. Even though $g_{0,GaAs}$ varies for each $\Delta_{GaAs}$ value, the difference in material index between the two waveguides only depends on $\pm\Delta_{GaAs}$. This is the key to establishing a PTS-like gain/loss profile. Figure 6.7(b) plots the variation of $|\delta_{mode}|$ with $g_{0,GaAs}$ for two cases of $\Delta d = \pm 50$ nm. The points where $\kappa_{eff}$ cuts $|\delta_{mode}|$ lines represent the occurrence of an abrupt change in the properties of these systems.

For any pair of waveguides with dissimilar core widths, we can always achieve perfect phase matching by using suitable pumping conditions. The gain range in which splittings in the eigenspectra of our coupled system occur, depends on the separation distance between the two waveguides. This gives us great flexibility in choosing geometric parameters to tune the operating gain range of the system for different applications.

We implemented the recovery process for $\Delta d = \pm 50$ nm, $d_1 = 500$ nm and $s = 150$ nm, and 200 nm. The evolution of $\sigma_0$ of the supermodes as a function of $\Delta_{GaAs}$ is shown in Fig. 6.8(a,c) and the change in their $n_{eff}$ is given in Fig. 6.8(b,d). Figure 6.8(a,c) confirms that an abrupt bifurcation of the two branches in both real and imaginary planes can be achieved with this recovery method. While maintaining zero modal index difference between the two waveguides ($\Re\{\delta_{mode}\} = 0$), their absolute values vary with $\Delta_{GaAs}$. Despite the net gain/loss and a geometrical asymmetry, bifurcations in the eigenspectra can still be observed. The excellent agreement between CMT and numerical solutions suggests that the recovery of the abrupt bifurcation is robust.

Taking a closer look at the behaviour of this recovered system at the EP, we notice a small residual splitting in the real and imaginary planes of $\sigma_0$ beyond $\alpha_{EP}$. This residual splitting comes from the imbalance in gain and loss required to achieve equal modal indices for unequal core thickness. An imbalance in gain/loss gives rise to

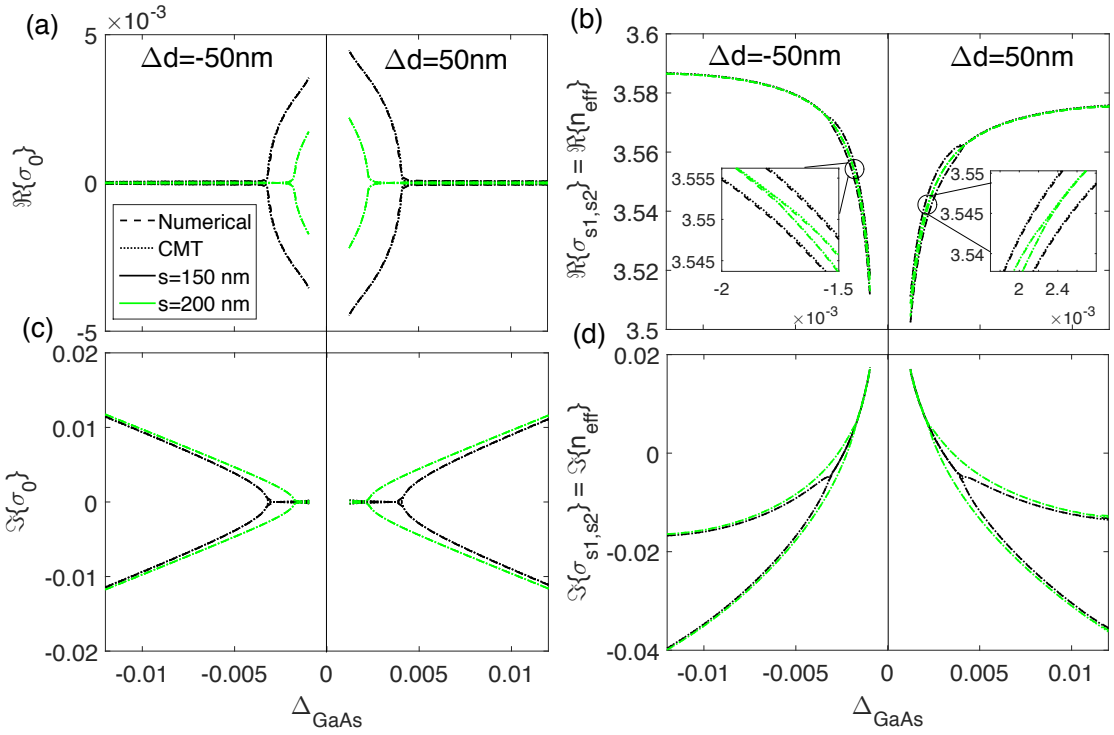



**Figure 6.8** – (a, c) $\pm\Re\{\sigma_0\}$ and $\pm\Im\{\sigma_0\}$, (b, d) $\Re\{n_{eff\pm}\}$ and $\Im\{n_{eff\pm}\}$ as a function of $\Delta_{GaAs}$ for the two cases of $\Delta d = 50$ nm (right panel) and $\Delta d = -50$ nm (left panel) with $d_1 = 500$ nm. In each panel, the results of two separation distances are plotted, s = 150 nm (black lines), and s = 200 nm (green lines) at $\lambda = 850$ nm. Insets in (c) show the corresponding enlarged locations where bifurcation of the system occurs. $g_{1,2}$ lie in the range of -1000 cm$^{-1}$ to 2000 cm$^{-1}$. As seen in these plots, the numerical and CMT results agree very well, leading to almost overlapping dash and dotted lines [161].

the familiar limitation of finite $\eta$ value close to $\alpha_{EP}$. The magnitude of the term $|\kappa_{21}|^2(f_2(x)(\epsilon_1''+\epsilon_2''))/(f_1^*(x)\delta\epsilon)$ in Eqn. 6.5 determines the effectiveness of the recovery mechanism described above [161]:

$$\sigma_0 \approx \sqrt{|\kappa_{21}|^2\frac{f_2(x)}{f_1^*(x)} + \delta_{mode}^2 + i|\kappa_{21}|^2\frac{f_2(x)}{f_1^*(x)}\frac{(\epsilon_1''+\epsilon_2'')}{\delta\epsilon}} \tag{6.5}$$

Figure 6.9 describes the evolution of $\eta$ with $\Delta_{GaAs}$. The increase in $\eta$ value reaches three orders of magnitude. For the case of s = 200 nm, a spike appears in the evolution of $\eta$. As both $\Delta_{GaAs}$ and $g_{0,GaAs}$ are varied, the value of $\Im\{\kappa_{eff}\}$ also changes. The point where $\Im\{\kappa_{eff}\} = 0$ signifies a crossing of the two branches, equivalent to the two supermodes; whether this crossing occurs in real or imaginary planes of the eigenspectrum depends precisely on the interplay between coupling strength and $\delta_{mode}$

at that point. Thus, the asymptote seen in Fig. 6.9 indicates a perfect crossing point in the real plane of the eigenspectrum. We also observe that no similar asymptote exists for s = 150 nm—implying that the crossing point occurs in the imaginary plane [161].

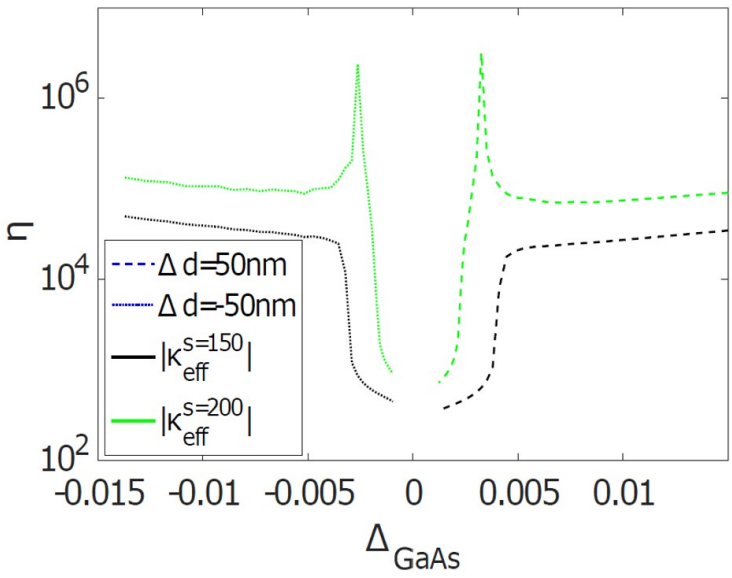



**Figure 6.9** – Characteristic parameters of the coupled system after recovery procedure (a) $\eta$—a property of the eigenspectrum. Here, the different colours correspond to the cases of s = 150 nm (black lines), and s = 200 nm (green lines) with dotted lines showing the results for $\Delta d = -50$ nm and dash lines for $\Delta d = 50$ nm [161].

## 6.6 Mode coalescence and phase rigidity

To further investigate the effectiveness of this recovery mechanism, we take a look at another property of non-Hermitian systems, commonly used in the literature to distinguish the two supermodes, called the phase rigidity, $r_{\pm}$. When non-Hermiticity is present, the conventional inner product of eigenvectors of the Hermitian Hamiltonian—defined as $\langle\Psi(x)|\Psi(x)\rangle = (\Psi_i^*)^T\Psi_i$ where $|\Psi_i\rangle$ is an eigenfunction of $\mathcal{H}$ corresponds to eigenvalue $\mathcal{Q}_i$—is replaced by a more generalized formulation:

$$\left\langle \Psi_i^L | \Psi_i^R \right\rangle = \Psi_i^T \Psi_i \tag{6.6}$$

where $\langle\Psi(x)_i^L|$ and $|\Psi(x)_i^R\rangle$ are the left and right eigenfunctions of $\mathcal{H}$ respectively. In a Hermitian system, $\mathcal{H} = \mathcal{H}^\dagger$, so the left and right eigenvectors are complex conjugates of each other, i.e., $(|\Psi(x)_i^R\rangle)^\dagger = \langle\Psi(x)_i^L|$. However, in a non-Hermitian system, this is not true, $(|\Psi(x)_i^R\rangle)^\dagger = (\Psi_i^*)^T \neq \langle\Psi(x)_i^L|$. In general, left and right eigenfunctions are defined as follows:

$$\begin{aligned} \mathcal{H}|\Psi(x)_i^R\rangle &= \mathcal{Q}_i|\Psi(x)_i^R\rangle \\ \langle\Psi(x)_i^L|\mathcal{H} &= \langle\Psi(x)_i^L|\mathcal{Q}_i \end{aligned} \tag{6.7}$$

For a Hermitian system, $\mathcal{Q}_i$ is always real and $\langle\Psi(x)_i|\Psi(x)_j\rangle = \delta_{ij}$—forming the well-known orthonormal basis vector—where $\delta_{ij}$ here denotes the conventional Delta function. In the non-Hermitian case, $\mathcal{Q}_i$ can take complex values and an orthogonality relationship is established with a clear distinction between right and left eigenvectors: $\langle\Psi(x)_i^L|\Psi(x)_j^R\rangle = 0$ for $i \neq j$. The two sets of $\langle\Psi(x)_i|$ and $|\Psi(x)_j\rangle$ form the so-called bi-orthogonal basis [163, 164]. The normalization condition is defined as $\langle\Psi(x)_i^L|\Psi(x)_i^R\rangle = 1$. Thus, for a non-Hermitian Hamiltonian, we can always establish a bi-orthogonal basis with respect to a new inner product space that gives rise to positive definite norms [165, 166]. For our non-Hermitian coupled system, the field amplitude takes the explicit form $|\Psi(z)\rangle = \begin{bmatrix} \phi_1(z) \\ \phi_2(z) \end{bmatrix}$, with $\phi(z)_{1,2}$ are the corresponding field in each channel. The left and right eigenvectors of $\mathcal{H}$ are written as:

$$|\Psi_\pm^R\rangle = \begin{bmatrix} 1 \\ \pm ae^{\mp i\theta} \end{bmatrix} \qquad and \qquad \langle\Psi_\pm^L| = \begin{bmatrix} 1 & \pm ae^{\mp i\theta} \end{bmatrix}$$

where $\pm ae^{\mp i\theta} = \frac{\pm\sigma_0 - \delta_{mode}}{\kappa_{eff}}$ and $a \in \mathbf{R}$.[b] Clearly, with this representation, the orthonormal definition of a bi-orthogonal system is fulfilled:

$$\langle\Psi_+^L|\Psi_-^R\rangle = \begin{bmatrix} 1 & ae^{-i\theta} \end{bmatrix} \begin{bmatrix} 1 \\ \pm ae^{\mp i\theta} \end{bmatrix} = 0 \tag{6.8}$$

$$\langle\Psi_\pm^L| = \frac{\langle\Psi_\pm^L|}{\sqrt{1 + a^2 e^{\mp 2i\theta}}} \qquad |\Psi_\pm^R\rangle = \frac{|\Psi_\pm^R\rangle}{\sqrt{1 + a^2 e^{\mp 2i\theta}}} \tag{6.9}$$

[b] Note here that $\delta_{mode}$ denotes the detuning between the two channels. It should not be confused with $\delta_{ij}$ the Delta function.

The phase rigidity, $r_\pm$, is defined as [167–169]:

$$r_\pm = \frac{\langle \Psi_\pm^L | A_\pm^R \rangle}{\langle \Psi_\pm^R | \Psi_\pm^R \rangle}$$

$|r_\pm|$ varies between 0 and 1 with $|r_\pm| = 1$ corresponding to orthogonal modes and $|r_\pm| = 0$ for the perfect coalescence of the two modes.

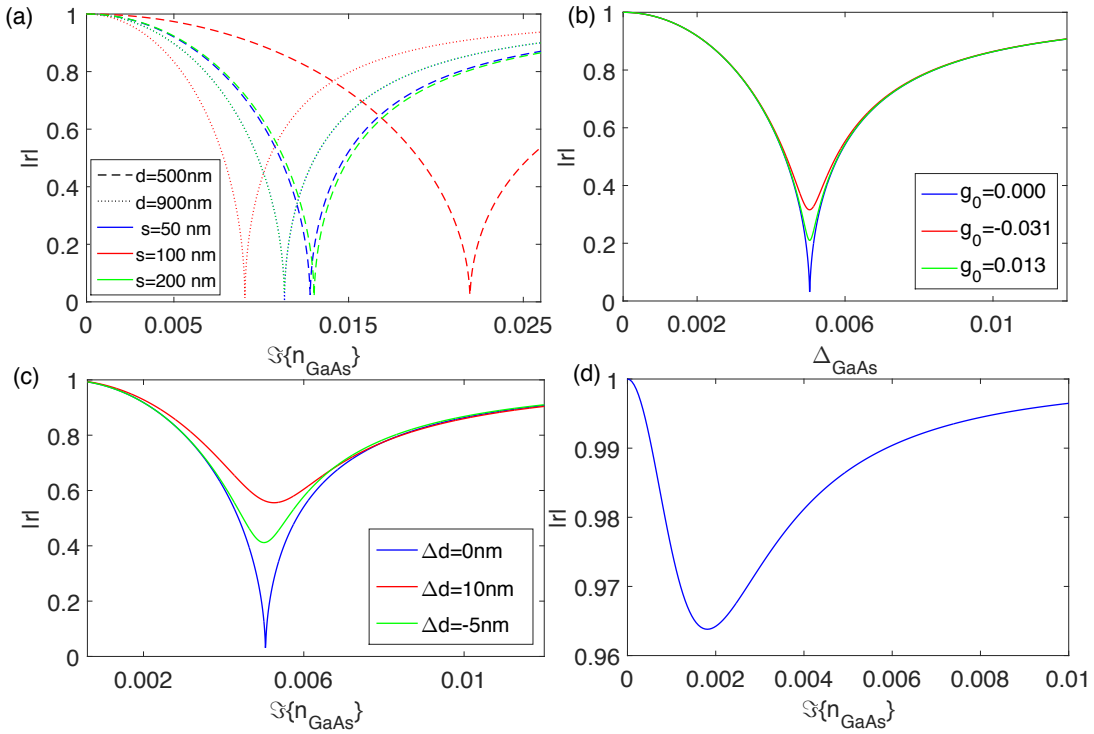



**Figure 6.10** – Phase rigidity as a function of gain in the case of (a) perfect PTS systems as described in section 6.1: the different colours correspond to different separations between the two waveguides. Two waveguide widths are considered: $d_1 = d_2 = 500$ nm (dash lines) and $d_1 = d_2 = 900$ nm (dotted lines); (b) an imbalance in gain/loss introduced to the coupled system as discussed in section 6.4.1: here, three values of $g_0$ are considered, leading to very different behaviours of $|r_\pm| = |r|$; (c) unequal core widths of the coupled waveguides considered in section 6.4.2 where three values of $\Delta d$ are investigated; (d) material dispersion taken into account without recovery procedure [161].

In the case of a lossless coupled system, i.e. $\Im\{n_{GaAs}\} = 0$, the two supermodes are distinct and orthogonal as the system is Hermitian. Once gain/loss is introduced into the system, the phases of the eigenfunctions are no longer fixed [167–169]. For our ideal PTS coupled system with equal gain and loss and zero modal detuning, the

value of $|r_+| = |r_-| = |r|$ decreases as the modes become highly mixed and $|r|$ sharply approaches zero at the EP where the two eigenfunctions are perfectly coalesced. This is clearly seen in Fig. 6.10(a). However, these characteristics of $|r|$ are significantly suppressed in imperfect PTS systems: $|r|$ does not reach 0 at $\alpha_{EP}$ and a smoother minimum occurs instead of a sharp one observed for perfect PTS (Fig. 6.10(b,c)). In particular, Fig. 6.10(d) shows that $|r|$ remains very close to 1 across the gain spectrum when the material dispersion is incorporated. The disappearance of key features in the phase rigidity evolution means that the huge effect of modal detuning generated by the gain-induced dispersion overpowers any coupling effects and thus the two modes remain isolated throughout the gain spectrum. This observation agrees with our analysis of the gain-induced dispersion effect in Section 6.4.3.

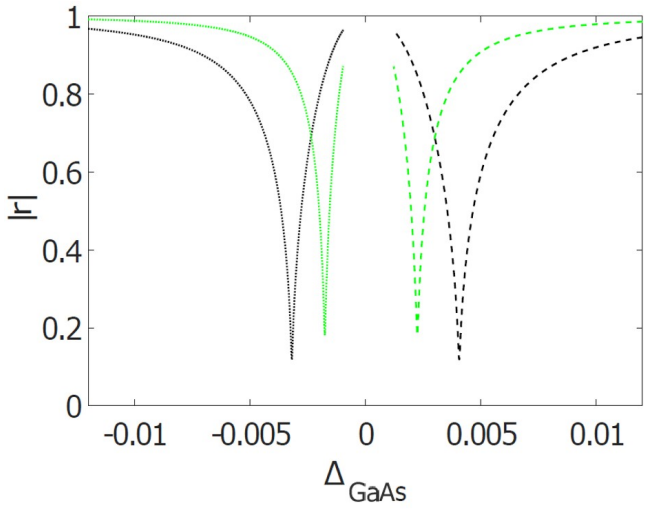



**Figure 6.11** – Characteristic parameter of the coupled system after recovery procedure: $|r|$, the phase rigidity. Here, the different colours correspond to the cases of s = 150 nm (black lines), and s = 200 nm (green lines) with dotted lines showing the results for $\Delta d = -50$ nm and dash lines for $\Delta d = 50$ nm [161].

As the phase rigidity has well-defined characteristics in an ideal PTS system, $|r|$ can also be used to assess the effectiveness of the recovery process described in Section 6.5. Figure 6.11 shows that with our recovery procedure, the sharp minimum behaviour of the phase rigidity near $\alpha_{EP}$ is recovered. However, due to an existing small imbalance in gain/loss, $|r|$ does not reach zero at the $\alpha_{EP}$.

## 6.7 Summary

Deviations from ideal PTS coupled waveguide systems are inevitable in practice as controlling gain/loss and dispersion simultaneously are extremely challenging. Once an imbalance in gain/loss or modal index appears, strictly speaking, the system is no longer Parity-Time symmetric. However, interesting physical phenomena arise whenever there exists an abrupt change in a system's behaviour. Thus, a smooth bifurcation of the eigenvalues near the original EP in imperfect PTS systems can still give rise to useful applications. Nonetheless, this smooth phase change reduces the effectiveness of any application based on PTS mechanism.

Our analysis made use of CMT's parameters to quantify smooth transitions between PTS phases under imperfect conditions. The complex coupling coefficient associated with asymmetric coupled waveguides was produced with an imbalance in gain and loss and a modal detuning. Coupled mode theory shows excellent agreement with numerical solutions, proving the robustness of coupled mode theory in describing various degrees of imperfection in PTS systems.

Gain-induced dispersion in GaAs completely overpowered any PTS coupling mechanism. Nonetheless, we found that by introducing a net gain/loss into the system together with a geometric asymmetry, we could shift the dispersion curve of a single waveguide and thus retrieve the condition of phase matching even when the core medium is highly dispersive. In practise, this recovery mechanism requires a bias pumping strategy that can deliver different pump powers to each waveguide. Such a bias pumping strategy can be implemented based on our optical pumping approach outlined in Chapter 5 . The effectiveness of this recovery mechanism relies on our ability to engineer suitable modal asymmetry with bias pumping of the two waveguides such that $(f_2(x)(\epsilon_1'' + \epsilon_2''))/(f_1^*(x)\delta\epsilon) \ll 1$. In this case, the characteristic sharp phase transition of PTS systems is recovered with $\eta$ increasing by three orders of magnitude near the position of the original EP. The effectiveness of the recovery procedure is also confirmed by a sharp minimum observed in the phase rigidity spectrum of the system at $\alpha_{EP}$.

# Chapter 7

# Active PTS gratings

While an ideal Parity-Time Symmetry (PTS) system requires a perfect balance of gain and loss, Chapters 5 and 6 show that in practice this is not only challenging to obtain but is also accompanied by gain-induced dispersion. Passive PTS gratings are ubiquitous in the literature with many theoretical and experimental works proving the versatility of such devices [37,67–72]. The main drawback of these devices is their inability to tune any exceptional point (EP) behaviour dynamically and accurately due to a rigid EP construction at the fabrication level. To make PTS gratings more applicable, a mechanism which can actively control the index modulation is needed.

Unlike lasers which require a gain material as the core layer, a PTS grating can be made up of transparent and lossy materials only. Stepping away from GaAs, we investigate a PTS grating whose core layer is made up of Silicon—one of the most relevant materials in nanophotonics. In order to establish an active control of PTS gratings, we require a material whose real and imaginary parts of the refractive index are relatively independent of each other under pumping. While the properties of an active PTS grating are essentially identical to those discussed in Chapter 2, the more fundamental question needs to be answered is whether Silicon is capable of producing the required PTS index modulation when it is optically pumped. We will start the chapter by describing the physical construction of a potential active Silicon-based PTS grating using free carrier absorption and dispersion. This is followed by an experimental investigation, assessing the feasibility of using Si as an active PTS material in a waveguide configuration. More specifically, we measure the magnitude of

the change in the real and imaginary parts of the refractive index of the propagating mode, $\Delta n'_m$ and $\Delta n''_m$, with increasing pump power then infer the corresponding changes in Silicon, $\Delta n'_{Si}$ and $\Delta n''_{Si}$ via an overlap factor. The final section presents the results of our preliminary work on the device construction and fabrication.

## 7.1 Passive vs active PTS gratings

The practical implementation of a passive PTS grating was first introduced in Chapter 2. A conventional PTS grating has a symmetric modulation of $\Re\{n(z)\}$ and an asymmetric modulation of $\Im\{n(z)\}$. Controlling both $\Re\{n(z)\}$ and $\Im\{n(z)\}$ independently is extremely challenging as they are always interlinked by Kramers-Kronig relations. As discussed in Section 2.4.2, an in-phase shift of $\Re\{n(z)\}$ distribution partly mitigates this problem by spatially separating the lossless and lossy units which control $\Re\{n(z)\}$ and $\Im\{n(z)\}$ respectively.

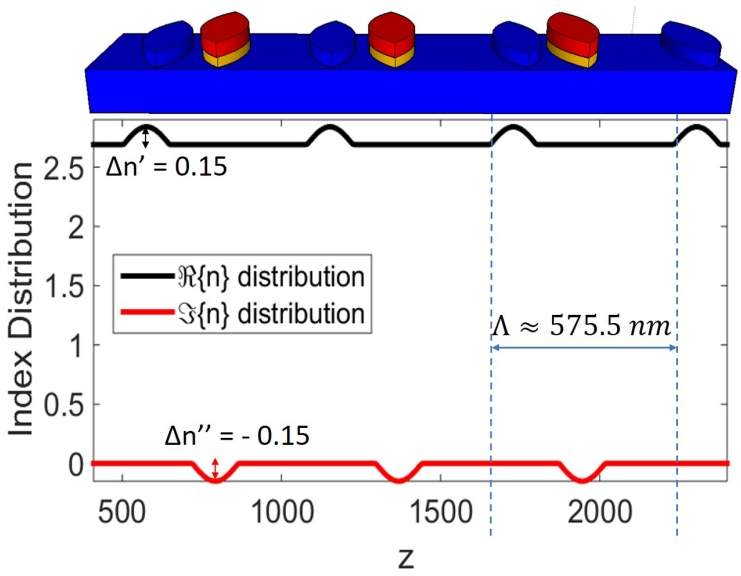



**Figure 7.1** – The index modulation and schematic sketch of a typical passive PTS grating as demonstrated in [36]. Blue denotes Silicon, yellow indicates Ge and red is Cr. $\Re\{n(z)\}$ and $\Im\{n(z)\}$ are modulated by the Si bars and Ge/Cr bars respectively.

The construction of a typical passive PTS grating is shown in Fig. 7.1. This configuration was adopted for the demonstration of unidirectional reflection in [36]. In this paper, the authors established an index modulation of the whole structure of $n(z) = n_{WG} + \Delta n' \cos(qz) + i\Delta n'' \sin(qz)$ where $n_{WG} = 2.69$ is the effective index of the ridge waveguide without the an index modulation on top, $\Delta n' = 0.15$ and $\Delta n'' =$ -0.15 at the EP. The device operates at $\lambda = 1550$ nm and the grating period corresponds to the second order of the Bragg grating with $\frac{2\Lambda n_{WG}}{\lambda} = 2$. $\Re\{n(z)\}$ is modulated by adding Si-bars on top of a Si ridge waveguide whereas $\Im\{n(z)\}$ is mod-

ulated by depositing the composite block of Ge/Cr next to the Si bars. It is the shape of the Si-bars and the Ge/Cr bars that gives rise to the sinusoidal shape of the index modulation. The periodicity of these bars satisfies the PTS grating conditions as described in Section 2.4.2. The thicknesses of the bars, $T_{Si,Ge,Cr}$ determine the value of $\Delta n'$ and $\Delta n''$. Adding materials on top of a Si ridge waveguide will inevitably affect the real part of the refractive index of the propagating mode. While this effect is desirable for Si bars, PTS index modulation requires that the lossy units (Ge/Cr bars in this case) must not perturb $\Re\{n(z)\}$. Since Ge has a higher refractive index than Si and Cr is a metal with a non-zero imaginary part of the refractive index at 1550 nm, an appropriate combination of Ge and Cr thicknesses results in a slight redistribution of the modal field across the material layers such that $\Re\{n(z)\}$ is not disturbed. This PTS grating was fabricated to investigate the physics of the device only at the exceptional point (EP) where $|\Delta n'| = |\Delta n''| = 0.15$ (See Appendix C and Section 2.4.2). To inspect another point on the eigenspectrum of the passive device, a new sample is needed with different values of $\Delta n'$ or $\Delta n''$. An active PTS device can potentially solve this problem. An active PTS grating has a dynamic range of either $\Delta n''$ or $\Delta n'$ or both, allowing the control over refractive index modulations to be implemented at the experimental stage.

The refractive index of a material can be changed dynamically by a variety of techniques. The interactions between light and a medium strongly depend on the carrier density of that medium. By either optically or electrically pumping a material, modifications to the real and imaginary parts of its refractive index ($\Re\{n\}$ and $\Im\{n\}$) can be made. However, as mentioned above, only influencing either $\Re\{n\}$ or $\Im\{n\}$ without perturbing the other to achieve an ideal PTS index distribution is not physical due to the fundamental limitation placed by Kramers-Kronig relations.[a] In practice, for an optically pumped PTS grating, it is sufficient to have carrier-induced effects strongly influence either $\Re\{n\}$ or $\Im\{n\}$ while having negligible impact on the other component.

Silicon—an indirect bandgap semiconductor—is a candidate for active PTS grating

[a] In the case of the passive PTS grating mentioned above, this inevitable perturbation has a magnitude of about 20% of the actual index modulation.

since Silicon is a poor emitter of light, i.e, $\Im\{n_{Si}\}$ at $\lambda > \lambda_{bandgap}$ is negligible. The questions remaining are what magnitude of $\Delta n'_{Si}$ at the wavelength of interest we can achieve by generating free carriers in Silicon and how large this magnitude of $\Delta n'_{Si}$ is compared with its accompanied $\Delta n''_{Si}$.

## 7.2 Optical properties of Silicon

### 7.2.1 Excited carriers in semiconductors and metals

To understand the response of Silicon to high laser powers, we take a look at the time dependence of the energy transfer of excited electrons and phonons—conveniently described by their temperature, $T_e$, $T_{phonon}$—in the context of band structure for a typical indirect semiconductor and a metal (See Fig. 7.2).

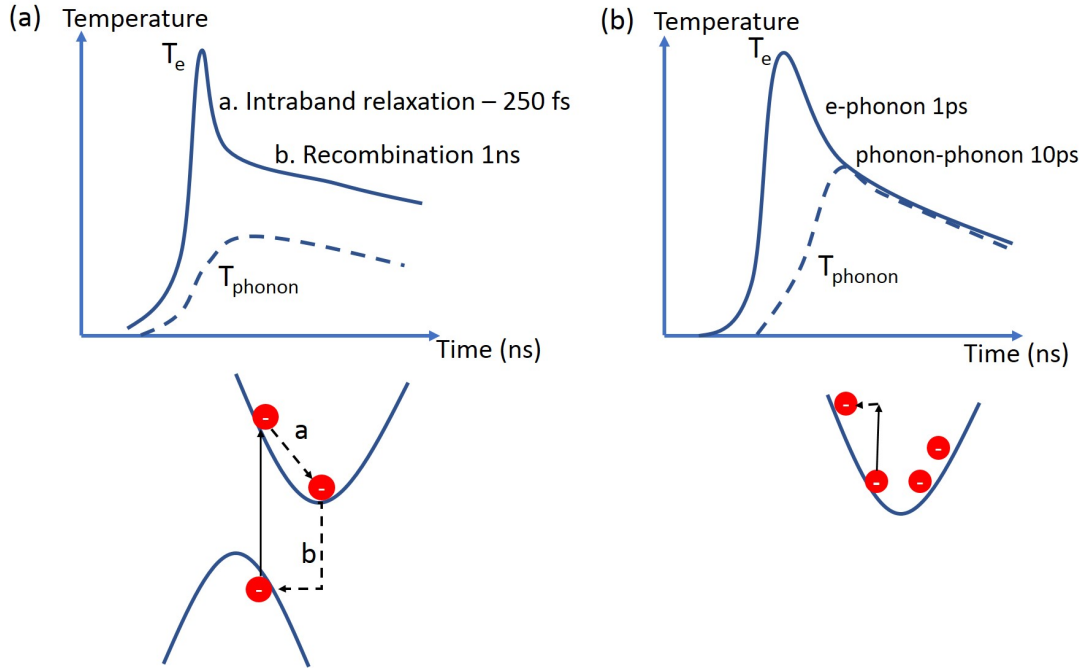



**Figure 7.2** – Temporal response of excited electrons and phonons in a typical indirect bandgap semiconductor (a) and metal (b). Correspondingly shown below each T(t) plot is the schematic sketch of the relevant optical processes in each kind of materials.

Silicon has an indirect bandgap of 1.1 eV, corresponding to a wavelength of $\lambda_{bandgap}$ = 1130 nm. When optically excited with a photon energy higher than its bandgap, electrons from the valence band of Silicon are promoted into the conduction band, establishing a new quasi-Fermi level which corresponds to a pump-induced occupation

of the conduction band. Here we are assuming that the pump photons come from a pulse laser with pulse width $\tau_p$. Multiple electron-phonon scattering events then occur: electrons lose their energies to phonons and subsequently relax to the bottom of the conduction band (denoted as process 'a' in the band diagram shown in Fig. 7.2(a)). Before this initial carrier relaxation process, a non-thermal carrier population exists for 10s fs while electron-electron scattering establishes a thermal population with a well-defined $T_e(t)$. After its peak, $T_e$ starts to decrease while $T_{phonon}$ rises. The decay of the long-time response is limited by nanosecond-scale interband recombination (denoted as process 'b' in Fig. 7.2(a)).

The temporal response of excited electrons in noble metals is also discussed here. This knowledge will be useful for our data analysis in the later sections of this chapter. For gold, interband transitions occur for $\lambda < 515$ nm, thus for a near IR pump wavelength of >700 nm, no interband transitions can take place. Instead, upon optical excitation, electrons available in the conduction band of gold are promoted to higher energy levels within the band. They then get scattered through electron-phonon interactions which occur in the picosecond timescale and phonon-phonon interactions which are slower, in the range of 10s of picoseconds. The different carrier decay mechanisms in semiconductors and noble metals lead to very distinct behaviour of $T_{phonon}$. While in metals, most of the energy from carrier relaxation is given to phonons, leading to the establishment of a thermal equilibrium between $T_e$ and $T_{phonon}$; in a semiconductor, phonon-assisted recombination is not the dominant process [170].

### 7.2.2 Pump-induced refractive index change in Silicon

Free electrons in Silicon exist in the conduction band for a few nanoseconds before they recombine with available holes in the valence band. Within this time frame, if another pulse of light is sent in with an energy smaller than the Silicon bandgap, this new beam will interact with the free electrons in the conduction band and will have its propagation properties modified as a result. In the experiments described below, a pump beam of $\lambda_{pump} = 820$ nm was used to excite electrons in Silicon from

the valence band to the conduction band and a time-delayed probe beam of $\lambda_{probe}$ = 1500 nm was also propagating through the material. Since $\lambda_{probe}$ = 1500 nm < $\lambda_{bandgap}$ = 1130 nm, interband transitions can only occur via two-photon absorption (TPA). TPA originates from a third order nonlinear process in Silicon which also leads to a modification in the real part of the refractive index, known as the Kerr effect. The probe beam can also interact with free electrons in the conduction band via free carrier absorption (FCA) and the carrier plasma effect, also known as the carrier-induced refractive index change. FCA promotes free electrons in the conduction band to higher energy levels within the band, changing the absorption coefficient hence $\Im\{n_{Si}\}$. These features are well understood and can be found in [171]. Here, we are more concerned with the potential magnitude of $\Delta n'_{Si}$ and $\Delta n''_{Si}$ that can be achieved in theory and the practicality of obtaining these values in experiments. The expressions for $\Delta n'_{plasma}$ and $\Delta n''_{FCA}$ are taken from [170, 171]:

$$\begin{aligned} \Delta n'_{plasma} &= [-8.8 \times 10^{-22} N_e - 8.5 \times 10^{-18} N_h^{0.8}](\frac{\lambda}{1.55})^2 \\ \Delta n''_{FCA} &= (2 \times 10^{-18} \lambda^2 N_e)/(2 \times 2\pi/\lambda) \end{aligned} \tag{7.1}$$

where $N_e$ and $N_h$ are the electron and hole densities.

We consider also the Kerr and the TPA effects alongside the FCA and dispersion. The magnitudes of third order nonlinear effects in Silicon are taken from a theoretical investigation of nonlinear properties of Silicon detailed in [172]. While the strength of FCA and the plasma effect depends on the excited carrier concentration in Silicon which is in turn a function of the pump power at $\lambda_{pump}$ = 820 nm, the magnitude of the third order nonlinear effects depends on the intensity of the probe beam at $\lambda_{probe}$ = 1500 nm, $I_{probe}$. To calculate $\Delta n'_{Kerr}$ and $\Delta n''_{TPA}$, we need an estimation of the field density of the probe beam. With a probe beam of approximately 300 $\mu$W, a laser system of repetition rate 80 MHz, a pulse duration of 150 fs and a spot area of approximately 16 $\mu m^2$, we achieve a beam intensity of $1.5 \times 10^{12}$ Wm$^{-2}$. The

dependence of $\Delta n'_{Kerr}$ and $\Delta n''_{TPA}$ on the beam intensity takes the form of [171]:

$$\begin{aligned} \Delta n'_{Kerr} &= n_{Kerr}(\lambda = 1500nm) I_{probe} \\ \frac{dI_{probe}}{dz} &= -\beta_{TPA}(\lambda = 1500nm) I^2_{probe} \end{aligned} \tag{7.2}$$

The values of $n_{Kerr}$ and $\beta_{TPA}$, the Kerr and TPA coefficients, are taken from [172]. We arrive at approximate values of $\Delta n'_{Kerr}$ and $\Delta n''_{TPA}$ in the order of $10^{-6}$.[b] Figure 7.3 shows a loglog plot of the magnitude of $\Delta n'_{Si}$ and $\Delta n''_{Si}$ as a function of carrier density. Carrier effects play a dominant role over third order nonlinear effects in manipulating $\Delta n'_{Si}$ and $\Delta n''_{Si}$ when N> $10^{18}$ cm$^{-3}$. Thus, we can approximate that $\Delta n'_{Si} \approx \Delta n'_{plasma}$ and $\Delta n''_{Si} \approx \Delta n''_{FCA}$ in this regime. In this high carrier concentration regime, $\Delta n'_{Si}$ is always two or more orders of magnitude larger than $\Delta n''_{Si}$ at the wavelengths considered. In this limit, we can assume that the effect of pumping Silicon mainly influences $\Re\{n_{Si}\}$ without disturbing $\Im\{n_{Si}\}$ much. For an active PTS system, $\Delta n'_{Si} \gg \Delta n''_{Si}$ is very useful as this facilitates the independent control of $\Re\{n_{Si}\}$ and $\Im\{n_{Si}\}$.

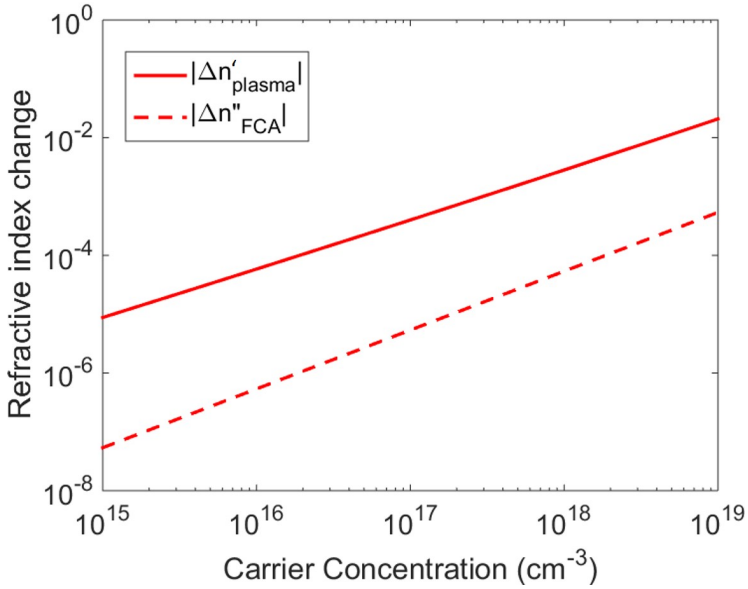



**Figure 7.3** – Various effects on the refractive index of Silicon as a function of carrier concentration at $\lambda = 1500$ nm. Note that the absolute values have been plotted.

[b] To solve Eqn. 7.2, the probe beam intensity is expressed as $I_{probe} = Ie^{-\alpha z}$ where $\alpha = 4\pi\Delta n''_{TPA}/\lambda_{probe}$.

## 7.3 Waveguide integrated pump-probe spectroscopy

Here, we aim to investigate how a typical indirect bandgap semiconductor changes its relevant optical properties when being exposed to light well above its bandgap. By performing two waveguide integrated pump-probe experiments, we are able to measure the magnitude of the modal index changes as a function of power, $\Delta n'_m$ and $\Delta n''_m$. The corresponding values of $\Delta n'_{Si}$ and $\Delta n''_{Si}$ can be inferred from these measurements via an overlap factor which links material properties in a waveguide environment to modal characteristics. While the inferred index changes of Silicon with pump power can be compared with theoretically predicted values to assess the accuracy of our measurement method, it is the modal index modulation, $\Delta n'_m$ and $\Delta n''_m$ that determines the effectiveness of the unidirectional reflection phenomenon.

### 7.3.1 Waveguide geometry and fabrication

A simple set of metallic gratings on top of a SOI wafer was used to experimentally investigate the pump-induced refractive index change of Silicon. The fabrication technique of the metallic gratings on top of a SOI wafer is identical to the description in Section 5.2. The SOI platform operated as a standard dielectric slab waveguide and the metallic gratings were responsible for coupling free space waves to the waveguide mode and vice versa. Figure 7.4(a) shows the theoretical simulation of the metallic grating efficiencies. Here the propagating mode is the fundamental TE mode of a slab waveguide with a core thickness of 220 nm. The fabricated devices were designed to have a grating period of approximately 540 nm with a filling factor of 0.4. For these grating parameters, we expect an in-coupling efficiency at $\lambda_{probe} = 1500$ nm of roughly 10%. Two grating configurations were employed: 2-coupler for $\Delta n''_{Si}$ characterization and 3-coupler for $\Delta n'_{Si}$ characterization. SEM images of these configurations are shown in Fig. 7.4(b) and (c).

### 7.3.2 Experimental apparatus

In order to characterize the dependence of the modal response $\Delta n'_m$ and $\Delta n''_m$ and hence the material response $\Delta n'_{Si}$ and $\Delta n''_{Si}$ on the carrier concentration, we utilized a time-resolved setup depicted in Fig. 7.5.

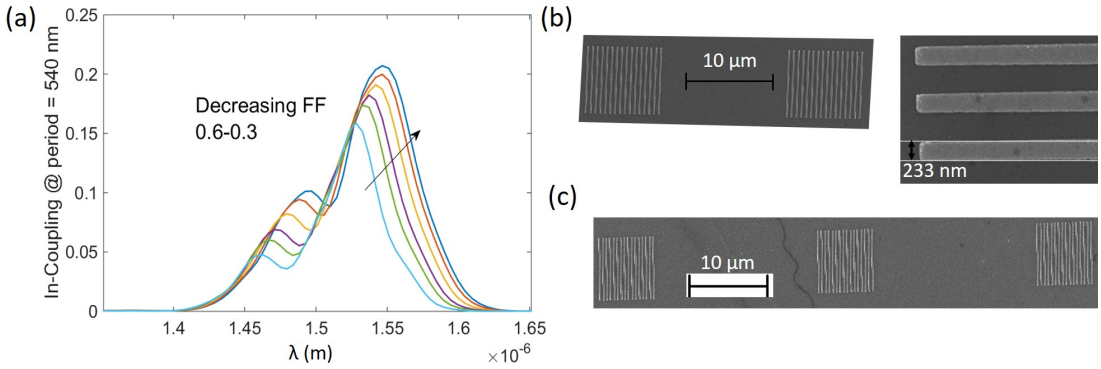



**Figure 7.4** – (a) Numerical simulation of the grating's in-coupling efficiency for a range of input wavelength from 1350 to 1650 nm. Various filling factor values were simulated. (b) SEM images of a 2-coupler configuration on SOI platform. (c) SEM images of a 3-coupler configuration on SOI platform.

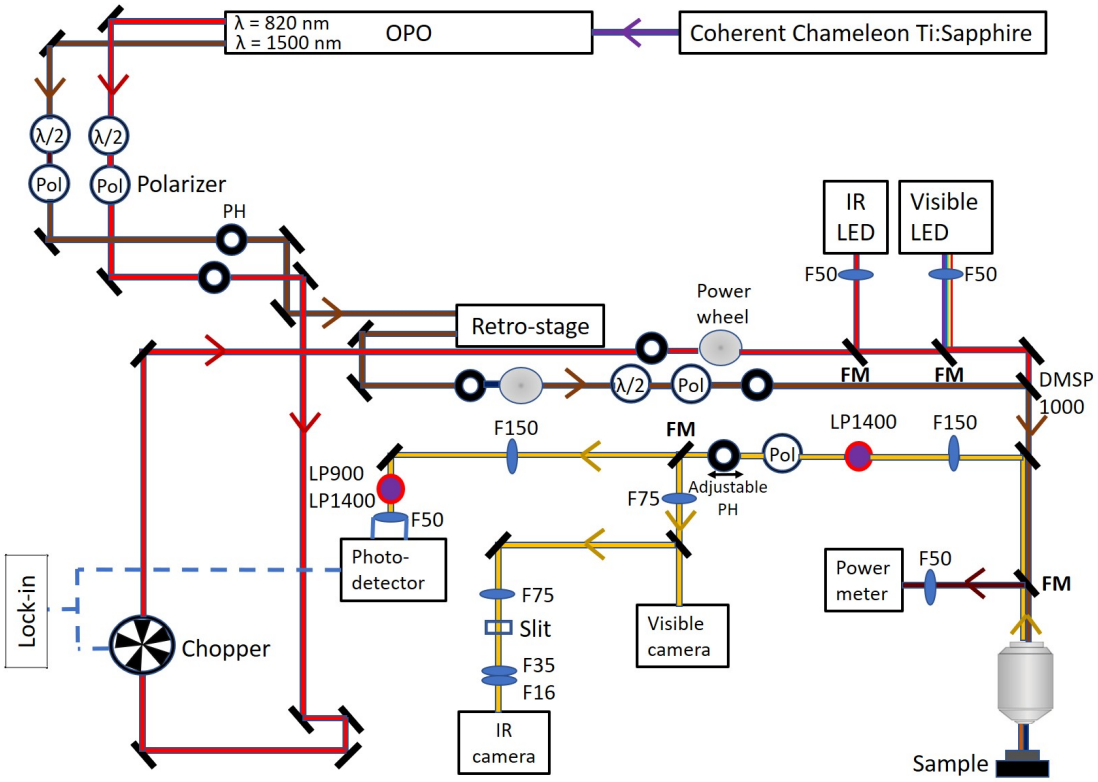



**Figure 7.5** – Time-resolved pump probe setup. Abbreviations: PH – pinhole, FM – flipper mirror, DMSP – shortpass dichroic mirror, LP – long pass filter.

Two beams of different wavelengths were sent down two independent lines and combined at the sample stage. The retro-stage as part of the probe line (brown lines)

was responsible for varying the path difference between the pump (red lines) and the probe, hence creating a temporal delay between them. The signal line (yellow lines) sent signals from the sample to either an imaging system consisting of an IR camera or a photo-detector. This photo-detector was connected to a Lock-in amplifier whose signal was modulated by mechanically chopping the pump beam. The Lock-in Amplifier facilitates low-noise measurements, allowing very small signal variations to be detected. However, it cannot resolve the signals spectrally and only measures the total integrated temporal response from the device. Along the signal line, a set of long pass filters was used to filter out the pump, leaving us with just the signal from the interaction between the probe and the pumped medium. This setup allowed an optimization procedure of the coupling processes and spatial separation of the pump and the probe on the sample to be performed.

### 7.3.3 The physics of pump-probe spectroscopy

When a pump beam and a probe beam are sent to the sample, temporally delaying the probe beam with respect to the pump can provide different snapshots of the system as carrier relaxation occurs. We define the delay time between the pump and the probe as the difference between their arrival time, $\tau_d$ and the temporal overlap of the two beams is $\tau_{overlap}$. A temporal scan of the overlap of the two beams is implemented:[c]

- $t < \tau_{overlap}$, $\tau_d < 0$: the probe arrives before the pump. No change in the behaviour of the material should be observed as the probe is not seeing any electronic modification in the material.

- $t > \tau_{overlap}$, $\tau_d > 0$: the probe arrives after the pump and has its propagation properties modified. As the carrier life time in Silicon is a few nanoseconds, we can assume that the excited carriers have already decayed substantially by the time the next pump pulse arrives.

[c]The range of this scan must fall within a single laser pulse temporal separation of 12.5 ns.

### 7.3.4 Experimental and data extraction procedure

#### $\Delta n''_{Si}$ measurement

Figure 7.6 shows a sketch of the measurement method implemented on a 2-coupler configuration to determine the influence of pumping above the bandgap ($\lambda_{bandgap}$ = 1130 nm, equivalent to 1.1 eV) on the absorption of Silicon at $\lambda_{probe}$ = 1500 nm, i.e., the effects of FCA in Silicon.

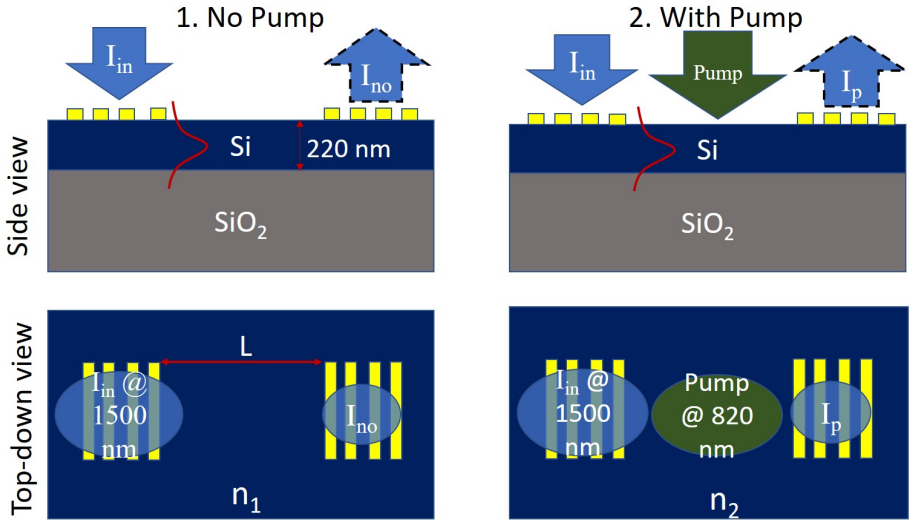



**Figure 7.6** – Side view and top-down view of metallic gratings on a standard SOI platform with a Si core thickness of 220 nm. Position of pump and probe beams on gratings.

A free space wave of intensity $I_{in}$ was coupled into the slab waveguide at one grating. This wave propagated along the waveguide and coupled out of the system via the second grating with an intensity, $I_{no}$ when there was no pump and $I_p$ when the pump was at work. We expected $I_p$ to reduce in value from $I_{no}$ as there were free carriers available in the conduction band to interact with photons from the probe beam. The relationship between $I_{no}$ and $I_p$ takes the form of:

$$\begin{aligned} I_{no} &= I_{in}\eta_{in}\eta_{out}|e^{i(n'_1+in''_1)KL}|^2 = I_{in}\eta_{in}\eta_{out}e^{-2n''_1KL} \\ I_p &= I_{in}\eta_{in}\eta_{out}|e^{i(n'_2+in''_2)KL}|^2 = I_{in}\eta_{in}\eta_{out}e^{-2n''_2KL} \end{aligned} \tag{7.3}$$

where $\eta_{in,out}$ signifies the in and out coupling efficiencies of the grating, $K = 2\pi/\lambda_{probe}$

and $n_{1,2} = n'_{1,2} + in''_{1,2}$ is the refractive index of the 'no-pump' and 'with-pump' Si slab. The transmission along the waveguide was modeled according to the Beer-Lambert relationship. An overlap factor between the modal field and the core layer, $\Gamma \approx 60\%$ was found. Thus, we could relate a change in the modal property, $\Delta n'_m$ and $\Delta n''_m$, to a change in the material property, $\Delta n'_{Si}$ and $\Delta n''_{Si}$, via $\Gamma$: $\Delta n'_m = \Gamma \Delta n'_{Si}$ and $\Delta n''_m = \Gamma \Delta n''_{Si}$ [133] (See Appendix G).

In deriving these relationships, we have made a few approximations. We assumed here that the coupling efficiency was not affected by the presence of the pump, which is valid when there is no spatial overlap between the pump spot and the grating. Even though the pump beam had a Gaussian profile, the power at the focus of the beam was averaged over the entire area illuminated in between the couplers. Thus, we assumed that the Silicon region between the gratings was illuminated uniformly, allowing us to treat this pumped area as an effective material with a new modal index of $n_2 = n'_2 + in''_2$.

The signal was spatially selected by closing a pinhole just around the second grating and spectrally filtering out the pump before reaching the photo-detector. The chopper played the role of a periodic beam block. When the pump hit the blade of the chopper, this corresponds to the configuration labelled '1. No pump' in Fig. 7.6; and when the chopper let the pump pass through, this is equivalent to '2. With pump' in Fig. 7.6. The Lock-in amplifier recorded a small difference between these two configurations, often denoted as $\frac{\Delta T}{T}$. The time-resolved experiment was implemented by running a scan of the probe's path length with respect to the fixed pump line, quantified by the delay time $\tau_d$. A time evolution of $\frac{\Delta T}{T}$ with respect to the relative pump-probe arrival time, as explained in Section 7.3.3, was recorded. At $\tau_d > 0$, we could use the information of $\frac{\Delta T}{T}$ at this point to quantify the magnitude of $\Delta n''_{Si}$ via:

$$\begin{aligned} \frac{\Delta T}{T} &= \frac{I_{no} - I_p}{I_{no}} = 1 - e^{2\Gamma \Delta n''_{Si} KL} \\ \Delta n''_{Si} &= ln\left(1 - \frac{\Delta T}{T}\right) / 2\Gamma KL \end{aligned} \tag{7.4}$$

### $\Delta n'_{Si}$ measurement

Since an interference pattern is sensitive to changes in the phase of initial light sources, this offers us a way to measure $\Delta n'_{Si}$. To measure the effects of pumping above the bandgap on $\Delta n'_{Si}$, we employed an optical setup which allowed small spatial shifts of the interference pattern of three beams to be detected. The temporal response of this system was investigated by combining this 3-beam interference setup with the pump-probe experiment described above.

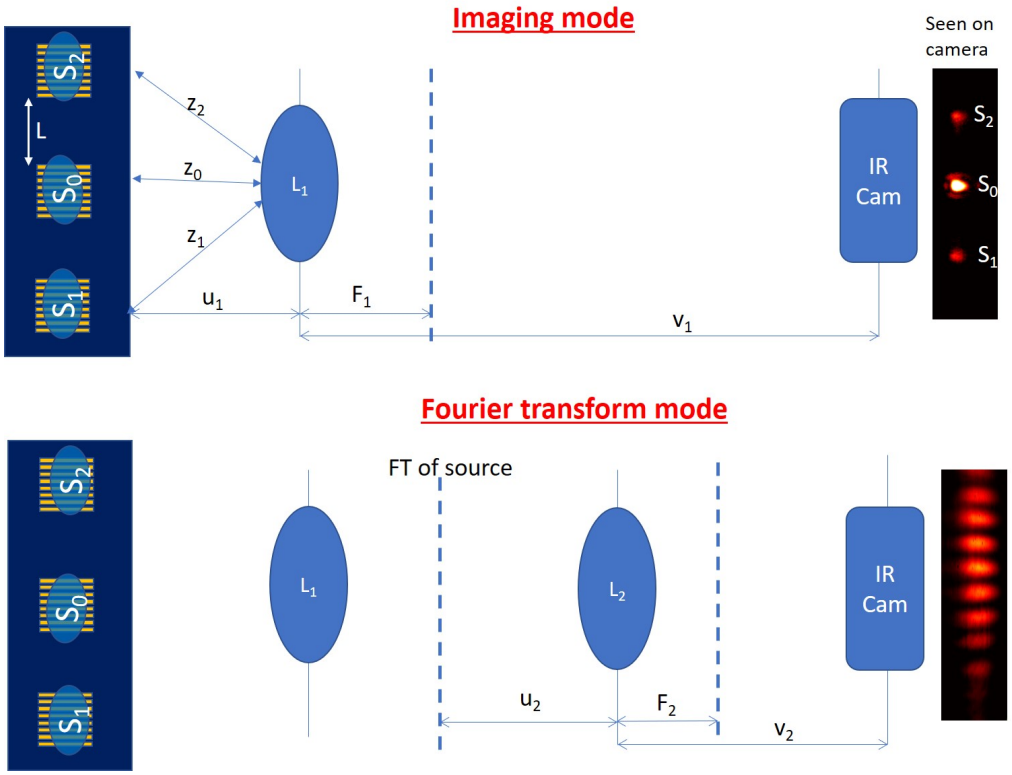



**Figure 7.7** – Two operational modes of the optical system: imaging and Fourier transform (FT) systems. $L_1$ and $L_2$ are lenses with focal lengths $F_1$ and $F_2$ respectively. Lens $L_2$ was mounted on a flipper mount to facilitate the switching between the two operational modes. The object to image under the Fourier transform mode can be thought of as the back focal plane of lens $L_1$. $z_{0,1,2}$ indicate the distance from source $S_{0,1,2}$ to lens $L_1$ where its diffraction pattern is formed.

The schematic of our 3-beam interference setup is depicted in Fig. 7.7. The second waveguide configuration shown in Fig. 7.4(c), a 3-coupler system, was used for these measurements. The probe beam was coupled into the system at the middle grating, then propagating in both directions with similar intensities and finally coupled out of the system at the end gratings. Our setup was able to operate in two modes: the

imaging mode and the Fourier transform mode. The imaging mode consists of a single lens which simply images the three light sources $S_{0,1,2}$ onto an IR camera. Note here that $S_0$ is not the input amplitude of the probe beam, but rather its reflection and $S_{1,2}$ are the electric field amplitudes of the transmitted light that has been scattered upward from the end gratings.

The three sources identified in the imaging mode were made to interfere via a projection onto the Fourier plane of lens $L_1$. Fourier optics dictates that using a thin lens, we can project the diffraction pattern of an object onto the back focal plane of that lens which is located at a distance equal to a focal length away from the lens itself. Using a second lens, $L_2$, we can image this diffraction pattern at the back focal plane of $L_1$ onto an IR camera, as seen in Fig. 7.7 'Fourier transform mode'. The fringe contrast of the interference pattern could have been improved by totally blocking $S_0$. However, this was not a simple task since the dimensions of the gratings were only a few microns across, making it difficult to accurately implement selective spatial blocking. We attempted to reduce the effect of $S_0$ by using a cross polarization technique. The gratings were designed to predominantly scattered TE light, defined as having an electric field parallel to the metallic bars. By using a 45 degree polarized input probe beam with respect to the metallic bars and installing a linear polarizer along the signal line, we could minimize the influence of $S_0$ on the final interference pattern. The mathematical formulation of our 3-source interference pattern has the form of:

$$\begin{aligned} &|S_0 e^{iKz_0} + S_1 e^{iKz_1} + S_2 e^{iKz_2}|^2 \\ &= \underbrace{|S_0|^2 + |S_1|^2 + |S_2|^2}_{0^{th}\text{ order}} + \underbrace{S_0 S_1 \cos(KL) + S_0 S_2 \cos(KL)}_{1^{st}\text{ order}} + \underbrace{S_1 S_2 \cos(2KL)}_{2^{nd}\text{ order}} \end{aligned} \tag{7.5}$$

The interference of three light sources leads to the superposition of three frequencies denoted as $0^{th}$, $1^{st}$ and $2^{nd}$ orders in Eqn. 7.5. The existence of these different orders could be further proven by performing a simple trick. An adjustable pinhole placed at the image plane of our optical system allowed us to select the individual light source that we would like to image. The schematic of such a selection process is presented

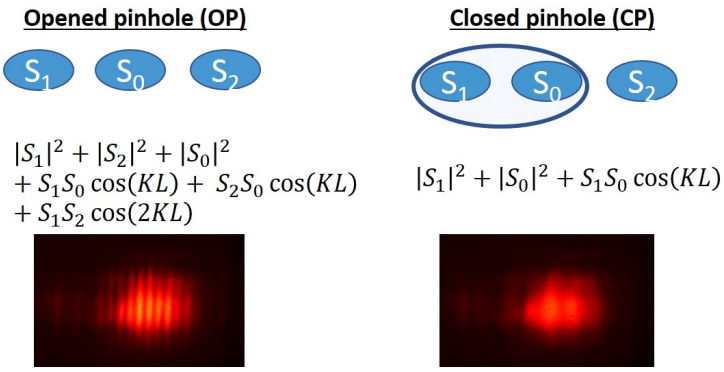



**Figure 7.8** – Selective interference of the three sources. When the adjustable pinhole is opened , we observe the interference pattern of all three sources at the camera; whereas when only two sources are selected ($S_0$ and $S_1$ in this case), the second order interference disappears.

in Fig. 7.8. When only $S_0$ and $S_1$ were selected (Closed pinhole configuration in Fig. 7.8), we could see that the second order interference coming from the interference of $S_1$ and $S_2$ disappeared, leaving just the first and the zeroth orders.

Taking this analysis a step further, using the fast fourier transform (FFT) and its inverse (iFFT), we recovered each component of the combined 3-source interference pattern both in frequency and time. Figure 7.9 demonstrates the process of FFT and iFFT. Firstly, an image of the interference pattern was taken. We then summed the counts along each column of pixels to get the total intensity plot. Next, the FFT was applied to this intensity pattern to determine its constituent frequency components. To recover the time variation of each component, we defined a bandpass filter around the frequency region of each interference order and implemented iFFT. It is worth noting that ideally the frequencies appear in FFT plots have the form of a Delta function. However, due to the limited data points available, i.e., the number of pixels on our camera (320x256), the FFT procedure only produced a frequency peak with a fairly broad linewidth, making it difficult to precisely define the diffraction order frequencies.

This process was applied to three interference patterns denoted as OP (Opened pinhole), CP (Closed pinhole) and Diff = (OP - CP). Depending on the relative magnitudes of the three orders, different components emerge in the FFT plots. For the case of OP, the $1^{st}$ order was suppressed as the magnitude of the other two orders

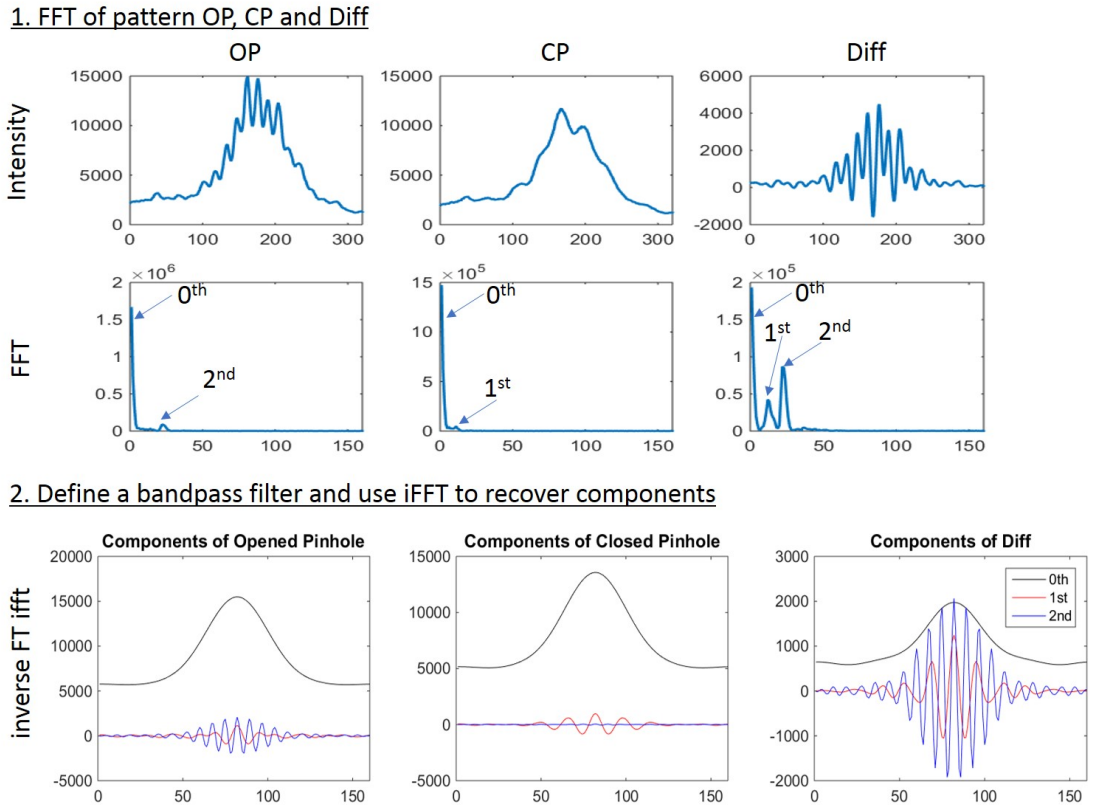



**Figure 7.9** – FFT and iFFT process of the three-source interference pattern for three measurements of interest: Opened pinhole (OP), closed pinhole (CP) and the difference between these two spectra (Diff).

dominated the spectrum. On the other hand, when the pinhole was closed, the interference of two sources only resulted in the generation of $0^{th}$ and $1^{st}$ orders. When the magnitude of the $0^{th}$ order was reduced by taking the difference between OP and CP, all three interference orders showed up in the FFT plot.

The 3-beam interference measurement was then combined with the time-resolved experiment in order to record the interference images at crucial temporal points, revealing the modified property of carrier-induced effects with respect to the temporal overlap of the two beams. The pump light was placed only at one arm of the three gratings, i.e., between $S_0$ and $S_1$ gratings as seen in Fig. 7.10.[d] Using the pump-probe method described above, the pump and the probe must also be overlapped temporally

[d]However, $\lambda_{pump} = 820$ nm cannot be effectively imaged using an IR camera. Instead the position of this beam was confirmed by using a visible camera and referencing the pump location with the gratings.

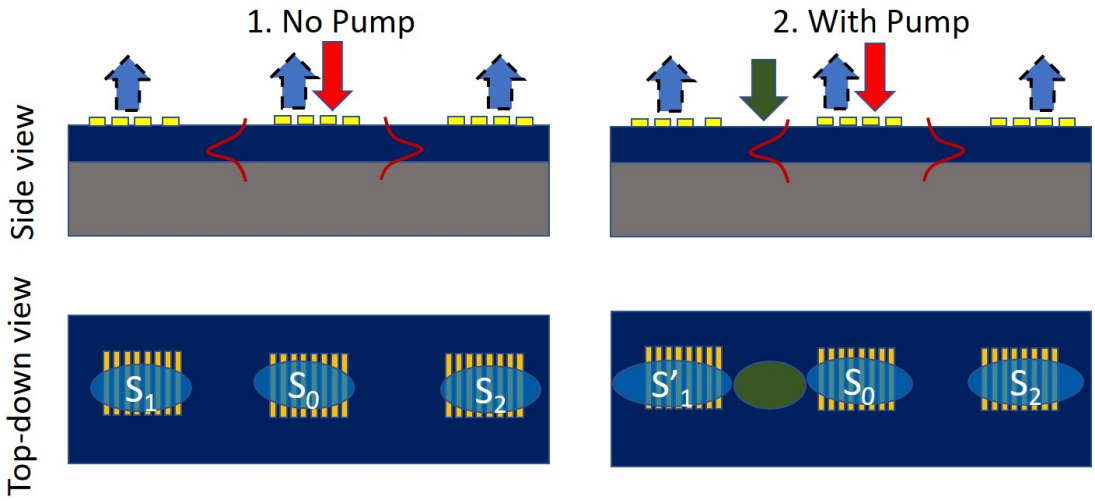



**Figure 7.10** – Schematic sketch of 3-beam interference when the pump is at work. The red and green arrows indicate the incoming probe and the pump beams respectively. The blue arrows describe the three interfering sources at the camera. $S_1'$ only differs from $S_1$ when the probe arrives after the pump.

in order to characterize pump-induced effects on the 3-beam interference pattern. Before the temporal overlap, the pump arrives after the probe; this is equivalent to the case where there is no pump at all, we expect to see results similar to Fig. 7.7. In contrast, when the probe arrives after the pump, the interference pattern is modified compared to Eqn. 7.5:

$$\begin{aligned}
&|S_0 e^{iKz_0} + S_2 e^{iKz_2} + S_1' e^{iKz_1}|^2 \\
&= |S_0 e^{iKz_0} + S_2 e^{iKz_2} + S_1 e^{i(\Delta n'_{Si} + i\Delta n''_{Si})\Gamma KL} e^{iKz_1}|^2 \\
&= |S_0|^2 + |S_1|^2 + |S_2 e^{-\Delta n''_{Si}\Gamma KL}|^2 + S_0 S_1 \cos(KL + \Delta\phi) \\
&+ S_0 S_2 \cos(KL) + S_1 S_2 \cos(2KL + \Delta\phi)
\end{aligned} \tag{7.6}$$

where $\Delta\phi = \Gamma \Delta n'_{Si} KL$ and $\Gamma \approx 60\%$ is the overlap factor.

### 7.3.5 Results of temporal responses of pumped silicon

#### Spatial and temporal overlap of the pump and probe beams

To find the temporal overlap of the pump and the probe, we first spatially overlapped both beams on a clean piece of Silicon and recorded the change in the reflection of the probe beam when the pump continuously supplied energy to the Silicon slab.

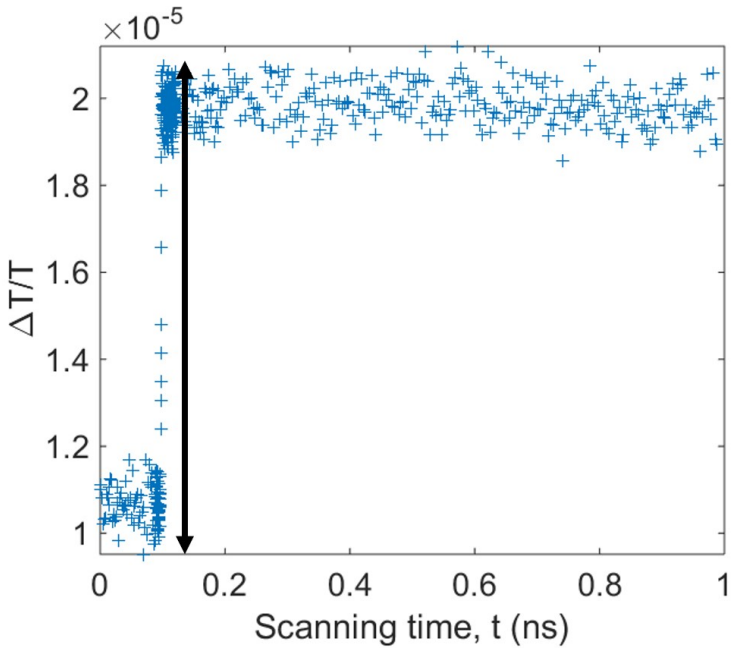



**Figure 7.11** – Finding the overlap of the pump and the probe beams on a piece of Silicon: spatially overlapping the two beams and scanning over the path length difference. A change in the $\frac{\Delta T}{T}$ signal signifies the overlap of the 2 beams.

Figure 7.11 shows the measured $\frac{\Delta T}{T}$ as a function of time for a Silicon substrate.[e] The scanning time corresponds to the position of the probe beam on the retro-stage. A change in the $\frac{\Delta T}{T}$ temporal spectrum signifies a change in the reflection of the probe beam. The onset of the rise of the step-function in Fig. 7.11 signifies the temporal overlap of the two beams. However, in this experiment, we are particularly interested in the magnitude of $\frac{\Delta T}{T}$, denoted by the length of the double arrow in Fig. 7.11. Within the scanning range of just above 1 ns, we did not observe significant decay of the $\frac{\Delta T}{T}$ signal as carrier life time in Silicon is a few nanoseconds [170].

### $\Delta n''_{Si}$ results

To measure $\Delta n''_{Si}$, the pump and the probe were spatially separated as depicted in Fig. 7.6. A similar temporal scan to the above was done and the change in the transmitted signal at the second grating was recorded (Fig. 7.12(a)). The background noise was

[e]There was no grating involved in this measurement. The reason why this Silicon only measurement is not sufficient is because the change in both $\Re\{n_{Si}\}$ and $\Im\{n_{Si}\}$ cannot be separated from this single measurement [173].

measured by moving both the pump and the probe away from the grating region and detecting a signal at the photo-detector (Fig. 7.12(b)).

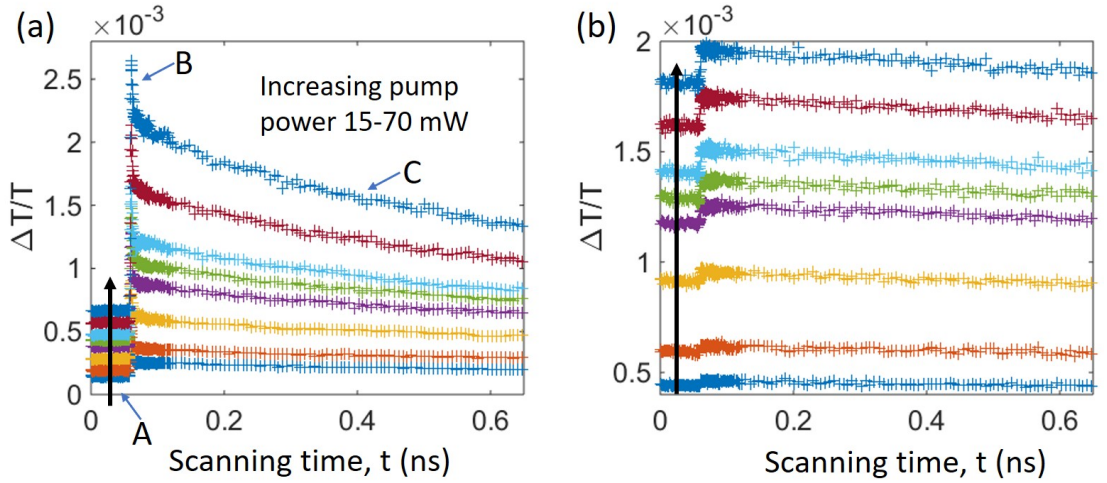



**Figure 7.12** – $\frac{\Delta T}{T}$ as a function of time for (a) when the probe is on the grating and (b) when both the probe and the pump are moved away from the grating area but remain spatially separated. The black arrows indicate the direction of increasing pump power from 15-70 mW while the probe power was kept at 150 $\mu$W. The blue arrows labeled A, B and C in (a) indicate 3 temporal points of interest. Note that feature B is missing in (b).

The temporal spectrum of $\frac{\Delta T}{T}$ possesses a few interesting features. Firstly, the magnitude of the base line, i.e., before the temporal overlap of the two beams occurs, increases with pump power. This increasing baseline can be associated with heating of the Silicon slab, which is not accounted for in the simple model of pump-probe. Heat dissipation might have taken longer than the pulse cycle of 12.5 ns between pulses. However, as we are only interested in the magnitude of the maximum rise of $\frac{\Delta T}{T}$, this offset does not contribute to the difference between $I_{no}$ and $I_p$.

Even though the magnitude of $\frac{\Delta T}{T}$ increases with pump power as expected, we noticed another unexpected feature in our $\frac{\Delta T}{T}$ temporal spectrum. Around 50 ps, a peak in the temporal response of the system appears (labeled B in Fig. 7.12(a)). When $\frac{\Delta T}{T}$ starts to decay, instead of a step-function-like decay as seen in Fig. 7.11, we observed a much faster decay in Fig. 7.12(a), suggesting another kind of light-matter interactions was at work. These fast decays can be associated with either intraband transitions in semiconductors or scattering processes in gold (Section 7.2.1). The femtosecond

regime of intraband transition reaches the limit of the resolution of our measurement method, thus, unlikely to be the mechanism behind this observation. However, the appearance of the metallic-like response in the temporal spectrum of $\frac{\Delta T}{T}$ suggests that the grating might have also been pumped by the 820 nm beam.

A typical laser beam has a Gaussian shape, regardless of how well the pump beam was positioned right in the middle of the two gratings, its tail could easily extend and touch the grating. This speculation is further confirmed by the behaviour of $\frac{\Delta T}{T}$ in Fig. 7.12(b). The fact that we actually detected a change in $\frac{\Delta T}{T}$ even when the probe was off the grating means that we had the pump and the probe spatially overlapped. The pure Silicon response from Fig. 7.12(b) resembles the result in Fig. 7.11 and has a larger amplitude of $\frac{\Delta T}{T}$ base lines compared to the mixed response of gold and silicon in Fig. 7.12(a).

We can single out this effect due to carriers in Silicon by decomposing the composite decay in Fig. 7.12(a) into its constituents. Figure 7.13 shows a typical example of how we can fit a triple exponential model to our data to separate the different components of the combined decay:

$$\frac{\Delta T}{T} = B_1 e^{-\frac{t}{\tau_1}} + B_2 e^{-\frac{t}{\tau_2}} + B_3 e^{-\frac{t}{\tau_3}} \tag{7.7}$$

Three temporal regimes were identified, together with three time constants: $\tau_1 = 2.4$ ps, $\tau_2 = 10$ ps and $\tau_3 = 2.4$ ns. These time constants were found by averaging the fitting coefficients across different pump powers. $\tau_1$ and $\tau_2$ can be associated with electron-phonon and phonon-phonon scattering in gold respectively while $\tau_3$ indicates the signature carrier recombination in Silicon. The time scale associated with Silicon response ($\tau_3$) is selected and the maximum change in $\frac{\Delta T}{T}$ due to this effect only is used to calculate $\Delta n''_{Si}$ according to Eqn. 7.4 (see Fig. 7.14(a)). The pump power can be converted into the carrier concentration, $N$ by evaluating the pump energy density and assuming that each pump photon absorbed by the Silicon slab creates an electron-hole pair. A calibration factor was also included to account for the absorption

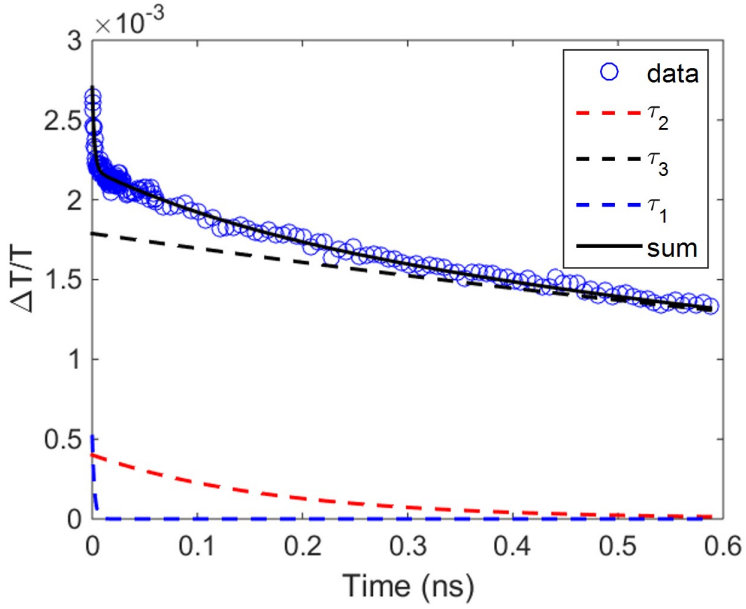



**Figure 7.13** – Fitting a three temperature model onto $\frac{\Delta T}{T}$ data, decomposing this combined decay effect into its three temporal regime: $\tau_{1,2,3}$.

efficiency of the measuring system, $< 5\%$. This includes the absorption factor of the 220 nm Si core based on transfer matrix method and the aperture coupling efficiency. The number of absorbed photons is then averaged over the beam path between the two gratings, leading to an approximated value of $N$. As expected, the magnitude of $\Delta n''_{Si}$ increases with the carrier concentration (Fig. 7.14(a)).

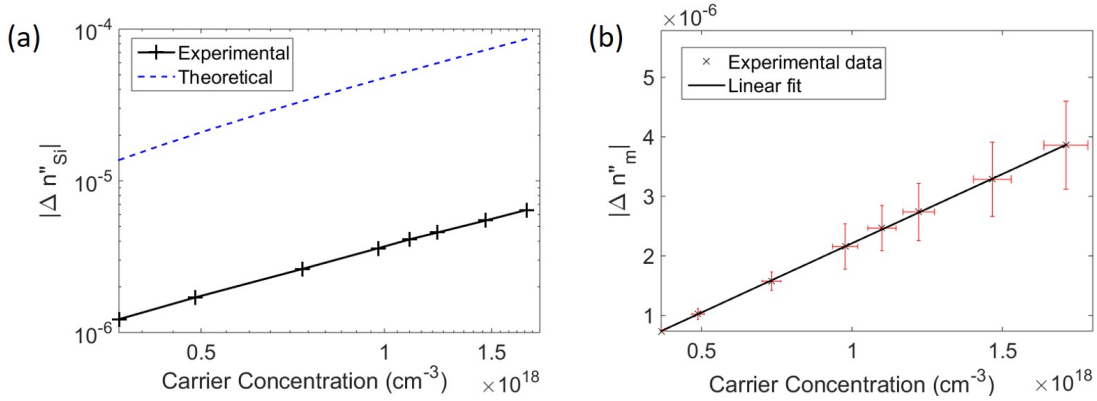



**Figure 7.14** – (a) $\Delta n''_{Si}$ as a function of carrier concentration for both experimental data and theoretically predicted values. (b) Experimental values of $\Delta n''_m$ as a function of carrier concentration. The power of the injected pump was converted into the number of photons fed into the system. This photon number is assumed to be equal to the number of electron-hole pair generated by the pump beam between the coupling gratings. L was taken to be 20 $\mu$m.

However, compared to the theoretical prediction of $\Delta n''_{Si}$, our result is approximately one order of magnitude smaller. Referring to Eqn. 7.4, the discrepancy between the experimental and theoretical values of $\Delta n''_{Si}$ suggests that the overlap between the pump and the grating might have reduced the in and out-coupling efficiencies of the grating. Since the effect of $\Delta n''_{Si}$ is expected to be small and is hence very sensitive to any changes to the resultant light intensity, a small reduction in the grating's coupling efficiency can greatly reduce the accuracy of our $\Delta n''_{Si}$ measurement. The one order of magnitude difference mentioned above can be accounted for by a decrease in the in and out coupling efficiency of the grating by less than 2%.

Figure 7.14(b) shows the corresponding experimental values of $\Delta n''_m$ as a function of carrier concentration. Above a carrier concentration of $5 \times 10^{17}$ cm$^{-3}$ as shown in Fig. 7.14(b), the magnitude of $\Delta n''_m$ is on the order of $10^{-6}$.

### $\Delta n'_{Si}$ results

The interference pattern of the three sources described above was taken at the temporal points A, B and C which are illustrated in Fig. 7.12. When the pump arrives after the probe; this is equivalent to point A. In contrast, at positions B and C, the probe arrives after the pump, influencing the resultant interference pattern. The biggest changes, a lateral shift and a decrease in the amplitude of the interference pattern, were found between the interference patterns recorded at A and B. No significant difference was observed when the pump beam was placed at locations equivalent to points B and C on the retro-stage.

The results of $\Delta n''_{Si}$ measurements suggest that the technique suffers from the spatial overlaps between the pump and the probe and also between the pump and the grating. These experimental limitations led to various uncertainty factors in estimating the intensity change of the interference pattern between points A and B. Thus, our 3-beam interference method could not give a reliable evaluation of $\Delta n''_{Si}$. Nonetheless, the magnitude of the lateral shift of the interference pattern could still be used to estimate $\Delta n'_{Si}$ as this value depended on the phase rather than the amplitude of the detected fields.

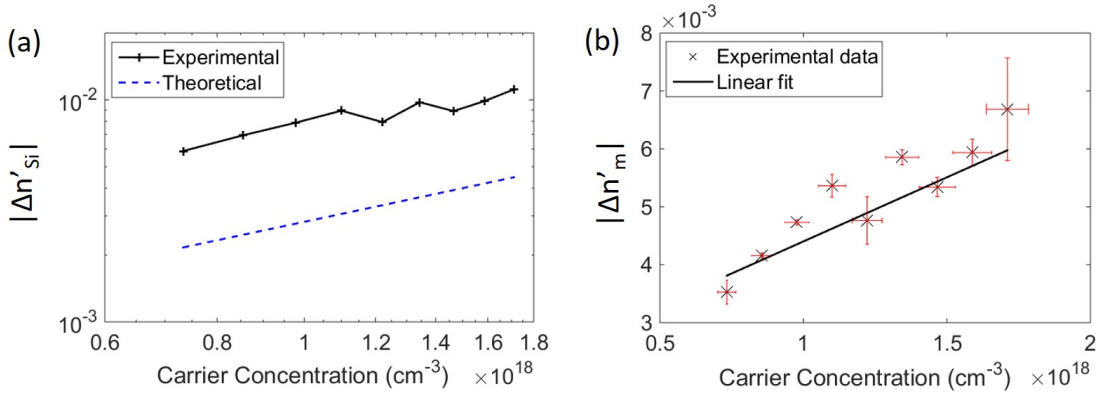



**Figure 7.15** – (a) $\Delta n'_{Si}$ as a function of carrier concentration for both experimental data and theoretically predicted values. (b) Experimental values of $\Delta n'_m$ as a function of carrier concentration. L was taken to be 20 $\mu$m.

After decomposing the interference pattern into its constituent frequencies, FFT allows us to extract the phase of each component. Using the $2^{nd}$ order diffraction, the phase difference between point A and point B was converted into $\Delta n'_{Si}$; this result is shown in Fig. 7.15(a).[f] We observed a general trend of increasing $\Delta n'_{Si}$ with increasing carrier concentration. More importantly, the magnitude of $\Delta n'_{Si}$ matches the predicted values within one order of magnitude. Figure 7.15(b) shows the measured modal response of the carrier-induced dispersion effect, with a maximum value of $|\Delta n'_m|$ being $\sim 0.007$. In the high carrier concentration regime, the increase of $\Delta n'_{Si}$ with pump power slowed down. When pumping above $N = 1.5 \times 10^{18}$ cm$^{-3}$, we noticed that the fringes became blurry at point B and no distinct fringes were formed. This phenomenon could either be attributed to the degenerate point of Si or to the enormous thermal energy in the material at high pump power. Since our carrier concentration calculation suggests that the maximum carrier concentration achieved was $< 2 \times 10^{18}$ cm$^{-3}$, five times smaller than the degenerate point of Silicon at $10^{19}$ cm$^{-3}$, it is likely that heating effects played the central role in diminishing the index response of Si. A higher accuracy was achieved in $\Delta n'_{Si}$ measurements compared to $\Delta n''_{Si}$ measurements because a phase dependent measurement is less susceptible to the pump-grating overlap problem than one that relies on the field intensity evaluation.

[f] Note here that we can implement similar procedure on the $1^{st}$ order as its interference pattern was also influenced by the pump, however, we found that as the amplitude difference between $S_0$ and $S_1$ was so large that this phase change was not as dominant as in the $2^{nd}$ order interference, hence giving less accurate results.

In theory, we can also directly convert a spatial shift seen on camera to a change in phase without invoking FFT and iFFT. Although these lateral shifts could be seen by eyes in the experiment, the actual shift was only within 2 to 3 pixels due to experimental limitations, rendering this direct calculation impractical. However, a quick back-of-the-envelope conversion between a physical lateral shift and $\Delta n'_{Si}$ gives us a value that has the same order of magnitude as those shown in Fig. 7.15, further confirming the validity of FFT approach.

## 7.4 Preliminary work

### 7.4.1 Construction of Si-based active PTS gratings

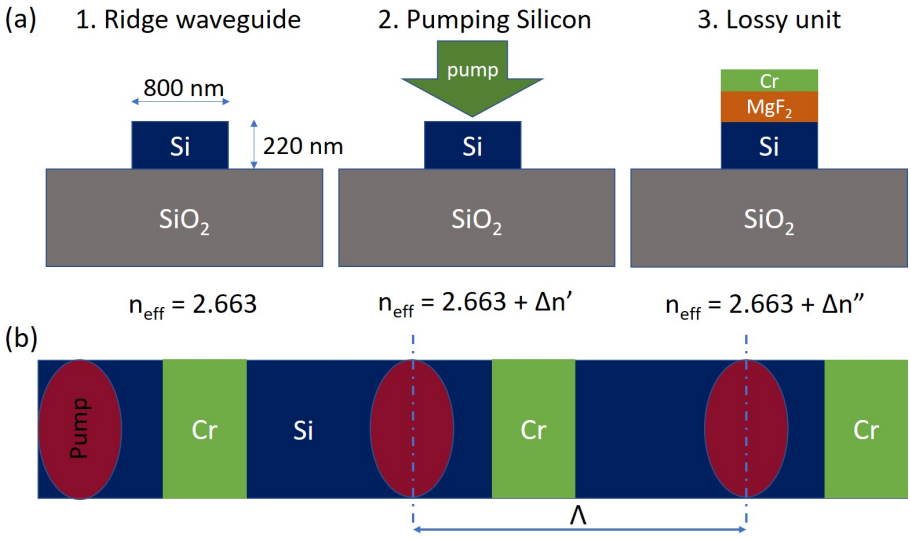



**Figure 7.16** – (a) Cross-section of the active PTS grating: 1. Ridge waveguide: $n_{eff} = 2.663$ without index perturbation; 2. Lossless unit: pumping Si to create a change in $\Delta n'$; 3. Lossy unit: depositing $MgF_2$ and Cr with appropriate thicknesses to achieve desired PTS grating index profile. For $T_{Cr} = 10$ nm and $T_{MgF_2} = 79$ nm, we achieved a mode of $n_{eff} = 2.663 + i0.02$. (b) Pumping strategy to establish the required $\Re\{n\}$ distribution for active PTS gratings.

Section 7.3.5 shows that the magnitude of $\Delta n'_{Si}$ is above 2 orders of magnitude larger than $\Delta n''_{Si}$ in the high pump regime; hence, pumping effects on $\Im\{n_{Si}\}$ can be neglected. This result is encouraging, proving the feasibility of constructing a similar PTS index profile as that shown in Fig. 7.1 using an active control, albeit the smaller

magnitudes of $\Delta n'$ and $\Delta n''$. Here $\Delta n'$ and $\Delta n''$ are equivalent to the modal charateristics $\Delta n'_m$ and $\Delta n''_m$ described in Section 7.3.

Assuming that the maximum achievable magnitude of $\Delta n'_m$ in Silicon active configuration is only on the order of 0.02 at the high carrier concentration regime ($N \sim 10^{19}$ $cm^{-3}$), much less than $\Delta n' = 0.15$ demonstrated in passive PTS [36], we require very delicate design of the lossy units to achieve the EP at $|\Delta n'| = |\Delta n''|$. A similar approach to [36] can potentially be followed: using two materials of appropriate thicknesses to obtain perfect phase matching with a loss amplitude of $\Delta n''$ on the order of 0.02.[g] The cross-section of the ridge waveguide, lossless units (pumped regions) and lossy units are depicted in Fig. 7.16(a). Owing to the availability of fabrication facilities in our group, $MgF_2$/Cr bars were considered for the construction of the lossy units. Figure 7.16(b) shows a schematic sketch of the spatial positioning of the optical pumping mechanism that generates a similar index distribution to that described in Fig. 7.1. The Si bars of passive PTS gratings are replaced by a spatially selective pumping strategy.

With these values of $\Delta n''$ and $\Delta n'$, using a simple 1D analytic model of PTS gratings described in Section 2.4.2, we can approximate potential values of the backward and forward reflections, $R_b$ and $R_f$, based on Eqn. 2.22. Here, a slab waveguide of 220 nm Si core thickness clad with $SiO_2$ and an index modulation of $|\Delta n''| = |\Delta n'| = 0.02$ were simulated. Figure 7.17(a) shows the theoretical prediction of the spectra of $R_f$ and $R_b$. With the current grating length, $L_g = 50\Lambda \sim 27\ \mu m$, a maximum contrast ratio, defined as $C_m = |max(R_f) - max(R_b)|$, of just above 10% is achieved. The small red-shift of the peak value from $\lambda_{Bragg} = 1500$ nm due to the lateral shift of the grating units (discussed in Section 2.4.2) is also seen here. The contrast ratio can be improved by increasing the length of the grating, $L_g$, as illustrated in Fig. 7.17(b). The increase in the contrast ratio with longer $L_g$ slows down once the grating length reaches approximately 80 $\mu m$, equivalent to a grating of 160 periods.

[g] There are many ways in which materials and shapes of these lossy units can be chosen.

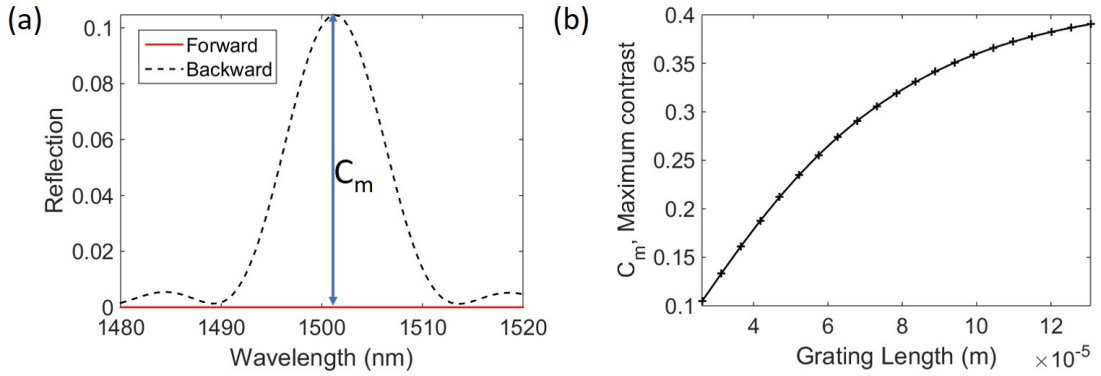



**Figure 7.17** – (a) Theoretical prediction of the potential forward and backward contrast ratio when $|\Delta n''| = |\Delta n'| = 0.02$ and the grating length, $L_g = 50\Lambda$. (b) Maximum contrast ratio between $R_f$ and $R_b$ as a function of grating length.

### 7.4.2 Fabrication

The first step in our preliminary work on device fabrication was carried out. An SEM image of the fabricated device is shown in Fig. 7.18.[h] The design consists of a long ridge waveguide with two U-shape couplers. In-couplers and out-couplers, numbered 1 and 6 in Fig. 7.18(a), are placed at the ends of the waveguide. The symmetric U-shape couplers, numbered 2-5, allow backward and forward reflection properties to be examined. The PTS index modulation will be positioned within the two blue dash lines which define the boundaries of the actual grating region. The detailed dimensions are given in Fig. 7.18(b-d), listing the required dimensions for a 50/50 U-shape beam splitter. For an initial input at the in-coupler 1, the transmission at the out-coupler 3 represents 50% of the initial input while the output at the out-coupler 2 measures 50% of the forward reflection, $R_f$. Similarly, for an initial input at the in-coupler 6, the measurement at the out-coupler 5 signifies 50% of the backward reflection, $R_b$.

Since this is only the first round of our fabrication work, there remains a few problems with our samples including residues on sample surfaces, rough side walls, overetching of the Silicon ridge and misalignment of EBL write fields. Though, our current PTS grating has $L_g \approx 27\ \mu m$ (indicated by blue dash lines in Fig. 7.18(a)), this particular design of a ridge waveguide and couplers can be further optimized

[h]The fabrication of these devices using Si-etching was done by Dr. Michael P. Nielsen. I was in charge of designing the devices using CAD and imaging them using SEM.

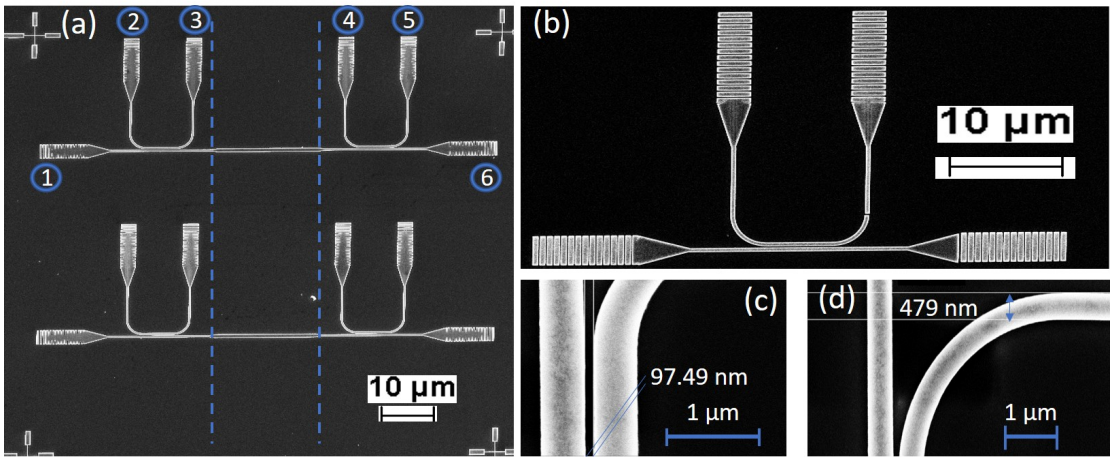



**Figure 7.18** – SEM images of potential designs of active PTS gratings. (a) Two full PTS gratings. The blue dash lines indicate the potential PTS region. (b) A single U-shape coupler. (c-d) Dimensions of detailed structures.

to achieve a longer value of $L_g$. Also, the complete design of an active PTS is not restricted to the index modulation based on the second order of Bragg diffraction presented in Fig. 7.1 or the device design shown in Fig. 7.16.

## 7.5 Summary

In this chapter, we investigated the feasibility of constructing an active PTS grating on a standard SOI platform. The two most important aspects of turning a conventional passive PTS grating into an active one are materials and device designs. As part of the preliminary work on active PTS, we focused on the experimental validation of optically pumping Silicon to generate PTS index modulation. Our time-resolved pump-probe and 3-beam interference experiments showed that in the high pump regime, the magnitude of $\Delta n'_{Si}$ is about two orders of magnitude larger than $\Delta n''_{Si}$, making Silicon a promising material for active PTS control. While $\Delta n'_{Si}$ results agreed reasonably well with theoretical prediction, our results for $\Delta n''_{Si}$ differed from theoretical values by one order of magnitude. We associated this discrepancy with the problem of overlapping pump beam and gratings.

The design aspect of active PTS was also discussed. The proposed design was based on the second order of Bragg diffraction. The experimental demonstration of such a

design requires the construction of an amplitude mask, which adds extra complication to the current fabrication flow, though readily fabricated using our current technique. The beauty of a PTS grating lies in the freedom in configuring an index modulation that matches the symmetry requirement of the system. If an appropriate modulation satisfying these requirements is found, a simple light induced photorefraction pumping strategy [174] can be used to actively control the index modulation, further proving the versatility and usefulness of active PTS gratings.

It is important to emphasize that the analysis of PTS gratings in this chapter assumed a purely real effective coupling coefficient between the forward and backward propagating modes even when only loss was present, resulting in the prediction of total elimination of reflection in one direction (Fig. 7.17(a)). However, as discussed in Chapter 6, this assumption can be refined further to include a complex coupling description which takes into account the asymmetry of the mutual coupling coefficients when non-ideal PTS situations arise. In practice, the magnitude of $R_f$ does not quite reach zero [36], due to the difficulty in precisely building the PTS index requirement and also the intrinsic limitation originated from complex coupling mechanism in imbalanced gain and loss PTS systems.

# Chapter 8

# Conclusion

## 8.1 Summary

The scientific goals first mentioned in Chapter 1 were to investigate the practicalities of nanophotonic devices where loss could be compensated by gain and loss manipulation played a role in the device operation.

Plasmonic lasers were chosen as a suitable platform to analyze the interplay between loss and gain in achieving lasing action. The problems associated with bottom-up approach were eradicated by employing a top-down hybrid gap plasmon waveguide (HGPW) design which enabled both the plasmonic cavity and feedback to be lithographically defined in the same fabrication step. Passivated suspended GaAs membranes provided sub-diffraction limit confinement and at the same time greatly reduced detrimental effects of surface recombination in semiconductors. Clearly, the gain supplied by our 100 nm thin GaAs membranes, in the range of 1300 - 2000 $cm^{-1}$, was sufficient to overcome the high cavity and modal losses of such a design. The gold slabs allow potential electrical injection with a required current density of approximately 6 - 8 $kAcm^{-2}$ to be realized. It was found that in the high pump regime, the effect of carrier-induced refractive index change in GaAs was severe, leading to deviations of the laser behaviour from numerical simulations. Though, a significant step was made in bringing plasmonic nanolasers closer to practical applications by having a flexible design, simple fabrication steps and efficient lasing actions, a few problems still need to be addressed including the use of non-CMOS compatible materials and

concerns over membrane snapping and its quality in the extremely high pump regime.

The second objective was to explore novel physical concepts that empower useful operation of loss. We investigated the physics of Parity-Time Symmetry (PTS) and its application in optics, focusing once again on problems that prevent PTS optical devices from making it to practice. Two main problems were identified. The first, associated with gain-induced dispersion effects which are prevalent in the high gain/loss regime, was theoretically investigated in the context of PTS coupled waveguides. The smooth transition at the EP was quantitatively analyzed using CMT parameters, showing excellent agreement with numerical solutions. A method to recover PTS characteristics in this highly dispersive system was found by introducing a net gain/loss into the system together with a geometric asymmetry in order to satisfy the condition $(f_2(x)(\epsilon_1'' + \epsilon_2''))/(f_1^*(x)\delta\epsilon) \ll 1$. The effectiveness of such a recovery mechanism was confirmed by quantitatively assessing the phase rigidity and the $\eta$ factor.

The other issue with practical passive PTS devices was its inflexible operation that hindered an active control of gain and loss. In the context of passive PTS Bragg gratings, their application as optical diodes was greatly impeded by the inability to tune the EP dynamically. The first few steps in assessing the feasibility of implementing SOI-based PTS active Bragg gratings were made. The most fundamental question we needed to answer was whether pump-induced effects in Silicon could establish the required PTS index profile. A two orders of magnitude difference between $\Delta n_{Si}'$ and $\Delta n_{Si}''$ was found in the high pump regime using our waveguide integrated pump-probe spectroscopy and 3-beam interference experiments. This finding makes Silicon a promising material for an active PTS control. The preliminary results on the device fabrication using Si-etching were also presented, further proving the versatility and usefulness of active PTS gratings.

The device footprints of PTS coupled waveguides and Bragg gratings can be further reduced by working with plasmonic guiding structures. The observation of lasing in hybrid gap plasmon GaAs lasers confirms the viability of extending optical PTS to

plasmonic platforms where high gain can be efficiently generated to compensate for the relatively large losses. Optical PTS with its clever manipulation of gain and loss offers a variety of configurations which do not only make use of loss for useful photonic applications but also allow carrier-induced effects to be part of the device operation.

## 8.2 Future work

A few subsequent lines of work stemmed from the results presented in this thesis can be implemented to confirm the validity of our approach and further improve our understanding of the systems of interest.

### 8.2.1 Plasmonic lasers

Though, lasing actions were demonstrated in hybrid gap plasmon GaAs lasers, several characteristics of lasing actions can be further investigated such as coherence. The device width was restricted to $\sim 195$ nm in order to draw comparisons amongst different designs: 1-step, 2-step and DBR-only. However, the study of width dependence lasing actions based on HGPWs can shed light into the behaviour of the system in the extreme plasmonic regime of small widths. As the hybrid mode gains a more plasmonic character with decreasing gap width, we would expect the modal loss to increase significantly. Our insights into the strong carrier-induced refractive index effects in GaAs can help us improve the efficiency of the lasing process. Laser feedback is directly linked to the cavity loss. Future studies can also look into ways of reducing the current cavity loss such as using curved gratings instead of conventional Bragg gratings as reflectors.

One key feature of our laser designs was the taper that aided the adiabatic guiding of light from the grating region to the gap. Also, the DBRs were designed to give the highest reflectivity to the fundamental mode. Thus, by extending our current study to cover a wider range of widths and even different spacer thicknesses, together with our knowledge of the theory of optical loss/gain in GaAs, we can map out the loss profile of the HGPW mode, further consolidating the work presented here.

The adiabatic nature of our taper can also be explored further by fabricating lasers of different taper lengths and widths and measuring their back reflection. A truly adiabatic taper would have a back reflection coefficient close to zero. Non-adiabatic guiding of the taper could hamper the efficiency of our lasers. Finding the theoretical/experimental limit at which the guiding of light in such a hybrid structure stops being adiabatic can help us optimize the taper length of our laser designs.

Tackling the issue of large dispersion in the high gain regime identified in Chapter 5 is also an interesting direction that subsequent work can follow. Currently, the large dispersion originates from the material aspect of the design. High gain often associates with large dispersion. Composite multilayer semiconductor gain materials can be considered to tailor the desired spectral response of the laser device in the required threshold regime. Correspondingly, the DBR stopband also needs to be engineered to match the spectral response of the gain medium. Here, the gain analysis outlined in Chapter 4 and Chapter 5 can provide us with insightful information about the threshold gain, the peak gain and its spectral characteristics to design the necessary DBR's spectral properties.

Going beyond this current hybrid plasmonic-photonic structure, the idea of a nanolaser based on GaAs membranes can be combined with the Tamm state notion where a combination of a vertical cavity and a plasmonic gap structure can further simplify the fabrication procedure and improve the durability of the membranes.

### 8.2.2 PTS optical devices

As explained earlier, the investigation of an active PTS Bragg grating is an ongoing project. The following aspects of Silicon-based active PTS gratings can be further investigated to achieve optimum operations.

Firstly, several aspects of the experimental method can be improved to increase the accuracy of $\Delta n'_{Si}$ and $\Delta n''_{Si}$ measurements. The estimation of carrier-induced effects depends on the approximation of the shape of the pump beam. The problem of overlapping pump and gratings can be reduced by using optical elements to shape the

beam as desired. However, the 20 $\mu$m length separation between the gratings is rather short for efficient shaping to be implemented. It should be emphasized here that there is a trade-off between reducing the pump-gratings spatial overlap and increasing the uniformity of the intensity density of the pump beam without using an amplitude mask to aid the pumping process.

The heating effect that damages the carrier-induced refractive index change in Silicon at the high pump regime can be reduced by pulse picking the pump beam—similar to the experimental method used in Chapter 5 to lessen thermal influences on the GaAs nanolasers.

Secondly, the implementation of a pumping mechanism that can establish the required spatial distribution of $\Re\{n(z)\}$ is challenging. This is because our proposed grating has a filling factor of 0.25. A standard method of creating a photorefractive grating of arbitrary filling factors is to employ an amplitude or phase mask. An amplitude mask can spatially block the pump beam in the region where $\Delta n' = 0$. On the other hand, a phase-shift mask has non-uniform optical thickness; hence light passing through this mask will experience a phase change. Light from different regions of the mask interferes and with appropriate thicknesses, an interference pattern with a periodicity and a filling factor equivalent to the desired index modulation can be achieved. Even though amplitude masks can give us exactly what we need for a PTS index modulation, it adds an extra complication to our fabrication flow and somewhat takes away the active component of the device as the mask would be created at the fabrication level. This mask must be made out of a material that transmits light at 1500 nm while absorbing or reflecting at 820 nm. One candidate could be Titanium Oxynitride [175].

A simpler pumping method is called light-induced dynamic grating. In brief, instead of a single pump beam, we can split this beam into two and make them interfere on the sample to create regions of dark fringes and bright fringes, thus, selectively pumping different regions of silicon. However, this mechanism will always result in a light-induced dynamic grating of a filling factor of 0.5, regardless of the incident

angle [174]. Recall that the 0.25 filling factor arises from the fact that we proposed a PTS Bragg grating based on the second order Bragg grating. A clever design of the PTS index profile using the first order diffraction can potentially allow such a 2-beam interference pumping mechanism to be implemented.

Thirdly, going beyond Si, we can explore other materials which have strong dependence of either the real or imaginary parts of their refractive indices on optical pumping and possess interesting non-linear optical properties.

Fourthly, an extended complex coupling mechanism investigation in contradirectional mode coupling can be carried out. The theoretical analysis of complex coupling mechanism in the context of PTS coupled waveguides can well be applied to PTS optical gratings, providing a convenient practical platform to assess the degree of imperfect PTS and the effectiveness of potential healing processes. An active PTS grating facilitates various tuning mechanisms of the parameter space, bringing us ever closer to the actual exceptional point and allowing the intrinsic limitations put in placed by the complex coupling mechanism to be experimentally quantified.

Finally, the simple coupled GaAs waveguides can be turned into lasers by adding appropriate feedback mechanism, facilitating the study of PTS in the spatiotemporal domain of nanophotonics. It would also be very interesting to apply the aforementioned PTS optical concept to plasmonic waveguides such as the HGPW, combining the novel concepts of sub-diffraction limit confinement and optical non-Hermiticity. Since the theoretical investigation of recovering PTS in coupled waveguides provided us with a thorough understanding of the physics in the highly dispersive regime, we can now design devices with high gain/loss functionalities without upsetting the delicate PTS index profile.

PTS coupled lasers can be studied using the suspended GaAs membrane configuration. The demonstration of plasmonic nanolasers based on suspended GaAs membranes presented in Chapter 5 and the bias pumping mechanism of PTS coupled waveguides proposed in Chapter 6 lay the foundation for PTS coupled nanolasers. By

bias pumping these two codirectional couplers, we can control their coupling length, which in turn allows us to tune the amount of energy being transferred between the two waveguides at the spatial locations of the laser feedback, effectively turning the lasing action on and off at will.

# References


[1] J. Bardeen and W. H. Brattain. "Transistor, a semiconductor triode". *Proceedings of the IEEE*, 86(1):29–30, 1948.

[2] W. Shockley, M. Sparks, and G. K. Teal. "p-n Junction Transistors". *Physical Review*, 83(1), 1951.

[3] W. F. Brinkman, D. E. Haggan, and W. W. Troutman. "A history of the invention of the transistor and where it will lead us". *IEEE Journal of Solid-State Circuits*, 32(12):1858–1864, 1997.

[4] J. D. Meindl. "Beyond Moore's law: The interconnect era". *Computing in Science & Engineering*, 5(1):20–24, 2003.

[5] H. Bu. "5 nanometer transistors inching their way into chips". *IBM Research, Innovation*, 2017.

[6] Y. S. Kivshar et al. "New horizons for nanophotonics". *Phil. Trans. R. Soc. A375*, (May 2016):2016–2018, 2017.

[7] K. Liu et al. "Fundamental Scaling Laws in Nanophotonics". *Scientific Reports*, 6(August):1–12, 2016.

[8] G. Keiser. *"Opical fiber communications"*. John Wiley & Sons, Inc., 2009.

[9] M. Haurylau et al. "On-Chip Optical Interconnect Roadmap : Challenges and Critical Directions". *IEEE Journal of selected topics in quantum electronics*, 12(6):1699–1705, 2006.

[10] D. A. B. Miller. "Optical interconnects to silicon". *IEEE Journal on Selected Topics in Quantum Electronics*, 6(6):1312–1317, 2000.

[11] V. J. Sorger et al. "Toward integrated plasmonic circuits". *MRS Bulletin*, 37(8):728–738, 2012.

[12] M. L. Brongersma and V. M. Shalaev. "The Case for Plasmonics". *Science*, 328(5977):440–441, 2010.

[13] R. Zia et al. "Plasmonics: the next chip-scale technology". *Materials Today*, 9(7-8):20–27, 2006.

[14] D. K. Gramotnev and S. I. Bozhevolnyi. "Plasmonics beyond the diffraction limit". *Nature Photonics*, 4(2):83–91, 2010.

[15] D. K. Gramotnev and S. I. Bozhevolnyi. "Nanofocusing of electromagnetic radiation". *Nature Photonics*, 8(1):13–22, 2014.

[16] S. A. Maier. *"Plasmonics: fundamentals and applications"*. Springer Science & Business Media, 2007.

[17] T. Chung et al. "Plasmonic nanostructures for nano-scale bio-sensing". *Sensors*, 11(11):10907–10929, 2011.

[18] J. P. Camden et al. "Controlled Plasmonic Nanostructures for Surface-Enhanced Spectroscopy and Sensing". *Accounts of Chemical Research*, 41(12):1653–1661, 2008.

[19] N. Hooshmand, J. A. Bordley, and M. A. El-Sayed. "Plasmonic Spectroscopy: The Electromagnetic Field Strength and its Distribution Determine the Sensitivity Factor of Face-to-Face Ag Nanocube Dimers in Solution and on a Substrate". *Journal of Physical Chemistry C*, 119(27):15579–15587, 2015.

[20] R. Adato et al. "Ultra-sensitive vibrational spectroscopy of protein monolayers with plasmonic nanoantenna arrays". *Proceedings of the National Academy of Sciences*, 106(46):19227–19232, 2009.

[21] V. Giannini et al. "Controlling light localization and light-matter interactions with nanoplasmonics". *Small*, 6(22):2498–2507, 2010.

[22] M. Kauranen and A. V. Zayats. "Nonlinear plasmonics". *Nature Photonics*, 6(11):737, 2012.

[23] N. Izhaky et al. "Development of CMOS-compatible integrated silicon photonics devices". *IEEE Journal on Selected Topics in Quantum Electronics*, 12(6):1688–1697, 2006.

[24] D. G. Baranov et al. "All-dielectric nanophotonics: the quest for better materials and fabrication techniques". *Optica*, 4(7):814–825, 2017.

[25] G. V. Naik, V. M. Shalaev, and Al. Boltasseva. "Alternative plasmonic materials: Beyond gold and silver". *Advanced Materials*, 25(24):3264–3294, 2013.

[26] A. Boltasseva and H. A. Atwater. "Low-Loss Plasmonic Metamaterials". *Science*, 331(6015):290–291, 2011.

[27] S. Xiao et al. "Loss-free and active optical negative-index metamaterials". *Nature*, 466(7307):735–738, 2010.

[28] W. A. Murray and W. L. Barnes. "Plasmonic materials". *Advanced Materials*, 19(22):3771–3782, 2007.

[29] J. B. Khurgin and G. Sun. "Practicality of compensating the loss in the plasmonic waveguides using semiconductor gain medium". *Applied Physics Letters*, 100(1):2012–2015, 2012.

[30] S. Longhi. "Parity-time symmetry meets photonics: A new twist in non-Hermitian optics". *EPL*, 120(6), 2017.

[31] B. Mayer et al. "Lasing from individual GaAs-AlGaAs core-shell nanowires up to room temperature". *Nature Communications*, 4:1–7, 2013.

[32] D. Saxena et al. "Optically pumped room-temperature GaAs nanowire lasers". *Nature Photonics*, 7(12):963–968, 2013.

[33] R. F. Oulton et al. "A hybrid plasmonic waveguide for subwavelength confinement and long-range propagation". *Nature Photonics*, 2(8):496–500, 2008.

[34] L. Lafone, T. P. H. Sidiropoulos, and R. F. Oulton. “Silicon-based metal-loaded plasmonic waveguides for low-loss nanofocusing”. *Optics letters*, 39(15):4356–4359, 2014.

[35] M. P. Nielsen et al. “Adiabatic Nanofocusing in Hybrid Gap Plasmon Waveguides on the Silicon-on-Insulator Platform”. *Nano Letters*, 16(2):1410–1414, 2016.

[36] L. Feng et al. “Experimental demonstration of a unidirectional reflectionless parity-time metamaterial at optical frequencies”. *Nature Materials*, 12(2):108–113, 2013.

[37] Y. L. Xu et al. “Unidirectional Transmission Based on a Passive PT Symmetric Grating With a Nonlinear Silicon Distributed Bragg Reflector Cavity”. *IEEE Photonics Journal*, 6(1):1–7, 2014.

[38] B. Peng et al. “Nonreciprocal light transmission in parity-time-symmetric whispering-gallery microcavities”. *arXiv:1308.4564 [cond-mat, physics:math-ph, physics:physics, physics:quant-ph]*, 2013.

[39] N. Hatano and D. R. Nelson. “Localization transitions in non-hermitian quantum mechanics”. *Physical Review Letters*, 77(3):570–573, 1996.

[40] C. M. Bender and S. Boettcher. “Real spectra in non-hermitian hamiltonians having PT symmetry”. *Physical Review Letters*, 80(24):5243–5246, 1998.

[41] C. M. Bender. “Introduction to -symmetric quantum theory”. *Contemporary Physics*, 46(4):277–292, 2005.

[42] K. G. Makris et al. “PT-Symmetric Periodic Optical Potentials”. *International Journal of Theoretical Physics*, 50(4):1019–1041, 2011.

[43] A. Regensburger et al. “Parity-time synthetic photonic lattices.”. *Nature*, 488(7410):167–71, 2012.

[44] K. G. Makris et al. “Beam dynamics in PT symmetric optical lattices”. *Physical Review Letters*, 100(10):1–4, 2008.

[45] R. El-Ganainy et al. “Theory of coupled optical PT-symmetric structures.”. *Optics Letters*, 32(17):2632–2634, 2007.

[46] C. E. Rüter et al. “Observation of parity–time symmetry in optics”. *Nature Physics*, 6(3):192–195, 2010.

[47] M. A. Miri and A. Alù. “Nonlinearity-induced PT-symmetry without material gain”. *New Journal of Physics*, 18(6):1–8, 2016.

[48] A. Lupu, H. Benisty, and A. Degiron. “Switching using PT symmetry in plasmonic systems: positive role of the losses”. *Optics Express*, 21(18):192–195, 2013.

[49] H. Alaeian and J. Dionne. “PT-Symmetric Plasmonic Metamaterials”. *arXiv preprint arXiv:1306.0059*, pages 1–7, 2013.

[50] H. Benisty et al. “Implementation of PT symmetric devices using plasmonics: principle and applications”. *Optics Express*, 19(19):18004, 2011.

[51] H. Benisty et al. “Healing Near-PT-Symmetric Structures to Restore Their Characteristic Singularities: Analysis and Examples”. *Journal of Lightwave Technology*, 30(16):2675–2683, 2012.

[52] S. Klaiman, U. Günther, and N. Moiseyev. “Visualization of branch points in PT-symmetric waveguides”. *Physical Review Letters*, 101(8):1–4, 2008.

[53] A. Lupu, H. Benisty, and A. Degiron. “Using PT-symmetry in plasmonic systems for switching and dynamic memory applications”. *2013 7th International Congress on Advanced Electromagnetic Materials in Microwaves and Optics, METAMATERIALS 2013*, (September):4–6, 2013.

[54] H. Ramezani et al. “Unidirectional nonlinear PT-symmetric optical structures”. *Physical Review A - Atomic, Molecular, and Optical Physics*, 82(4):1–6, 2010.

[55] Y. Huang, G. Veronis, and C. Min. “Unidirectional reflectionless propagation in plasmonic waveguide-cavity systems at exceptional points”. *Optics Express*, 23(23):29882, 2015.

[56] M. Liertzer et al. “Pump-induced exceptional points in lasers”. *Physical Review Letters*, 108(17):1–5, 2012.

[57] L. Feng et al. “Single-mode laser by parity-time symmetry breaking”. *Science*, 346(6212):972–975, 2014.

[58] M. Brandstetter et al. “Reversing the pump dependence of a laser at an exceptional point”. *Nature communications*, 5:4034, 2014.

[59] B. Baum, H. Alaeian, and J. Dionne. “A parity-time symmetric coherent plasmonic absorber-amplifier”. *Journal of Applied Physics*, 117(6):063106, 2015.

[60] S. Longhi. “PT-symmetric laser absorber”. *Physical Review A - Atomic, Molecular, and Optical Physics*, 82(3):1–4, 2010.

[61] S. Phang et al. “Coupled Parity-Time symmetric cavities: Results from Transmission Line Modelling simulations”. *International Conference on Transparent Optical Networks*, 2015 July:1–4, 2015.

[62] Y. Sun et al. “Experimental demonstration of a coherent perfect absorber with pt phase transition”. *Physical Review Letters*, 112(14):1–5, 2014.

[63] N. M. Estakhri and A. Alù. “Parity-time symmetry breaking and amplifier-absorber transitions in plasmonic nanoparticles”. *CLEO: QELS Fundamental Science. Optical Society of America*, 2015.

[64] Y. D. Chong, L. Ge, and A. D. Stone. “PT-symmetry breaking and laser-absorber modes in optical scattering systems”. *Physical Review Letters*, 106(9):093902„ 2011.

[65] C. Hang, G. Huang, and V. V. Konotop. “Tunable spectral singularities: Coherent perfect absorber and laser in an atomic medium”. *New Journal of Physics*, 18(8):1–16, 2016.

[66] Z. Gu et al. “Experimental demonstration of PT-symmetric stripe lasers”. *Laser and Photonics Reviews*, 10(4):588–594, 2016.

[67] S. Phang et al. “Ultrafast optical switching using parity–time symmetric Bragg gratings”. *Journal of the Optical Society of America B*, 30(11):2984, 2013.

[68] X. Y. Zhu et al. “Asymmetric diffraction based on a passive parity-time grating”. *Applied Physics Letters*, 109(11):111101, 2016.

[69] M. Kulishov et al. “Nonreciprocal waveguide Bragg gratings”. *Optics Express*, 13(8):3068, 2005.

[70] C. Hahn et al. “Single-mode lasers and parity-time symmetry broken gratings based on active dielectric-loaded long-range surface plasmon polariton waveguides”. *Optics Express*, 23(15):19922, 2015.

[71] A. Lupu, H. Benisty, and A. Degiron. “Using optical PT-symmetry for switching applications”. *Photonics and Nanostructures - Fundamentals and Applications*, 12(4):305–311, 2014.

[72] Z. Lin et al. “Unidirectional invisibility induced by PT-symmetric periodic structures”. *Physical Review Letters*, 106(21):1–4, 2011.

[73] K. G. Makris, L. Ge, and H. E. Türeci. “Anomalous transient amplification of waves in non-normal photonic media”. *Physical Review X*, 4(4):1–11, 2014.

[74] E. Narevicius et al. “Anisotropic reflection oscillation in periodic multilayer structures of parity-time symmetry.”. *Nature Physics*, 6(3):166–167, 2015.

[75] Y. L. Xu et al. “Experimental realization of Bloch oscillations in a parity-time synthetic silicon photonic lattice”. *Nature Communications*, 7:1–6, 2016.

[76] A. Guo et al. “Observation of PT-symmetry breaking in complex optical potentials”. *Physical Review Letters*, 103(9):1–4, 2009.

[77] H. Hodaei et al. “Parity-time-symmetric microring lasers”. *Science*, 346(6212):975–978, 2014.

[78] P. Miao et al. “Orbital Angular Momentum Microlaser”. *Science*, 353(6298):464–467, 2016.

[79] B. Peng et al. “Loss-induced suppression and revival of lasing”. *Science (New York, N.Y.)*, 346(6207):328–332, 2014.

[80] L. Chang et al. “Parity-time symmetry and variable optical isolation in active-passive-coupled microresonators”. *Nature Photonics*, 8(7):524–529, 2014.

[81] Zhaoyang Zhang et al. “Observation of Parity-Time Symmetry in Optically Induced Atomic Lattices”. *Physical Review Letters*, 117(12):1–5, 2016.

[82] C. Hahn et al. “Observation of exceptional points in reconfigurable non-Hermitian vector-field holographic lattices”. *Nature communications*, 7:12201, 2016.

[83] P. Peng et al. “Anti-parity-time symmetry with flying atoms”. *Nature Physics*, 12(12):1139–1145, 2016.

[84] K. Jones-Smith. *“Non-Hermitian Quantum Mechanics”*. Phd thesis, CASE WESTERN RESERVE UNIVERSITY, 2010.

[85] T. Kottos. “Optical physics: Broken symmetry makes light work”. *Nature Physics*, 6(3):166–167, 2010.

[86] J. M. Liu. *“Photonics devices”*. Cambridge University Press, 2009.

[87] J. D. Jackson. *“Electrodynamics”*. Wiley-VCH Verlag GmbH & Co. KGaA, 1975.

[88] L. D. Landau and E. M. Lifshitz. *“Electrodynamics of continuous media”*. Pergamon Press, New York, 1960.

[89] S. Phang. *“Theory and Numerical Modelling of Parity-Time Symmetric Structures of Photonics”*. Phd thesis, The University of Nottingham, 2016.

[90] A. E. Siegman. *“Lasers”*. Mill Valley, CA, 1986.

[91] H. A. Haus and W. Huang. “Coupled-Mode Theory”. *Proceedings of the IEEE*, 79(10):1505–1518, 1991.

[92] W. P. Huang. "Coupled-mode theory for optical waveguides: an overview". *Journal of the Optical Society of America A*, 11(3):963, 1994.

[93] L. A. Coldren et al. *"Diode lasers and photonic integrated circuits. Vol. 218"*. John Wiley & Sons, 2012.

[94] D. Jalas et al. "What is — and what is not — an optical isolator". *Nature Photonics*, 7(8):579–582, 2013.

[95] J. Petráček. "Nonreciprocal switching in nonlinear plasmonic couplers with loss and gain". *Optical and Quantum Electronics*, 48(9):446, 2016.

[96] J. R. Salgueiro and Y. S. Kivshar. "Optimization of biased PT-symmetric plasmonic directional couplers". *IEEE Journal of Selected Topics in Quantum Electronics*, 22(5):60–66, 2016.

[97] P. Yeh. *"Optical waves in layered media. Vol. 61"*. Wiley-Interscience, 2005.

[98] J. R. Nagel, S. Blair, and M. A. Scarpulla. "Exact field solution to guided wave propagation in lossy thin films". *Optics Express*, 19(21):20159, 2011.

[99] J. Snyman. *"Practical mathematical optimization: an introduction to basic optimization theory and classical and new gradient-based algorithms. Vol. 97"*. Springer Science & Business Media, 2005.

[100] R. Ma et al. "Room-temperature sub-diffraction-limited plasmon laser by total internal reflection". *Nature Materials*, 10(2):110–113, 2011.

[101] R. F Oulton et al. "Plasmon lasers at deep subwavelength scale". *Nature*, 461(October):629–632, 2009.

[102] A. V. Akimov et al. "Generation of single optical plasmons in metallic nanowires coupled to quantum dots". *Nature*, 450(7168):402–406, 2007.

[103] R. Kolesov et al. "Wave-particle duality of single surface plasmonpolaritons". *Nature Physics*, 5(7):470–474, 2009.

[104] M. A. Noginov et al. “Demonstration of a spaser-based nanolaser”. *Nature*, 460(7259):1110–1112, 2009.

[105] D. K. Gramotnev, M. W. Vogel, and M. I. Stockman. “Optimized nonadiabatic nanofocusing of plasmons by tapered metal rods”. *Journal of Applied Physics*, 104(3):1–8, 2008.

[106] E. Verhagen et al. “Nanowire plasmon excitation by adiabatic mode transformation”. *Physical Review Letters*, 102(20):1–4, 2009.

[107] M. I. Stockman. “Nanofocusing of optical energy in tapered plasmonic waveguides”. *Physical Review Letters*, 93(13):1–4, 2004.

[108] Q. Lu et al. “Extreme light confinement and low loss in triangle hybrid plasmonic waveguide”. *Optics Communications*, 319:141–146, 2014.

[109] D. Dai and S. He. “A silicon-based hybrid plasmonic waveguide with a metal cap for a nano-scale light confinement”. *Optics Express*, 17(19):16646–53, 2009.

[110] J. T. Kim et al. “Hybrid plasmonic waveguide for low-loss lightwave guiding”. *Optics Express*, 18(3):2808–2813, 2010.

[111] M. Z. Alam, J. S. Aitchison, and M. Mojahedi. “Theoretical Analysis of Hybrid Plasmonic Waveguide”. *IEEE JOURNAL OF SELECTED TOPICS IN QUANTUM ELECTRONICS*, 19(3), 2013.

[112] E. Prodan et al. “A Hybridization Model for the”. *Science*, 302(2003):419–422, 2003.

[113] B. Chen et al. “Hybrid Photon-Plasmon Coupling and Ultrafast Control of Nanoantennas on a Silicon Photonic Chip”. *Nano Letters*, 18(1):610–617, 2018.

[114] V. J. Sorger et al. “Experimental demonstration of low-loss optical waveguiding at deep sub-wavelength scales.”. *Nature communications*, 2:331, 2011.

[115] A. D. Rakic et al. “Optical properties of metallic films for vertical-cavity optoelectronic devices”. *Appl. Optics*, 37(22):5271–5283, 1998.

[116] D. Gerard and S. K. Gray. "Aluminium plasmonics". *Journal of Physics D: Applied Physics*, 48(18):184001, 2015.

[117] M. P. Nielsen et al. "Plasmonic materials for metal-insulator-semiconductor-insulator-metal nanoplasmonic waveguides on silicon-on-insulator platform". *Optical Materials*, 36(2):294–298, 2013.

[118] V. M. Goldschmidt. "Crystal structure and chemical constitution". *Transactions of the Faraday Scociety*, 25:253–283, 1929.

[119] R. Sturdivant and M. Harris. *"Transmit Receive Modules for Radas and Communication Systems"*. Artech House, 2015.

[120] H. Welker. "Über neue halbleitende Verbindungen". *Zeitschrift für Naturforschung A*, 7(11):744–749, 1952.

[121] M. I. Nathan et al. "Stimulated emission of radiation from GaAs p-n junctions". *Applied Physics Letters*, 1(3):62–64, 1962.

[122] T. M. Quist et al. "Semiconductor maser of GaAs". *Applied Physics Letters*, 1(4):91–92, 1962.

[123] R. N. Hall. "Coherent light emission from p-n junctions". *Solid-State Electronics*, 6(5):405–408, 1963.

[124] N. Holonyak and S. F. Bevacqua. "Coherent (visible) light emission from Ga(As1-xPx) junctions". *Applied Physics Letters*, 1(4):82–83, 1962.

[125] "Semiconductor Lasers: An Overview of Commercial Devices". `http://www.photonics.com/a25099/Semiconductor_Lasers_An_Overview_of_Commercial`.

[126] C. Klingshirn. *"Semiconductor Optics"*. Springer Science & Business Media, 2005.

[127] W. W. Chow and S. W. Koch. *"Semiconductor-laser fundamentals: physics of the gain materials"*. Springer-Verlag Berlin Heidelberg, 1999.

[128] M. A. Omar. *"Elementary solid state physics: principles and applications"*. Pearson Education India, 1975.

[129] J. Singh. *"Semiconductor optoelectronics: physics and technology"*. 1995.

[130] T. Suhara. *"Semiconductor laser fundamentals"*. CRC press, 2004.

[131] W. Nagourney. *"Quantum electronics and atomic physics and telecommunication"*. OUP Oxford, 2014.

[132] P. Bhattacharya. *"Semiconductor optoelectronic devices"*. Prentice-Hall, Inc., 1994.

[133] L. Lafone et al. "Feasibility of GaAs-based metal strip surface plasmon nanolasers". *IET Optoelectronics*, 8(2):122–128, 2014.

[134] B. R. Bennett et al. "Carrier-Induced Change in Refractive Index of InP, GaAs, and InGaAsP". *IEEE Journal of Quantum Electronics*, 26(1):113–122, 1990.

[135] P. A. Wolff. "Theory of the Band Structure of very degenerate semiconductors". *Physical Review*, 126(2):405, 1962.

[136] J. Zoroofchi and J. K. Butler. "Refractive index of n-type gallium arsenide". *Journal of Applied Physics*, 44(8):3697–3699, 1973.

[137] D. D. Sell, H. C. Casey, and K. W. Wecht. "Concentration dependence of the refractive index for n - And p -type GaAs between 1.2 and 1.8 eV". *Journal of Applied Physics*, 45(6):2650–2657, 1974.

[138] C. Cohen-Tannoudji, B. Diu, and F. Laloë. *"Quantum Mechanics"*. Hermann, Paris, 1977.

[139] R. Shankar. *"The principles of quantum mechanics"*. Springer Science & Business Media, 2012.

[140] D. J. Griffiths. *"Introduction to quantum mechanics"*. Cambridge University Press, 2016.

[141] E. M. Purcell. “Spontaneous emission probabilities at radio frequencies”. *Physical Review*, 69:681, 1946.

[142] K. J. Vahala. “Optical microcavities”. *Nature*, 424(6950):839–846, 2003.

[143] S. Strauf et al. “Self-tuned quantum dot gain in photonic crystal lasers”. *Physical Review Letters*, 96(12):25–28, 2006.

[144] Y. S. Choi et al. “Evolution of the onset of coherence in a family of photonic crystal nanolasers”. *Applied Physics Letters*, 91(3):3–6, 2007.

[145] S. M. Ulrich et al. “Photon statistics of semiconductor microcavity lasers”. *Physical Review Letters*, 98(4):3–6, 2007.

[146] H. Yokoyama and S. D. Brorson. “Rate equation analysis of microcavity lasers”. *Journal of Applied Physics*, 66(10):4801–4805, 1989.

[147] F. De Martini and G. R. Jacobovitz. “Anomalous spontaneous stimulated-decay phase transition and zero-threshold laser action in a microscopic cavity”. *Physical Review Letters*, 60(17):1711–1714, 1988.

[148] M. Khajavikhan et al. “Thresholdless nanoscale coaxial lasers”. *Nature*, 482(7384):204–207, 2012.

[149] S. Kumar et al. “Probing ultrafast carrier dynamics, nonlinear absorption and refraction in core–shell silicon nanowires”. *Pramana*, 79(3):471–481, 2012.

[150] T. P. H. Sidiropoulos et al. “Ultrafast plasmonic nanowire lasers near the surface plasmon frequency”. *Nature Physics*, 10(11):870, 2014.

[151] N. Liu et al. “Lithographically Defined, Room Temperature Low Threshold Subwavelength Red-Emitting Hybrid Plasmonic Lasers”. *Nano Letters*, 16(12):7822–7828, 2016.

[152] N. B. Nguyen et al. “Hybrid gap plasmon GaAs nanolasers”. *Applied Physics Letters*, 111(26):261107, 2017.

[153] L. D. Landau and E. M. Lifshitz. *"Electrodynamics of Continuous Media"*. Pergamon, 1984.

[154] E. Hecht. *"Optics"*. Addison-Wesley, San Francisco, 4th edition, 2002.

[155] M. Wille et al. "Carrier density driven lasing dynamics in ZnO nanowires". *Nanotechnology*, 27(22):225702, 2016.

[156] L. L. Goddard et al. "Recombination, gain, band structure, efficiency, and reliability of 1.5-$\mu$m GaInNAsSb/GaAs lasers". *Journal of Applied Physics*, 97(8):083101, 2005.

[157] Y. Li et al. "Room-temperature continuous-wave lasing from monolayer molybdenum ditelluride integrated with a silicon nanobeam cavity". *Nature Nanotechnology*, 12(10):987–992, 2017.

[158] K. Ding et al. "Room-temperature continuous wave lasing in deep-subwavelength metallic cavities under electrical injection". *Physical Review B - Condensed Matter and Materials Physics*, 85(4):1–5, 2012.

[159] D. Costantini et al. "A hybrid plasmonic semiconductor laser". *Applied Physics Letters*, 102(10), 2013.

[160] M. T. Hill et al. "Lasing in metal-insulator-metal sub-wavelength plasmonic waveguides". *Optics Express*, 17(13):11107, 2009.

[161] N. B. Nguyen et al. "Recovering parity-time symmetry in highly dispersive coupled optical waveguides". *New Journal of Physics*, 18(12):125012, 2016.

[162] BATOP Optoelectronics. "Refractive index n of AlGaAs, batop.com/information/n_AlGaAs.html". `batop.com/information/n{_}AlGaAs.html`.

[163] D. C. Brody. "Biorthogonal Quantum Mechanics". *Journal of Physics A: Mathematical and Theoretical*, 47(035305):3, 2013.

[164] A. Tumin. "The biorthogonal eigenfunction system of linear stability equations : A survey of applications to receptivity problems and to analysis of experimental and computational results". *41st AIAA Fluid Dynamics Conference and Exhibit*, page 3244, 2011.

[165] T. Shi and C. P. Sun. "Recovering Unitarity of Lee Model in Bi-Orthogonal Basis". *arXiv preprint arXiv:0905.1771*, 2009.

[166] F. Kleefeld. "The construction of a general inner product in non-Hermitian quantum theory and some explanation for the nonuniqueness of the C operator in PT quantum mechanics". *arXiv preprint arXiv:0906.1011*, 2009.

[167] I. Rotter. "The brachistochrone problem in open quantum systems". *Journal of Physics A: Mathematical and Theoretical*, 40(48):14515, 2007.

[168] Z. Liu et al. "Absence of Exceptional Points in Square Waveguide Arrays with Apparently Balanced Gain and Loss". *Scientific Reports*, 6:22711, 2016.

[169] K. Ding et al. "Emergence, Coalescence, and Topological Properties of Multiple Exceptional Points and Their Experimental Realization". *Physical Review X*, 6(2):021007, 2016.

[170] D. K. Schroder. "Carrier Lifetimes in Silicon". *IEEE transactions on Electron Devices*, 44(1):160–170, 1997.

[171] N. Suzuki. "FDTD analysis of two-photon absorption and free-carrier absorption in Si high-index-contrast waveguides". *Journal of Lightwave Technology*, 25(9):2495–2501, 2007.

[172] L. Zhang et al. "Nonlinear Group IV photonics based on silicon and germanium: From near-infrared to mid-infrared". *Nanophotonics*, 3(4-5):247–268, 2014.

[173] C. K. Sun et al. "Femtosecond-tunable measurement of electron thermalization in gold". *Physical Review B*, 50(20):15337–15348, 1994.

[174] H. J. Eichler and A. Hermerschmidt. "Light-induced dynamic gratings and photorefraction". *Springer Series in Optical Sciences*, 113:7–42, 2006.

[175] L. Braic et al. “Titanium Oxynitride Thin Films with Tunable Double Epsilon-Near-Zero Behavior for Nanophotonic Applications”. *ACS Applied Materials and Interfaces*, 9(35):29857–29862, 2017.

[176] B. E. Little and W. P. Huang. “Coupled-mode theory for optical waveguides”. 10:217–270, 1995.

[177] R. H. Ritchie. “Plasma Losses by Fast Electrons in Thin Films”. *Physical Review*, 106(5):874–881, 1957.

[178] R. F. Oulton et al. “Confinement and propagation characteristics of subwavelength plasmonic modes”. *New Journal of Physics*, 10:105018, 2008.

[179] H. U. Yang et al. “Optical dielectric function of silver”. *Physical Review B*, 91(23):235137, 2015.

[180] E. D. Palik. *“Handbook of Optical Constants of Solids”*. Academic, Orlando, 1985.

[181] E. Ozbay. “Plasmonics : Merging Photonics and Electronics at Nanoscale Dimensions ”. *Science*, 311(5758):189–194, 2006.

[182] A. D. Boardman and A. V. Zayats. “Nonlinear plasmonics”. *Handbook of Surface Science*, 4(October):329–347, 2014.

[183] H. W. Lee et al. “Nanoscale conducting oxide PlasMOStor”. *Nano Letters*, 14(11):6463–6468, 2014.

[184] B. R. Cooper, H. Ehrenreich, and H. R. Philipp. “Optical properties of noble metals. II.”. *Physical Review*, 138(2):494, 1965.

[185] U. Kreibig and M. Vollmer. *“Optical properties of metal clusters. Vol. 25”*. Springer Science & Business Media, 2013.

# Appendix A

# Parity-time inner product

Parity is a linear operator, defined as $\hat{P}\psi = \boldsymbol{Q}\psi$ where $\boldsymbol{Q} = \boldsymbol{Q}^*$, $\boldsymbol{Q}^2 = \boldsymbol{I}$. The time reversal operator is assumed to turn a wavefunction into its complex conjugate: $\hat{T}\psi = \psi^*$. $\hat{P}$ is a linear operator and $\hat{T}$ is an antilinear operator. As $\hat{P}\hat{T}$ now plays the role of hermiticity in QM, one way to define the inner product is $(\phi,\psi)_{PT} = (\hat{P}\hat{T}\phi)^T\psi = \phi^\dagger \boldsymbol{Q}\psi$. With this above definition, there will be vectors with negative norm, contradicts one of the most fundamental postulates of QM. The correct inner product used in PTS is defined slightly differently in order to ensure positive definiteness of the norm of a vector by introducing a new linear operator $\hat{C}$ which turns any state of the Hamiltonian with negative norm under the above $\hat{P}\hat{T}$ inner product into positive. $\hat{C}$ is a linear operator with $\hat{C}^2 = 1$ and $[\hat{C},\hat{P}\hat{T}] = 0$, $\hat{C}\psi = \boldsymbol{K}\psi$. Thus, the new CPT inner product used in PTS QM has the form [84]:

$$(\phi,\psi)_{CPT} = (\hat{C}\hat{P}\hat{T}\phi)^T\psi = \phi^\dagger K^T S\psi \tag{A.1}$$

Operator $\hat{C}$ is determined according to the specific Hamiltonian being used. Any operator in Hilbert space that represents an observable must be self-adjoint. In conventional QM, these operators are hermitian with respect to standard inner product. However, in a PTS QM framework, CPT adjoint of $\hat{A}$, $\hat{A}^{CPT}$ is defined such that $(\phi,\hat{A}\psi)_{CPT} = (\hat{A}^{CPT}\phi,\psi)_{CPT}$. To be self-adjoint with respect to CPT inner product, $\hat{A} = \hat{A}_{CPT}$. The use of CPT inner product ensures both positive norm of vectors and unitary time evolution. Thus, it is feasible to construct a QM framework with respect to this new inner product (For further details, refer to [84]).

# Appendix B

# Detailed calculation of CMT

## B.1 Calculation of CMT coefficients

Whether the coupled modes travel in the same direction or in opposite directions, their coupling mechanism can be modeled using the familiar coupled-mode theory approach. The formalism of CMT outlined here follows the standard CMT description in [86,91–93]. CMT applies to weakly coupled systems where the field of one mode can be treated as a perturbation to the field of the other. The electric field of a mode in a waveguide takes the form of $\mathcal{E}_\mu(x,z) = A_\mu(z)\mathcal{E}_\mu(x)e^{i\beta_\mu z}$, where the amplitude, $A_\mu(z)$, varies in the propagation direction [91, 92, 176] and the subscript $\mu$ marks a specific mode in the system. The field perturbation is then modeled by a linear polarization term, $\Delta P = \Delta\epsilon \cdot \mathcal{E}$, which can be input into the Lorentz reciprocity theorem:

$$\nabla \cdot (\boldsymbol{\mathcal{E}}_\mu \times \boldsymbol{\mathcal{H}}_\nu^* + \boldsymbol{\mathcal{E}}_\nu^* \times \boldsymbol{\mathcal{H}}_\mu) = -i\omega(\boldsymbol{\mathcal{E}}_\mu \cdot \Delta\boldsymbol{P}_\nu^* - \boldsymbol{\mathcal{E}}_\nu^* \cdot \Delta\boldsymbol{P}_\mu) \tag{B.1}$$

By integrating both sides of Eqn. B.1 over the cross-section of the waveguides, the familiar CMT equations and explicit functional forms of coupling coefficients are retrieved:

$$\pm \frac{dA_\nu(z)}{dz} = \sum_\mu i\kappa_{\nu\mu}A_\mu e^{i(\beta_\mu - \beta_\nu)z} \tag{B.2}$$

and the explicit functional forms of the CMT coupling coefficients are

$$\begin{aligned}
\kappa_{\mu\mu} &= \frac{\hat{\kappa}_{\mu\mu} - \frac{c_{\mu\nu}\hat{\kappa}_{\nu\mu}}{c_{\nu\nu}}}{1 - c_{\mu\nu}c_{\nu\mu}/c_{\mu\mu}c_{\nu\nu}} \approx \hat{\kappa}_{\mu\mu}(1 - \frac{c_{\mu\nu}\hat{\kappa}_{\nu\mu}}{c_{\nu\nu}\hat{\kappa_{\mu\mu}}}) \ll \hat{\kappa}_{\mu\nu} \\
\kappa_{\mu\nu} &= \frac{\hat{\kappa}_{\mu\nu} - \frac{c_{\mu\nu}\hat{\kappa}_{\nu\nu}}{c_{\nu\nu}}}{1 - c_{\mu\nu}c_{\nu\mu}/c_{\mu\mu}c_{\nu\nu}} \approx \hat{\kappa}_{\mu\nu}(1 - \frac{c_{\mu\nu}\hat{\kappa}_{\nu\nu}}{c_{\nu\nu}\hat{\kappa_{\mu\nu}}}) \approx \hat{\kappa}_{\mu\nu}
\end{aligned} \tag{B.3}$$

with the analytic functions of the coefficients taking the form of:

$$\hat{\kappa}_{\mu\nu} = \omega \int_{-\infty}^{\infty} \boldsymbol{\mathcal{E}}_{\mu}^{*} \cdot \Delta\epsilon_{\nu}(x) \cdot \boldsymbol{\mathcal{E}}_{\nu} dx \qquad c_{\mu\nu} = \int (\boldsymbol{\mathcal{E}}_{\mu}^{*} \times \boldsymbol{\mathcal{H}}_{\nu} + \boldsymbol{\mathcal{E}}_{\nu} \times \boldsymbol{\mathcal{H}}_{\mu}^{*}) \cdot \boldsymbol{z} dx \tag{B.4}$$

$\kappa_{\nu\mu}$ are the coupling coefficients and $\pm$ denotes the propagation direction of the waves, either backward or forward, and the summation runs through all modes of every waveguides involved in the coupling system. The approximations in Eqn. B.3 are valid when the two coupled modes are in the weak coupling limit. This implies that the overlap coefficients $c_{\mu\nu} \ll 1$, the field normalization $c_{\mu\mu} \approx 1$, and self-coupling is ignored for the case where $\kappa_{\mu\nu} \gg \kappa_{\mu\mu}$.

For simplicity's sake, consider the case where there are only two modes involved in the coupling process, the indices $\mu$ and $\nu$ take only values of 1 and 2, Eqn. B.2 leads to a set of coupled differential equation:

$$\begin{aligned} \pm\frac{dA_1(z)}{dz} &= i\kappa_{11}A_1(z) + i\kappa_{12}A_2(z)e^{i(\beta_2-\beta_1)z} \\ \pm\frac{dA_2(z)}{dz} &= i\kappa_{22}A_2(z) + i\kappa_{21}A_1(z)e^{i(\beta_1-\beta_2)z} \end{aligned} \tag{B.5}$$

However, CMT is often used for lossless coupled systems. This means that conventional CMT requires reasonable modifications to be used in loss/gain PTS systems. Going beyond standard CMT, in this analysis, we allow the propagation constants, $\beta_{1,2}$ to take complex values in order to accommodate the gain/loss requirement of optical PTS: $\beta_{1,2} = \beta'_{1,2} + i\beta''_{1,2} = (n'_{1,2} + in''_{1,2})\omega/c$. Here $\beta'_{1,2}$, $\beta''_{1,2}$ are real numbers and $n' + in''$ is the effective refractive index of each propagating mode.

## B.2 The simplified Hamiltonian of coupled codirection modes

To recast Eqn. 2.10 into its well-known CMT form, the self coupling coefficient can be absorbed into the overall magnitude expression: $\boldsymbol{A} = \begin{bmatrix} A_1(z) \\ A_2(z) \end{bmatrix} = \begin{bmatrix} a_1(z)e^{i\kappa_{11}z} \\ a_2(z)e^{i\kappa_{22}z} \end{bmatrix}$.

This has led to a significant simplification of Eqn. 2.10:

$$\begin{aligned} \frac{da_1(z)}{dz} &= i\kappa_{12}a_2(z)e^{i2\delta_{mode}z} \\ \frac{da_2(z)}{dz} &= i\kappa_{21}a_1(z)e^{-i2\delta_{mode}z} \end{aligned} \tag{B.6}$$

where $\delta_{mode} = (\beta_2 + \kappa_{22} - \beta_1 - \kappa_{11})/2$. We further make the substitution $\begin{bmatrix} a_1(z) \\ a_2(z) \end{bmatrix} = \begin{bmatrix} u_1(z)e^{i\delta_{mode}z} \\ u_2(z)e^{i\delta_{mode}z} \end{bmatrix}$. Thus, the original $\mathcal{E}(z)$ can be rewritten using a phasor with propagation phase $\beta_0 = \frac{(\beta_1+\kappa_{11}+\beta_2+\kappa_{22})}{2}$ as:

$$\boldsymbol{\mathcal{E}} = \begin{bmatrix} \mathcal{E}_1(z) \\ \mathcal{E}_2(z) \end{bmatrix} = \begin{bmatrix} e^{i\beta_0 z} & 0 \\ 0 & e^{i\beta_0 z} \end{bmatrix} \boldsymbol{A'} \qquad where \qquad \boldsymbol{A'} = \begin{bmatrix} u_1 \\ u_2 \end{bmatrix} \qquad and \qquad i\frac{\partial}{\partial z}\boldsymbol{A'} = \boldsymbol{H}\,\boldsymbol{A'}$$

Consider the case where $\kappa_{11,22}$ are negligible. The Hamiltonian that governs the propagation of the two coupled codirectional modes can now be recast into:

$$\boldsymbol{H} = \begin{bmatrix} \delta_{mode} & \kappa_{eff} \\ \kappa_{eff} & -\delta_{mode} \end{bmatrix} \tag{B.7}$$

## B.3 Finding the transfer matrix of coupled codirection modes

The following manipulation is then carried out to analyze the system [91, 92]:

1. Finding eigenvalues of $\boldsymbol{H}$: The eigenvalues of $\boldsymbol{H}$, corresponding to the formation of two supermodes, are:

$$\sigma_{\pm} = \beta_0 \pm \sqrt{\delta_{mode}^2 + \kappa_{eff}^2} = \beta_0 \pm \sigma_0 \tag{B.8}$$

2. Finding the eigenfunctions of $\boldsymbol{H}$:

$$\boldsymbol{A'} = \begin{bmatrix} u_1 \\ u_2 \end{bmatrix} = \begin{bmatrix} cos(\theta/2) \\ sin(\theta/2) \end{bmatrix} or \begin{bmatrix} -sin(\theta/2) \\ cos(\theta/2) \end{bmatrix}$$

where $tan(\theta) = \frac{\kappa_{eff}}{\delta_{mode}}$. Thus, $cos(\theta) = \frac{\delta_{mode}}{\sigma_0}$ and $sin(\theta) = \frac{\kappa_{eff}}{\sigma_0}$.

3. Finding the transfer matrix, $M(z)$, which governs the propagation of fields:

$$\begin{bmatrix} \mathcal{E}_1(z) \\ \mathcal{E}_2(z) \end{bmatrix} = \boldsymbol{M(z)} \begin{bmatrix} \mathcal{E}_1(0) \\ \mathcal{E}_2(0) \end{bmatrix}$$

- Diagonalizing the Hamiltonian: $\boldsymbol{Q^\dagger H Q = B}$ where

$$\boldsymbol{Q(z)} = \begin{bmatrix} cos(\theta/2) & -sin(\theta/2) \\ sin(\theta/2) & cos(\theta/2) \end{bmatrix} \quad and \quad \boldsymbol{B(z)} = \begin{bmatrix} \sigma_0 & 0 \\ 0 & -\sigma_0 \end{bmatrix}$$

- Transforming into another basis: $i\frac{\partial}{\partial z}\boldsymbol{K} = \boldsymbol{BK}$ where $\boldsymbol{A' = QK}$. Since $\boldsymbol{B}$ is a diagonal matrix, the obvious solution of $\boldsymbol{K}$ would be:

$$\boldsymbol{K(z)} = \begin{bmatrix} e^{-i\sigma_0 z} & 0 \\ 0 & e^{i\sigma_0 z} \end{bmatrix} \boldsymbol{K(0)}$$

- Transforming back to $\boldsymbol{A'}$ basis we achieve:

$$\boldsymbol{M'(z)} = \boldsymbol{Q} \begin{bmatrix} e^{-i\sigma_0 z} & 0 \\ 0 & e^{i\sigma_0 z} \end{bmatrix} \boldsymbol{Q}^{-1} \tag{B.9}$$

- Find the corresponding transfer matrix in $\boldsymbol{\mathcal{E}(z)}$ basis [48, 50]:

$$\begin{aligned} \boldsymbol{M(z)} &= \begin{bmatrix} e^{i\beta_0 z} & 0 \\ 0 & e^{i\beta_0 z} \end{bmatrix} \boldsymbol{M'(z)} \\ &= \begin{bmatrix} cos(\sigma_0 z) - \frac{i\delta_{mode}}{\sigma_0} sin(\sigma_0 z) & \frac{\kappa_{eff}}{\sigma_0} sin(\sigma_0 z) \\ \frac{\kappa_{eff}}{\sigma_0} sin(\sigma_0 z) & cos(\sigma_0 z) + \frac{i\delta_{mode}}{\sigma_0} sin(\sigma_0 z) \end{bmatrix} e^{-i\beta_0 z} \end{aligned}$$

## B.4 Fourier analysis and CMT in contradirectional coupled modes

The rich physics and applications of Bragg gratings have been illustrated in many excellent textbooks [86, 93, 154]. Combining all equations B.5, 2.17 and 2.18, we have

the following coupled differential equations in terms of Fourier coefficients:

$$\begin{aligned}\frac{dA_1(z)}{dz} &= iA_1(z)\sum_{\xi=\pm}^{\infty}\kappa_{11}(\xi)e^{i\left(\beta_1-\beta_1-\frac{2\pi\xi}{\Lambda}\right)z} + iA_2(z)\sum_{\xi=\pm}^{\infty}\kappa_{12}(\xi)e^{i\left(\beta_2-\beta_1-\frac{2\pi n}{\Lambda}\right)z}\\ -\frac{dA_2(z)}{dz} &= iA_2(z)\sum_{\xi=\pm}^{\infty}\kappa_{22}(\xi)e^{i\left(\beta_2-\beta_2-\frac{2\pi\xi}{\Lambda}\right)z} + iA_1(z)\sum_{\xi=\pm}^{\infty}\kappa_{21}(\xi)e^{i\left(\beta_1-\beta_2-\frac{2\pi\xi}{\Lambda}\right)z}\end{aligned} \tag{B.10}$$

Only one term in the Fourier transform that yields the minimum value of $|\delta = \beta_\mu - \beta_\nu - 2\pi\xi\Lambda| = 0$ is kept because only this term effectively contribute to the coupling of the two contradirectional modes of the grating. Equating the exponential terms on the LHS and RHS of Eqn. B.10, we arrive at:

- For $\kappa_{11,22}(\xi)$: the only Fourier term that satisfies the above condition is $\xi = 0$, giving rise to a DC term.

- For $\kappa_{12,21}(\xi)$: the only Fourier term that satisfies the above condition is $\frac{2\pi\xi}{\Lambda} = \pm|\beta_2 - \beta_1| = 2\beta$ for the case of contradirectional modes with $|\beta_1| = |\beta_2| = \beta = 2\pi n_{eff}/\lambda$ where $n_{eff}$ is the effective index of the propagating mode.

This result gives rise to the familiar Bragg condition: $\Lambda = \frac{\pi\xi}{\beta}$. The first Bragg order occurs at $q = 2|\beta|$ where q is the grating vector and $\Lambda = 2\pi/q = \pi/\beta$ with $\xi = 1$. Higher order Bragg occurs at $\xi > 1$ and a grating vector of $\xi q$ corresponding to a grating period of $\Lambda = 2\pi\xi/2\beta = \xi\pi/\beta$. From Eqn. 2.17, we can see that for a given index distribution, we can separate the dependence of the permittivity in transverse and along propagation directions as $\Delta\epsilon(x,z) = \Delta\epsilon(x)\Delta\epsilon(z)$. For a Bragg grating, the coefficients, $\kappa(\xi)$, can be simplified as:

$$\begin{aligned}\kappa_{\mu\mu}(\xi) &= \frac{1}{\Lambda}\int_0^{\Lambda}\Delta\epsilon(z)e^{\frac{i2\pi\xi z}{\Lambda}}dz \times \omega\int\mathcal{E}_\mu^*(x)\Delta\epsilon(x)\mathcal{E}_\mu(x)dx &&= C_\xi\alpha_0\\ \kappa_{\mu\nu}(\xi) &= \frac{1}{\Lambda}\int_0^{\Lambda}\Delta\epsilon(z)e^{\frac{i2\pi\xi z}{\Lambda}}dz \times \omega\int\mathcal{E}_\mu^*(x)\Delta\epsilon(x)\mathcal{E}_\nu(x)dx &&= C_\xi\kappa_0\end{aligned} \tag{B.11}$$

where $C_\xi = \frac{1}{\Lambda}\int_0^{\Lambda}\Delta\epsilon(z)e^{\frac{i2\pi\xi z}{\Lambda}}dz$. Note that we only keep the Fourier term that gives rise to the coupling of backward and forward propagating modes: $\sum_{\xi=\pm}^{\infty}\kappa_{\mu\nu}(\xi)e^{i\left(\beta_\nu-\beta_\mu-\frac{2\pi\xi}{\Lambda}\right)z}$ $\longrightarrow \kappa_{\mu\nu}(\xi = \frac{(\beta_\nu-\beta_\mu)\Lambda}{2\pi})$. To find the transmission matrix of this Bragg grating, $\boldsymbol{M(z)}$, we follow similar steps as outlined in the analysis of $\boldsymbol{H}$ mentioned in Section 2.4.1.

According to Eqn. B.10, the Hamiltonian of a Bragg grating takes the form of:

$$\boldsymbol{H} = \begin{bmatrix} iC_0\alpha_0 & iC_\xi\kappa_0 \\ -iC_{-\xi}\kappa_0 & -iC_0\alpha_0 \end{bmatrix} \tag{B.12}$$

1. Recast the above wavefunction into:

$$\frac{\partial}{\partial z}\boldsymbol{A} = \begin{bmatrix} iC_0\alpha_0 & iC_\xi\kappa_0 \\ -iC_{-\xi}\kappa_0 & -iC_0\alpha_0 \end{bmatrix}\boldsymbol{A} = \begin{bmatrix} ia & ib_1 \\ -ib_2 & -ia \end{bmatrix}\boldsymbol{A}$$

2. Finding eigenvalues of $\boldsymbol{H}$: $\sigma_{1,2} = \pm\sqrt{b_1 b_2 - a^2} = \pm\sigma$.

3. Finding the eigenfunctions of $\boldsymbol{H}$:

$$\begin{bmatrix} u_1 \\ u_2 \end{bmatrix} = \begin{bmatrix} 1 \\ \frac{ia-\sigma}{b_1} \end{bmatrix} or \begin{bmatrix} 1 \\ \frac{ia+\sigma}{b_1} \end{bmatrix}$$

4. Analysing the transfer matrix which governs the propagation of fields.

   - Diagonalize the Hamiltonian using:

$$\boldsymbol{Q(z)} = \begin{bmatrix} 1 & 1 \\ \frac{ia-\sigma}{b_1} & \frac{ia+\sigma}{b_1} \end{bmatrix} \qquad hence, \qquad \boldsymbol{Q(z)}^{-1} = \frac{b_1}{2\sigma}\begin{bmatrix} \frac{ia+\sigma}{b_1} & -1 \\ \frac{\sigma-ia}{b_1} & 1 \end{bmatrix}$$

   - Finding the transfer matrix $\boldsymbol{M(z)}$. Rewrite $\sigma = i\phi$ where $\phi = \sqrt{a^2 - b_1 b_2}$.

$$\begin{aligned} \boldsymbol{M(z)} &= \boldsymbol{Q(z)}\begin{bmatrix} e^{-i\sigma z} & 0 \\ 0 & e^{i\sigma z} \end{bmatrix}\boldsymbol{Q(z)}^{-1} \\ &= \begin{bmatrix} cosh(\phi z) + \frac{a}{\sigma}sinh(\phi z) & \frac{ib_1}{\sigma}sinh(\phi z) \\ \frac{ib_2}{\sigma}sinh(\phi z) & cosh(\phi z) - \frac{a}{\sigma}sinh(\phi z) \end{bmatrix} \end{aligned}$$

5. The forward and backward reflections are defined as follows:

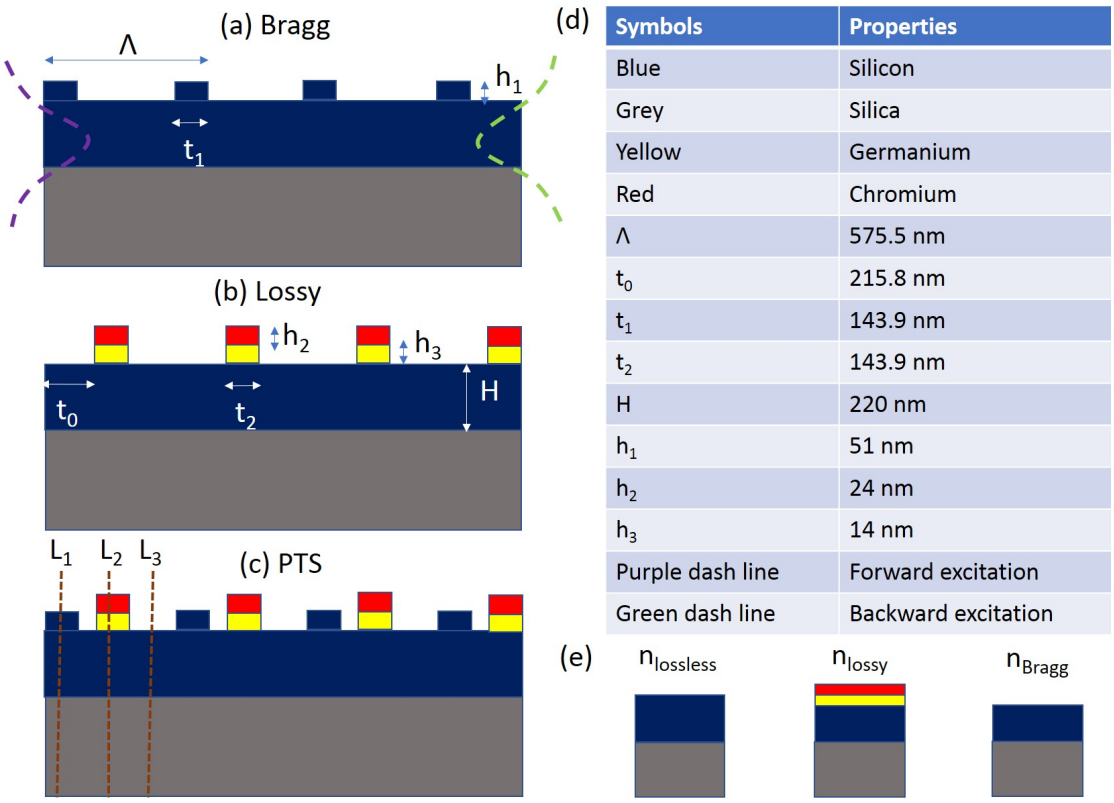
$$\begin{aligned} R_f &= \left|\frac{M_{21}}{M_{22}}\right|^2 \\ R_b &= \left|\frac{M_{12}}{M_{22}}\right|^2 \end{aligned} \tag{B.13}$$

# Appendix C

# FDTD simulation of PTS and conventional gratings

The backward and forward propagation of light in the following three configurations were simulated, details shown in Fig. C.1.

The simulation was implemented for a wavelength range input of 1500 - 1700 nm. For each structure, 2 simulations of forward and backward propagation were implemented. A fairly course mesh of 20x20 nm was used. The thickness of the bars is a quarter of the grating period, as indicated in Fig. C.1. Note here that the grating period was chosen to meet the second order Bragg condition. For a propagating TE mode slab waveguide of effective index, $n_{Bragg} = 2.69$, the second order Bragg period is, $\Lambda = \lambda_{Bragg}/n_{Bragg} = 1550/2.69 = 575.5$ nm. The height of the bars were chosen to satisfy the symmetric $\Re\{n(z)\}$ and antisymmetric $\Im\{n(z)\}$profiles of PTS. In this case, it requires that $\Re\{n_{Bragg}\} = \Re\{n_{lossy}\}$. The exceptional point behaviour of the system occurs when we achieve $|\Re\{n_{Bragg}\} - \Re\{n_{lossless}\}| = |\Im\{n_{lossy}\}|$ by choosing the appropriate dimensions of the bars (Lossless, lossy and Bragg modes are defined in Fig. C.1(e)). Note here that, the perfect suppression of reflection in one direction at the EP of the system only occurs at the point where the above conditions are fulfilled exactly. Results shown in Fig. 2.9 with a non-zero magnitude of $R_b$ implies that the system dimension can be further tuned to achieve perfect unidirectional reflection effect.




| Symbols | Properties |
|---|---|
| Blue | Silicon |
| Grey | Silica |
| Yellow | Germanium |
| Red | Chromium |
| Λ | 575.5 nm |
| $t_0$ | 215.8 nm |
| $t_1$ | 143.9 nm |
| $t_2$ | 143.9 nm |
| H | 220 nm |
| $h_1$ | 51 nm |
| $h_2$ | 24 nm |
| $h_3$ | 14 nm |
| Purple dash line | Forward excitation |
| Green dash line | Backward excitation |

**Figure C.1** – FDTD numerical simulation of (a) conventional Bragg grating (b) Periodic loss only and (c) PTS grating under broadband excitation. Backward and forward refer to the input propagation directions shown in Fig. 2.7. (d) Table shows the details of the simulation setup. The simulated system is composed of 15 periods of lossy and lossless bars. (e) The cutlines $L_{1,2,3}$ shown in (c) represent the cross-section of the effective modes of interest: $L_{1,2,3}$ correspond to the lossless, lossy and Bragg modes whose material compositions are shown in (e).

# Appendix D

# Iterative steepest descent method with linear line search

The iterative steepest descent method with linear line search detailed in [98,99] follows:

1. Rewrite the transcendental eigen-equation as: $f_{TE}(h) = h\tan(hd/2) - [K_2^2 - K_1^2 - h]^{1/2}$ where $K_1$ and $K_2$ are the wavevectors in the cladding and the core.

2. Find the first derivative of $f_{TE}(K)$: $f'_{TE} = \frac{df_{TE}}{dK} = hd/2\sec^2(hd/2) + \tan(hd/2) + h[K_2^2 - K_1^2 - h^2]^{-1/2}$.

3. Execute the following iterative algorithm where $l$ denotes the iteration number:

$$f_l = f_{TE}(h,l) \tag{D.1}$$

$$f'_l = \frac{df_{TE}(h,l)}{dk} \tag{D.2}$$

$$T_l = f'^{*}_l f_l \tag{D.3}$$

$$G_l = -f'_l f_l \tag{D.4}$$

$$p_l = \frac{T_l T_l^*}{G_l G_l^*} \tag{D.5}$$

$$h_{l+1} = h_l - p_l T_l \tag{D.6}$$

4. Define the error function $\phi = f_l(h) f_l(h)^*$. When $\phi < \phi_{tolerance} \approx 10^{-9}$, the algorithm is terminated. The above algorithm can lead to divergence when the value of $p_l$ is overestimated. To force the next iteration to give a smaller value of $\phi$, we can simply make the search step size smaller by halving the value of $p_l$ before starting the next iteration.

# Appendix E

# Surface Plasmon Polariton

The interesting optical properties of metals below its plasma frequencies led to the prediction of the existence of surface plasmon (SPs) in 1957 [177]. Since then SPs has been extensively studied, forming the foundation of plasmonics. SPs are the collective oscillations of electrons at the interface between a metal and a dielectric. Movement of this electron cloud results in the generation of field inside and outside the metal slab. The coupling between a SP and its associated photon gives rise to surface plasmon polariton (SPP). The schematic sketch of a SPP is shown in Fig. E.1.

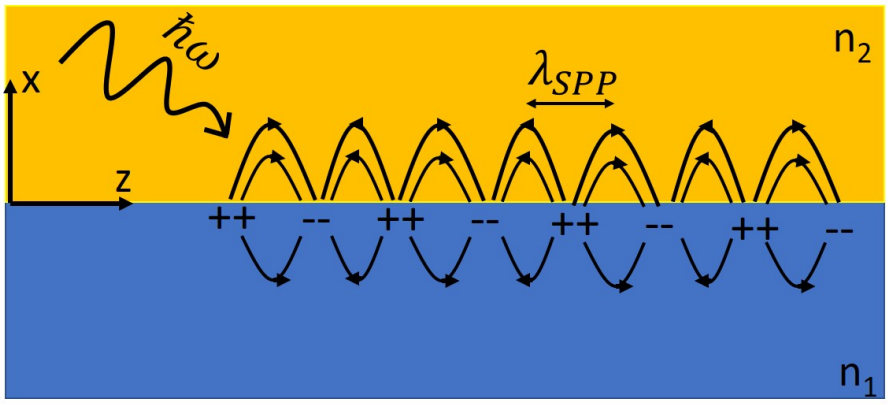



**Figure E.1** – Interface of two slabs. Blue: metal; Yellow: dielectric. An incident field of energy $\hbar\omega$ move the electron cloud collectively.

In this section, we take a look at the classical treatment of SPPs following an analysis of plasmonic mode in [16, 178]. Consider a general system of two slabs made of different materials in contact with each other (Fig. E.1). For a confined surface mode to exist, we assume that the field propagating in the $z$ direction with a single

propagation constant $\beta$, and its components in the $x$ direction are evanescent waves. For a TM mode, the field components have the following form where the subscript $i$ takes the value 1 or 2:

$$\begin{aligned}\mathcal{H}_y &= C_i e^{i\beta z} e^{\mp K_i x} \\ \mathcal{E}_z &= -\frac{i}{\omega\epsilon_0\epsilon}\frac{\partial \mathcal{H}_y}{\partial x} = \frac{iC_i K_i}{\epsilon_0\epsilon_2} e^{i\beta z} e^{\mp K_i x} \\ \mathcal{E}_x &= -\frac{\beta}{\omega\epsilon_0\epsilon_i}\mathcal{H}_y = -\frac{C_i\beta}{\omega\epsilon_0\epsilon_i} e^{i\beta z} e^{\mp K_i x}\end{aligned} \tag{E.1}$$

The $\mp$ corresponds to an evanescent field in $x > 0$ and $x < 0$ respectively. Imposing the continuity of $\mathcal{H}_y$, $\mathcal{E}_z$ across the interface, we deduce that:

$$\begin{aligned}C_1 &= C_2 \\ \frac{K_2}{\epsilon_2} &= -\frac{K_1}{\epsilon_1}\end{aligned} \tag{E.2}$$

For a mode to exist, $K_{1,2}$ must be positive according to the definition of a decaying field in Eqn. E.1. Therefore, $\epsilon_{1,2}$ must have opposite signs. Applying these conditions to Eqn 3.2 for a waveguiding structure, we have:

$$\begin{aligned}K_1^2 &= \beta^2 - K^2\epsilon_1^2 \\ K_2^2 &= \beta^2 - K^2\epsilon_2^2\end{aligned} \tag{E.3}$$

Note that a similar derivation for TE modes results in $C_1 = C_2 = 0$, hence, a slab plasmonic mode is always of TM nature. Combining Eqn. E.2 and E.3, we arrive at the familiar SPP dispersion expression:

$$\beta = K\sqrt{\frac{\epsilon_1\epsilon_2}{\epsilon_1 + \epsilon_2}} \tag{E.4}$$

We know that metals can have negative permittivity when $\omega < \omega_p$, while most dielectric materials have positive permittivity [16]. Thus, using the result from Drude model for metals, $\epsilon_1 = \epsilon_m \approx 1 - \frac{\omega_p^2}{\omega^2}$ and $\epsilon_2 = \epsilon_d$. Our dispersion relation is simplified to $\beta = K\sqrt{\frac{\epsilon_d(1-\frac{\omega_p^2}{\omega^2})}{\epsilon_d+1-\frac{\omega_p^2}{\omega^2}}}$ (Fig. E.2(a)). We take a SPP system consisting of a silver slab in air as an example. At small frequencies, the dispersion curve is very close to the lightline.

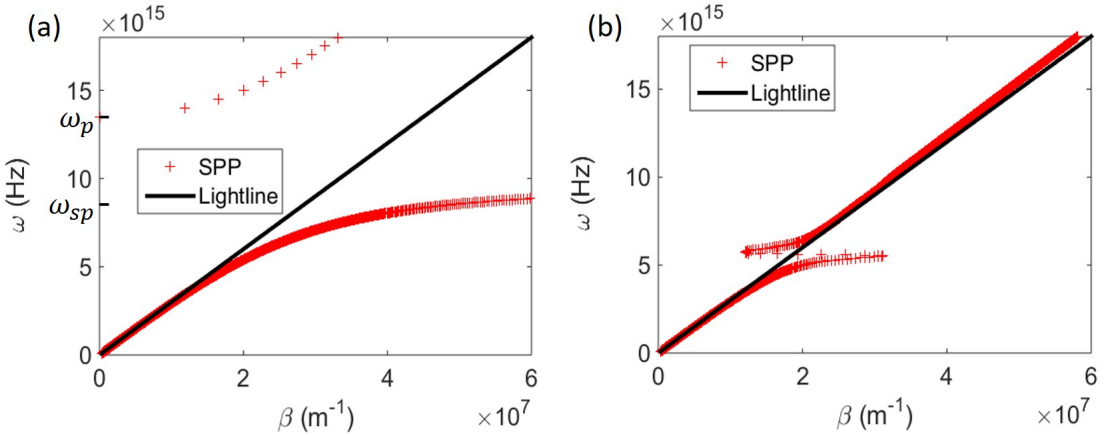



**Figure E.2** – (a) Dispersion of SPP without consideration of losses. (b) Dispersion of SPP with experimental data of the permittivity of silver [115]. In both cases the dielectric layer is taken to be air with $\epsilon_d = 1$ and the plasma frequency of silver is 8.9 eV [179].

This means that $\lambda_{SPP} \approx \lambda$ where $\lambda$ is the wavelength in the dieletric material and $\lambda_{SPP} = \frac{2\pi}{\Re\{\beta\}}$. As the input frequency increases, $\beta$ increases and the dispersion starts to diverge from the light line, leading to a decrease in $\lambda_{SPP}$. $\beta$ tends to infinity when $\omega = \omega_{sp} = \sqrt{\frac{\omega_p^2}{\epsilon_2+1}}$, called the surface plasmon frequency. At this point $\lambda_{SPP} \to 0$ and the group velocity reaches 0, $v_g = \frac{\partial\omega}{\partial\beta} = 0$, the mode in theory becomes stationary. There is a gap between $\omega_{sp}$ and $\omega_p$ where SPP mode does not exist. This energy gap corresponds to purely imaginary solutions of $\beta$.

However, the effects of electronic collisions and interband transitions at visible frequencies of noble metals lead to losses in the propagation of the plasmonic mode. This means that $\epsilon_m$ is complex and $\beta$ is no longer purely real. These losses damp the traveling SPPs resulting in a finite propagation length, $L_p = \frac{1}{2\Im\{\beta\}}$. Figure E.2(b) describes the dispersion of SPP when the experimental data of the permittivity of silver is used [180]. The presence of the imaginary part of $\epsilon$ leads to a finite SPP wavevector at $\omega = \omega_{sp}$. Moreover, the forbidden region of the dispersion spectrum shown in Fig. E.2(a) now can accommodate *quasibound* modes.

Next, we take the full expression of the permittivity of metal in Eqn. F.2 (See

Appendix F) to account for collisional losses, the expression for $\beta$ is greatly modified:

$$\beta = k\sqrt{\frac{\epsilon_d\epsilon_\infty}{\epsilon_d+\epsilon_\infty}}\sqrt{\frac{\omega(\omega+i\gamma)-\omega_p^2/\epsilon_\infty}{\omega(\omega+i\gamma)-\omega_p^2/(\epsilon_\infty+\epsilon_d)}} \tag{E.5}$$

Here, $\epsilon_\infty$ denotes a residual polarization and $\gamma$ signifies the collision rate.

The main problem in plasmonics is the trade-off between confinement and propagation length [181]. To quantify confinement, we need to calculate the extent of field in the dielectric and metal layers. $L_{d,m}$. This field penetration is evaluated as $L_{d,m} = \frac{1}{2\Im\{K_{d,m}\}}$. Clearly, the greater the confinement, the smaller the value of $L_{d,m}$:

$$\begin{aligned}\frac{L_d}{\lambda} &= \frac{\sqrt{\epsilon_d+\epsilon_\infty}}{4\pi\epsilon_d}\Re\left[\frac{1}{\sqrt{\omega_{sp}^2/\omega(\omega+i\gamma)-1}}\right]^{-1}\\ \frac{L_m}{\lambda} &= \frac{\sqrt{\epsilon_d+\epsilon_\infty}}{4\pi}\Re\left[\frac{\omega_p^2/\omega(\omega+i\gamma)-\epsilon_\infty}{\sqrt{\omega_{sp}^2/\omega(\omega+i\gamma)-1}}\right]^{-1}\end{aligned} \tag{E.6}$$

- $\omega \ll \omega_{sp}$: $L_m \to 0$ and $L_d \to \infty$. Metals are reflective at these frequencies. The penetration of field inside the material is not beyond its skindepth, which is usually in the $\mu$m range. In this limit, the solutions are called Sommerfeld-Zenneck waves. They are distinguished from SPPs which are considered to be more confined.

- $\omega \to \omega_{sp}$: as $\beta \to \infty$, $K_{d,m}$ also tends to explode, leading to extreme confinement. Here, more light can penetrate into the metal, and less in the dielectric layer, resulting in an increase in optical momentum, which corresponds to a reduction in wavelength and thus a greater confinement is achieved. Close to $\omega_{sp}$, $L_m \approx L_d$. At high frequencies, electrons in the metals become more involved in the propagation of SPPs, and more energy is stored as electronic polarization within the metal slab. Due to the existence of losses in metals, $\beta$ does not reach infinity at $\omega_{sp}$, limiting our ability to access extreme confinement.

# Appendix F

# Optical properties of metals

The distinction between metals and dielectrics lies in the sign of their permittivity which describes how the materials react to an electromagnetic field. Whenever a material is exposed to an electromagnetic field, since atoms are made up of charged particles, these particles are acted upon by the electric and magnetic fields, and thus, they can start to move. The positively charged ions are assumed to be immobile or rigid, whereas the electron clouds can be moved by these forces. Electrons in atoms are bound; in solids, electrons can move between atoms. Depending on the particular material, two possible processes can occur. Electrons can move directionally and create a current. Or they are only displaced from their equilibrium position, leading to a shift in the centre of mass of the positive and negative charges. This is called polarization. Dielectric response is dominated by polarization whereas the abundance of free electrons in metals allow them to conduct a DC electrical current. In an AC field, they will oscillate.

The plasma model describes the optical behaviour of metals. The model depicts solids as a structure of rigid positively charged ionic background surrounded by a cloud of negatively charged electrons of number density, $n_e$. The interaction of this electron cloud with an electric force is described by a damped harmonic oscillator or a Lorenz oscillator [16]:

$$m_e\ddot{x} + m_e\gamma\dot{x} = -e\mathcal{E} \tag{F.1}$$

where $e$, $m_e$ are the charge and mass of an electron, $\gamma = 1/\tau$ is the collision rate and $\tau$ is the relaxation time between collisions, leading to energy dissipation. For

an applied field, $\mathcal{E} = \mathcal{E}_0 e^{-i\omega t}$, we can find an expression for the displacement of the electron cloud, assuming that the motion matches the driving frequency, $x = x_0 e^{-i\omega t}$, thus, $x_0(t) = \frac{e\mathcal{E}}{m_e(\omega^2 + i\gamma\omega)}$. It is worth noting that the propagation of light in a metal is still described by the Maxwell equations 2.4-2.7, albeit the presence of free charges. This is because the field due to these free electrons is incorporated via the polarization $\mathcal{P} = -n_e e x = -\epsilon_0 \chi \mathcal{E}$; thus, the free charge density is no longer needed. We arrive at an expression for the permittivity of a metal:

$$\epsilon = 1 + \chi = 1 - \frac{\omega_p^2}{\omega^2 + i\gamma\omega} = \left(1 - \frac{\omega_p^2 \tau^2}{1 + \omega^2\tau^2}\right) + i\left(\frac{\omega_p^2 \tau}{\omega(1 + \omega^2\tau^2)}\right) \tag{F.2}$$

where $\omega_p^2 = \frac{n_e e^2}{m_e \epsilon_0}$, often called the plasma frequency. For metals, typically $\omega_p \approx 10^{15}$ Hz, corresponding to the UV range. To understand the behaviour of metal under different excitation energies, we consider the following cases:

- $\omega < \omega_p$
  - $\omega \ll \gamma$, $\epsilon'' \gg \epsilon'$. Here, $n'' = n' = \sqrt{\frac{\epsilon''}{2}}$ with $n = n' + in'' = \sqrt{\epsilon}$, the material is mainly absorbing. Following the Beer-Lambert's law of intensity variation: $I = I_0 e^{-\alpha z}$, the absorption coefficient has the form $\alpha = 2n''K$. The distance the field can penetrate the metal is given by the skin depth, $\delta_d = \frac{2}{\alpha}$.
  - $\omega = \gamma$, $\epsilon' \approx \epsilon''$ where $\epsilon = \epsilon' + i\epsilon''$ [175, 182, 183].
  - $\omega \gg \gamma => \omega\tau \gg 1$: $\epsilon = 1 - \frac{\omega_p^2}{\omega^2}$. The permittivity is pure real and negative, leading to a purely imaginary refractive index. Hence, the reflection coefficient $R = |\frac{1-n}{1+n}|^2 = 1$. For metals, this reflective regime occurs in the in the infra-red to visible range. However, at visible frequencies, interband transition in noble metals starts to take an active role. Interband absorption of the bluer end of the spectrum results in the yellow colour of gold we often see.
- $\omega = \omega_p$. At this point, the real part of the permitivity becomes 0.
- $\omega > \omega_p$. The permittivity approaches 1 and the metal becomes transparent. In this regime, for noble metals, however, we have to take into account the

fact that electrons in the inner orbits can react to this large input field. At low input energies, the behaviour of noble metals is dominated by *s*-orbital electrons. At higher energies, the filled *d*-band causes a highly polarizable environment, generating a residual polarization $\epsilon_\infty$ which is added to the permitivity such that $D = \epsilon_0 E + \mathcal{P}_s + \mathcal{P}_\infty$, where $\mathcal{P}_s$ now denotes contribution from the *s*-orbital electrons [16, 184, 185]. Hence $\epsilon = \epsilon_\infty - \frac{\omega_p^2}{\omega^2 + i\gamma\omega}$.

Bound electrons can be displaced when acted upon by an incident field. The displacement amount is dependent on the applied field in a metal and a dielectric. In dielectrics, the electrons are bound and this leads to a restoring force, which is not present in metals. In turn this creates a resonant response, whereby the amplitude of motion is aided by more efficient energy transfer to electrons. This leads to the polarization of the material in the direction of the applied field. Most dielectrics are transparent at visible frequencies and have positive permittivity.

# Appendix G

# Energy and power flow in plasmonics

Poynting's theorem describes the relationship between power flow out of a bound surface, $\boldsymbol{W} = \boldsymbol{\mathcal{E}} \times \boldsymbol{\mathcal{H}}$ and the field that is induced by the polarization inside the volume, $V$ enclosed within that surface:

$$-\oint \boldsymbol{\mathcal{E}} \times \boldsymbol{\mathcal{H}} d\boldsymbol{S} = \frac{1}{2}\frac{\partial}{\partial t}\int (\epsilon_0 \boldsymbol{\mathcal{E}}^2 + \mu_0 \boldsymbol{\mathcal{H}}^2) dV + \int \boldsymbol{\mathcal{E}}.\frac{\partial \boldsymbol{\mathcal{P}}}{\partial t} dV \tag{G.1}$$

The polarization, $\boldsymbol{\mathcal{P}}$ has a defined frequency response: $\boldsymbol{\mathcal{P}}(\boldsymbol{r},\omega) = \epsilon_0 \chi(\boldsymbol{r},\omega)\boldsymbol{\mathcal{E}}(\boldsymbol{r},\omega)$ where $\chi(\boldsymbol{r},\omega)$ denotes the susceptibility of the material. However, the time response of the polarization is more complicated due to the principle of causality. The polarization at one point in time depends on the electric field at an earlier point: $\boldsymbol{\mathcal{P}}(r,t) = \epsilon_0 \int \chi(\boldsymbol{r},t-\tau)\boldsymbol{\mathcal{E}}(\boldsymbol{r},\tau)d\tau$. Due to losses in dispersive media, the electric field decays as the wave propagates, $\boldsymbol{\mathcal{E}}(\boldsymbol{r},t) = \boldsymbol{\mathcal{E}_0}(\boldsymbol{r},t)e^{i\omega t}$. $\boldsymbol{\mathcal{E}_0}(\boldsymbol{r},t)$ describes the temporal envelope of the electric field, having a different frequency response from the carrier frequency $\omega$. Providing that the loss is small, the time variation of the envelope is much slower than the carrier frequency. Making use of the slow varying envelope approximation, we can approximate the time derivative of the polarization as [178]:

$$\frac{\partial \boldsymbol{\mathcal{P}}(\boldsymbol{r},t)}{\partial t} = i\epsilon_0 \omega \chi(\boldsymbol{r},\omega)\boldsymbol{\mathcal{E}}(\boldsymbol{r}.t) + \epsilon_0 \frac{d[\omega\chi(\boldsymbol{r},\omega)]}{d\omega}\frac{\partial \boldsymbol{\mathcal{E}_0}(\boldsymbol{r},t)}{\partial t}e^{i\omega t} \tag{G.2}$$

For a dispersive system where the permittivity becomes frequency-dependent, the average stored energy and power flow in the system are expressed as:

$$U(\boldsymbol{r},t) = \frac{1}{2}\left(\epsilon_0 \frac{d(\Re\{\omega\epsilon(\omega)\})}{d\omega}|\boldsymbol{\mathcal{E}_0}|^2 + \mu_0|\boldsymbol{\mathcal{H}_0}|^2\right) \tag{G.3}$$

where $\boldsymbol{\mathcal{H}_0}$ denotes the temporal envelope of the magnetic field and:

$$-\oint \Re\{\boldsymbol{\mathcal{E}_0} \times \boldsymbol{\mathcal{H}_0^*}\} d\boldsymbol{S} = \frac{1}{2}\int \frac{\partial U}{\partial t} dV + \epsilon_0 \omega \int \Im\left\{\chi(\boldsymbol{r},\omega)\right\} |\boldsymbol{\mathcal{E}_0}|^2 dV \tag{G.4}$$

The modal loss in a plasmonic system leads to an exponential decay of the initial power, $P_0$, in the propagation direction, $P(z) = P_0 e^{-\alpha z}$. Note here that power is denoted as $P$ to distinguish from the polarization, $\mathcal{P}$. In steady state, there is no temporal change in the power flow, $\frac{dU}{dt} = 0$, and integrating over the mode volume gives us an expression of the absorption coefficient:

$$\alpha = \omega \frac{\int \epsilon_0 \Im\{\chi(\boldsymbol{r},\omega)\} |\boldsymbol{\mathcal{E}}|^2 dA}{\Re\{\boldsymbol{\mathcal{E}_0} \times \boldsymbol{\mathcal{H}_0^*}\}.\hat{\boldsymbol{z}} dA} \tag{G.5}$$

The velocity at which the mode energy flows, $v_E$, is well-defined based on the Poynting vector relating the power and total energy in the mode:

$$v_E = \frac{\int \Re\{\boldsymbol{\mathcal{E}_0} \times \boldsymbol{\mathcal{H}_0^*}\}.\hat{\boldsymbol{z}} dA}{\int U dA} \tag{G.6}$$

Let $U = 2U_E$, rearranging Eqn. G.3, we have $|\boldsymbol{\mathcal{E}_0}|^2 = \frac{2U_E}{\epsilon_0 \frac{d(\Re\{\omega\epsilon(\omega)\})}{d\omega}}$. Assuming that most of the modal losses originated from the metal, $\alpha$ can be approximated as:

$$\alpha = \frac{4\pi}{\lambda} \frac{c}{v_E} \frac{\int_{metal} U_E dA}{\int_{total} U dA} \frac{\Im\{\chi_m\}}{\Re\{d(\omega\epsilon_m)/d\omega\}} \tag{G.7}$$

As indicated in Eqn. G.7, the slower the energy moves, the higher the loss the system will encounter. The amount of loss also depends on the proportion of the mode residing in the lossy medium, $\frac{\int_{metal} U_E dA}{\int_{total} U dA}$. Taking $\frac{\int_{metal} U_E dA}{\int_{total} U dA} \approx \frac{L_m}{L_m + L_d}$, we can see that near $\omega_{sp}$, this ratio is 1/2. With this approximation, $\alpha \propto \epsilon_d^{3/2}$. This finding has an important implication for practical construction of plasmonic waveguides: the higher the refractive index of the dielectric layer, the greater the propagtion loss of the waveguide.

Even though the energy is moving at $v_E$, information equivalent to a modulation of signals can only move at the group velocity, $v_g$. In the case of low losses, the group velocity and energy velocity are the same. We define the group index as:

$$n_g = \frac{c}{v_g} = \frac{d[\omega \Re\{\sqrt{\epsilon(\omega)}\}]}{d\omega} \tag{G.8}$$

The overlap factor, $\Gamma$ which defines the spatial confinement of the propagating mode relates a material property to a modal property, is formulated as:

$$\Gamma = \frac{n_g n_s}{\frac{d(\epsilon_s \omega)}{d\omega}} \frac{\int_{A_s} 2U_E dA}{\int U dA} \tag{G.9}$$

where $\epsilon_s$ and $n_s$ are the real part of the permittivity and the refractive index of the semiconductor layer. With this expression, both the modal and the material dispersion properties are accounted for based on $\frac{n_g n_s}{\frac{d(\epsilon_s \omega)}{d\omega}}$. Clearly, when a non-dispersive media and fairly weak confinement is considered, $U = 2U_E = n_s^2 \epsilon_0 \mathcal{E}^2$, the overlap factor only describes the proportion of the modal field in the core layer [133].

# Appendix H

# Semiconductor gain formulation

| | Schrödinger picture | Heisenberg picture |
|---|---|---|
| Definition | Operators are stationary and eigenvectors evolve in time under $U(t)$ | Wavefunctions are stationary, the transformation using $U(t)$ make operator evolves in time. This picture makes more physical sense as observables in reality do have a time-dependence characteristic. |
| Operators and Eigenvectors | Time-dependent eigenvector $\|\psi_S(t)\rangle = U(t)\|\psi(t_0)\rangle$ where $U(t) = e^{-i\hat{H}t/\hbar}$. Time-independent operator: $\frac{d\hat{A}}{dt} = 0$ | Time-independent eigenvector: $\|\psi_H(t)\rangle = U^\dagger(t)\|\psi_S(t) = \|\psi(t_0)\rangle$ Time-dependent operator: $\hat{A}_H(t) = U^\dagger(t)\hat{A}U(t)$ |
| Equation of motion | Schödinger equation: $i\hbar\frac{d}{dt}\|\psi\rangle = \hat{H}\|\psi\rangle$ Equation of motion of expectation value: $i\hbar\frac{d}{dt}\langle\hat{A}\rangle = i\hbar\frac{d}{dt}\langle\psi_S(t)\|\hat{A}\|\psi_S(t)\rangle = \langle\psi\|[A,H]^+\|\psi\rangle$ | Equation of motion: $i\hbar\frac{d\hat{A}_H}{dt} = [\hat{A}_H,H_H]^+_H$ where $H_H = U^\dagger HU$ |

**Table H.1** – A comparison between the Schrödinger and Heisenberg QM descriptions.

The semiconductor gain analysis using the second quantization is summarized below:

| Language | Physical description and origin |
|---|---|
| Electron field operator:<br>$\hat{\psi}(\mathbf{r},t) = \sum_{\zeta}\sum_{\mathbf{k}}\sum_{s_z} a_{\zeta\mathbf{k}s_z}(t)\phi_{\zeta\mathbf{k}s_z}(\mathbf{r})$ | $\zeta$: $c$, $v$ for conduction and valence. $\mathbf{k}$, $s_z$: crystal momentum and spin state of electron. $\phi_{\zeta\mathbf{k}s_z}(\mathbf{r})$: the single particle eigenfunction for an electron in the semiconductor. $a_{\zeta\mathbf{k}s_z}(t)$: the annihilation operator, $a^{\dagger}_{\zeta\mathbf{k}s_z}$: the creation operator |
| Anticommutation relations:<br>$[\mathrm{a}_{\zeta\mathbf{k}s_z},a_{\zeta'\mathbf{k}',s'_z}]^{+} = [\mathrm{a}^{\dagger}_{\zeta\mathbf{k}s_z}(t),a^{\dagger}_{\zeta'\mathbf{k}',s'_z}(t)]^{+} = 0$<br>$[\mathrm{a}_{\zeta\mathbf{k}s_z}(t),a^{\dagger}_{\zeta'\mathbf{k}',s'_z}(t)]^{+} = \delta_{\zeta,\zeta'}\delta_{\mathbf{k},\mathbf{k}'}\delta_{s_z,s'_z}$ | Fermions obey Pauli exclusion principle and hence their creation and annihilation operators follow anticommutation relations: $[A_1,A_2]^{+} \equiv A_1A_2 + A_2A_1$ |
| The number operator for an electron with a specific set of $\zeta$, $\mathbf{k}$, $s_z$: $a^{\dagger}_{\zeta\mathbf{k}s_z}a_{\zeta\mathbf{k}s_z}$ | The eigenfunctions of this number operator are $\lvert n0_{\zeta\mathbf{k}s_z}\rangle$ and $\lvert n1_{\zeta\mathbf{k}s_z}\rangle$ indicating an unoccupied and occupied state respectively. |
| $b^{\dagger}_{-\mathbf{k}-s_z} = a_{v\mathbf{k}s_z}$<br>$b_{-\mathbf{k},-s_z} = a^{\dagger}_{v\mathbf{k},s_z}$ | The annihilation of an electron in the valence band with a particular $\mathbf{k}$ and $s_z$ is equivalent to the creation of a hole with -$\mathbf{k}$ and $-s_z$. |
| $\langle a^{\dagger}_{v\mathbf{k}s_z}a_{v\mathbf{k}s_z}\rangle = 1 - \langle b^{\dagger}_{-\mathbf{k},-s_z}b_{-\mathbf{k},-s_z}\rangle$ | Only 2 possible occupation variations for each set of unique $\mathbf{k}$ and $s_z$: one or zero electron. Electrons here imply those in the conduction band. |
| $E_{c\mathbf{k}} = E_{e\mathbf{k}} = \frac{\hbar^2k^2}{2m_e}$ and $E_{v\mathbf{k}} = E_{e\mathbf{h}} = \frac{\hbar^2k^2}{2m_h}$. | The unrenormalized energy gap: $E_g$.<br>Setting $m_h = -m_{ve}$. Only true for non-interacting electrons. |
| $\mathcal{P}(z,t) = \frac{1}{V}\sum_{\mathbf{k}}\left(\bar{\mu}_{\mathbf{k}}a^{\dagger}_{c\mathbf{k}}a_{v\mathbf{k}} + \bar{\mu}^{*}_{\mathbf{k}}a^{\dagger}_{v\mathbf{k}}a_{c\mathbf{k}}\right)$<br>$= \frac{1}{V}\sum_{\mathbf{k}}\left(\bar{\mu}_{\mathbf{k}}a^{\dagger}_{c\mathbf{k}}b^{\dagger}_{-\mathbf{k}} + \bar{\mu}^{*}_{\mathbf{k}}b_{-\mathbf{k}}a_{c\mathbf{k}}\right)$ | Quantum mechanical semiconductor gain medium $\mathcal{P}(z,t) = \langle\mathcal{P}\rangle$. This is equivalent to the classical expression of polarization in Eqn. 4.5.[a] |

[a]The details calculation of statistical summation based on the density operator (quantum optics can be found in Chow)

| | |
|---|---|
| $\mathcal{P}(z) = 2e^{-i[Kz-\omega t-\phi(z)]}\frac{1}{V}\sum_{\mathbf{k}}\bar{\mu}^*_{\mathbf{k}}\langle b_{-\mathbf{k}}a_{\mathbf{k}}\rangle$ | $\mathcal{P}(z)$ is the polarization amplitude that appears in Eqn. 4.5 |
| $p_{\mathbf{k}} = \langle b_{-\mathbf{k}}a_{\mathbf{k}}\rangle$<br>$n_{e\mathbf{k}} = \langle a^\dagger_{\mathbf{k}}a_{\mathbf{k}}\rangle$; $n_{h\mathbf{k}} = \langle b^\dagger_{-\mathbf{k}}b_{-\mathbf{k}}\rangle$ | Gain medium variable.<br>(Conduction) electron/hole occupation number.<br>These variables must the Heisenberg equation of motion. |
| $\frac{d\hat{T}}{dt} = \frac{i}{\hbar}\left[H,\hat{T}\right]$; $\frac{d\hat{T}_{\mathbf{k}}}{dt} = \frac{i}{\hbar}\left[H_{\mathbf{k}},\hat{T}_{\mathbf{k}}\right]$ | Since $H = \sum_{\mathbf{k}} H_{\mathbf{k}}$ each $\mathbf{k}$ part can be evaluated separately. |
| $H_{KE} = \int d^3r\hat{\psi}^\dagger(\mathbf{r})\left(-\frac{\hbar^2\nabla^2}{2m_\zeta}\right)\hat{\psi}(\mathbf{r})$<br>$= \sum_{\mathbf{k}}\left(E_{c\mathbf{k}}a^\dagger_{c\mathbf{k}}a_{c\mathbf{k}} + E_{v\mathbf{k}}a^\dagger_{c\mathbf{k}}a_{v\mathbf{k}}\right)$<br>$= \sum_{\mathbf{k}}\left(\left(E_g + \frac{\hbar^2k^2}{2m_e}\right)a^\dagger_{c\mathbf{k}}a_{c\mathbf{k}} + \frac{\hbar^2k^2}{2m_h}b^\dagger_{-\mathbf{k}}b_{-\mathbf{k}}\right)$ | Kinetic energy expression for N non-interacting electrons.<br>Summing over all bands: valence and conduction.<br>Summation over spin states and $\mathbf{k}$: $\sum_{\mathbf{k}}\sum_{s_z} = \sum_{\mathbf{k}}$.<br>Setting an arbitrary origin, leaving out the constant term: $\sum_{\mathbf{k},s_z} E_{v\mathbf{k}}$. |
| $H_d = -\sum_{\mathbf{k}}\left(\bar{\mu}_{\mathbf{k}}a^\dagger_{c\mathbf{k}}a_{v\mathbf{k}} + \bar{\mu}^*_{\mathbf{k}}a^\dagger_{v\mathbf{k}}a_{c\mathbf{k}}\right)\mathcal{E}(z,t)$<br>$= -\sum_{\mathbf{k}}\left(\bar{\mu}_{\mathbf{k}}a^\dagger_{c\mathbf{k}}b^\dagger_{-\mathbf{k}} + \bar{\mu}^*_{\mathbf{k}}b_{-\mathbf{k}}a_{c\mathbf{k}}\right)\mathcal{E}(z,t)$ | $H_d$ Describes the dipole interaction between the field and the carriers: $\mu_{\mathbf{k}}$ is the dipole matrix element between the valence and conduction band.<br>$H_d = -V\boldsymbol{\mathcal{P}}\cdot\boldsymbol{\mathcal{E}}$ with $V$ being the volume of the active region. |
| $H_{\mathbf{k}} = H_{KE,\mathbf{k}} + H_{d,\mathbf{k}}$<br>$= \left(E_g + \frac{\hbar^2k^2}{2m_e}\right)a^\dagger_{\mathbf{k}}a_{\mathbf{k}} + \frac{\hbar^2k^2}{2m_h}b^\dagger_{-\mathbf{k}}b_{-\mathbf{k}}$<br>$-\left(\bar{\mu}_{\mathbf{k}}a^\dagger_{\mathbf{k}}b^\dagger_{-\mathbf{k}} + \bar{\mu}^*b_{-\mathbf{k}}a_{\mathbf{k}}\right)\mathcal{E}(z,t)$ | The simplified Hamiltonian for each $\mathbf{k}$ state (direct transitions). Transition energy between the bands: $\hbar\omega_{\mathbf{k}} = E_g + \frac{\hbar^2k^2}{2m_e} + \frac{\hbar^2k^2}{2m_h} = E_g + \frac{\hbar^2k^2}{2m_r}$ where $m_r = (1/m_e + 1/m_h)^{-1}$ is the reduced mass. |

**Table H.2** – The language of second quantization (Fock formalism) used in this analysis of gain: symbols, notations and physical meaning/implications of relevant variables.

# Appendix I

# Fabrication details of hybrid gap plasmon nanolasers

The following procedure was carried out by Dr. Michael Nielsen to fabricate the hybrid gap plasmon nanolasers using EBL at Imperial College London.

1. Clean sample in acetone and IPA. Dry in air for at least 10 minutes. Avoid using nitrogen gun for drying at all time.
2. Sputter 20 nm $SiO_2$.
3. Spin coat PMMA: pre-bake at 180°C for 3 minutes. Spin 950 A4 at 3000 RPM for 1 minute, 3000 acceleration, 5 minutes post-bake at 180°C.
4. EBL: using 20 $\mu$m aperature at 20 kV, step size: 10 nm.
5. Develop 1 minute in MIBK/IPA 1:3, rinse 30 seconds in IPA.
6. Plasma ash for 0.2 minute at 40% power.
7. Deposit SAM: mix 0.3 mL SAM in 5 mL ethanol. Put on sample for 30 seconds, rinse in ethanol for 30 seconds. Dry in air for 10 minutes. Place on hot plate at 90°C for 15 minutes.
8. Evaporate 40 nm Au.
9. Lift-off: place in acetone overnight. Periodically wash using acetone squeeze bottle and move to new fresh acetone while spraying on it. Remove from acetone once lift-off is completed and dry in air for 10 minutes.

# List of Tables

2.1 Comparison of basic properties of Hermitian and PTS matrices. . . . . 15
2.2 Comparison of QM's Schrödinger equation and classical optics's wave equation. . . . . 17
2.3 Different types of periodic distribution of indices on top of a waveguide. 29

H.1 A comparison between the Schrödinger and Heisenberg QM descriptions. 188
H.2 The language of second quantization (Fock formalism) used in this analysis of gain: symbols, notations and physical meaning/implications of relevant variables. . . . . 190

# List of Figures


2.1 Schematics of optical PTS systems. . . . . 18
2.2 Initial conditions of a PTS coupled waveguide system. . . . . 21
2.3 Eigenspectra of an ideal PTS coupled waveguide system. . . . . 23
2.4 Output fields of an ideal PTS coupled waveguide system. . . . . 24
2.5 Normalized field amplitudes along propagation direction of Hermitian and PTS coupled waveguide systems. . . . . 25
2.6 Eigenspectra of a fixed loss PTS coupled waveguide system. . . . . 25
2.7 1D PTS grating excitation setup. . . . . 28
2.8 Index distribution of a PTS system with an in-phase shift . . . . . 31
2.9 Transmission, reflection and absorption of the PTS grating vs conventional cases . . . . . 32

3.1 Material composition of a typical dielectric slab waveguide with the corresponding refractive indices of each layer. . . . . 36
3.2 Modal properties of fundamental modes in a 3-layer dielectric guiding structure. . . . . 38
3.3 Various plasmonic waveguide geometries and their field distributions. . 40
3.4 Various HWG designs and their field distributions. . . . . 41
3.5 Setup and material properties of a typical HGPW. . . . . 42
3.6 Modal properties of the fundamental HGPW mode. . . . . 44
3.7 Confinement and propagation loss trade off in HGPW. . . . . 46
3.8 Constituent modes of the fundamental hybrid mode. . . . . 47

4.1 Band Structure: basic concepts. . . . . 54
4.2 Summary of Free-Carrier theory. . . . . 55
4.3 Lorentzian and Sech lineshapes. . . . . 60

4.4 Various effects on the gain spectrum of GaAs. . . . . 63
4.5 Various effects on the carrier-induced refractive change. . . . . 63
4.6 The analytic and experimental results of bandgap shrinkage effect in many-body interaction analysis. . . . . 65
4.7 Many-body and other effects on the carrier-induced refractive index change. . . . . 66
4.8 Cavity setup. . . . . 67
4.9 Optical transition processes in a two-level system. . . . . 69
4.10 2-band structure equivalent of optical transitions in a three-level system. 71
4.11 The effect of $\beta_f$ on the photon number and the state occupation. . . . . 76

5.1 Different views of a HGPW laser. . . . . 79
5.2 Modal loss of the fundamental HGPW mode and Eikonal value for different taper angles as a function of gap width. . . . . 80
5.3 Reflectivity spectra of various DBR design for lasers. . . . . 82
5.4 Summary of the hybrid gap GaAs nanolaser fabrication steps. . . . . 83
5.5 Overview of GaAs growth results. . . . . 84
5.6 Flow chart of fabrication process. . . . . 84
5.7 SEM images of the hybrid gap plasmon GaAs nanolasers. . . . . 85
5.8 Pumping and collection method of hybrid gap plasmon GaAs nanolaser experiment. . . . . 86
5.9 Simulation results of the scattering properties of TE and TM modes of the DBRs . . . . . 87
5.10 Set-up of the GaAs hybrid plasmonic-photonic laser experiment. . . . . 88
5.11 2D CCD images of spatial and spectral resolution of the signal from a 1-step device with $\Lambda = 150$ nm. . . . . 89
5.12 Experimental results of the lasing action in hybrid gap plasmon GaAs lasers. . . . . 90
5.13 Lasing and GaAs properties at different power/spectral regimes. . . . . 92
5.14 Photoluminescence spectra of DBR-only and 2-step devices. . . . . 94

6.1 Spatial dimensions of the coupled waveguide system of interest. . . . . 99

6.2 Relevant gain properties of GaAs for different carrier concentrations. . 101
6.3 Simulation and analytic results of $\pm\sigma_0$ as a function of $\Im\{n_{GaAs}\}$. . . . 102
6.4 Eigenspectra and their properties of the coupled system in the case of imbalanced gain and loss. . . . . 104
6.5 Eigenspectra and their properties of the coupled system in the case of imbalanced modal index. . . . . 106
6.6 Eigenspectra of the coupled system in the highly dispersive regime. . . 108
6.7 The effects of different corewidths on the waveguide dispersion properties. 108
6.8 Eigenspectra of the highly dispersive coupled system when the recovery process is implemented. . . . . 110
6.9 Characteristic parameters of the coupled system after recovery procedure. 111
6.10 Phase rigidity as a function of gain of the system under different conditions. . . . . 113
6.11 Characteristic $|r|$ of the coupled system after recovery procedure. . . . 114

7.1 The index modulation and schematic sketch of a typical passive PTS grating. . . . . 118
7.2 Temporal response of excited electrons and phonons in a typical indirect bandgap semiconductor and a metal. . . . . 120
7.3 Various effects on the refractive index of Silicon as a function of carrier concentration at $\lambda = 1500$ nm. . . . . 123
7.4 Coupler geometries in Silicon characterization experiment. . . . . 125
7.5 Time-resolved pump probe setup. . . . . 125
7.6 Side view and top-down view of metallic gratings on a standard SOI platform. . . . . 127
7.7 Two operational modes of the experimental optical system: imaging and Fourier transform (FT) modes. . . . . 129
7.8 Selective interference of the three sources. . . . . 131
7.9 FFT and iFFT process of the three-source interference pattern for three measurements of interest. . . . . 132
7.10 Schematic sketch of 3-beam interference when the pump is at work. . . 133

7.11 Experimental result on the overlap of the pump and the probe beams on a piece of Silicon. . . . . 134
7.12 $\frac{\Delta T}{T}$ as a function of time in $\Delta n''_{Si}$ experiment. . . . . 135
7.13 Fitting a three temperature model onto $\frac{\Delta T}{T}$ experimental data. . . . . 137
7.14 $\Delta n''_{Si}$ and $\Delta n''_{m}$ as a function of carrier concentration. . . . . 137
7.15 $\Delta n'_{Si}$ and $\Delta n'_{m}$ as a function of carrier concentration. . . . . 139
7.16 Cross-section of the active PTS grating of interest and pumping strategy 140
7.17 Theoretical prediction of the potential forward and backward contrast ratio. . . . . 142
7.18 SEM images of potential designs of active PTS gratings . . . . . 143

C.1 FDTD simulation of conventional Bragg and PTS gratings. . . . . 176

E.1 SPP at the interface of a metal and a dielectric slab. . . . . 178
E.2 Dispersion of SPP. . . . . 180

# Publications

## Journal Publications

1. N. B. Nguyen *et al.,* 'Hybrid gap plasmon GaAs nanolasers'. Applied Physics Letters, 111(26), p.261107 (2017).

2. N. B. Nguyen *et al.,* 'Recovering parity-time symmetry in highly dispersive coupled optical waveguides.' New Journal of Physics, 18(12), 125012 (2016).

## Conference Contributions

1. Oral - SPP8 Taipei, Taiwan, May 2017 - Hybrid gap plasmon nanolasers.

2. Poster - SIOE Cardiff, UK, April 2016 - Printed GaAs Nanolaser.

3. Poster - Post graduate Symposium June 2016 - From active to functional hybrid gap plasmon waveguides.

4. Poster - London Plasmonics Forum June 2016 - Printed GaAs Nanolaser.

# Author's Contribution

- The fabrication of hybrid gap plasmon GaAs nanolasers described in **Chapter 5**, the fabrication of the Au gratings on SOI platform and the fabrication of Silicon waveguides and couplers detailed in **Chapter 7** were done by Dr. Micheal Nielsen. I was in charge of designing all these devices using a CAD machine and imaging them using SEM.
- The growth of the GaAs membranes described in **Chapter 5** was done at the University of Sheffield by Dr. Edmund Clarke and Dr. Paul Fry.
- The measurement of PL of different GaAs samples was carried out by Dr. Lucas Lafone. This result is presented in **Chapter 5** Fig. 5.4(b).

## Acknowledgements

I would like to dedicate the last few lines of this thesis to thank all the people who greatly supported me during my PhD both in Singapore and in London. First of all, I want to thank Prof. Stefan Maier and Prof. Minghui Hong for giving me this opportunity to embark on a unique PhD journey and for supporting me every step of the way. Dr. Rupert Oulton is the best supervisor I could ever wish for; I am very grateful for his knowledge, creativity and patience.

I would like to thank the group of very young, talented and enthusiastic postdocs: Dr. Themis Sidiropoulos, Dr. Sylvain Gennaro, Dr. Michael Nielsen, Dr. Lucas Lafone and Dr. Yi li, without whom the work presented in this thesis would have not materialized. All the members of the plasmonics group and the EXSS cluster office, I would like to thank them all for their help, support and the fun times we had together as a group.

I would like to thank the members of the Optical Science and Engineering Centre at NUS for their support and generosity, in particular Dr. Binghao Ng for his advice and guidance during my time in Singapore.

To my friends from H722+, thank you all for having been there for me in good times and bad times too: Albi, Brock, Daan, Haichao, Hattie, Javi, Monica, Nico, Paul, Rodri, Tom, Xiaofei and Zhijie (names appear in alphabetical order to avoid future dispute on favourism). And to a special friend whom I call brother, Dr. Toshihiko Shibanuma, I am grateful for his time, patience and wisdom and above all for letting me be closer to his wife, the beautiful Keiko and my goddaughter Karen.

These past three and a half years with a few ups and many downs, I would not be able to make it this far without the endless love that my Mum and my brother, Long, gave me. Thank you both! I would like to thank my Dad for always watching over me and reminding me to not ever give up. I also want to thank my girl, Tam, for staying by my side all these years and never complaining about my temper. And finally, to a certain someone, thank you for all the heartache and butterflies, and for being You!

# Re: Permission to use figures for thesis

Permissions <permissions@iop.org>

Mon 16/04/2018 11:35

Inbox

To: Nguyen, Ngoc <n.nguyen14@imperial.ac.uk>;

Dear Ngoc Nguyen,

Thank you for your request to reproduce content from http://iopscience.iop.org/article/10.1088/1367-2630/18/12/125012.

The content you have requested was published under a CC BY licence which permits reuse for any purposes, even commercial, provided the licence terms are adhered to.

Therefore you may reuse the content without permission, so long as you reference it adequately and adhere to the terms of the CC BY licence.

Please note this does not apply to any content/figure which is credited to another source in our publication or has been obtained from a third party, which is not available under a suitable open access licence. Express permission for such content/figures must be obtained from the copyright owner.

Kind regards,
Christina

**Copyright & Permissions Team**
Gemma Alaway – Senior Rights & Permissions Adviser
Christina Colwell - Rights & Permissions Assistant

Contact Details
E-mail: permissions@iop.org
For further information about copyright and how to request permission: http://iopscience.iop.org/page/copyright
Please see our Author Rights Policy http://ioppublishing.org/author-rights/
**Please note**: We do not provide signed permission forms as a separate attachment. Please print this email and provide it to your publisher as proof of permission.

**Please note**: Any statements made by IOP Publishing to the effect that authors do not need to get permission to use any content where IOP Publishing is not the publisher is not intended to constitute any sort of legal advice. Authors must make their own decisions as to the suitability of the content they are using and whether they require permission for it to be published within their article.

---

**From:** Nguyen, Ngoc <n.nguyen14@imperial.ac.uk>
**Sent:** 12 April 2018 17:12
**To:** Permissions
**Subject:** Permission to use figures for thesis

Dear Sir/Madam,

I am the first author of the article: "Recovering parity-time symmetry in highly dispersive coupled optical waveguides" published on 23rd December 2016, *New Journal of Physics* 18.12 (2016): 125012, which is under the Creative Commons Attribution 3.0 license.

I would like to ask permission to use the figures from the paper for my PhD thesis, which I am currently writing at Imperial college London, please.

Thank you very much.

Kind regards,
Ngoc Nguyen

---

This email (and attachments) are confidential and intended for the addressee(s) only. If you are not the intended recipient please notify the sender, delete any copies and do not take action in reliance on it. Any views expressed are the author's and do not represent those of IOP, except where specifically stated. IOP takes reasonable precautions to protect against viruses but accepts no responsibility for loss or damage arising from virus infection. For the protection of IOP's systems and staff emails are scanned automatically.

IOP Publishing Limited Registered in England under Registration No 467514. Registered Office: Temple Circus, Bristol BS1 6HG England Vat No GB 461 6000 84.

**Please consider the environment before printing this email**

---

## AIP PUBLISHING LICENSE
## TERMS AND CONDITIONS

Apr 12, 2018

This Agreement between Miss. Ngoc Bao Nguyen ("You") and AIP Publishing ("AIP Publishing") consists of your license details and the terms and conditions provided by AIP Publishing and Copyright Clearance Center.

| | |
|---|---|
| License Number | 4326580551441 |
| License date | Apr 12, 2018 |
| Licensed Content Publisher | AIP Publishing |
| Licensed Content Publication | Applied Physics Letters |
| Licensed Content Title | Hybrid gap plasmon GaAs nanolasers |
| Licensed Content Author | Ngoc B. Nguyen, Michael P. Nielsen, Lucas Lafone, et al |
| Licensed Content Date | Dec 25, 2017 |
| Licensed Content Volume | 111 |
| Licensed Content Issue | 26 |
| Type of Use | Thesis/Dissertation |
| Requestor type | Author (original article) |
| Format | Electronic |
| Portion | Figure/Table |
| Number of figures/tables | 4 |
| Title of your thesis / dissertation | Optical gain and loss in nanophotonic devices |
| Expected completion date | May 2018 |
| Estimated size (number of pages) | 200 |
| Requestor Location | Miss. Ngoc Bao Nguyen<br>100 Gosterwood Street<br><br>London, London SE8 5NY<br>United Kingdom<br>Attn: Miss. Ngoc Bao Nguyen |
| Billing Type | Invoice |
| Billing Address | Miss. Ngoc Bao Nguyen<br>100 Gosterwood Street<br><br>London, United Kingdom SE8 5NY<br>Attn: Miss. Ngoc Bao Nguyen |
| Total | 0.00 USD |

Terms and Conditions

AIP Publishing -- Terms and Conditions: Permissions Uses

AIP Publishing hereby grants to you the non-exclusive right and license to use and/or distribute the Material according to the use specified in your order, on a one-time basis, for the specified term, with a maximum distribution equal to the number that you have ordered. Any links or other content accompanying the Material are not the subject of this license.

1. You agree to include the following copyright and permission notice with the reproduction of the Material:"Reprinted from [FULL CITATION], with the permission of AIP Publishing." For

an article, the credit line and permission notice must be printed on the first page of the article or book chapter. For photographs, covers, or tables, the notice may appear with the Material, in a footnote, or in the reference list.

2. If you have licensed reuse of a figure, photograph, cover, or table, it is your responsibility to ensure that the material is original to AIP Publishing and does not contain the copyright of another entity, and that the copyright notice of the figure, photograph, cover, or table does not indicate that it was reprinted by AIP Publishing, with permission, from another source. Under no circumstances does AIP Publishing purport or intend to grant permission to reuse material to which it does not hold appropriate rights.
   You may not alter or modify the Material in any manner. You may translate the Material into another language only if you have licensed translation rights. You may not use the Material for promotional purposes.
3. The foregoing license shall not take effect unless and until AIP Publishing or its agent, Copyright Clearance Center, receives the Payment in accordance with Copyright Clearance Center Billing and Payment Terms and Conditions, which are incorporated herein by reference.
4. AIP Publishing or Copyright Clearance Center may, within two business days of granting this license, revoke the license for any reason whatsoever, with a full refund payable to you. Should you violate the terms of this license at any time, AIP Publishing, or Copyright Clearance Center may revoke the license with no refund to you. Notice of such revocation will be made using the contact information provided by you. Failure to receive such notice will not nullify the revocation.
5. AIP Publishing makes no representations or warranties with respect to the Material. You agree to indemnify and hold harmless AIP Publishing, and their officers, directors, employees or agents from and against any and all claims arising out of your use of the Material other than as specifically authorized herein.
6. The permission granted herein is personal to you and is not transferable or assignable without the prior written permission of AIP Publishing. This license may not be amended except in a writing signed by the party to be charged.
7. If purchase orders, acknowledgments or check endorsements are issued on any forms containing terms and conditions which are inconsistent with these provisions, such inconsistent terms and conditions shall be of no force and effect. This document, including the CCC Billing and Payment Terms and Conditions, shall be the entire agreement between the parties relating to the subject matter hereof.

This Agreement shall be governed by and construed in accordance with the laws of the State of New York. Both parties hereby submit to the jurisdiction of the courts of New York County for purposes of resolving any disputes that may arise hereunder.

V1.2

**Questions? customercare@copyright.com or +1-855-239-3415 (toll free in the US) or +1-978-646-2777.**